Skoltech

Skolkovo Institute of Science and Technology

Skolkovo Institute of Science and Technology

FIRST-PRINCIPLES STUDY OF ADVANCED THERMOELECTRIC MATERIALS:
METHODOLOGY AND APPLICATION

Doctoral Thesis

by

TAO FAN

DOCTORAL PROGRAM IN MATERIALS SCIENCE AND ENGINEERING

Supervisor
Professor Artem R. Oganov

Moscow - 2022

I hereby declare that the work presented in this thesis was carried out by myself at Skolkovo Institute of Science and Technology, Moscow, except where due acknowledgement is made, and has not been submitted for any other degree.

Candidate (Tao Fan)

Supervisor (Prof. Artem R. Oganov)

Abstract

Searching for thermoelectric materials with high energy conversion efficiency is important to solve the energy and environment issues of our society. A good thermoelectric material requires high Seebeck coefficient and electrical conductivity, in combination with low thermal conductivity. These properties are interconnected with each other, which makes it difficult to improve the overall performance of a material. Studies of thermoelectric materials mainly rely on experiments. However, calculations, especially those based on first-principles methods, are becoming popular in the thermoelectric community because of convenience and low cost. The main difficulty of using calculation to study thermoelectric materials is how to calculate transport properties of a material, which means solving the Boltzmann transport equation for both electrons and phonons. Although there are many models for solving such problems, they are either too simple and narrow to calculate a wide range of materials, or too complex and time-consuming to do high-throughput screening. In this work, we developed a computer program to calculate the thermoelectric transport properties of bulk materials on the basis of widely used models. Specifically, the electronic transport properties were computed using the generalized Kane band model and perturbation theory under the relaxation time approximation, whereas the lattice thermal conductivity was calculated using a modified Debye–Callaway model. The capability of the program was tested on a group of semiconductors, and the obtained results show reasonable agreement with experiment. The program works fast and is suitable for high-throughput screening. We used it to calculate the transport properties of 463 chalcogenides taken from a database and found that 94 of them are promising n-type or p-type materials, including six already well-known thermoelectric materials. We discuss 46 novel compositions having the maximum figure of merit larger than 1, such as CoAsS-like compounds of p-type and $CdSe_2$ of n-type, and show their thermoelectric transport properties in detail. This study shows an efficient way to search for novel thermoelectric materials and expands the field of current research of thermoelectric materials.

3

Publications

1. Tao Fan, Artem R. Oganov. "AICON: A program for calculating thermal conductivity quickly and accurately." *Computer Physics Communications* 251 (2020): 107074.

2. Tao Fan, Artem R. Oganov. "AICON2: A program for calculating transport properties quickly and accurately." *Computer Physics Communications* 266 (2021): 108027.

3. Tao Fan, Artem R. Oganov. "Discovery of high performance thermoelectric chalcogenides through first-principles high-throughput screening." *Journal of Materials Chemistry C* 9.38 (2021): 13226–13235.

4. Zhong, Yaqiong, Debalaya Sarker, Tao Fan, Liangliang Xu, Xie Li, Guang-Zhao Qin, Zhong-Kang Han, and Jiaolin Cui. "Computationally Guided Synthesis of High Performance Thermoelectric Materials: Defect Engineering in $AgGaTe_2$." *Advanced Electronic Materials* 7.4 (2021): 2001262.

Acknowledgements

I would like to give my sincere gratitude to my supervisor, Prof. Artem R. Oganov, who trusted me and gave me great support during PhD. Thanks for his ideas, advices and corrections in every paper we published, and in this thesis. I have learned a lot from him to be an excellent researcher.

I am also grateful to my colleagues in Skoltech, Zhenghai Wang, Congwei Xie, Hao Li, Zahed Allahyari, Aleksandr Kvashnin, Ilia Chepkasov and Pavel Bushlanov, who discussed with me or gave me support from other aspects.

Finally, I want to thank Skoltech for giving me the opportunity to do my PhD studies. I have a lot of wonderful memories in this place.

Table of Contents

List of Symbols, Abbreviations

A – Hall factor

BTE – Boltzmann transport equation

B – bulk modulus

CMFP – constant mean free path approximation

CEPC – constant electron-phonon coupling approximation

C_{ii} – elastic constant matrix element

c – direction-averaged elastic constant

c_i – fractional atomic natural abundance

DFT – density functional theory

DFPT – density functional perturbation theory

EMF – electromotive force

E_n – energy of the nth band

e – elementary charge

f_D – Debye function

f_E – Einstein function

G – shear modulus

I – electrical current

IFCs – interatomic force constants

K – effective mass anisotropic factor

$\mathbf{k}$ – wave vector for charge carriers

k_B – Boltzmann constant

L, L_0 – Lorenz number

MD – molecular dynamics

MLWF – maximally localized Wannier functions

M – mean atomic mass in crystal

M_i – average atomic mass of element i

m_i – atomic mass of the ith isotope

N – band degeneracy

n – carrier concentration

PAW – projector augmented wave

PBE-GGA – Perdew-Burke-Ernzerhof generalized gradient approximation

PF – thermoelectric power factor

PGEC – phonon glass and electron single crystal

PLEC – phonon liquid and electron single crystal

p – number of atoms in the primitive cell

q – rate of heat flow

q – wave vector for phonons

RTA – relaxation time approximation

RMSrD – root-mean-square relative deviation

R – Hall coefficient

r – Pearson correlation coefficient

r_s – Spearman rank coefficient

r_∞ – screening radius of the medium with ε_∞

r_0 – screening radius of the medium with ε_0

SOC – spin-orbit coupling

T – absolute temperature in Kelvin

ΔT – temperature difference

V – voltage; volume of the primitive cell

ZT – dimensionless thermoelectric figure of merit

z – reduced band energy

α – Seebeck coefficient or thermopower

α_{ab} – relative Seebeck coefficient or thermopower

β – reciprocal of the reduced band gap

β_{SE} – semi-empirical descriptor

Γ – mass fluctuation phonon scattering parameter

γ – Grüneisen parameter

ε – band energy

ε_g – band gap

ε_∞ – high-frequency dielectric constant

ε_0 – static dielectric constant

ξ – reduced Fermi energy

η – Fermi energy

κ_e – electronic thermal conductivity

κ_L – lattice thermal conductivity

κ – total thermal conductivity

Φ – logarithmic factor

μ – carrier mobility

π_{ab} – relative Peltier coefficient

$\rho(z)$ – density of states at reduced energy z

ρ – mass density

σ – electrical conductivity

τ – relaxation time of carriers

τ_{aco} – carrier relaxation time due to acoustic phonon scattering

τ_{opt} – carrier relaxation time due to polar optical phonon scattering

τ_{imp} – carrier relaxation time due to ionized impurity scattering

τ_N – relaxation time for normal scattering process

τ_U – relaxation time for Umklapp scattering process

τ_I – relaxation time for phonon-isotope scattering process

τ_R – relaxation time for all resistive scattering processes

Θ_D – Debye temperature

Θ_E – Einstein temperature

θ – branch Debye temperature

v – phonon velocity

v_L – longitudinal acoustic phonon velocity

v_T – transverse acoustic phonon velocity

ω – phonon frequency

$\varXi$ – deformation potential constant

$\hbar$ – Planck constant

m_b^* – inertial effective mass

m_c^* – conductivity effective mass

m_d^* – density of states (DOS) effective mass

$m_\perp^*$ – transverse component of band effective mass

$m_\parallel^*$ – longitudinal component of band effective mass

$k_\perp$ – transverse component of the wave vector **k**

$k_\parallel$ – longitudinal components of the wave vector **k**

Δl_V – volumetric strain

List of Figures

16

List of Tables

Chapter 1. Introduction

1.1. Thermoelectric Materials: An Overview

Massive usage of fossil fuel has caused a lot of problems in the world, such as climate change, water and air pollution, and so forth. Meanwhile, the fossil fuel itself faces the increasing risk of being exhausted, as the world's demand for energy keeps increasing. Finding alternative energy sources to enrich the current energy structure is the key for the human society to achieve sustainable development. Besides the widely explored renewable energy sources such as solar energy, wind, and nuclear energy, improving the utilization rate of the traditional energy sources is thought of as another type of "renewable energy". A higher utilization rate not only means lower cost and improvement of the energy sustainability, it could also reduce the emission of greenhouse gases. For example, during the industrial production and use of automobiles, a large amount of energy is wasted as heat, which has a high use value, with the temperature of parts generating it usually lying between 400 °C and 1000 °C [1]. Thermoelectric technology aims to collect and reuse such kinds of waste heat, which, if reused fully, can bring considerable economic and environmental benefits.

Thermoelectric material is a functional material which can convert heat into electricity and vice versa, via the internal carrier movement [2,3]. The physical principles underlying the thermoelectric energy conversion are the Seebeck effect (thermoelectric generator) and the Peltier effect (thermoelectric refrigerator). As a simple schematic shown in Fig. 1.1, it can be considered as a circuit formed from two different conductors **a** and **b** (referred to as thermocouple legs in a thermoelectric device), which are connected electrically in series but thermally in parallel. Two junction points are A and B. Conductor **b** is divided into two parts (the breaking points are C and D) so that a voltmeter can be connected in the gap. Supposing a temperature difference ΔT is established between the two junctions while the two free ends of conductor **b** are maintained at the same temperature, the potential difference V will appear between points C and D. The differential Seebeck coefficient α_{ab}, is defined as the ratio of V to ΔT,

$$\alpha_{ab} = \frac{V}{\Delta T}$$

α_{ab} is considered positive if the electromotive force (EMF) tends to drive electric current through conductor **a** from the hot junction to the cold junction.

If a source of the EMF is connected to points C and D so as to drive electric current in the circuit in the clockwise direction, the Peltier coefficient is regarded as positive if junction A is heated and junction B is cooled. The relative Peltier coefficient π_{ab} is equal to the ratio of the rate of heating or cooling q at each junction to the electric current I:

$$\pi_{ab} = \frac{q}{I}$$
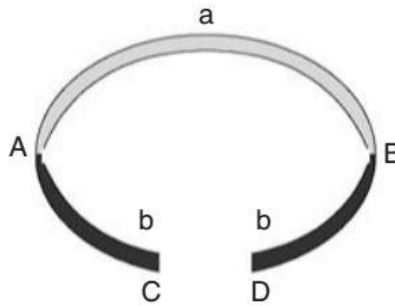
Figure 1.1. Diagram of the thermoelectric effect [2].

For a thermoelectric material, no matter if it is used as a generator or refrigerator, the highest energy conversion efficiency at a given temperature T is quantified by its dimensionless figure of merit (ZT). ZT is defined as $ZT = \alpha^2 \sigma T / (\kappa_e + \kappa_L)$, where α is the Seebeck coefficient, σ is the electrical conductivity, κ_e is the electronic thermal conductivity, and κ_L is the lattice thermal conductivity. Particularly, $\alpha^2 \sigma$ is called the power factor (PF). To obtain high ZT, both α and σ must be maximized, whereas κ_e and κ_L need to be minimized. However, the interdependence of these parameters makes it challenging to improve an average ZT of a material, as shown in Fig. 1.2. For example, both α and σ are related with carrier concentration n. σ is proportional to n, while α is inversely proportional to n (the Pisarenko relation). In addition, according to the Wiedemann-Franz

law, $\kappa_e = L\sigma T$, where L is the Lorenz number. Thus, any method increasing σ will also increase κ_e.
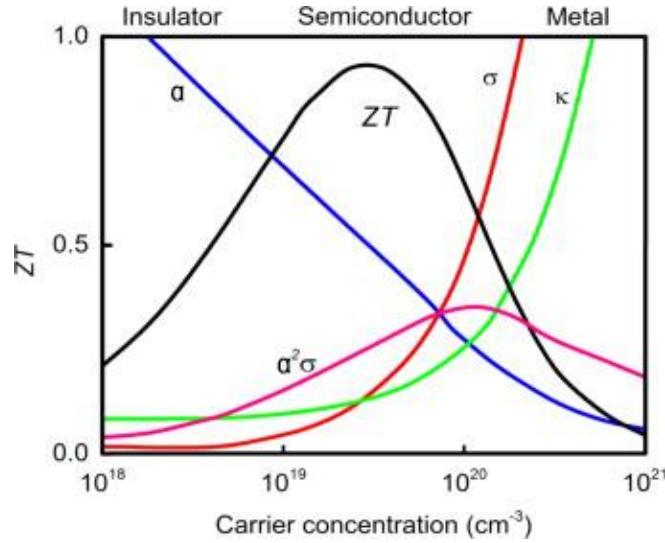
Figure 1.2. Schematic of the dependence of the electrical conductivity σ, Seebeck coefficient α, thermal conductivity κ, power factor $\alpha^2\sigma$, and figure of merit ZT on the concentration of free carriers [4].

Although the Seebeck effect has long been applied to temperature measurement and detection of thermal radiation, it was not until the introduction of semiconductors as thermoelectric materials in the 1950s that thermoelectric devices for power generation and cooling with practical application value were produced. The first climax of thermoelectric research was triggered at that time. In 1954, Goldsmid discovered that a thermocouple composed of p-type bismuth telluride (Bi_2Te_3) and a negative thermoelement made from metallic bismuth (Bi) can produce a cooling effect of 26 K below room temperature [5]. Subsequent studies have shown that the alloy systems composed of Bi_2Te_3, Sb_2Te_3 and Bi_2Se_3 are ideal room temperature thermoelectric materials [6–10]. The best p-type composition is near $(Sb_{0.8}Bi_{0.2})_2Te_3$, whereas the best n-type composition is near $Bi_2(Te_{0.8}Se_{0.2})_3$. These alloy systems have low thermal conductivity, and their power factor can be improved by adjusting the carrier concentration. The maximum figure of merit ZT of these alloys is about 0.8 – 1.1. Thermoelectric materials used in the mid-temperature

22

range (500 – 900 K) are mainly based on group-IV tellurides, such as PbTe, GeTe and SnTe [6, 8, 11, 12]. Among them, alloys composed of PbTe and $AgSbTe_2$ (also called "LAST") have shown maximum ZT > 1 for both n-type and p-type materials [13,14]. Another p-type material $(GeTe)_{0.85}(AgSbTe_2)_{0.15}$ (named "TAGS") can exhibit a maximum *ZT* value larger than 1.2 [15], which has been successfully used in long-life thermoelectric generators. For thermoelectric devices working at high temperatures (> 900 K), Si-Ge alloys are typically used for both n-type and p-type legs [16]. However, because of high lattice thermal conductivity, their *ZT* values are relatively low. For n-type material, it is near 1 (900 K); for p-type material, 0.6 (900 K).

From 1960 to 1990, thermoelectric technology began to move from the laboratories to various practical application fields [17]. However, the research on thermoelectric materials themselves had stagnated, and the figure of merit *ZT* of thermoelectric materials had not made major breakthroughs. By the mid-1990s, two factors had led to a resurgence of thermoelectric research: first, people had gradually realized that fossil fuels will eventually be exhausted and their use had caused serious environmental problems, therefore finding alternative energy sources and energy protection had become the consensus of various countries; second, advances in science and technology such as the improvement of the theory of transport properties of mesoscopic systems, the rise of nanomaterials research, advanced synthesis techniques and analytical tools, had promoted the understanding of the structure–properties relations in materials.

In the past twenty years, major breakthroughs have been made in the field of thermoelectric research, not only discovering many new and efficient thermoelectric materials, but also greatly improving the performance of classic ones. The research of modern thermoelectric materials is based on two main ideas: one is to use low-dimensional materials, that is, to introduce nanostructures; the other is to develop new bulk materials with complex structures. The low-dimensional materials method is mainly based on two considerations: that a nanoscale structure can introduce quantum confinement effects to enhance the power factor *PF*, and that a large number of nano-level grain boundaries existing in these materials can effectively reduce thermal conductivity while having little

23

effect on the electrical conductivity [18,19]. The research of thermoelectric nanomaterials mainly includes two-dimensional quantum wells/superlattices [20], nanowires [21], quantum dots [22,23] and nanocomposites [24–27]. By exploring nanoscale effects, the thermoelectric properties of these materials have been greatly improved compared with traditional bulk thermoelectric materials. For example, for the quantum dot superlattices formed by PbTe and PbSe while adding Bi as an electron donor, the figure of merit *ZT* reached 1.6 and 3.5 at 300 K and 570 K, respectively [28]. On the other hand, guided by "phonon glass electron crystal" (PGEC) principle proposed by Slack [29], many new bulk materials with complex unit cells have been discovered to have enhanced thermoelectric performance. For example, in clathrates [30] and skutterudites [31,32] some structural sites in the unit cell are occupied by heavy atoms, which often have a large vibration amplitude and can be used as effective phonon scattering centers to reduce thermal conductivity. Zintl alloys [33] and anisotropic chalcogenides [34–36] have very low thermal conductivity due to strong anharmonicity. Particularly, single crystal of binary compound SnSe — an orthogonal crystal at room temperature — has an extremely low thermal conductivity (0.23 $W \cdot m^{-1} \cdot K^{-1}$, at 900 K) due to strong anharmonicity and bond anisotropy in the lattice. The *ZT* value along the *b* axis could reach 2.6 at 900 K [36]. Although single crystal SnSe has a very good performance, its polycrystalline versions show much lower *ZT*, mainly due to much higher thermal conductivity in polycrystalline samples. This higher thermal conductivity is attributed to the presence of SnO_x at grain boundaries and surfaces of polycrystalline SnSe samples [37]. Recently, Zhou et al. have developed an efficient two-step process to minimize the presence of SnO_x in SnSe, thus greatly reducing the thermal conductivity in polycrystalline samples [38]. Their samples show surprisingly high values of *ZT* — the maximum value is about 3.1 at 783 K and the average value is near 2 in the temperature range of 400 to 783 K. Besides SnSe, it was also reported that $SnS_{0.91}Se_{0.09}$ has an average ZT ~ 1.25 in the range from 300 to 873 K [39]. This is achieved by optimizing the effective mass and carrier mobility synergistically, thus improving the power factor while keeping the relatively low lattice thermal conductivity. Beyond the PGEC concept, researchers have proposed a new strategy, named "phonon liquid electron

crystal" (PLEC), to further decrease κ_L below that of glass [40]. The representatives of such materials are $Cu_{2-\delta}X$ (X = S, Se, or Te) liquid-like ionic conductors [41,42]. These compounds have a rigid face-centered cubic sublattice X that provides a crystalline pathway for conducting electrons, whereas copper ions are disorderedly distributed around the X sublattice and have a liquid-like mobility. The transverse vibrational modes are inhibited, and heat-conducting phonons are strongly scattered. Therefore, the specific heat and thermal conductivity of these compounds could be limited to the liquid limit (two-thirds of the value of the solid). Because of such exceptionally low values of the lattice thermal conductivity (0.2–0.5 $W \cdot m^{-1} \cdot K^{-1}$), their ZT values are high (1.1 – 1.7) in the high temperature range. With the improvement of synthesis methods and introduction of various engineering techniques, such as solid solution, porosity engineering and introducing additional graphene, the peak ZT values of Cu_2X-based thermoelectric materials are currently higher than 2. In addition to the above materials, other widely studied thermoelectric materials include silicides [43], half-Heusler intermetallic compounds [44,45], and organic matters [46–48]. Those interested in the topic can refer to the excellent review articles [49–57].

In terms of application, limited by the low conversion efficiency (< 10%) of early thermoelectric materials, thermoelectric devices can only be used in such areas where reliability and simplicity are more demanding than cost and efficiency considerations. For example, all deep space probes launched by the United States in the last century were equipped with isotopic thermoelectric power generation devices, which use the heat generated by the decay of radioisotopes to generate electricity to power the probes. In recent years, with the advancement of technology, thermoelectric devices have found much wider applications [58,59], such as small and mobile refrigerators, automobile seat cooling devices, industrial electronic devices, micro self-powered wireless platforms, health monitoring and tracking systems, and so forth. However, there is still a lot of space for improvement. Theoretically, if ZT could reach 3, thermoelectric home refrigerators would be competitive with traditional compressor-based refrigerators. If ZT could reach 4, then the energy conversion efficiency between heat and electricity would be around 30%, which

would be a very promising prospect for practical systems. Fortunately, from the viewpoint of thermodynamics, there is no limitation of the value of *ZT* [60].

1.2. Computer Aided Discovery of Thermoelectric Materials

From the definition of the figure of merit *ZT*, the performance of thermoelectric materials is mainly determined by the Seebeck coefficient, electrical conductivity, and thermal conductivity (including the electronic and lattice parts). Currently, these parameters can be calculated using modern first-principles methods. In this section, we review the methods for calculating these transport properties and works using these methods to screen thermoelectric materials.

1.2.1. Electrical transport properties

The electrical transport properties, such as the electrical conductivity, are fundamental in various scientific and technological applications. For example, a thermoelectric material should be a good conductor to have a high figure of merit, whereas other applications like piezoelectric materials require an insulator. Theoretically, electrical conductivity can be calculated using modern density functional theory (DFT) and density functional perturbation theory (DFPT). Currently, there are several software programs released for this purpose, such as BoltzTraP [61], BoltzWann [62], EPA [63], EPIC STAR [64], AMSET [65], PERTURBO [66] and elphbolt [67]. Among them, BoltzTraP and BoltzWann are based on the semiclassical transport theory with the constant relaxation time approximation (CRTA). They differ in the method of interpolating the bands: the former uses the Fourier expansion of the band energies with symmetry being kept by star functions, whereas the latter utilizes the maximally localized Wannier functions (MLWF) basis to interpolate the plane wave results. Although these calculations are easier and faster than a fully ab initio method, the CRTA itself is a rough approximation because the relaxation time, which is usually a function of the temperature and chemical potential, cannot be considered constant. EPA uses the electron-phonon averaged approximation to calculate the electron energy relaxation time induced by electron-phonon coupling. The

core idea of the EPA approximation is to change the complex momentum space integration in the relaxation time expression into an integration over energies through replacing momentum-dependent quantities with their energy-dependent averages. The program can be combined with BoltzTrap to calculate the electrical transport coefficients. The results of testing on half-Heusler compounds show reasonable agreement with experimental values at high temperatures. EPIC STAR uses the so-called "Energy-dependent Phonon- and Impurity-limited Carrier Scattering Time Approximation" method to evaluate the electronic relaxation time. The electron-phonon scattering process is split into two parts: the short-range scattering and the long-range scattering. The short-range electron-phonon interactions are described numerically using the generalized Eliashberg function $\alpha^2 F(E, \omega)$, which depends on both electron energy E and phonon frequency ω. The long- range polar-optical phonon scattering and impurity scattering are treated using analytical expressions. The whole calculating process is relatively fast and the time is mainly limited by the DFPT calculations. The method is validated on several representative semiconductors and shows quantitative agreement with experimental measurements for both polar and non-polar, isotropic and anisotropic materials. AMSET (Ab initio Scattering and Transport) calculates the scattering rates using the momentum relaxation time approximation (MRTA) for the Boltzmann transport equation (BTE). The method extends existing polar and non-polar electron-phonon coupling, ionized impurity, and piezoelectric scattering formulas for isotropic band structures to support anisotropic materials. The program has been tested on a wide range of semiconductors and agreement of mobility with experiment improved significantly (Spearman rank coefficient $r_s = 0.93$), compared with the results obtained by BoltzTrap ($r_s = 0.52$). PERTURBO uses a fully first-principles approach to calculate the electron-phonon coupling based on the DFPT and employs an iterative solution of the linearized Boltzmann transport equation. However, in order to make the calculations converge, the electron-phonon matrix elements need to be computed on extremely dense k- and q-point meshes in the Brillouin zone (BZ), usually having millions of points. Although it uses the Wannier interpolation to map matrix elements calculated on a coarse grid into a fine grid, still the multistep construction procedure for

the Wannier functions and a huge number of grid points makes such calculations too expensive. Therefore, this method has only been used to study highly symmetric systems with a small number of atoms [68–70]. The method implemented in elphbolt is even beyond that in PERTURBO — it solves the electron-phonon coupled BTEs using ab initio methods. Specifically, there exists a momentum-mixing between the electrons and the phonons in real transport situations, which cause both particles to move under the influence of external fields. Therefore, instead of only solving the transport equations for electrons, this program solves four transport equations for both electrons and phonons in electric and temperature gradient fields at the same time. Because of that, such calculations are prohibitively expensive even for very simple systems, such as Si [67]. Besides the mentioned methods of calculating the transport properties, there is another, much easier way based on the deformation potential theory.

In 1950, Bardeen and Shockley proposed the deformation potential theory to calculate mobilities in non-polar crystals [71], which is based on assumptions that the energy surface is isotropic, the electrons only interact with the acoustic phonon modes having long wave-lengths, and the local deformations produced by the lattice waves are similar to those in homogeneously deformed crystals. Therefore, a matrix element of the interaction between electrons and phonons can be formulated with a key parameter, the deformation potential constant E_1. This constant can be calculated from the variation in the energy band edges with the lattice constant. Later, Herring and Vogt had generalized this theory to include anisotropy in the scattering processes for semiconductors with multiple nondegenerate band edges [72]. The energy surface for each band edge point is assumed to be ellipsoidal, whereas the strength of the electron-phonon interaction is still characterized by the deformation potential constant. However, in this generalized method, there are two deformation potential constants, E_d and E_u, and they can be obtained from fitting experimental data. The authors applied this method to calculate charge carrier mobilities in n-type germanium and silicon, and the results were in reasonable agreement with the observations. Based on the generalized Kane band model and perturbation theory, Ravich et al. have developed a method to calculate the transport properties and analyzed the

experimental data in lead chalcogenides [73,74]. In this method, four scattering mechanisms, including acoustic phonon scattering, polar optical phonon scattering, impurity scattering, and collisions between carriers, are mainly considered, and all necessary parameters can be obtained from experiment. The calculated transport coefficients showed quite close agreement with the experimental values in a wide range of temperatures and carrier concentrations. Many applications have been developed in recent years on the basis of Ravich's method [75–78], verifying its reliability.

1.2.2. Lattice thermal conductivity

Calculation of the lattice thermal conductivity is computationally demanding because it involves multiple-phonon scattering processes. Currently, the methods most commonly used in such calculations are based on solving the phonon Boltzmann transport equation (PBTE), for which the most conventional way is to use the relaxation time approximation (RTA) along with the Debye approximation. Such solution involves calculation of the phonon frequencies, group velocities, and harmonic and anharmonic interatomic force constants (IFCs) [79]. Although the density functional theory (DFT) is a convenient tool for accurately calculating the interatomic interactions in many cases, obtaining high-order, at least the third-order, force constants used in the description of anharmonicity in phonon–phonon processes is still time-consuming. This approach has been implemented in several software packages, including Phono3py [80], ShengBTE [81], and ALAMODE [82]. Alternatively, the lattice thermal conductivity can be calculated directly using the temperature gradient from the nonequilibrium molecular dynamics (MD) simulation at a given heat current [83,84] or from the equilibrium MD simulations using the Green-Kubo method [85,86]. However, the MD simulations need a large unit cell to take into account the finite size effect and a long simulation time to converge the autocorrelation function. Moreover, these methods require very accurate force fields at specified conditions of temperature and pressure, which are usually lacking for most of inorganic compounds. Besides the methods mentioned above, some semi-empirical models could also be used. For example, as implemented in AFLOW-AGL [87], the lattice thermal conductivity can

be calculated using a model proposed by Slack [88]. The required input parameters are the Debye temperature and Grüneisen parameter, which can be calculated using the quasi-harmonic Debye model. The predicted lattice thermal conductivities for compounds with different structural types have high correlation coefficients with the experimental ones (average 0.88). Another more widely used semi-empirical model is the Debye-Callaway model.

In 1959, Callaway proposed a solution for the PBTE based on three assumptions [89]: first, only four scattering mechanisms are considered, including point impurities (isotopes disorder), normal three-phonon processes, Umklapp processes and boundary scattering; second, all phonon scattering processes can be represented by frequency-dependent relaxation times; third, the crystal vibration spectrum is isotropic and dispersion-free. Based on this model, κ_L of germanium was calculated in the temperature range from 2 K to 100 K. The results showed reasonable agreement with experiment for both normal and single-isotope material. Asen-Palmer [90] modified the Debye-Callaway model by accounting for the contributions of longitudinal and transverse acoustic branches differently. In addition, this approach uses six freely adjustable parameters for longitudinal and transverse modes to include the anharmonic effect and contributions from the boundary and isotope scattering. Unfortunately, these models lack the predictive power because they incorporate parameters that are either fitted to experimental data or freely adjustable. Morelli et al. [91] modeled the lattice thermal conductivity and isotope effect in Ge, Si, and diamond using an approach similar to that of Asen-Palmer. However, they used the known phonon dispersion relations of these crystals to derive all the necessary parameters except the Grüneisen parameter. Recently, Zhang [92] has developed a first-principles Debye-Callaway approach where all the parameters (i.e., the Debye temperature θ, phonon velocity v, and Grüneisen parameter γ) can be directly calculated from the vibrational properties of compounds within the quasi-harmonic approximation.

1.2.3. High-throughput screening for thermoelectric materials

With the advance of theory and growth of computing power, materials research and discovery based on first-principles methods are becoming popular. This approach has been used in many research fields and led to interesting discoveries [93–95]. The first high-throughput search for thermoelectric materials was done by Madsen using BoltzTrap [96]. In this work, transport properties of 570 Sb-containing compounds were assessed and LiZnSb was identified as a promising n-type candidate. Later, Yang et al. used the same method to study 36 half-Heusler (HH) compounds. On the basis of the calculated maximum power factors, the researchers suggested Co-, Rh- and Fe- based HHs as p-type, and LaPdBi as n-type prospective materials [97]. Zhu et al. used the same method to screen ~9000 materials on the basis of the Materials Project database [98]. They identified trigonal and tetragonal $TmAgTe_2$ as potential candidates with the ZT values around 1.8 at 600 K. Later the authors synthesized trigonal $TmAgTe_2$ and showed, although it had a very low thermal conductivity, the highest ZT achieved was 0.35 because of the limited hole concentration. Carrete et al. have combined the Boltzmann transport theory with the constant mean free path approximation (CMFP) to study the thermoelectric properties of 75 nanograined HH compounds [99]. Five candidates have been identified for room and high-temperature applications, respectively. Xi et al. have combined the Boltzmann transport theory with the constant electron-phonon coupling approximation (CEPC) to calculate the electrical transport properties of 161 p-type diamond-like chalcogenides [100]. They have found that vacancy-containing chalcogenides, such as $CdIn_2Te_4$ and $ZnIn_2Te_4$, could have high thermoelectric performance. One of the variations, $Cd_2Cu_3In_3Te_8$, was synthesized and showed ZT values above 1 at high temperatures.

Besides these works which calculate thermoelectric properties directly with all kinds of approximation, there are also other works based on semi-empirical models to screen the materials. For example, Toberer et al. have proposed the descriptor β_{SE} to quantify the material's potential for high ZT when appropriately doped [101]. β_{SE} is composed of the room temperature intrinsic charge carrier mobility μ_0 and lattice thermal conductivity κ_L, both of which can be computed using semi-empirical models. Tests showed that good

thermoelectric materials are correctly identified as those with large values of β_{SE}. Using this descriptor, the researchers have studied the thermoelectric properties of 518 binary A1B1 compounds and 427 binary quasi-2D compounds successively, and found many promising candidates that had not been previously considered [102,103]. Jia et al. have proposed two descriptors — the electrical descriptor χ and the lattice anharmonicity descriptor γ — in order to characterize the power factor and lattice thermal conductivity, respectively [104]. χ can be calculated using the deformation potential theory and the rigid band approximation, while γ can be evaluated based on the variation of the elastic properties with the volume. The authors screened 243 binary semiconductor chalcogenides in the database using the two descriptors. 50 compounds have been identified as promising thermoelectric materials with both good electronic properties and low thermal conductivities. Among them, 9 p-type and 14 n-type materials were new.

The methods mentioned above have been widely used and led to many discoveries. However, some issues remain within them. For example, both CRTA and CMFP assume the electronic relaxation time is energy independent and has the same constant value for different materials. The accuracy of such assumptions has always been questioned. Moreover, in all of these high-throughput works, the lattice thermal conductivity values are either taken from experiments of already known materials or values calculated by simple and empirical models are used.

1.3. Research Contents of This Work

Thermoelectric researches have made great progress in recent decades. However, the current energy conversion efficiency and manufacture cost still do not support massive application. A material with a higher figure of merit and lower cost is always desirable. On the other hand, although several computational tools can be used currently to calculate the thermoelectric related transport properties, these tools are unsuitable for rapid screening of large databases of materials with the purpose of identifying promising candidates for more in-depth experimental analysis. Such calculations have to balance well between speed and accuracy. Therefore, the work in this thesis aims to achieve two goals: first, develop a

software program for calculating the transport properties quickly and accurately; second, screen materials in a database to find novel compounds with promising properties, thus providing guidance to the experiment. Specifically, the research contents of this work includes:

1. Developing an algorithm for calculating the lattice thermal conductivity on the basis of the Debye-Callaway model;

2. Developing an algorithm for calculating the electrical transport properties on the basis of Ravich's model [73,74];

3. Using the developed software program to calculate the figure of merit *ZT* of chalcogenide compounds taken from the Materials Project database;

4. Processing and analyzing data;

5. Writing the thesis.

Chapter 2. Methodology

This section introduces the mathematical model used in the research, including the models of the lattice thermal conductivity and electronic transport properties, the calculating procedures, their specific implementation in our AICON program, and the results of their testing on carefully selected sets of materials.

2.1. Model of Lattice Thermal Conductivity

2.1.1. Modified Debye-Callaway model

The commonly used formulas of the Debye-Callaway model, which was proposed by Morelli [91], only include contributions from acoustic phonons (eq. 2.1b – 2.1c). We updated the formulas by adding the contribution from optical phonons, because they are important at high temperature and in compounds with complex structure (eq. 2.1e). The total lattice thermal conductivity κ is the sum of the contributions from the acoustic branches (one longitudinal κ_{LA}, two transverse κ_{TA} and $\kappa_{TA'}$) and one pseudo-optical branch κ_O:

$$\kappa = \kappa_{LA} + \kappa_{TA} + \kappa_{TA'} + \kappa_{O} \tag{2.1a}$$

$$\kappa_i = \kappa_{i1} + \kappa_{i2} \quad (i = \text{TA, TA', LA}) \tag{2.1b}$$

$$\kappa_{i1} = \frac{1}{3} C_i T^3 \int_0^{\theta_i/T} \frac{\tau_C^i(x) x^4 e^x}{(e^x - 1)^2} dx \tag{2.1c}$$

$$\kappa_{i2} = \frac{1}{3} C_i T^3 \frac{\left[\int_0^{\theta_i/T} \frac{\tau_C^i(x) x^4 e^x}{(e^x - 1)^2} dx \right]^2}{\int_0^{\theta_i/T} \frac{\tau_C^i(x) x^4 e^x}{\tau_N^i(x) \tau_R^i(x)(e^x - 1)^2} dx} \tag{2.1d}$$

$$\kappa_{O} = \frac{1}{3}(3p - 3)\frac{N}{V} k_B f_E\left(\frac{\Theta_E}{T}\right) v_O^2 \tau_C^O \left| 1 + \frac{\tau_R^O}{\tau_N^O} \right| \tag{2.1e}$$

In these formulas, θ_i is the Debye temperature for each phonon branch, $C_i = k_B^4/(2\pi^2 \hbar^3 v_i)$ and $x = \hbar\omega/k_B T$, where $\hbar$ is the Planck constant, k_B is the Boltzmann

constant, ω is the phonon frequency, and v_i is the phonon velocity for each branch; $\left(\tau_N^i\right)^{-1}$ is the scattering rate of the normal phonon process, $\left(\tau_R^i\right)^{-1}$ is the total scattering rate of all the resistive scattering processes, and $\left(\tau_C^i\right)^{-1} = \left(\tau_N^i\right)^{-1} + \left(\tau_R^i\right)^{-1}$. According to Callaway, $\left(\tau_R^i\right)^{-1}$ should be equal to the sum of the scattering rates of the phonon–phonon Umklapp scattering, isotope point defect scattering, and scattering on the crystal boundary. In our model, only the Umklapp scattering and isotope scattering are considered, so that $\left(\tau_R^i\right)^{-1} = \left(\tau_U^i\right)^{-1} + \left(\tau_I^i\right)^{-1}$. For most practical applications like thermoelectricity, where the temperature is usually above 300 K, it is reasonable to omit boundary scattering because it becomes significant only at very low temperatures, usually tens of Kelvins. Further, p is the number of atoms in a primitive cell, thus $3p - 3$ is the number of the optical phonon branches; N is the number of primitive cells (usually, $N = 1$), V is the volume of a primitive cell, v_O is the average velocity of an optical phonon, Θ_E is the Einstein temperature and the function f_E is the so-called Einstein function.

2.1.2. Phonon–phonon normal scattering

Although the normal phonon scattering is not a resistive process, it can redistribute the momentum and energy among phonons and influence other resistive scattering processes (such as the Umklapp scattering). Following the approach of Asen-Palmer [90], the appropriate forms for the longitudinal and transverse acoustic phonons are

$$\left[\tau_N^L(x)\right]^{-1} = B_N^L \left(\frac{k_B}{\hbar}\right)^2 x^2 T^5 \tag{2.2a}$$

and

$$\left[\tau_N^T(x)\right]^{-1} = B_N^T \left(\frac{k_B}{\hbar}\right) x T^5 \tag{2.2b}$$

with magnitudes B_N depending on the phonon velocity v and Grüneisen parameter γ:

$$B_N^L = \frac{k_B^3 \gamma_L^2 V}{M \hbar^2 v_L^5} \tag{2.3a}$$

and

$$B_N^T = \frac{k_B^4 \gamma_T^2 V}{M \hbar^3 v_T^5} \tag{2.3b}$$

where M is the average atomic mass in the crystal and V is the volume per atom. A more general case and further discussion are included in the Appendix of Ref. [91]. For the optical branch, we assume the same formula as for the longitudinal acoustic branch because of simplicity and consistency.

2.1.3. Phonon–phonon Umklapp scattering

The phonon–phonon Umklapp processes dominate at high temperatures, following an exponential behavior. According to Morelli [91], the Umklapp scattering rate for the longitudinal and transverse acoustic phonons is:

$$\left[\tau_U^i(x) \right]^{-1} = B_U^i \left(\frac{k_B}{\hbar} \right)^2 x^2 T^3 e^{-\theta_i/3T} \tag{2.4a}$$

where

$$B_U^i = \frac{\hbar \gamma_i^2}{M v_i^2 \theta_i} \tag{2.4b}$$

The Umklapp scattering rate thus depends on the Debye temperature, phonon velocity, and Grüneisen parameter of each branch. Again, we assume the optical branch to be described by the same formula as the longitudinal acoustic branch.

2.1.4. Phonon–isotope scattering

According to Klemens [105], the scattering rate of mass fluctuation due to the presence of isotopes should take the form

$$\left[\tau_I^i(x) \right]^{-1} = \frac{V k_B^4 \Gamma}{4 \pi \hbar^4 v_i^3} x^4 T^4 \tag{2.5}$$

Therefore, the isotope scattering rate also depends on the phonon velocity. The mass fluctuation phonon scattering parameter Γ for a single element composed of several naturally occurring isotopes is

$$\Gamma = \sum_i c_i \left[\frac{m_i - \bar{m}}{\bar{m}}\right]^2 \tag{2.6a}$$

where

$$\bar{m} = \sum_i c_i m_i \tag{2.6b}$$

Here, m_i is the atomic mass of the ith isotope and c_i is the fractional atomic natural abundance. For a compound including N different elements,

$$\Gamma(AB...) = N\left[\left(\frac{M_A}{M_A + M_B + ...}\right)^2 \Gamma(A) + \left(\frac{M_B}{M_A + M_B + ...}\right)^2 \Gamma(B) + ...\right] \tag{2.7}$$

where M_i ($i = A, B, ...$) denotes the average atomic mass of element i.

2.1.5. Specific heat

The specific heat is usually calculated using the Debye model, which is only suitable for the acoustic branches. For structures whose primitive cell contains more than one atom ($p > 1$), a more accurate method would be using the Debye model for the acoustic branches, and approximating the optical branches using the Einstein model. Then, the specific heat is

$$c_V^{aco} = 3\frac{N}{V}k_B f_D\left(\frac{\Theta_D}{T}\right) \tag{2.8a}$$

$$c_V^{opt} = (3p - 3)\frac{N}{V}k_B f_E\left(\frac{\Theta_E}{T}\right) \tag{2.8b}$$

$$f_D(x) = \frac{3}{x^3}\int_0^x \frac{y^4 e^y \, dy}{(e^y - 1)^2} \tag{2.8c}$$

and

$$f_E(x) = x^2 \frac{e^x}{(e^x - 1)^2} \tag{2.8d}$$

where Θ_D is the Debye temperature, Θ_E is the Einstein temperature, N is the number of primitive cells, f_D and f_E are the Debye function and Einstein function respectively. In this

way, at high temperature T >> Θ_E, f_E is approaching 1, the contribution of each optical phonon branch to specific heat is k_B/V, which is in consistent with classical Dulong-Petit law. At low temperature, T << Θ_E, f_E decreases exponentially, which means the optical phonons are hardly to be excited, thus their contribution to specific heat can be omitted. Such a way to process optical phonons is rarely used in previous methods.

2.1.6. Debye temperature, Grüneisen parameter, and phonon velocity

The lattice thermal conductivity is a function of the Debye temperature θ_i, Grüneisen parameter γ_i and phonon velocity v_i of each phonon branch. These parameters can be readily obtained from Phonopy software using supercell method or finite displacement method[106]. For the branch Debye temperature, we selected the highest frequency of each branch to calculate θ_i:

$$\theta_i = \frac{\hbar \omega_i^{\max}}{k_B} \tag{2.9}$$

The Debye temperature Θ_D in eq. (2.8a) could, in principle, be calculated from the specific heat at low temperatures or, equivalently, from the elastic constants. However, this determination is implicitly based on the assumption that acoustic frequencies depend linearly on the wave vector, and will overestimate the maximum acoustic frequency. Here we determine the Debye temperatures from the maximum θ_i of the three acoustic branches, which gives Θ_D somewhat lower than standard values of the Debye temperature.

The phonon velocity and Grüneisen parameter of each branch are calculated using a two-step averaging. The results of the Phonopy calculation of the phonon velocity and Grüneisen parameter are functions of the band index i and wave vector $\mathbf{q}$: $v(i, \mathbf{q})$ and $\gamma(i, \mathbf{q})$. The first average is taken within each high symmetry path of the same branch:

$$v(i, j) = \overline{v(i, \mathbf{q})} \tag{2.10a}$$

$$\gamma^2(i, j) = \overline{\left[\gamma(i, \mathbf{q})\right]^2} \tag{2.10b}$$

where j denotes a different high symmetry path in each branch. The second average is taken from these high symmetry paths:

$$v_i = \frac{\sum_j m_j v(i,j)}{\sum_j m_j} \tag{2.11a}$$

$$\gamma_i = \sqrt{\frac{\sum_j m_j \gamma^2(i,j)}{\sum_j m_j}} \tag{2.11b}$$

where m_j is the multiplicity of each path, a value related to the symmetry of the structure.

We did not use all the optical branches in the thermal conductivity calculations. Instead, to correspond with the Einstein model and treat the optical branches' contribution as a correction to the original Callaway model, we used a "pseudo-optical" branch, which is an average of all the optical branches. Θ_E in eqs. (2.1e) and (2.8b) is the characteristic Einstein temperature of this "pseudo-optical" branch.

2.2. Model of Electronic Transport Properties

2.2.1. Semiclassical transport theory

Electronic transport properties can be computed in the framework of the semiclassical BTE. Assuming the material is homogeneous and the relaxation time τ is independent of the direction of the crystal momentum **k**, when the external field is weak, according to the relaxation time approximation (RTA), all the transport coefficients can be expressed in terms of some averaged quantities, namely $\langle \tau^l z^q \rangle$ [73],

$$\left\langle \tau^l z^q \right\rangle = \frac{\int_0^\infty \left(-\frac{\partial f}{\partial z}\right)\left[\frac{\tau(z)}{m_d^*(z)}\right]^l z^q k^3 dz}{\int_0^\infty \left(-\frac{\partial f}{\partial z}\right)\frac{k^3}{m_{d_0}^{*l}} dz} \tag{2.12}$$

where $f = 1/\left(e^{(\varepsilon-\eta)/k_B T} + 1\right)$ is the Fermi-Dirac distribution function; $z = \varepsilon/k_B T$ is the reduced band energy, k_B is the Boltzmann constant, T is the temperature; $m_{d_0}^*$ is the density of states (DOS) effective mass at the band edge, while m_d^* is the DOS effective mass at energy z; l and q are constants. The parameters τ, k and m_d^* are all functions of z, and their detailed expressions are given later.

Therefore, the formulas for the carrier mobility μ, carrier concentration n, electrical conductivity σ, Seebeck coefficient α, Hall factor A, Hall coefficient R, Lorenz number L_0, and electronic thermal conductivity κ_e are:

$$\mu = \frac{e\langle\tau\rangle}{m_c^*} \tag{2.13}$$

$$n = \frac{\left(2m_{d_0}^* k_B T\right)^{3/2}}{3\pi^2 \hbar^3} \int_0^\infty \left(-\frac{\partial f}{\partial z}\right)\left(z + \beta z^2\right)^{3/2} dz \tag{2.14}$$

$$\sigma = ne\mu \tag{2.15}$$

$$\alpha = \frac{k_B}{e}\langle\tau(z-\zeta)\rangle/\langle\tau\rangle \tag{2.16}$$

$$A = \frac{3K(K+2)}{(2K+1)^2}\frac{\langle\tau^2\rangle}{\langle\tau\rangle^2} \tag{2.17}$$

$$R = \frac{A}{en} \tag{2.18}$$

$$L_0 = \left(\frac{k_B}{e}\right)^2 \left\{ \frac{\langle\tau z^2\rangle}{\langle\tau\rangle} - \left[\frac{\langle\tau z\rangle}{\langle\tau\rangle}\right]^2 \right\} \tag{2.19}$$

$$\kappa_e = L_0 T\sigma \tag{2.20}$$

where e is the elementary charge and $\hbar$ is the Planck constant; $\zeta = \eta/k_B T$ is the reduced chemical potential; m_c^* is the conductivity effective mass; K is the ratio of the effective mass $m_\parallel^* / m_\perp^*$, reflecting the anisotropy of the band.

2.2.2. Modified Kane band model

In the Kane band model, the constant energy surface for any energy value is assumed to be ellipsoidal. It is also assumed that the longitudinal and transverse effective masses of electrons and holes are governed by the interaction of the lowest conduction band with the highest valence band, whereas the contributions of other bands are negligibly small. This model is also called "two-band" model. The relationship between the energy and crystal momentum is expressed as [73,74]

40

$$\frac{\hbar^2 k_\perp^2}{m_{\perp 0}^*} + \frac{\hbar^2 k_\parallel^2}{2m_{\parallel 0}^*} = \varepsilon \left(1 + \frac{\varepsilon}{\varepsilon_g}\right) \qquad (2.21)$$

here ε_g is the band gap; $k_\perp$ and $k_\parallel$ are the transverse and longitudinal components of the momentum $\mathbf{k}$; $m_{\perp 0}^*$ and $m_{\parallel 0}^*$ are the transverse and longitudinal components of the effective mass tensor at the band edge. The part in parentheses indicates the nonparabolicity of the band. Then, the energy dependence of the effective mass is

$$m_i^* = m_{i0}^* \left(1 + \frac{2\varepsilon}{\varepsilon_g}\right) = m_{i0}^* \left(1 + 2\beta z\right) \qquad (2.22)$$

with $\beta = k_B T / \varepsilon_g$, i denotes $\parallel$ or $\perp$. The DOS effective mass is expressed as

$$m_d^* = N^{2/3} m_b^* = N^{2/3} \left(m_\parallel^* m_\perp^{*2}\right)^{1/3} \qquad (2.23)$$

where N is the degeneracy of the band due to the symmetry. The conductivity effective mass is

$$\frac{1}{m_c^*} = \frac{1}{3} \left(\frac{1}{m_\parallel^*} + 2\frac{1}{m_\perp^*}\right) \qquad (2.24)$$

When the effective mass is known, the value of the momentum k can be defined as

$$k(z) = \frac{\left(2k_B T m_{b_0}^*\right)^{1/2}}{\hbar} \left[z(1+\beta z)\right]^{1/2} \qquad (2.25)$$

and the density of states is

$$\rho(z) = \frac{\left(2k_B T\right)^{1/2} m_{d_0}^{*3/2}}{\pi^2 \hbar^3} \left[z(1+\beta z)\right]^{1/2} \left(1 + 2\beta z\right) \qquad (2.26)$$

Although the model is called "two-band" model, sometimes bands besides the valence band maximum (VBM) and conduction band minimum (CBM) should also be considered. For example, in p-type PbTe, there is a second band near the VBM in energy and this band becomes dominant at high temperatures. In our model, one more band can be taken into account for n- or p-type situation if it exists. Such a second band is assumed to be independent of the CBM or VBM.

2.2.3. Scattering mechanisms for the relaxation time of electrons

Three scattering mechanisms — acoustic phonon scattering, polar optical phonon scattering and ionized impurities scattering — are considered here, with corresponding relaxation times: τ_{aco}, τ_{opt}, τ_{imp}. The total relaxation time is the sum of these relaxation times according to Matthiessen's rule:

$$\frac{1}{\tau} = \frac{1}{\tau_{\text{aco}}} + \frac{1}{\tau_{\text{opt}}} + \frac{1}{\tau_{\text{imp}}}$$ (2.27)

Here we only present the final expressions for each relaxation time and discuss the parameters involved and application range of each mechanism. Detailed derivations can be found in the literature [73,74].

2.2.3.1. Acoustic phonon scattering

At high temperatures and carrier densities, scattering by acoustic phonons predominates. The strength of the acoustic phonon scattering can be represented by the deformation potential constants, and the corresponding relaxation time is almost isotropic. The main expression for this type of scattering was originally provided by Bardeen [71] and is widely used. Ravich added the effect of band nonparabolicity as well as the dependence of the matrix element of the interaction of carriers with the acoustic phonons on the energy in the nonparabolic region. The formula is given by [74]

$$\frac{1}{\tau_{\text{aco}}(z)} = \frac{\pi k_{\text{B}} T \rho \Xi^2}{\hbar c N} \left[1 - \frac{8\beta\left(z + \beta z^2\right)}{3\left(1 + 2\beta z\right)^2} \right]$$ (2.28)

where Ξ is the deformation potential constant; c is the elastic constant related with the longitudinal and transverse acoustic wave velocity. The factor in brackets describes the energy dependence of the squared matrix element of the electron-phonon interaction.

2.2.3.2. Polar optical phonon scattering

In a polar crystal, at some temperatures the polar scattering by long-wavelength longitudinal optical phonons shows approximately the same temperature dependence as the acoustic phonon scattering. The polar scattering is strongly inelastic at low temperatures. However, it can be regarded as almost elastic above the compound's Debye temperature, and the relaxation time concept can be used. As in the case of the acoustic

phonon scattering, nonparabolicity should be allowed for. Moreover, free carriers, because of their high density in real applications, screen the electric field produced by optical vibrations in polar crystals. This screening effect reduces the strength of the polar scattering and should also be included. The formula for the polar scattering is [74]

$$
\begin{aligned}
\frac{1}{\tau_{\text{opt}}(z)} = & \frac{2^{1/2} k_{\text{B}} T e^2 m_{b_0}^{*1/2} \left(\varepsilon_\infty^{-1} - \varepsilon_0^{-1} \right)}{\hbar^2 \left(z k_{\text{B}} T \right)^{1/2}} \frac{1 + 2\beta z}{\left(1 + \beta z \right)^{1/2}} \\
& \times \left\{ \left[1 - \delta \ln \left(1 + \frac{1}{\delta} \right) \right] - \frac{2\beta \left(z + \beta z^2 \right)}{\left(1 + 2\beta z \right)^2} \left[1 - 2\delta + 2\delta^2 \ln \left(1 + \frac{1}{\delta} \right) \right] \right\}
\end{aligned}
\tag{2.29}
$$

where ε_∞ and ε_0 are the high-frequency and static dielectric constant; $\delta = (2kr_\infty)^{-2}$ with the screening radius r_∞ of the medium with ε_∞,

$$
r_\infty^{-2} = \frac{4\pi e^2 \rho(z)}{\varepsilon_\infty}
\tag{2.30}
$$

In the original formula proposed in ref. [74], the density of state in the above is $\rho(\zeta)$, which is a Fermi integral of $\rho(z)$. However, we found that using $\rho(\zeta)$ would make the calculation of $<\tau>$ in eq. 2.12 extremely slow due to the appearance of double integrals. By changing to $\rho(z)$, the results just have small difference, while the computing speed is improved several order of magnitude.

2.2.3.3. Ionized impurities scattering

Scattering by ionized impurities and vacancies is the dominant mechanism at very low (liquid helium) temperatures in highly degenerate samples, which is described by the formula [73]

$$
\frac{1}{\tau_{\text{imp}}(\zeta)} = \frac{2e^4 N m_{b_0}^* \left(1 + 2\beta\zeta \right) \Phi(\delta_0)}{3\pi \varepsilon_0^2 \hbar^3}
\tag{2.31}
$$

where $\Phi(\delta_0)$ is the logarithmic factor:

$$
\Phi(\delta_0) = \ln \left(1 + \delta_0^{-1} \right) - \left(1 + \delta_0 \right)^{-1}
\tag{2.32}
$$

with $\delta_0 = (2k_F r_0)^{-2}$ and r_0 is the screening radius of a medium with the dielectric constant ε_0. In highly degenerate samples,

$$
r_0^{-2} = \frac{4\pi e^2 \rho(\zeta)}{\varepsilon_0}
\tag{2.33}
$$

where $\rho(\zeta)$ is the density of states at the reduced chemical potential ζ. k_F is expressed in terms of the carrier concentration for one valley:

$$k_{\mathrm{F}} = \left(\frac{3\pi^2 n}{N} \right)^{1/3} \tag{2.34}$$

In the simplest case, the concentration of carriers is equal to the concentration of impurities. Note that τ_{imp} is a function of the chemical potential directly, which is different from τ_{aco} and τ_{opt}. In the implementation of this code, to get the total relaxation time, τ_{aco} and τ_{opt} are first added and applied in eq. (2.12) to transform to a function of the chemical potential, the results are then added to τ_{imp}.

2.2.3.4. Deformation potential constant

The deformation potential constant is a key parameter for the relaxation time of the acoustic phonon scattering. It can be calculated as:

$$\Xi_i = \frac{\Delta E_{i,V}}{\Delta l_V} \tag{2.35}$$

where $\Delta E_{i,V}$ is the energy difference of the band edge i at different volume V; Δl_V is the dimensionless volumetric strain. When this strain is small, it can be assumed that the same band edge belonging to different volumes has the same reference energy; thus, these energies can be compared directly. For a given material, three calculations of the band energies are required: one at the equilibrium volume, the other two could be done at slightly smaller and larger volumes. Then, using our code, the calculations of the deformation potential constant of each band edge can be done automatically.

2.2.3.5. Elastic constant

The elastic constant c is also an important parameter for the relaxation time of the acoustic phonon scattering. Only the longitudinal acoustic wave was considered in Bardeen's work, and this leads to a commonly underestimation of the scattering rate, thus, overestimation of mobility according to our test. Here we take into account contributions from both longitudinal and transverse acoustic waves. Using the Voigt−Reuss−Hill approximation [107−109], the bulk modulus B and shear modulus G can be calculated:

$$9B_V = \left(C_{11} + C_{22} + C_{33} \right) + 2 \left(C_{12} + C_{23} + C_{31} \right) \tag{2.36}$$

$$15G_V = \left(C_{11} + C_{22} + C_{33}\right) - \left(C_{12} + C_{23} + C_{31}\right) + 3\left(C_{44} + C_{55} + C_{66}\right) \tag{2.37}$$

$$\frac{1}{B_R} = \left(S_{11} + S_{22} + S_{33}\right) + 2\left(S_{12} + S_{23} + S_{31}\right) \tag{2.38}$$

$$\frac{15}{G_R} = 4\left(S_{11} + S_{22} + S_{33}\right) - 4\left(S_{12} + S_{23} + S_{31}\right) + 3\left(S_{44} + S_{55} + S_{66}\right) \tag{2.39}$$

$$B_H = \frac{\left(B_R + B_V\right)}{2} \tag{2.40}$$

$$G_H = \frac{\left(G_R + G_V\right)}{2} \tag{2.41}$$

where C and S are the elastic constant matrix and its inverse matrix. Then the acoustic phonon velocity can be obtained:

$$v_L = \left(\frac{B_H + 4/3G_H}{\rho}\right)^{1/2} \tag{2.42}$$

$$v_T = \left(\frac{G_H}{\rho}\right)^{1/2} \tag{2.43}$$

$$\frac{1}{v_m} = \frac{1}{3}\left(\frac{1}{v_L} + \frac{2}{v_T}\right) \tag{2.44}$$

where ρ is the mass density of the compound and v_m is the average phonon velocity. The direction-averaged elastic constant c is calculated as

$$c = \rho v_m^2 \tag{2.45}$$

2.2.3.6. Effective mass of the band edge

Under an external electric field, the effective mass of a charge carrier is defined as:

$$\left(\frac{1}{m^*}\right)_{ij} = \frac{1}{\hbar^2}\frac{\partial^2 E_n(\mathbf{k})}{\partial k_i k_j}, \quad i, j = x, y, z \tag{2.46}$$

where the indices i and j denote reciprocal components, and $E_n(\mathbf{k})$ is the dispersion relation of the n-th band. The derivatives can be evaluated numerically, using the finite difference method. The explicit form of the right-hand-side symmetry tensor in eq. (2.46) is:

$$\frac{d^2E(\mathbf{k})}{dk^2} = \begin{pmatrix} \dfrac{d^2E}{dk_x^2} & \dfrac{d^2E}{dk_x dk_y} & \dfrac{d^2E}{dk_x dk_z} \\[2ex] \dfrac{d^2E}{dk_x dk_y} & \dfrac{d^2E}{dk_x^2} & \dfrac{d^2E}{dk_y dk_z} \\[2ex] \dfrac{d^2E}{dk_x dk_z} & \dfrac{d^2E}{dk_y dk_z} & \dfrac{d^2E}{dk_x^2} \end{pmatrix} \tag{2.47}$$

where second and mixed derivatives are evaluated on five-point stencil, with error of the order of $O(h^4)$.

The above methods have been implemented in the Effective Mass Calculator (EMC) [110]. In our program, we modified the original EMC code to obtain the effective masses internally during the calculation of the transport coefficients.

2.3. Implementation

2.3.1. Workflow and technical issues

The above models of the lattice thermal conductivity and electrical transport properties have been implemented in AICON program [111,112], which is written in Python3 programming language. The program is open source under the GNU general public license version 3 (GPLv3). The current version is developed and maintained using Git and is accessible at https://github.com/Baijianlu/AICON2.git. The code can be run on computing clusters or a personal laptop. The program can be called from a command-line interface or from a script.

Fig. 2.1 shows the workflow of calculating the lattice thermal conductivity. The main inputs for AICON are POSCAR, band.yaml and gruneisen.yaml files generated using Phonopy combined with DFT software, from which AICON can extract the phonon dispersion curves, phonon velocities and mode Grüneisen parameters. Noting that the phonon curves and Grüneisen parameters should be calculated on high symmetry paths as AICON suggests. Additional settings, such as the temperature, can be specified as command-line arguments.

Fig. 2.2 shows the workflow of calculating the electrical transport properties. The band structure calculation at three different volumes is for determining the deformation potential

constants. The effective mass calculation is for determining effective masses at CBM and VBM (and the second band if it exists). The dielectric constant calculation is for determining the high-frequency and static dielectric constants. The elastic constant calculation is for determining elastic constant tensor. After these calculations are finished, the resulting files (such as vasprun.xml) should be collected in a directory and the naming rule should be exactly the same as the examples distributed with the program. Then, AICON can be called to calculate the transport properties either from a command-line or python script. Additional settings, such as the temperature and carrier concentration, can be specified at the same time.

The program stores results as pandas.DataFrame object, which is flexible and easy to manipulate, analyze, and plot the data. It can also be saved in any file format supported by pandas [113].

When calculating the transport properties using AICON, the most time is spent on those DFT calculations for obtaining key parameters. For example, at least 13 DFT calculations need to be done before calling AICON to calculate the electrical transport properties. Although each of these calculations is relatively simple, managing the workflow becomes an intensive task, which involves checking the results of each step and copying the necessary files from the last step. To alleviate this problem for high-throughput calculations, in AICON we also implemented automatic workflow tools based on pymatgen [114], Atomate [115] and FireWorks [116]. The users only need to provide structural files and some necessary settings for each DFT calculation, then the whole workflow can run automatically. Besides, it is convenient to build users' own databases this way.

Installation and usage of AICON are documented in the user manual and examples distributed along with the source code package.
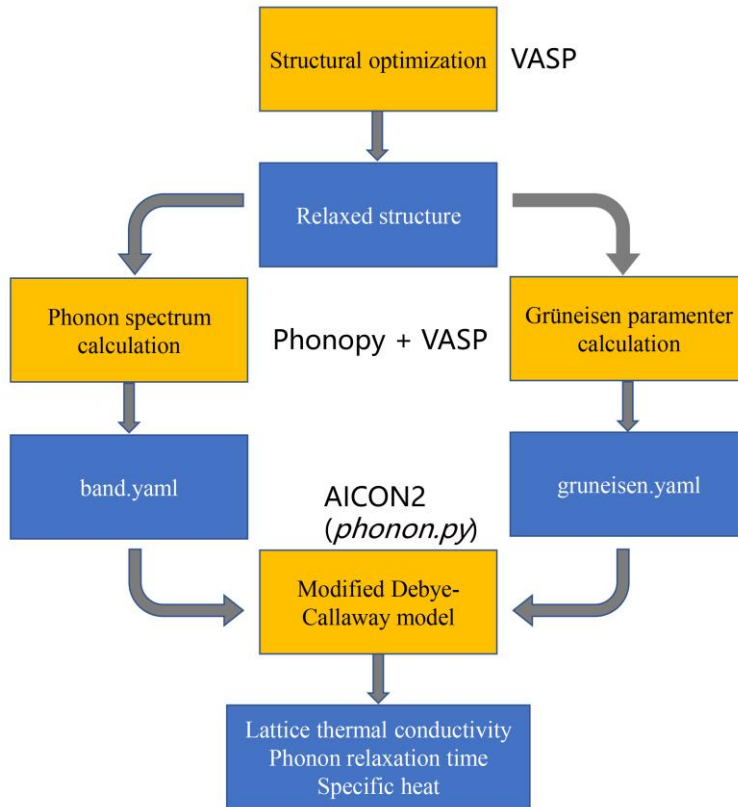
Figure 2.1. Workflow of the lattice thermal conductivity calculations using AICON. Gold boxes represent steps of the calculation, blue boxes for the results of these steps, and computer programs are denoted as black text outside of the box.
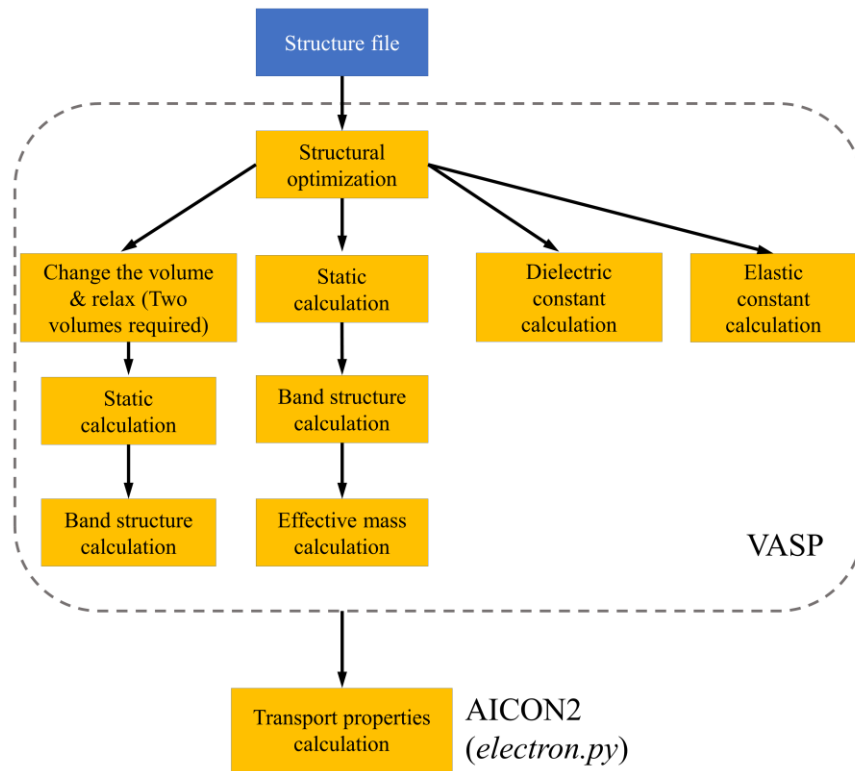
Figure 2.2. Workflow of the electrical transport properties calculation using AICON. Gold boxes represent steps of the calculation, and computer programs are denoted as black text outside of the box.

2.3.2. Testing of the model of lattice thermal conductivity

The model was tested on a data set containing 28 well-studied compounds. The list of materials includes semiconductors and insulators that belong to different structural prototypes, such as diamond, rocksalt, and fluorite. Meanwhile, to maximize the heterogeneity of the data set, materials are selected containing as many different elements as possible. The comparison of the calculated and experimental values of κ_L is summarized in Table 2.1 and Fig. 2.3. Two statistical quantities are used to measure qualitative and quantitative agreement between the calculated and experimental results (Table 2.2). The Pearson correlation coefficient r, which is a measure of the linear correlation between two variables, X and Y, is

$$r = \frac{\sum_i (X_i - \bar{X})(Y_i - \bar{Y})}{\sqrt{\sum_i (X_i - \bar{X})^2} \sqrt{\sum_i (Y_i - \bar{Y})^2}} \qquad (2.46)$$

The root-mean-square relative deviation (RMSrD), which is a measure of the quantitative difference between two variables, is

$$\text{RMSrD} = \sqrt{\frac{\sum_i \left(\frac{X_i - Y_i}{X_i}\right)^2}{N_{\{X,Y\}} - 1}} \qquad (2.47)$$

Lower values of RMSrD indicate better agreement.

As shown in Table 2.2, the calculated results strongly correlate with experimental values (Pearson coefficient is 0.9999). However, the RMSrD value is rather large. In order to reduce the RMSrD value, we introduced a scale factor w, which can be obtained by doing the least squares fitting between the experimental and the calculated values (Fig. 2.3). The factor value we calculated is 0.6037. Therefore, the corrected lattice thermal conductivity can be calculated as,

$$\kappa = w * \left(\kappa_{LA} + \kappa_{TA} + \kappa_{TA'} + \kappa_O\right) \qquad (2.48)$$

The calculated values of the lattice thermal conductivity taking into account the scale factor are listed in Table 2.1 as $\kappa_{\text{cal cor}}$. The Pearson correlation coefficient and RMSrD were again calculated and shown in Table 2.2. The r value doesn't change, whereas the RMSrD value is reduced to 50.13%, much lower than that without scaling. The testing results suggest that it would be better to use this scaling factor if a compound has high lattice thermal conductivity, while not use it if its lattice thermal conductivity is already quite low ($\kappa_{\text{cal}} < 2$ W·m^{-1}·K^{-1} at 300 K). In this way, the RMSrD could be reduced further to ~ 30%. Note that this scaling factor is just used to match the calculated results with experimental values as close as possible. The factor itself is flexible and the users can train their own values according to the materials they study.

Fig. 2.4 – 2.6 show the calculated lattice thermal conductivity compared with the experimental values and other ab initio results for three typical compounds in a wide temperature range: (1) diamond, an insulator with very high thermal conductivity; (2)

silicon, the most studied semiconductor with medium values of thermal conductivity; (3) SnSe, an anisotropic crystal with extremely low thermal conductivity. These cases further validate the robustness and accuracy of our method.

Table 2.1. Calculated and experimental lattice thermal conductivity [88,117,118] of the test compounds at 300 K ($W \cdot m^{-1} \cdot K^{-1}$). κ_{exp} is the experimental value, κ_{cal} is the calculated value without multiplying scale factor, κ_{cal_cor} is the calculated value with scaling

Formula	κ_{exp}	κ_{cal}	κ_{cal_cor}	Formula	κ_{exp}	κ_{cal}	κ_{cal_cor}
C(Dia)	2200	3851.90	2325.41	NaI	1.8	1.92	1.16
Si	141	225.00	135.83	PbS	2.9	2.69	1.62
AgCl	1	0.57	0.34	RbBr	3.8	1.55	0.94
BaO	2.3	7.07	4.27	RbI	2.3	0.99	0.60
CaO	27	49.34	29.79	SrO	12	24.82	14.98
KBr	3.4	2.41	1.46	CdF_2	4.3	3.72	2.25
KCl	7.1	4	2.42	$SrCl_2$	2.3	2.84	1.72
KI	2.6	1.29	0.78	Mg_2Si	12.14	22.31	13.47
LiF	17.6	27.29	16.48	Mg_2Ge	15.7	33.91	20.47
LiH	15	55.12	33.28	Mg_2Sn	11.1	16.01	9.67
MgO	60	108.36	65.42	CaF_2	9.76	11.94	7.21
NaBr	2.8	3.35	2.02	CeO_2	10.8	13.22	7.98
NaCl	7.1	6.69	4.04	ZnO	37.5	31.08	18.76
NaF	16.5	21.48	12.97	SnSe	0.7	0.31	0.19

Table 2.2. Root mean square relative deviation (RMSrD) and Pearson correlations coefficient r for the calculated results

	κ_{cal}	κ_{cal_cor}
r	0.9999	0.9999
RMSrD	85.77%	50.13%
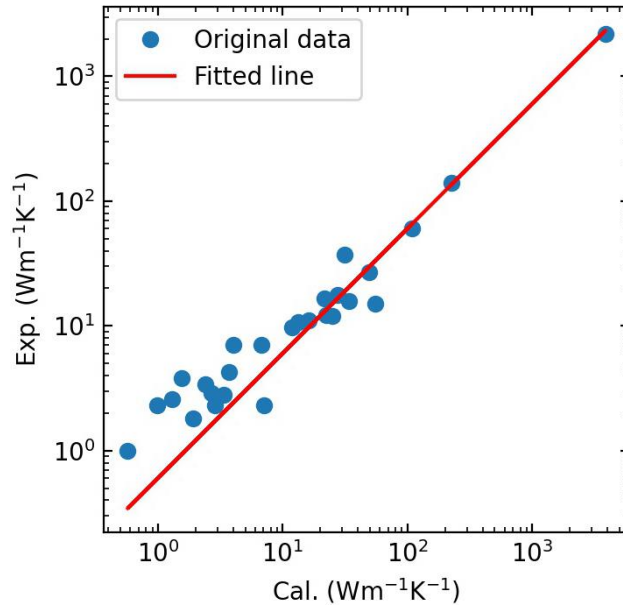
Figure 2.3. Calculated lattice thermal conductivity versus the experimental values for test materials at 300 K. A red line shows the fitting values obtained by multiplying the calculated values by the scale factor *w*.
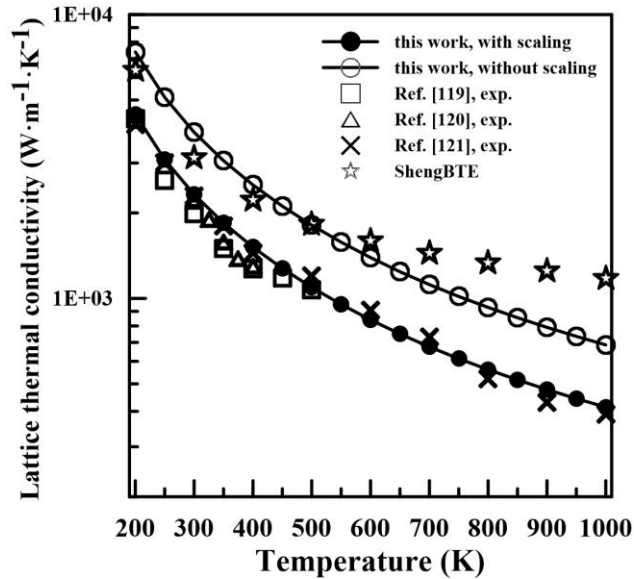
Figure 2.4. Lattice thermal conductivity of diamond calculated using our method compared with the experimental and full ab initio calculation results.
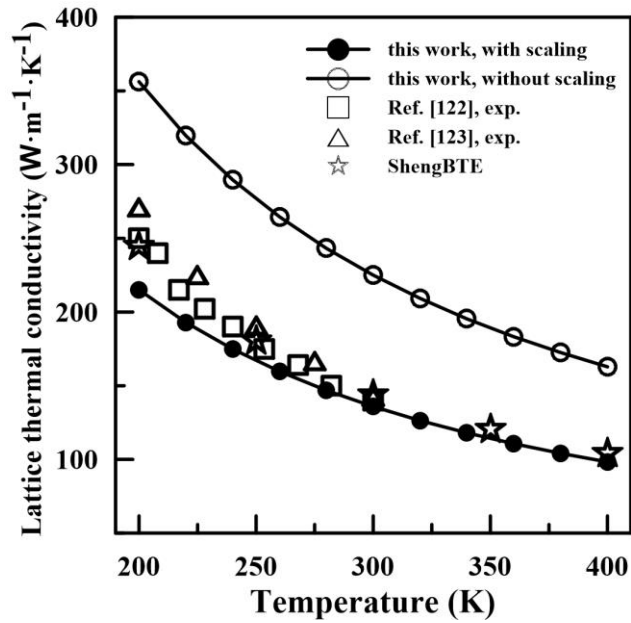
Figure 2.5. Lattice thermal conductivity of Si calculated using our method compared with the experimental and full ab initio calculation results.
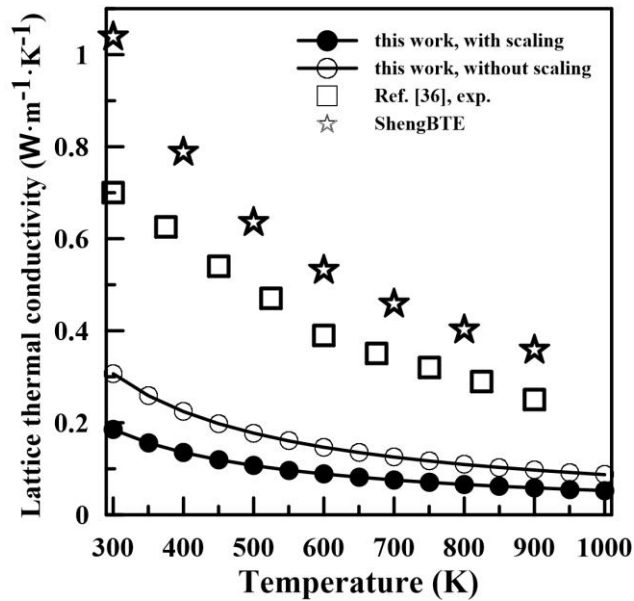
Figure 2.6. Lattice thermal conductivity of SnSe calculated using our method compared with the experimental and full ab initio calculation results.

2.3.3. Testing of the model of electrical transport properties

In order to further test the accuracy of our model, we calculated the carrier mobility and Seebeck coefficient for 17 common semiconductors and compared the results with the experimental values. The test set included both isotropic and anisotropic materials having a wide range of chemistries and doping polarities to make it representative. A summary of key parameters that we used for calculating the carrier transport properties are listed in Table 2.3. The range of temperatures and carrier concentrations at which the carrier mobility and Seebeck coefficient were calculated are listed in Table 2.4 and 2.5.

Fig. 2.7 shows the calculated mobilities compared with experimental values for the test set. The calculated values agree reasonably with experiment across all materials, covering several orders of magnitude from 3 cm^2/Vs for p-type $CuAlO_2$ at 300 K to 1×10^4 cm^2/Vs for n-type GaAs at 300 K. Most examples show a slightly larger difference at lower temperature, while the difference becomes smaller at higher temperature. The difference between calculation and experiment has several origins. From the aspect of the model, for example, for electron-acoustic phonon scattering, the deformation potential theory is a rough approximation because of its basic assumptions, such as isotropic crystal, elastic scattering. Also, we only consider three scattering processes. Other processes, such as scattering from grain boundary, could be important while not being included in our model. From the aspect of the experimental results, for example, the measured Hall concentration could be different from real carrier concentration. In addition, the carrier concentration could change with temperature, whereas we use a fixed value from the experimental measurement in calculation. Noting such an arrangement is reasonable, since for extrinsic semiconductor above certain temperature, the carrier concentration is decided by the concentration of donor or acceptor (suppose fully ionized), before the intrinsic excitation becomes dominant.

Fig. 2.8 shows the calculated Seebeck coefficients against those obtained experimentally. Again, reasonable agreement with experiment is achieved for these samples. The reasons for deviation between calculation and experiment are the same as the above.

54

Table 2.3. Key parameters of the test materials at the CBM and VBM: conductivity effective mass m_c^*, DOS effective mass m_d^*, deformation potential constant Ξ, band degeneracy N, band gap E_g, direction-averaged elastic constant c, high-frequency and static dielectric constants ε_∞ and ε_0

		m_c^* (m_e)	m_d^* (m_e)	Ξ (eV)	N	E_g (eV)	c (GPa)	ε_∞	ε_0
CuAlO$_2$	CBM	0.674	0.765	14.77	1	1.81	112.50	5.6	9.6
	VBM	5.016	17.540	11.22	6	1.81	112.50	5.6	9.6
CdS	CBM	0.122	0.122	10.28	1	1.10	25.11	6.1	10.0
	VBM	1.700	1.701	7.95	1	1.10	25.11	6.1	10.0
CdSe	CBM	0.056	0.056	9.47	1	0.53	21.38	8.4	12.2
	VBM	1.548	1.549	7.24	1	0.53	21.38	8.4	12.2
CdTe	CBM	0.052	0.052	11.24	1	0.58	19.23	9.7	13.2
	VBM	0.574	0.574	8.31	1	0.58	19.23	9.7	13.2
GaAs	CBM	0.013	0.013	16.06	1	0.14	54.23	14.8	17.3
	VBM	0.366	0.366	8.83	1	0.14	54.23	14.8	17.3
GaN	CBM	0.154	0.154	17.17	1	1.72	140.67	6.0	10.8
	VBM	2.126	2.127	10.45	1	1.72	140.67	6.0	10.8
GaP	CBM	0.100	0.100	17.98	1	1.58	68.09	10.6	12.8
	VBM	0.395	0.395	9.81	1	1.58	68.09	10.6	12.8
InP	CBM	0.037	0.037	15.73	1	0.44	44.11	13.5	16.2
	VBM	0.464	0.464	10.25	1	0.44	44.11	13.5	16.2
PbS	CBM	0.068	0.171	10.34	4	0.15	41.78	15.7	347.3
	VBM	0.069	0.175	13.52	4	0.15	41.78	15.7	347.3
PbTe	CBM	0.032	0.089	10.28	4	0.13	32.43	26.3	446.0
	VBM	0.037	0.101	12.10	4	0.13	32.43	26.3	446.0
	VSB	0.150	1.721	11.33	12	0.24	32.43	26.3	446.0
SiC	CBM	0.293	0.681	10.18	3	1.37	236.43	7.0	10.3
	VBM	0.593	0.593	11.08	1	1.37	236.43	7.0	10.3
SnO$_2$	CBM	0.163	0.163	20.57	1	0.63	117	4.8	12.2
	VBM	1.466	1.487	11.31	1	0.63	117	4.8	12.2
SnSe	CBM	0.173	0.352	8.70	2	0.54	23.96	18.8	38.9
	VBM	0.278	0.521	11.90	2	0.54	23.96	18.8	38.9
ZnO	CBM	0.132	0.132	10.07	1	0.72	59.90	5.3	10.6
	VBM	2.757	2.761	8.58	1	0.72	59.90	5.3	10.6
ZnS	CBM	0.166	0.166	13.31	1	2.01	46.32	5.9	9.3
	VBM	0.720	0.720	9.01	1	2.01	46.32	5.9	9.3
ZnSe	CBM	0.089	0.089	12.04	1	1.14	37.86	7.4	10.7
	VBM	0.634	0.634	8.15	1	1.14	37.86	7.4	10.7
Bi$_2$Te$_3$	CBM	0.393	0.634	13.01	2	0.165	27.28	37.0	91.6
	VBM	0.072	0.378	13.14	6	0.165	27.28	37.0	91.6

CSB	0.056	0.695	10.29	6	0.182	27.28	37.0	91.6
VSB	0.057	0.512	12.26	6	0.168	27.28	37.0	91.6

Table 2.4. Temperature and doping conditions used for calculating the carrier mobility

Materials	Doping	T (K)	n (cm^{-3})	Exp. Ref.
CuAlO$_2$	p-type	300–430	1.3×10^{17}	[124]
CdS	n-type	100–400	5.0×10^{15}	[125]
CdSe	n-type	200–1200	1.0×10^{17}	[126,127]
CdTe	n-type	200–1200	1.0×10^{15}	[128,129]
GaAs	n-type	300–1000	3.0×10^{13}	[130]
GaAs	p-type	300–600	6.4×10^{19}	[131]
GaN	n-type	150–500	3.0×10^{16}	[132]
GaP	n-type	100–500	3.0×10^{16}	[133]
InP	n-type	100–700	1.5×10^{16}	[134]
PbS	n-type	300–900	3.6×10^{17}	[135]
PbTe	n-type	300–600	1.8×10^{19}	[77]
PbTe	p-type	300–800	1.4×10^{20}	[136]
SiC	n-type	100–900	4.0×10^{15}	[137]
SnO$_2$	n-type	300–700	1.0×10^{17}	[138]
SnSe	p-type	300–900	3.3×10^{17}	[36]
ZnO	n-type	300–000	8.2×10^{16}	[139]
ZnS	n-type	300–650	1.0×10^{16}	[140]
ZnSe	n-type	200–1300	1.0×10^{15}	[141]
Bi$_2$Te$_3$	n-type	300–500	3.3×10^{19}	[142]
Bi$_2$Te$_3$	p-type	200–500	1.1×10^{19}	[143]

Table 2.5. Temperature and doping conditions used for calculating the Seebeck coefficient

Materials	Doping	T (K)	n (cm^{-3})	Exp. Ref.
CdS	n-type	100–300	2.8×10^{15}	[144]
GaAs	n-type	400–750	3.5×10^{17}	[145]
GaAs	p-type	300–700	6.4×10^{19}	[131]
GaN	n-type	100–300	1.3×10^{19}	[146]
InP	n-type	150–700	2.1×10^{17}	[147]
PbS	n-type	300–800	2.5×10^{19}	[148]
PbTe	n-type	300–800	1.8×10^{19}	[77]
PbTe	p-type	300–800	1.4×10^{20}	[136]
SnO$_2$	n-type	300–800	8.2×10^{18}	[149]
SnSe	p-type	300–900	3.3×10^{17}	[36]
ZnO	n-type	200–1000	5.2×10^{17}	[150]
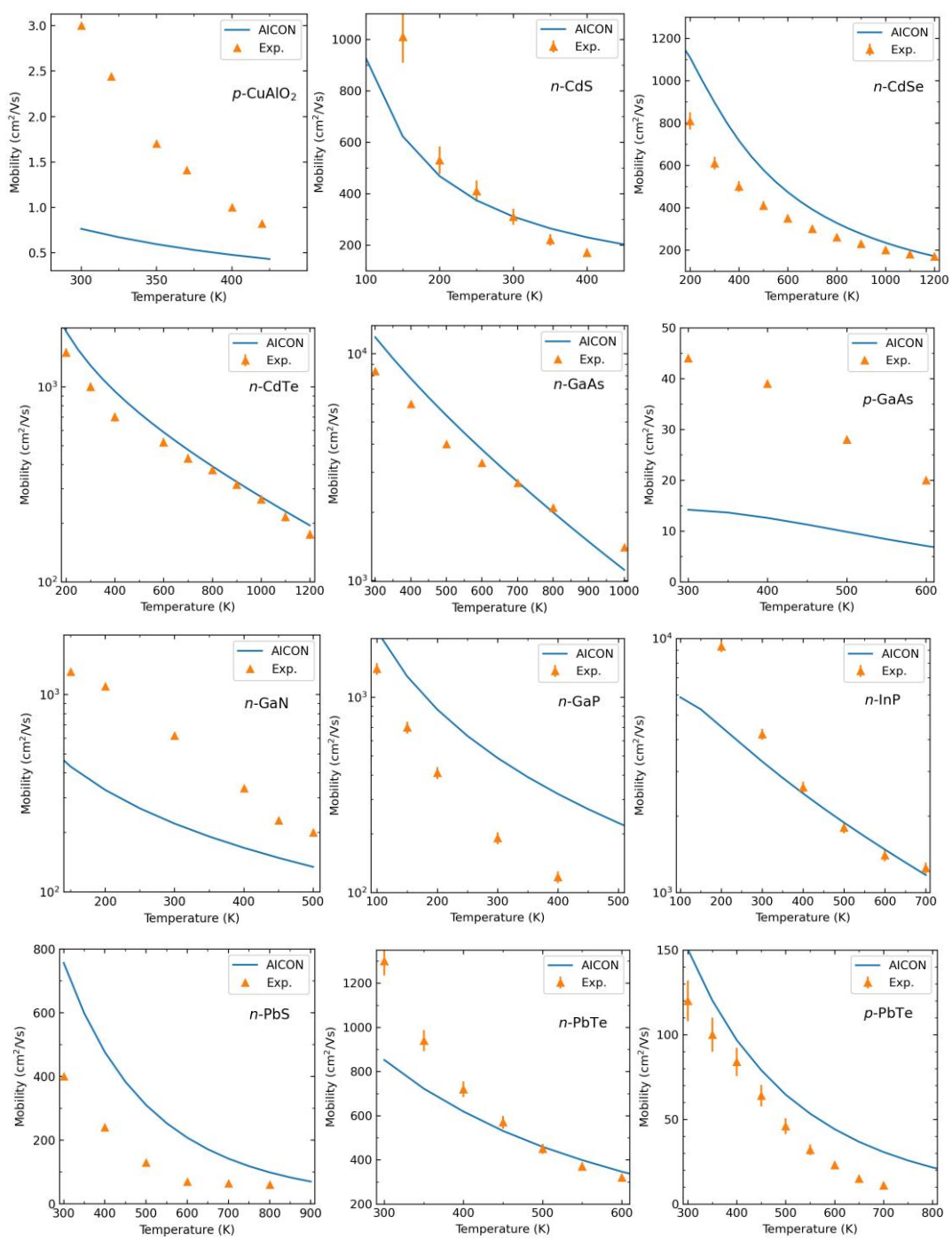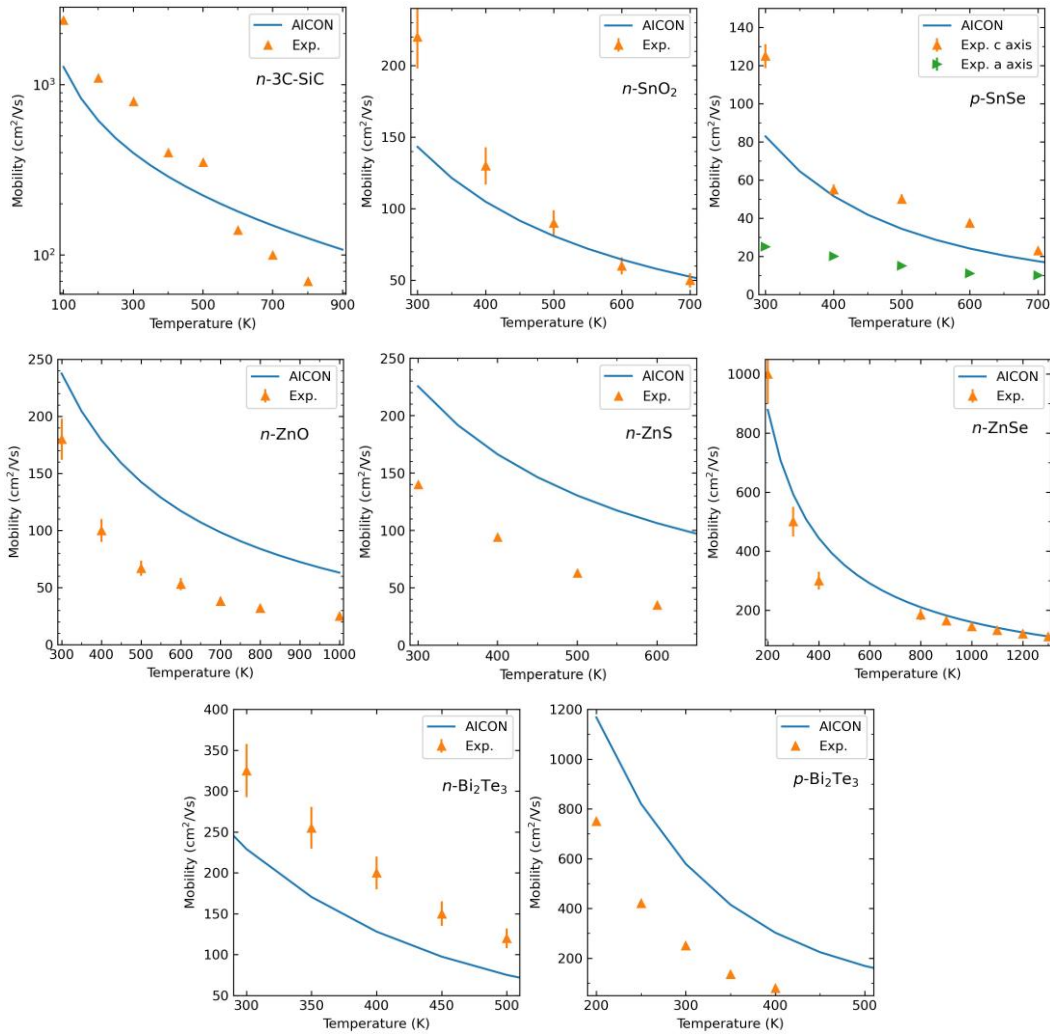
Figure 2.7. Calculated and experimental carrier mobility values for the test materials at temperatures and carrier concentrations specified in Table 2.4.
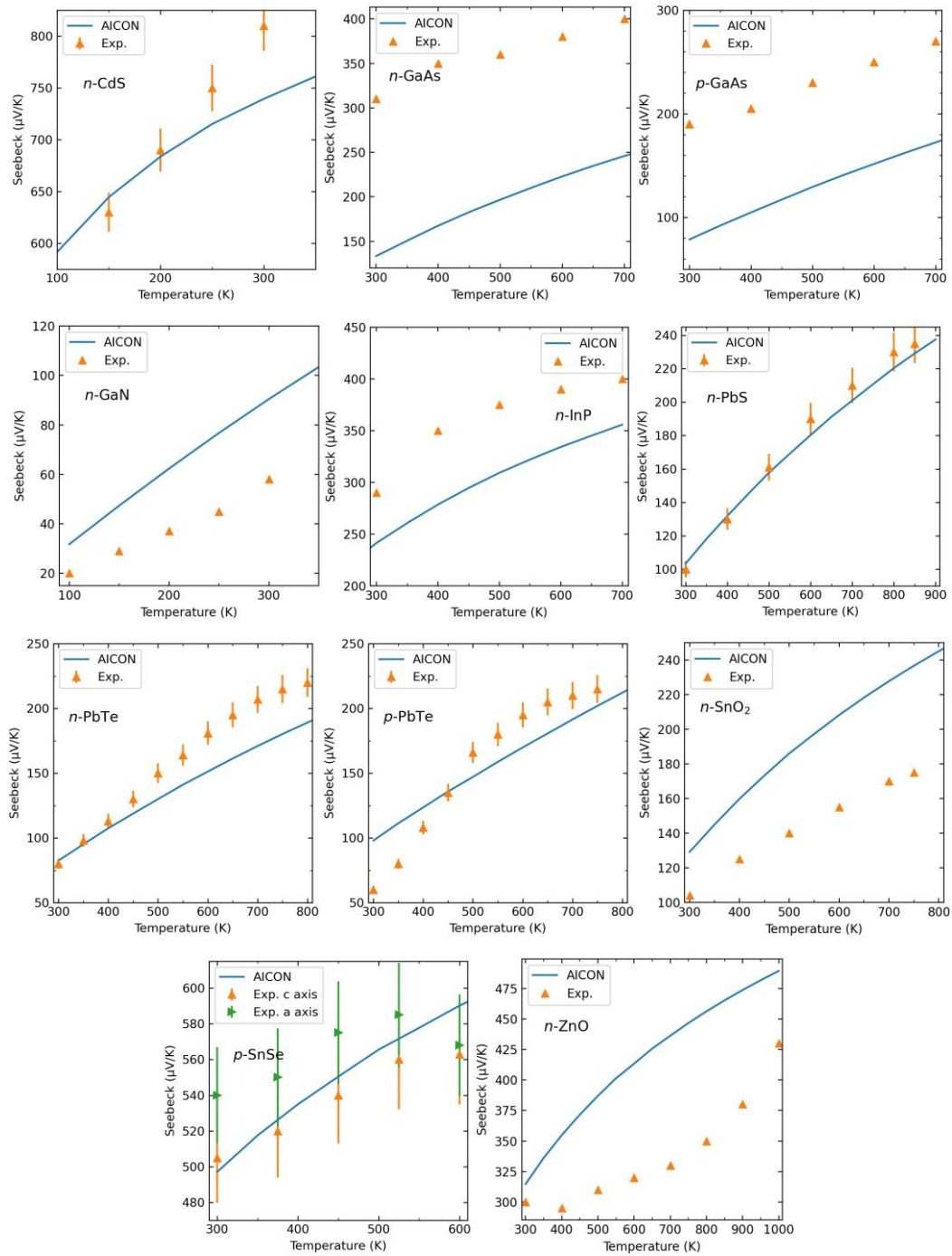
Figure 2.8. Calculated and experimental Seebeck coefficient values for the test materials at temperatures and carrier concentrations specified in Table 2.5.

2.3.4. Testing of the figure of merit

The above shows the tests for model of lattice thermal conductivity and model of electronic transport properties, respectively. However, the thermoelectric figure of merit is the combination of these quantities; thus, how accurate of the program for this combinatorial property? we calculated the figure of merit for 3 well-known thermoelectric materials and compared the results with the experimental values. The Table 2.6 lists the compounds and their experimental conditions.

Fig. 2.9 shows the calculated figure of merit compared with experimental values for the testing set. The situation could be quite different for different compounds. For example, for PbTe, the calculated ZT matches with the experimental values quite well for both n-type and p-type transport. For SnSe, the calculation agrees with the experiment well below 700 K. Above 700 K, the difference becomes larger. That's because, first, SnSe goes through a phase transition from α-phase (s.g. *Pnma*) to β phase (s.g. *Cmcm*) at around 700 K; second, the concentration of holes increases due to the thermal excitation instead of the constant value (3.3e17 cm^{-3}) used in the calculation. However, if using a higher hole concentration (5e18 cm^{-3}, from the experimental measurement) for α-phase SnSe, the calculated ZT is close to the average experimental values measured along different directions in the high temperature range. Thus, the calculation is still reasonable. For Bi$_2$Te$_3$, ZT is overestimated greatly by the calculation. It is mainly because our calculated lattice thermal conductivity is much lower than that from the experiment (for example, Cal. 0.36 W·m^{-1}·K^{-1} versus Exp. 1.7 W·m^{-1}·K^{-1}, at 300 K). Moreover, Bi$_2$Te$_3$ is a typical narrow-gap semiconductor, in which both electrons and holes are excited at an elevated temperature. It has been shown in experiment that the concentrations of both electrons and holes increase greatly above 300 K [143]. This bipolar effect diminishes the Seebeck coefficient and increases the electronic thermal conductivity. In our method, this bipolar effect is not included, and the trends at higher temperatures cannot be correctly reflected. Therefore, this case reminds us, for a compound with narrow bandgap and very low lattice thermal conductivity (< 1 W·m^{-1}·K^{-1} at 300 K), its figure of merit values are most probably being overestimated by our methods.

Table 2.6. Temperature and doping conditions used for calculating the figure of merit

Materials	Doping	T (K)	n (cm^{-3})	Exp. Ref.
PbTe	n-type	300–800	1.8×10^{19}	[77]
PbTe	p-type	300–800	1.4×10^{20}	[136]
SnSe	p-type	300–900	3.3×10^{17} 5.0×10^{18}	[36]
Bi$_2$Te$_3$	n-type	300–500	3.3×10^{19}	[142]
Bi$_2$Te$_3$	p-type	200–500	1.1×10^{19}	[143]
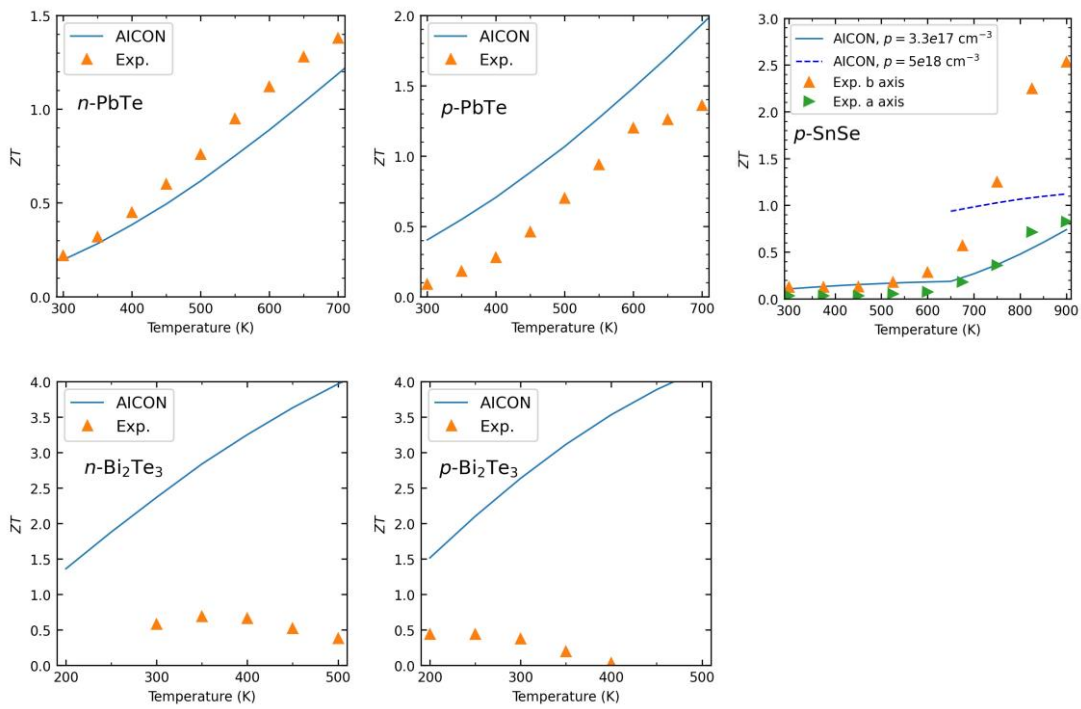
Figure 2.9. Calculated and experimental figure of merit for the test materials at temperatures and carrier concentrations specified in Table 2.6.

Chapter 3. Screening For Thermoelectric Materials

In this chapter, we applied the methods introduced in the Chapter 2 to search for promising thermoelectric materials among the structures taken from a database. An overview of the calculation results and a list of all promising compounds are presented here.

3.1. Structures and First-Principles Settings

All structures were taken from the Materials Project database [151] on the basis of five search criteria: (1) S, Se and Te as anions; (2) the band gap should be larger than 0 eV but smaller than 1.2 eV, because good thermoelectric materials are usually narrow gap semiconductors; (3) the energy above the convex hull line should be less than 0.1 eV per atom to ensure the structure is thermodynamically stable or at least potentially synthesizable in experimental conditions; (4) belonging to cubic, tetragonal and orthorhombic crystal system; (5) nonferromagnetic phase, because the band structures of ferromagnetic phases need a special consideration within the DFT and are thus unsuitable for an automatic approach like the one used here. These criteria resulted in over 1000 entries out of the database. Currently, 463 structures (127 cubic, 336 tetragonal and orthorhombic) have been sent to run the transport properties calculation. In the future, more compounds, belonging to hexagonal or other low symmetrical crystal system, will also be calculated.

All first-principles calculations were performed using the Vienna Ab initio Simulation Package (VASP) with the Perdew–Burke–Ernzerhof generalized gradient approximation (PBE–GGA) and the projector augmented wave (PAW) pseudo-potentials [152–154]. For structure relaxation, the plane wave kinetic energy cut-off was set to 600 eV and the Brillouin zone was sampled using Γ-centered meshes with the reciprocal-space resolution of $2\pi \times 0.03$ Å^{-1}. Kohn–Sham equations were solved self-consistently with the total energy tolerance of 10^{-7} eV/cell and structures were relaxed until the maximum force became smaller than 10^{-3} eV/Å. The dielectric constants were calculated using the DFPT [155], and the elastic constants were calculated using the finite difference method as implemented in VASP. To obtain the deformation potential constants of a compound, three band

structure calculations were run: one at the equilibrium volume, the other two at volumes larger by 0.1% and 0.2%. For compounds containing heavy atoms (Z > 80), the spin-orbit coupling (SOC) effect was included in all band-related calculations.

The phonon related properties, including the phonon frequency, phonon velocity, and the Grüneisen parameter, were calculated using Phonopy package [156] combined with VASP. The forces were calculated for a minimal set of supercells with the atomic displacements generated by Phonopy, and then collected to obtain the second-order interatomic force constants (IFCs). In order to calculate the Grüneisen parameter, three phonon calculations have to be run: one at the equilibrium volume, the other two at slightly smaller (-0.4%) and larger (+0.4%) volumes.

3.2. Overview of the Results

For some structures, the calculations could fail because of various reasons. For example, since GGA is known to underestimate the band gap, the calculated band gaps of some structures with very small gap values could be zero. In addition, the eigenvalues of the elastic constant matrix of some compounds have negative values. Such structures were just discarded. Finally, the complete calculations of the electronic transport properties were finished for 361 compounds (94 cubic, 267 tetragonal and orthorhombic).

Fig. 3.1 shows the maximum power factor with respect to the carrier concentration reaching this maximum value for the 361 compounds in the temperature range from 300 K to 1000 K. A compound is thought as promising if its maximum power factor is larger than 10 $\mu W \cdot cm^{-1} \cdot K^{-2}$ (above the red line) and it will go forward for the lattice thermal conductivity and figure of merit calculations. In total, we found 94 possible candidates for either n-type or p-type thermoelectric materials. Among them, PbTe, PbS, PbSe, GeTe, SnTe and SnSe are already well-known thermoelectric materials; our calculations show high power factor values for these compounds, which validates our methods.
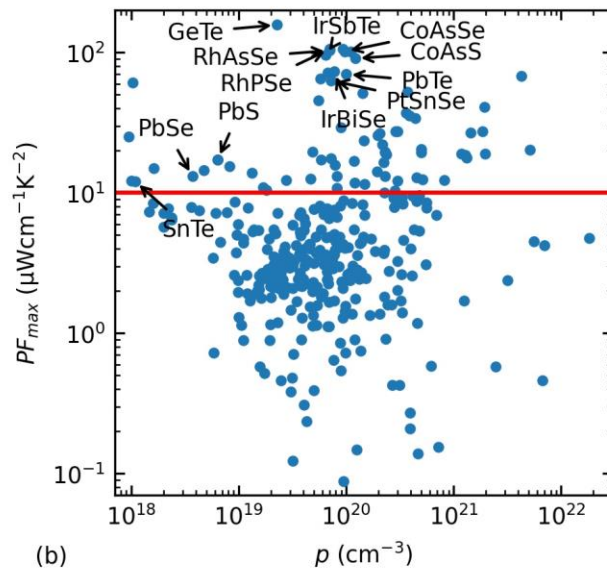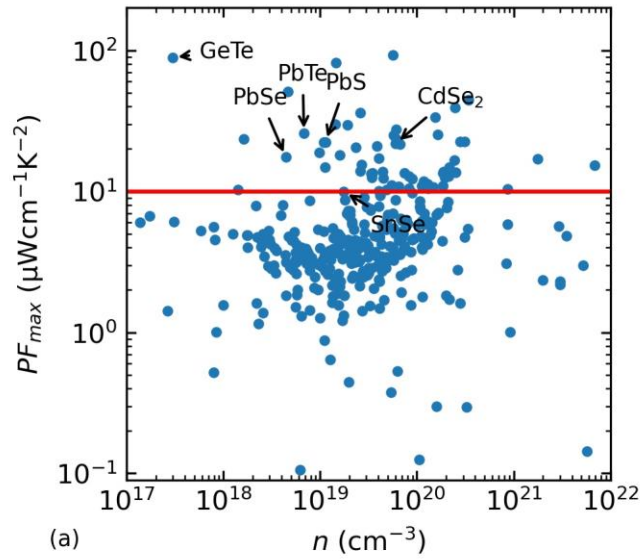
Figure 3.1. Maximum power factor as a function of the corresponding carrier concentration for the studied compounds in the temperature range from 300 K to 1000 K for (a) n-type and (b) p-type transport. Some compounds with high power factor are marked.

Let's look at some statistical data of these 361 compounds to have an overall impression about what they are. In Fig. 3.2, we grouped the compounds according to their (1) composition, (2) number of atoms in the primitive cell, and (3) crystal system. The

statistical data shows that compounds with high power factor tend to have a simple structure: most of the promising candidates are binary or ternary compounds with number of atoms in a primitive cell less than 20. Moreover, half of the promising compounds have cubic symmetry (47 cubic vs 47 tetra. & ortho.), although the proportion of cubic compounds among all compounds is much smaller (94 cubic vs 267 tetra. & ortho.).
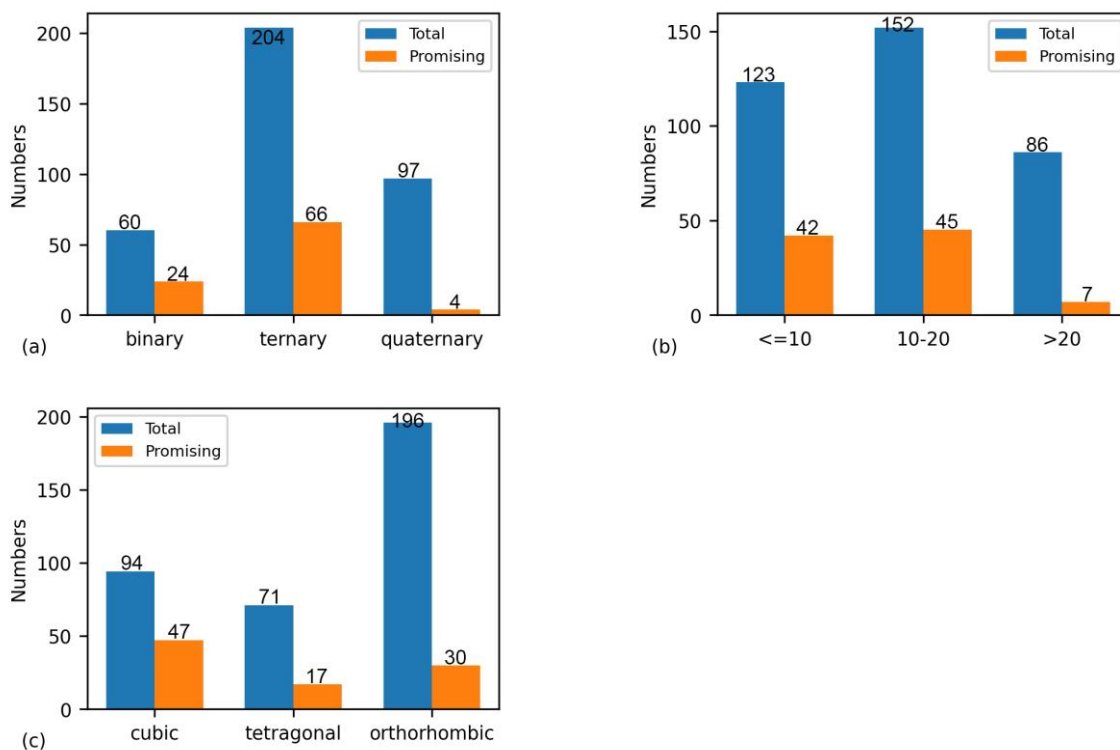
Figure 3.2. The number of calculated compounds in different classifications: (a) by the number of chemical elements in the composition; (b) by the number of atoms in the primitive cell; (c) by the crystal system.

In Table 3.1, all novel compounds we found promising to be good thermoelectric materials are listed with their thermoelectric properties. The lattice thermal conductivity and figure of merit data of some compounds are missing in the table, because there is serious imaginary frequency in their phonon spectrum. Therefore, these compounds are dynamically unstable at least at 0 K and our model cannot calculate their lattice thermal conductivity properly. However, this doesn't mean these compounds cannot exist, since

they could become stable and their phonon spectrum could have no minus frequency at high temperature. A representative compound like this is cubic-GeTe, it is unstable and its phonon spectrum has serious imaginary frequency at 0 K, However, it becomes stable and was also verified to have high figure of merit in experiment at high temperature. We still mark these compounds as promising due to their high power factor values.

Table 3.1. Novel compounds found to be good thermoelectric materials. Maximum power factor and figure of merit were calculated within temperature range from 300 K to 1000 K

Formula	Entry id	E_above _hull (eV)	Doping	PF_{max} ($\mu W \cdot cm^{-1} \cdot K^{-2}$)	$\kappa_{L,300K}$ ($W \cdot m^{-1} \cdot K^{-1}$)	ZT_{max}
$Co_4P_4Se_4$	mp-1226014	0.033	p	106.38	22.23	0.97
$P_4Rh_4Se_4$	mp-1102531	0	p	105.54	18.10	1.21
$As_4Rh_4Se_4$	mp-1228724	0	p	103.27	16.88	1.13
$Co_4As_4Se_4$	mp-1226036	0.013	p	101.91	13.30	1.25
$Co_4P_4S_4$	mp-1226003	0	p	101.50	32.66	0.79
$Sb_4Te_4Ir_4$	mp-1102430	0	p	96.18	10.03	1.43
$Co_4As_4S_4$	mp-16363	0.004	p	90.58	15.48	1.14
$Bi_4Ir_4Se_4$	mp-1103228	0	p	73.27	6.77	1.18
$Bi_4Te_4Ir_4$	mp-1227372	0.073	p	71.69	7.63	0.98

(Continued)

$Hg_2Al_4Se_8$	mp-1103510	0.042	p	67.72	5.74	1.63
$Sb_4Te_4Rh_4$	mp-1219458	0	p	65.10	9.12	0.85
$Sn_4Pt_4Se_4$	mp-1218926	0	p	63.22	4.38	1.51
$Ge_5Te_4Se_1$	mp-1224356	0.038	n, p	82.03(n) 61.02(p)		
Mg_1Te_1	mp-1008786	0.065	n, p	13.92(n) 52.55(p)	4.28	0.74(n) 1.32(p)
$Co_4Sb_4S_4$	mp-1102443	0.011	p	51.47	10.35	0.77
$Ge_4Te_4Pt_4$	mp-1224373	0	p	45.58	7.80	0.43
$Hg_2In_4S_8$	mp-22356	0	p	41.04	2.79	1.30
$Mg_2Co_4S_8$	mp-1390919	0.072	n, p	21.58(n) 18.96(p)	20.33	0.25(n) 0.20(p)
$Nb_6Sb_4Te_{10}$	mp-569571	0	p	37.13	5.21	1.11
$Li_4Co_4S_8$	mp-1176776	0.05	p	17.83	7.28	0.49
$Al_5Cu_1Se_8$	mp-37405	0.02	p	35.54	8.22	0.60
$Ba_2Hf_1S_4$	mp-9321	0	n, p	16.68(n) 34.08(p)	0.89	2.63(n) 3.70(p)
$Bi_4Rh_4Se_4$	mp-1101765	0	p	29.28	6.05	0.32

(Continued)

Ba$_2$Zr$_1$S$_4$	mp-3813	0.004	n, p	13.78(n) 27.44(p)	0.48	3.32(n) 4.18(p)
Ba$_4$Hf$_3$S$_{10}$	mp-1189858	0.02	n, p	12.54(n) 27.42(p)		
Cd$_2$In$_4$Se$_4$S$_4$	mp-1226914	0.032	p	27.29	2.53	1.12
Mg$_2$In$_4$Se$_8$	mp-1001034	0.036	p	26.76	4.81	0.84
Pb$_2$S$_2$	mp-1018115	0.039	n, p	44.41(n) 26.50(p)	1.73	2.40(n) 2.06 (p)
Ru$_4$S$_8$	mp-2030	0	p	25.66	26.82	0.20
Dy$_4$As$_4$Se$_4$	mp-1102952	0	n, p	50.95(n) 25.26(p)	2.99	2.22(n) 0.87(p)
Pb$_2$Se$_2$	mp-1063670	0.052	n, p	39.25(n) 23.62(p)	1.48	2.81(n) 2.28(p)
Ba$_4$Zr$_3$S$_{10}$	mp-14883	0.028	n, p	10.52(n) 22.20(p)		
Fe$_4$S$_8$	mp-226	0.008	p	20.17	32.10	0.11
Ba$_3$Zr$_2$S$_7$	mp-9179	0.012	n, p	11.23(n) 19.70(p)		
Er$_2$Se$_3$	mp-1225508	0.062	p	19.59	6.11	0.36
Ba$_6$Zr$_4$S$_{14}$	mp-554172	0.017	n, p	11.03(n) 19.40(p)		
Ce$_1$Se$_2$	mp-1080251	0.011	p	19.38	5.11	0.66
Y$_4$Pt$_4$S$_{14}$	mp-1245981	0.081	p	19.00	12.51	0.34

$Ru_4Se_4S_4$	mp-1219501	0.017	p	18.72	21.72	0.13
$Zn_2Co_4S_8$	mp-1400406	0.019	n, p	23.39(n) 18.56(p)	41.25	0.11(n) 0.08(p)
$Dy_8P_8S_8$	mp-1192185	0	n, p	10.52(n) 17.63(p)	2.29	1.11(n) 1.21(p)
Ge_2S_2	mp-12910	0.044	n, p	13.43(n) 17.15(p)		
$Co_4As_4S_4$	mp-4627	0.001	p	16.94	20.29	0.25
Ru_4Se_8	mp-1922	0	p	16.45	20.32	0.09
$Bi_4Te_4Rh_4$	mp-1227426	0	p	15.74	5.13	0.15
Sn_2S_2	mp-559676	0.015	p	15.44		
$Er_4As_4Se_4$	mp-1213048	0	n, p	23.45(n) 14.93(p)	3.45	0.32(n) 0.18(p)
$Sn_1Te_4Pb_3$	mp-1218925	0.004	p	14.48		
$Er_4Te_4As_4$	mp-1212634	0	p	14.18	2.88	0.78
Ge_4Te_4	mp-1080459	0.053	n, p	27.55(n) 13.89(p)	1.11	2.96(n) 1.90(p)
$Dy_4Te_4As_4$	mp-1212803	0	p	13.20	3.37	0.64
$Rb_1Ac_1Te_2$	mp-862797	0	n, p	13.51(n) 13.11(p)	0.64	2.93(n) 2.72(p)
$Ba_1Ag_2Ge_1S_4$	mp-7394	0	p	12.88		

(Continued)

$K_1Ac_1Te_2$	mp-863710	0	n, p	11.05(n) 12.61(p)	0.82	2.17(n) 2.24(p)
$Ga_2Hg_1Te_4$	mp-1224839	0.012	p	12.51	3.02	0.68
$Sn_1Pb_4S_5$	mp-1218954	0.02	p	12.34		
$Cs_1Ac_1Te_2$	mp-863760	0	n, p	10.35(n) 12.22(p)	0.48	2.84(n) 3.07(p)
$Ge_1Te_2Pb_1$	mp-1224318	0.081	n, p	10.33(n) 12.20(p)		
$Zr_1Fe_1Te_1$	mp-961649	0.067	n, p	25.37(n) 11.85(p)	14.72	0.43(n) 0.23(p)
$Ti_1Fe_1Te_1$	mp-961673	0	n, p	12.27(n) 11.50(p)	14.37	0.26(n) 0.21(p)
$In_1Ac_1Te_2$	mp-861460	0	n, p	29.83(n) 10.89(p)	0.97	2.99(n) 1.67(p)
$Ca_1In_2Te_4$	mp-677072	0.064	p	10.82	1.09	1.37
$Cd_4Te_1Se_3$	mp-1226768	0.009	p	10.43	0.62	1.61
$Ba_1Cu_2Se_2$	mp-10437	0.037	p	10.35	0.83	1.83
$Tl_1Ac_1Te_2$	mp-865028	0	n, p	36.01(n) 8.78(p)	0.73	4.27(n) 1.38(p)
$Sc_1Co_1Te_1$	mp-961678	0.006	n	33.48	12.54	0.57
$Ga_1Ac_1Te_2$	mp-861884	0	n, p	29.58(n) 7.68(p)	0.20	6.99(n) 3.05(p)

(Continued)

Ga_2Te_5	mp-2371	0	n	25.12	1.51	2.54
$Bi_8Se_8S_4$	mp-1227504	0.023	n	22.62		
Cd_4Se_8	mp-1095493	0	n	21.77	2.06	1.35
Ba_2Te_4	mp-2150	0	n	17.08	2.29	0.85
$Bi_4Sb_4Se_{12}$	mp-1227508	0.015	n	14.87		
$Er_8P_8S_8$	mp-1191596	0	n	14.76		
$Dy_{12}Cu_4Se_{24}$	mp-1225646	0.027	n	13.85		
$Ba_5Hf_4S_{13}$	mp-557032	0.026	n	13.67		
$Sn_2Pb_2S_4$	mp-1218951	0.014	n	13.52	0.34	3.93
$Cu_4Sb_4Se_8$	mp-20331	0	n	12.82	2.34	1.09
Bi_8Se_{12}	mp-23164	0.028	n	12.79		
Ge_4Se_4	mp-700	0	n	12.54	0.41	3.17
$Ba_4Cu_8Te_8$	mp-30133	0.019	n	12.42	0.35	3.40
Er_8Te_{12}	mp-14643	0	n	11.79		
$Ca_4Sn_4S_{12}$	mp-866811	0.074	n	10.97	1.87	1.34

Ge₄Se₂S₂	mp-1224376	0.006	n	10.92	0.40	3.34
Cs₆Cu₄Bi₁₀S₂₀	mp-669419	0.011	n	10.88	0.22	3.76
Sn₂Se₂	mp-628773	0.076	n	10.68		
Sn₂Ge₂Se₄	mp-1218835	0.009	n	10.64	0.22	4.34
Cs₂Hg₂Sb₂Se₆	mp-1225936	0.023	n	10.30		
Na₁Ac₁Te₂	mp-865081	0	n, p	7.29(n) 7.26(p)	1.28	0.99(n) 0.87(p)

The PBE functional is known to usually underestimate the band gap value, which has a profound impact on the electronic transport properties in our model. In order to explore the influence of a more accurate band gap on the thermoelectric transport properties, we selected two representative compounds, $Co_4As_4S_4$ and Cd_4Se_8, and recalculated their band-structure-related key parameters, including the band gap, deformation potential constant, and band effective mass, using the modified Becke–Johnson (MBJ) method [157,158]. The MBJ potential in combination with LDA-correlation yields band gaps with an accuracy similar to hybrid functional, but computationally less expensive (although still expensive than PBE functional). Then, their electronic transport properties were calculated on the basis of the newly obtained parameters. Compared with the PBE approach, the MBJ method yields larger values of the band gap for both compounds: 1.18 eV (MBJ) vs 0.85 eV (PBE) for $Co_4As_4S_4$ and 1.47 eV (MBJ) vs 0.58 eV (PBE) for Cd_4Se_8. Fig. 3.3 shows the power factor for $Co_4As_4S_4$ and Cd_4Se_8 calculated using the PBE and MBJ parameters; the use of MBJ parameters results in larger power factor values for both compounds. For example, the maximum *PF* value for $Co_4As_4S_4$ is 99.11 μW·cm⁻¹·K⁻² (MBJ) vs 90.58

μW·cm^{-1}·K^{-2} (PBE); for Cd$_4$Se$_8$, it is 23.50 μW·cm^{-1}·K^{-2} (MBJ) vs 21.77 μW·cm^{-1}·K^{-2} (PBE). As can be seen, the gain is quite small using a more accurate gap value. Moreover, the main function of band gap in our model is indicating the band nonparabolicity, as shown in the eq. 2.21. The larger the band gap, the closer the energy band to single parabolic band model. Usually, single parabolic band model tends to underestimate the scattering rate of carriers because it doesn't involve the interaction from other energy bands. In our relaxation time model, we only consider acoustic phonon, polar optical phonon and ionized impurity scattering processes, while other scattering processes, such as nonpolar optical phonon scattering, inter-valley scattering, grain boundary, are omitted. Therefore, we intentionally hope the nonparabolicity could be stronger so that the scattering rate of the current implemented model could be larger to offset the deficiency of the model itself. By this way, the calculated transport properties could be closer to the experimental values. Therefore, the PBE method is still the best choice providing a balance between accuracy and speed.
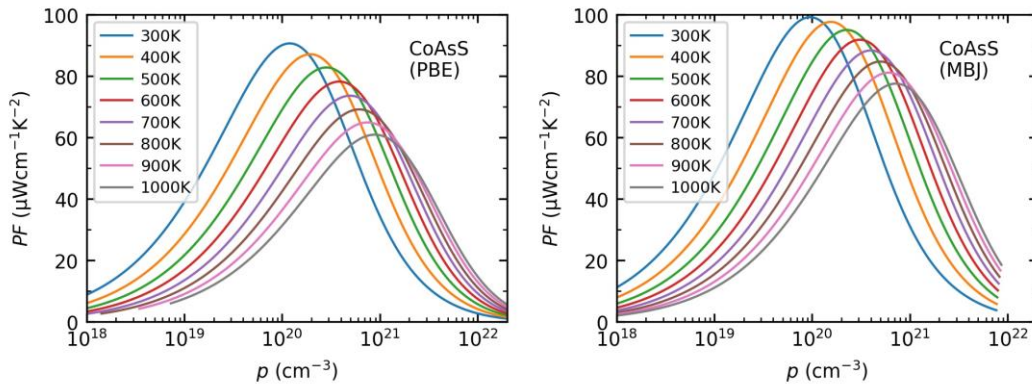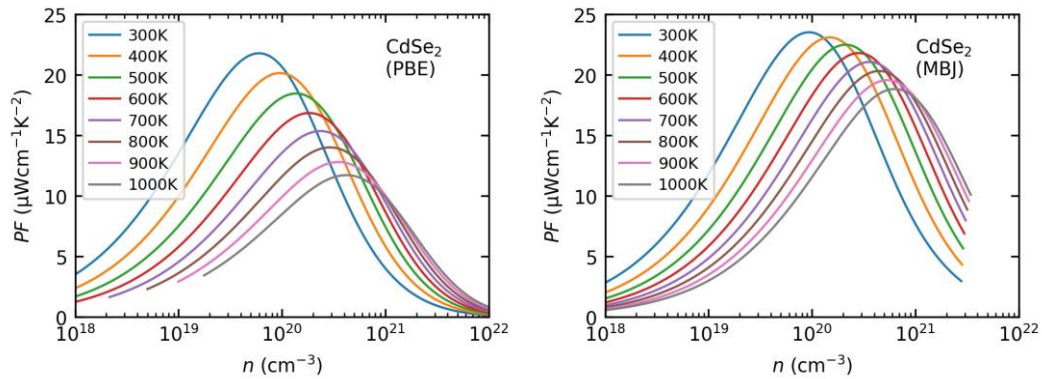
Figure 3.3. Power factor of $Co_4As_4S_4$ and Cd_4Se_8 calculated using the PBE and MBJ parameters.

3.3. Simple Indicator for Screening for Thermoelectric Materials

It would be convenient to have some simple indicators that help quickly evaluate the thermoelectric performance of a material. Recently, researchers have begun to use some easily obtained properties, such as the average atomic mass, volume per atom, and electronegativity, combined with machine learning models to predict the figure of merit or other complex properties [159–161]. The key to success for such a method is identifying easy to calculate properties which are most relevant to the complex properties of interest.

In Fig. 3.4, the materials under study are presented according to their average atomic mass and the number of atoms in the primitive cell, which are two commonly used indicators. Materials with a high power factor are found all across this chemical space, showing quite a high diversity. Thus, these two properties are not an ideal index.
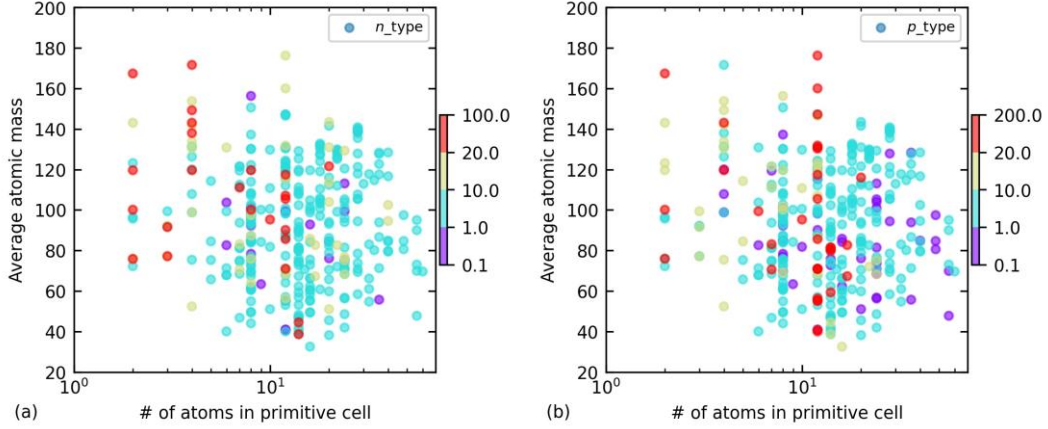
Figure 3.4. Maximum power factor values, represented by color for (a) n-type and (b) p-type transport, of the studied compounds in the chemical space defined by the average atomic mass and the number of atoms in the primitive cell.

What simple properties are strongly correlated with the thermoelectric properties, such as the power factor? As shown in Section 2.2, the effective mass (m^*) appears in many places and is the key parameter to determine the scattering rate of each scattering process involved. According to single parabolic band approximation, the Seebeck coefficient is proportional to the density of states effective mass m_d^* [74],

$$\alpha \approx \frac{2\pi^{2/3} k_B^2 T m_d^*}{3^{5/3} e n^{2/3} \hbar^2} (r + 3/2)$$

whereas the carrier mobility is inversely proportional to the conductivity effective mass m_c^* (eq. 2.13). m_d^* can be increased either by increasing band degeneracy N or by increasing $m_\parallel^* m_\perp^{*2}$ (eq. 2.23). However, increasing the latter will also increase m_c^* (eq. 2.24). Therefore, the ideal situation would be the band degeneracy N is very large while $m_\parallel^*$ and $m_\perp^*$ keep small. In this case, a material should have large power factor. This is possible if the conduction band or valence band locates along specific directions in Brillouin zone for those high-symmetrical compounds (such as cubic ones), or make several different bands converge to the same energy level. Fig. 3.5 shows the maximum power factor values in the chemical space defined by m_d^* and m_c^*. At similar values of m_d^*, a material with smaller m_c^* tends to have a higher power factor; at similar m_c^* values, a

material with larger m_d^* tends to have higher power factor. The maximum power factor plotted against m_d^*/m_c^* for the studied compounds (Fig. 3.6) shows a generally rising trend, which is clearer for p-type transport than n-type transport because of higher Pearson correlation coefficient (0.5857 for p-type transport vs 0.4030 for n-type transport). By adding one more parameter $\kappa_{L,300K}$ at the denominator, Fig. 3.7 shows the maximum figure of merit plotted against $m_d^*/\left(m_c^*\kappa_{L,300K}\right)$ for the promising compounds. There is also a clear trend that the higher the $m_d^*/\left(m_c^*\kappa_{L,300K}\right)$, the higher the maximum figure or merit. The Pearson correlation coefficient for n-type transport is 0.7977, while that is 0.6220 for p-type transport. However, such a correlation coefficient is still a bit low and these parameters cannot be used directly to predict figure of merit values. Nevertheless, we believe that using these three parameters or the indicators most related with them as an input in a machine learning model could results in a high-accuracy prediction of the figure of merit.
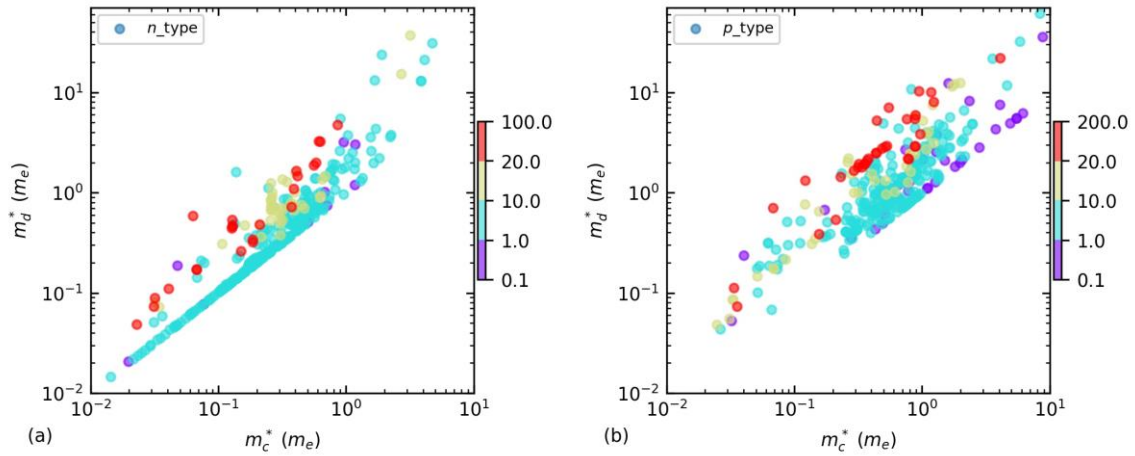
Figure 3.5. Maximum power factor values, represented by color for (a) n-type and (b) p-type transport, of the studied compounds in the chemical space defined by the density of states effective mass m_d^* and conductivity effective mass m_c^*.
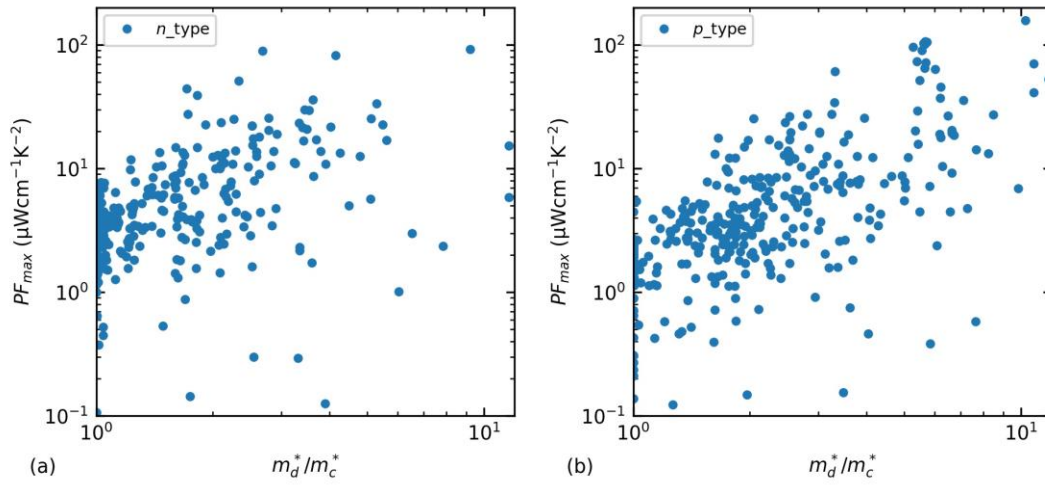
Figure 3.6. Maximum power factor versus m_d^*/m_c^* for the studied compounds.
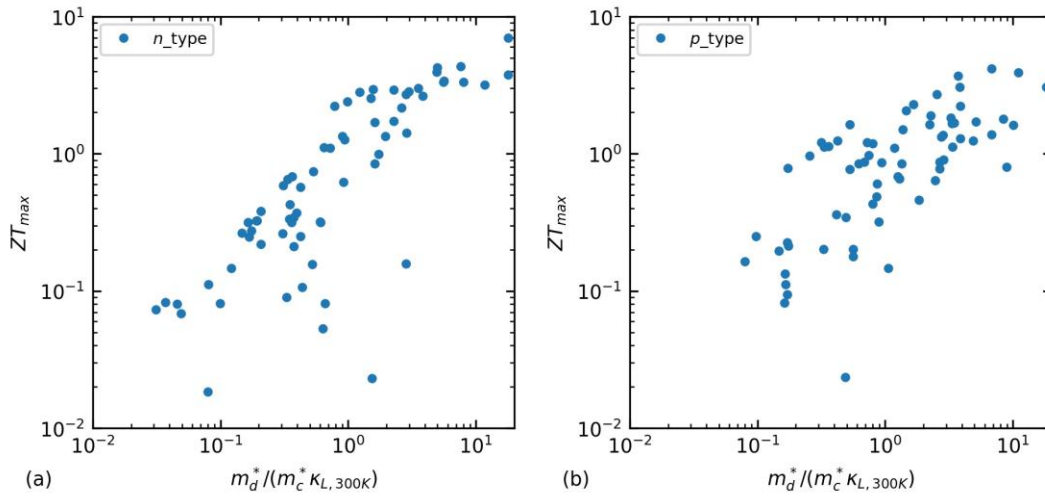
Figure 3.7. Maximum figure of merit versus $m_d^*/\left(m_c^*\kappa_{L,300K}\right)$ for the studied compounds.

Chapter 4. Promising Thermoelectric Materials

The novel compounds we found as promising and most interesting thermoelectric materials are introduced in detail in this chapter, with their crystal structures, band structures, and transport properties (mainly the power factor, lattice thermal conductivity, and figure of merit) displayed and analyzed. Other information can be found in Appendix.

4.1. $X_4Y_4Z_4$ (X = VIII B; Y = IV A, V A; Z = VI A)

Compounds with this chemical formula, including RhAsSe, RhSbTe, IrSbTe, IrBiSe, IrBiTe, RhBiSe, RhBiTe, CoAsS, CoAsSe, CoPS, CoPSe, RhPSe, CoSbS, PtSnSe, and PtGeTe, were found to be good p-type thermoelectric materials because of their large power factor. These compounds have the same structure (space group $P2_13$) and belong to the pyrite structure type, as shown in Fig. 4.1. The transition metal X atoms are bonded to six Y and Z atoms, forming a distorted octahedron, whereas the Y (Z) atoms are tetrahedral, being bound to three X atoms and one other Z (Y) atom.
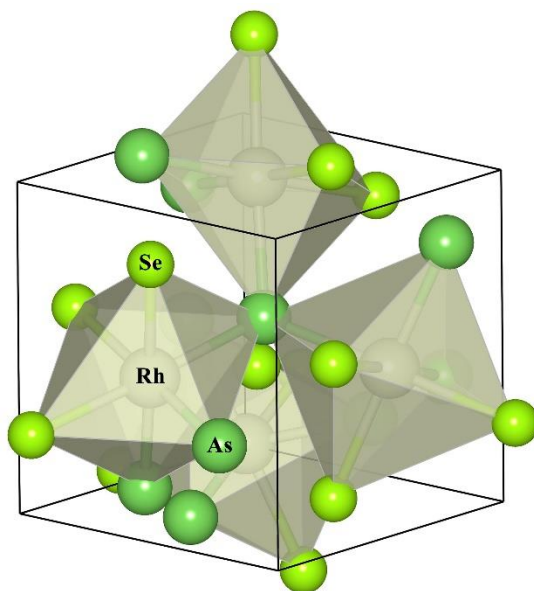
Figure 4.1. Crystal structure of RhAsSe.

Fig. 4.2 shows the band structures of these compounds, taking RhAsSe, CoAsS, CoAsSe, and PtSnSe as examples. They are all indirect gap semiconductors, with the

CBMs located along the Γ–R or Γ–M or Γ–X paths. However, the energy difference among these conduction bands is quite small, and they are probably all involved in electronic transport. Moreover, the CBMs of these compounds are quite flat, implying large effective masses. On the contrary, their VBMs are well-defined and located along the Γ–M path. Besides, the VBMs are dispersive and the corresponding effective masses are expected to be small. The merit of RhAsSe and other compounds belonging to this group is that the degeneracy of points along the Γ–M path is large ($N = 12$). Therefore, for p-type conduction, these compounds have a large DOS effective mass but small conductivity effective mass (see Table 4.1). This will lead to large power factor values.
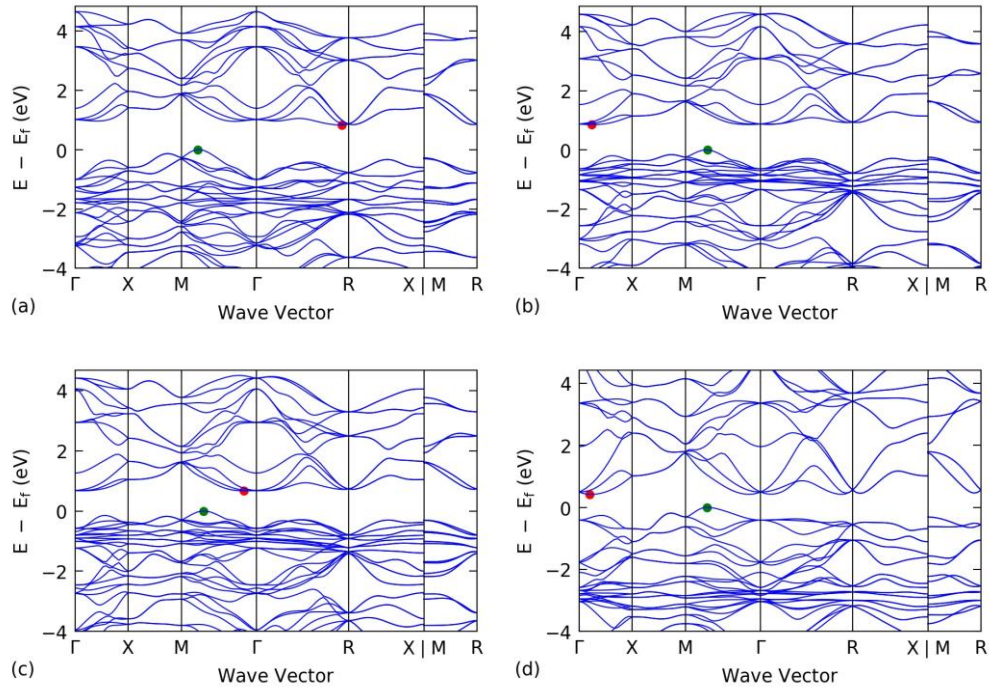
Figure 4.2. Band structures of (a) RhAsSe, (b) CoAsS, (c) CoAsSe, and (d) PtSnSe. The CBM and VBM are shown by red and green dots, respectively.

Table 4.1. Key parameters for p-type transport: conductivity effective mass m_c^*, DOS effective mass m_d^*, deformation potential constant Ξ, band degeneracy N, band gap E_g, direction-averaged elastic constant c, high-frequency and static dielectric constants ε_∞ and ε_0

	m_c^* (m_e)	m_d^* (m_e)	Ξ (eV)	N	E_g (eV)	c (GPa)	ε_∞	ε_0
CoAsS	0.5128	2.8524	13.58	12	0.85	139.60	24.79	31.91
CoAsSe	0.4413	2.4915	12.45	12	0.67	121.86	28.29	36.55
CoPS	0.4862	2.7459	14.49	12	1.14	164.48	21.40	27.02
CoPSe	0.4349	2.4668	13.50	12	0.84	142.05	24.88	31.81
CoSbS	0.5315	2.9145	14.93	12	0.55	105.20	28.54	38.17
RhPSe	0.3805	2.1787	13.94	12	1.11	126.03	19.99	24.02
RhAsSe	0.3712	2.0853	12.97	12	0.83	109.46	22.04	27.08
RhBiSe	0.3545	1.9159	13.25	12	0.13	74.64	34.54	44.90
RhBiTe	0.2798	1.5197	13.67	12	0.07	69.88	41.99	53.79
RhSbTe	0.2929	1.6533	14.66	12	0.37	84.43	28.13	36.32
IrBiSe	0.3601	1.9450	12.94	12	0.38	90.84	25.90	34.50
IrBiTe	0.3152	1.7895	13.33	12	0.33	87.55	28.69	38.23
IrSbTe	0.3045	1.8577	14.20	12	0.70	102.02	20.93	27.82
PtSnSe	0.3206	1.9248	13.67	12	0.42	73.29	27.61	36.34
PtGeTe	0.2307	1.4327	15.46	12	0.17	84.80	33.18	41.78

In order to explore the origin of high band degeneracy and low band effective mass of the VBMs of these compounds, we also calculated the orbital-projected band structures for them using LOBSTER program with the pbeVaspFit2015 basis set [162–164]. For example, in CoPS (Fig. 4.3a), the VBM includes contributions from all three types of atoms; the orbital-projected band structure mainly consists of the 3d and 4p orbitals of Co, 3p orbital of P, and 3p orbital of S. The variation of the effective mass of the VBMs for these compounds could be partly explained by the amount of contributions from these orbitals. For example, in the series CoPS–CoAsS–CoSbS, the effective mass increases as Table 4.1 shows. A comparison of the orbital-projected band structures of these compounds (Fig. 4.3) shows that the contribution of the 3d orbital of Co increases while those of the p orbital of sulfur and Y-type atom decrease as the Y atom changes from P to Sb. Since d electrons are more localized than p electrons, the effective mass is supposed to be heavier.

(a)

(b)
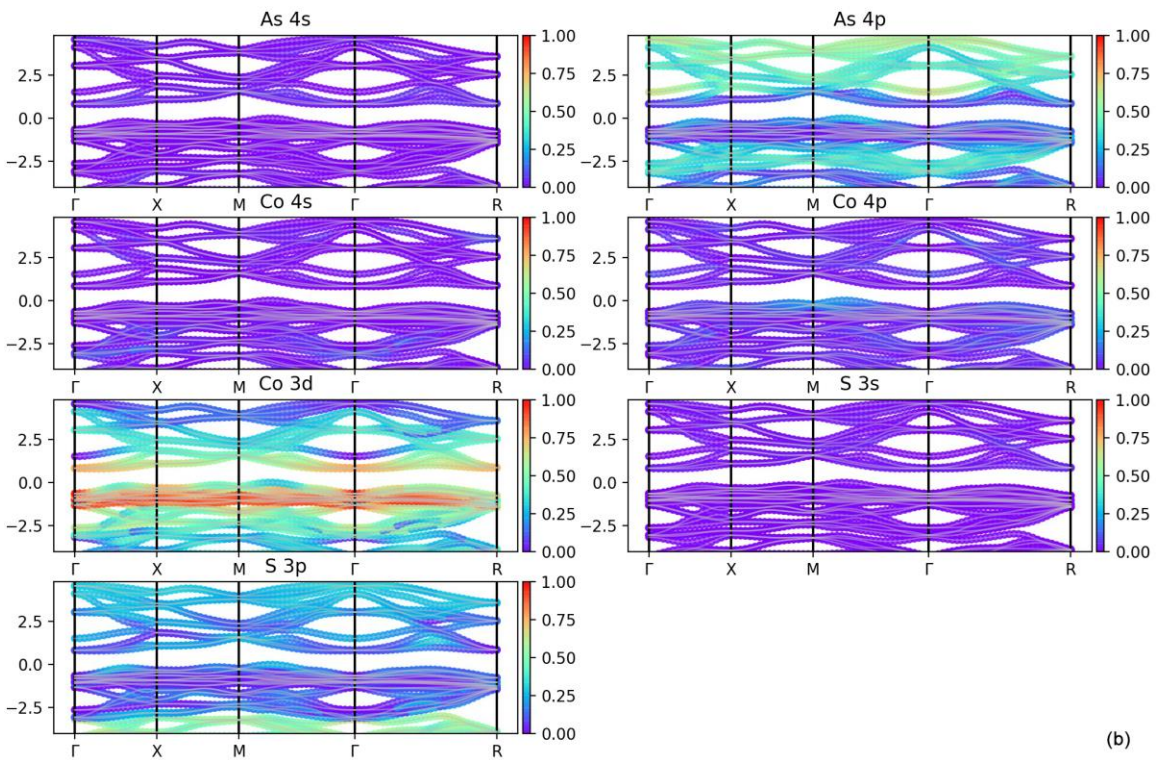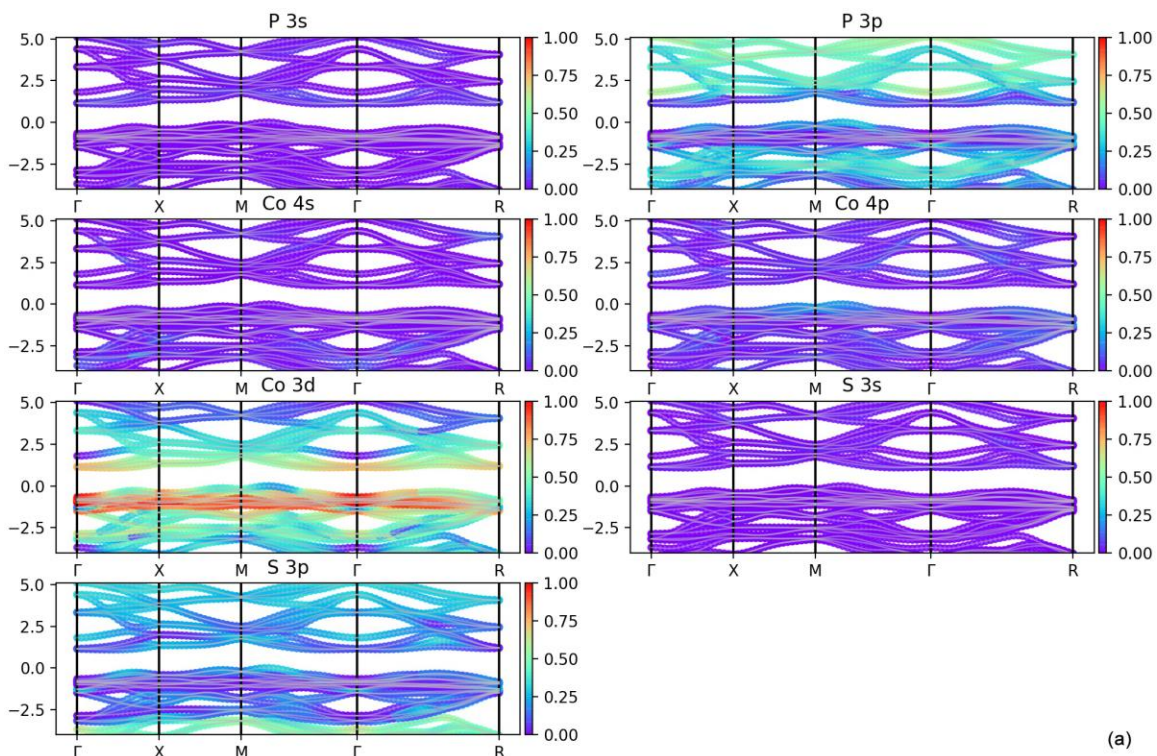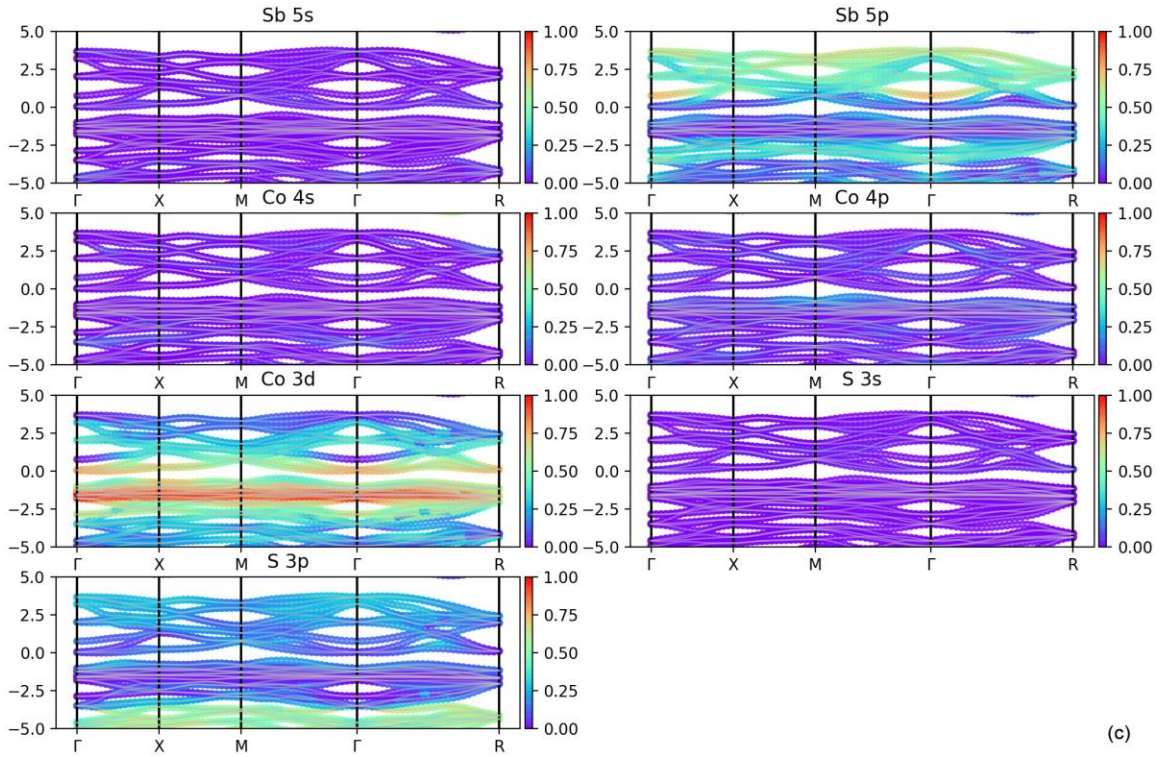
Figure 4.3. Orbital-projected band structure of (a) CoPS, (b) CoAsS, and (c) CoSbS.

Fig. 4.4 shows the power factor as a function of temperature and carrier concentration for this group of compounds. The power factor of these compounds is extremely high in a wide range of temperatures and carrier concentrations. The maximum values of some of them, such as CoAsSe, CoPS, CoPSe, RhPSe, and RhAsSe, could be even higher than 100 $\mu W \cdot cm^{-1} \cdot K^{-2}$. For comparison, the maximum power factor of the state-of-the-art thermoelectric materials, such as Bi_2Te_3 and PbTe, is usually 30–50 $\mu W \cdot cm^{-1} \cdot K^{-2}$. As explained above, such a large power factor is due to the special characteristics of their band structures: large m_d^* around the VBM resulting from high degeneracy, but small m_c^* for each carrier pocket. Therefore, they could achieve both a high Seebeck coefficient and high electrical conductivity.

(a)

(b)

(c)

(d)

(e)

(f)

83

(g)

(h)

(i)

(j)

(k)

(l)

84
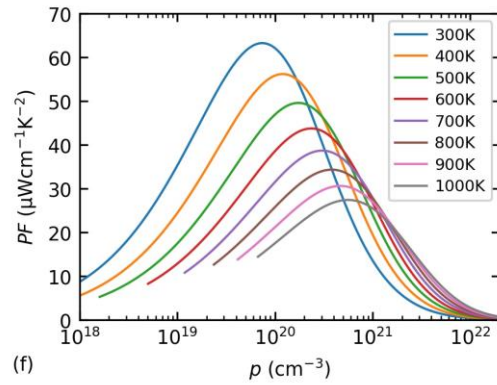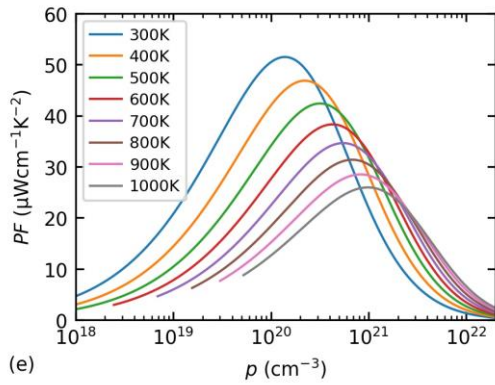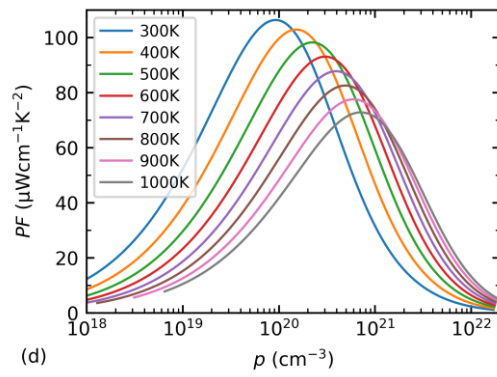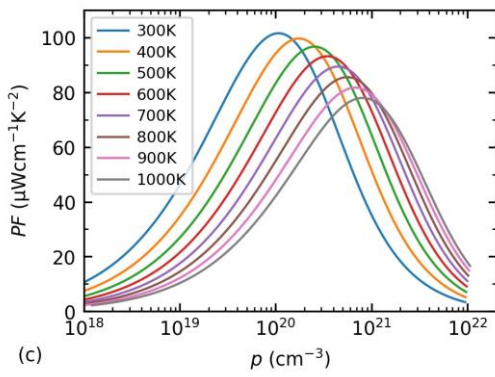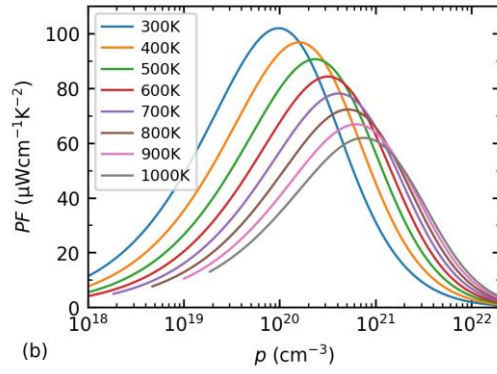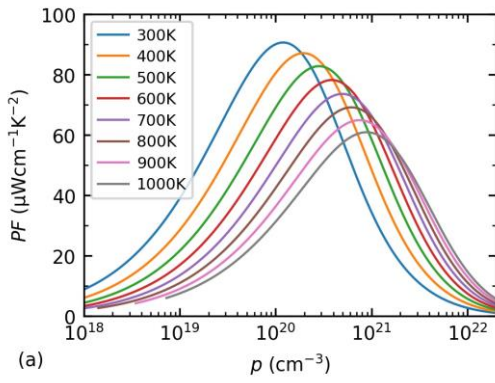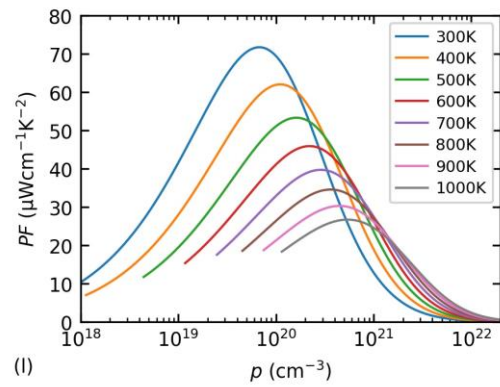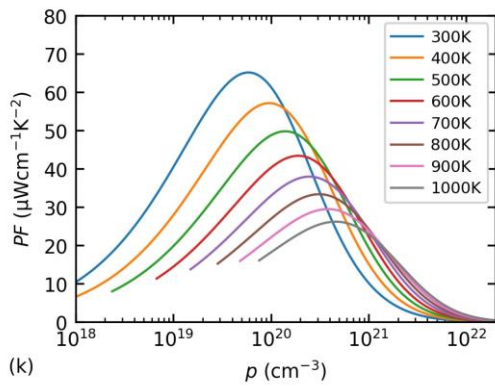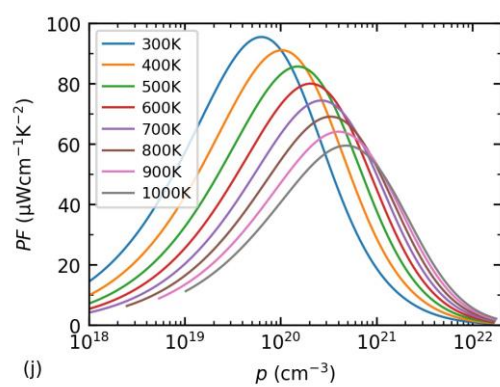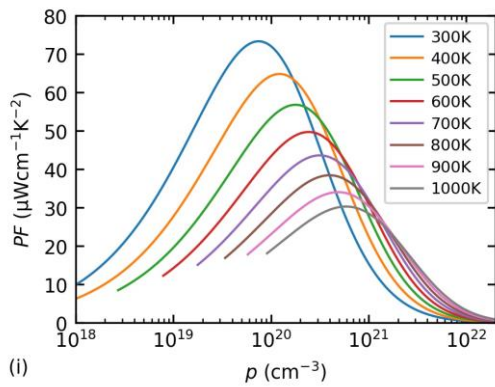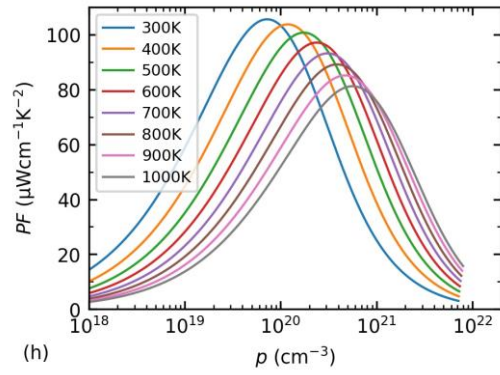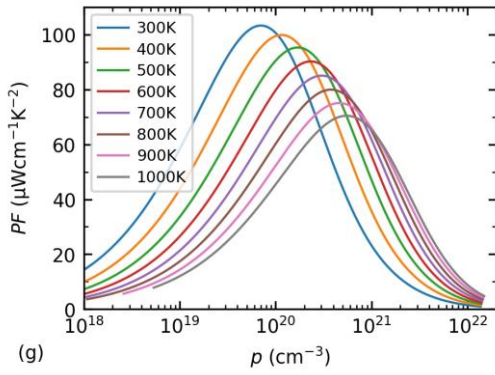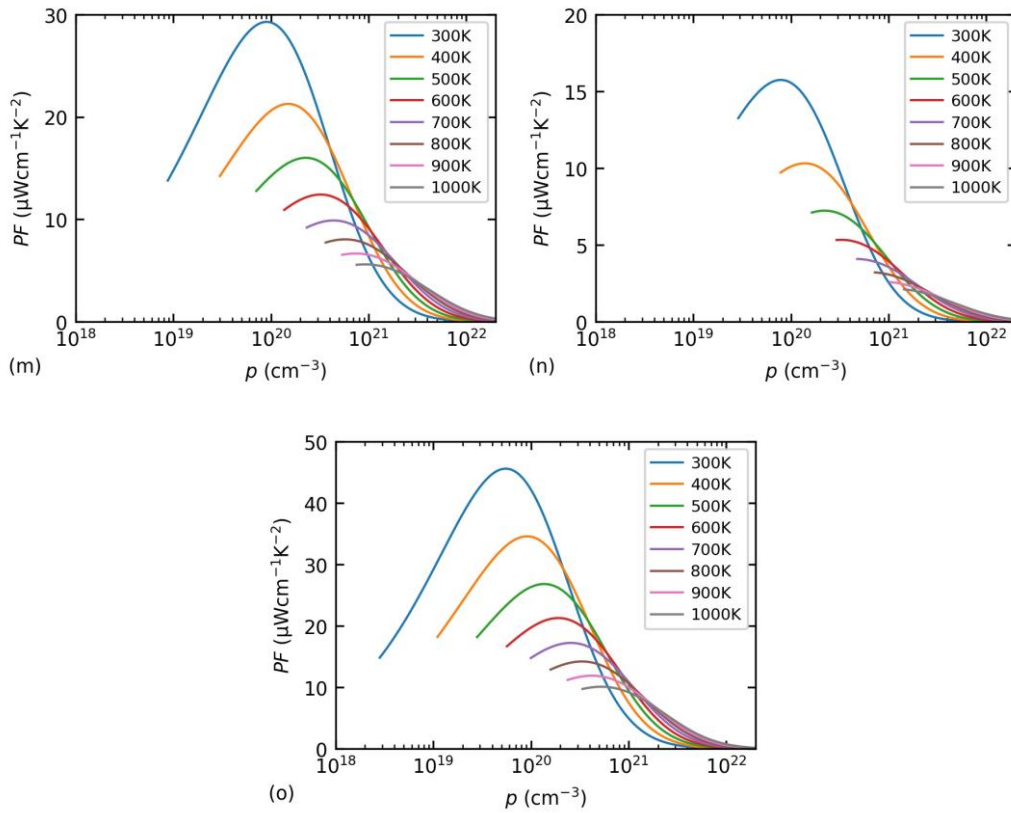
Figure 4.4. Power factor at varying temperatures and carrier concentrations for (a) CoAsS, (b) CoAsSe, (c) CoPS, (d) CoPSe, (e) CoSbS, (f) PtSnSe, (g) RhAsSe, (h) RhPSe, (i) IrBiSe, and (j) IrSbTe, (k) RhSbTe, (l) IrBiTe, (m) RhBiSe, (n) RhBiTe, (o) PtGeTe.

However, the problem with these compounds is that they also have high lattice thermal conductivity, as shown in Fig. 4.5. Because of that, their figure of merit values are not much larger than those of the state-of-the-art thermoelectric materials (Fig. 4.6). Still, some of them could have figure of merit values above 1 at high temperatures, such as CoAsS, CoAsSe, PtSnSe, RhAsSe, RhPSe, IrBiSe, and IrSbTe. Furthermore, there are ways to reduce the lattice thermal conductivity of these compounds. For example, by alloying to form compounds like CoP(As,Sb)S(Se) that could reduce the lattice thermal conductivity efficiently while retaining the high power factor. Therefore, this group of compounds is quite promising for thermoelectric applications.
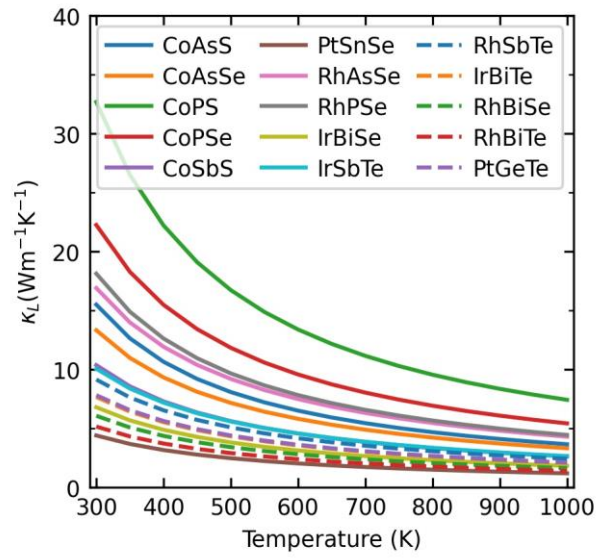
Figure 4.5. Lattice thermal conductivity of the selected compounds.

(e)

(f)

(g)

(h)

(i)

(j)

87
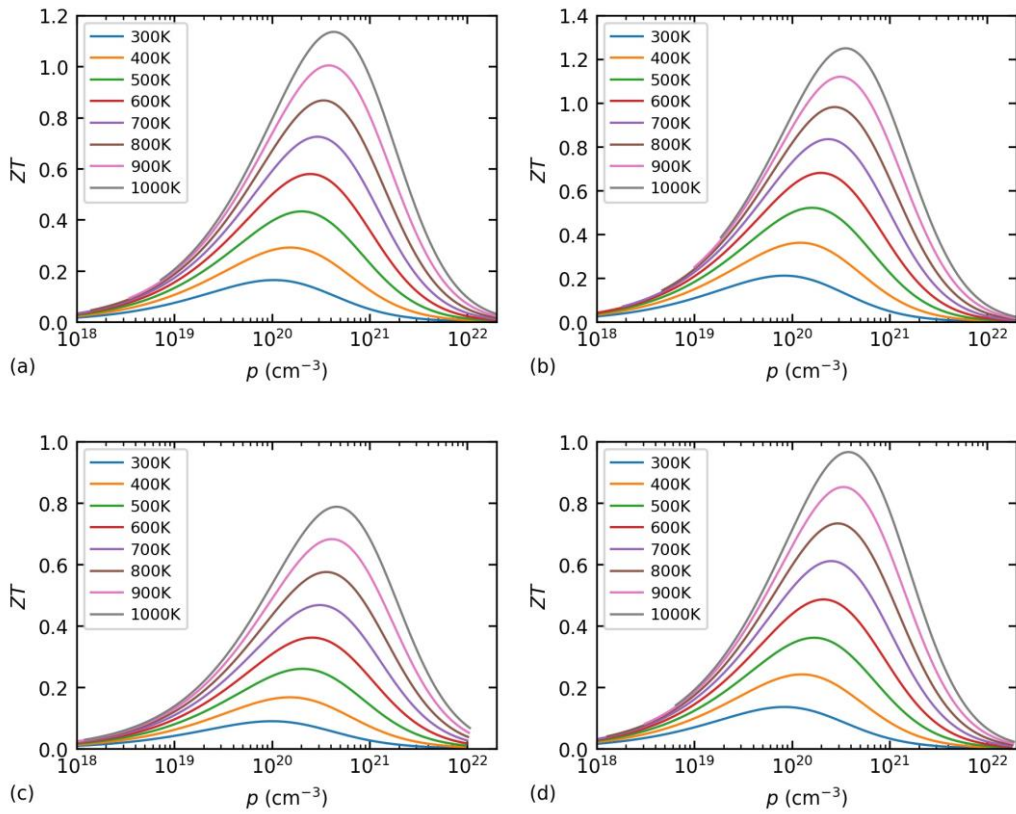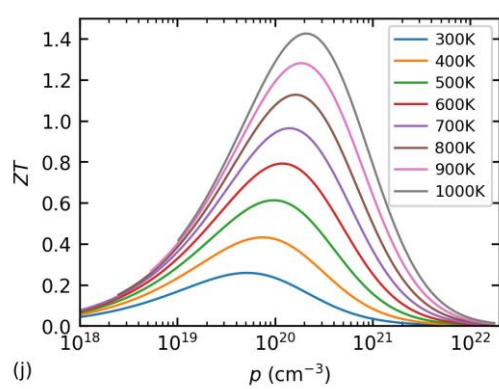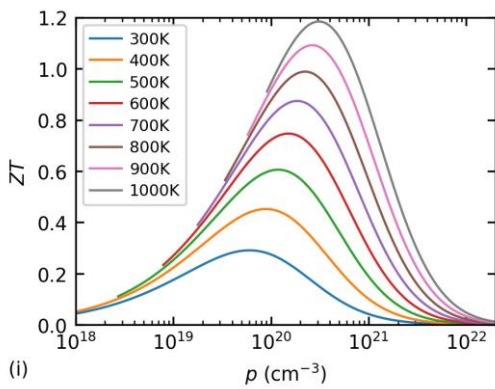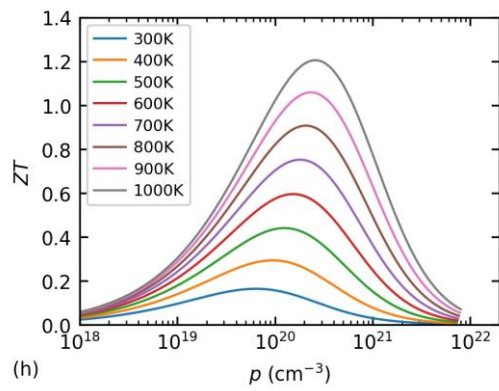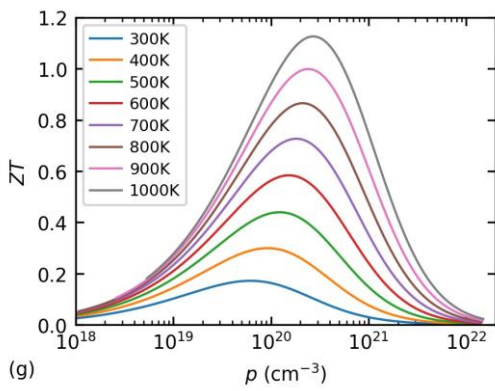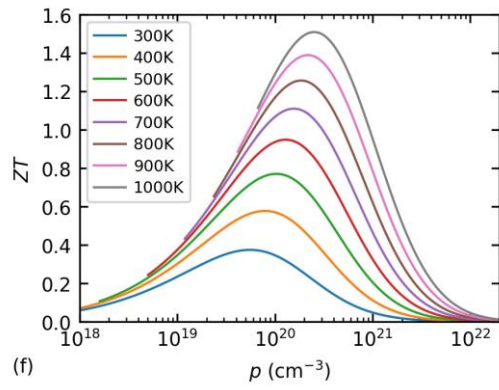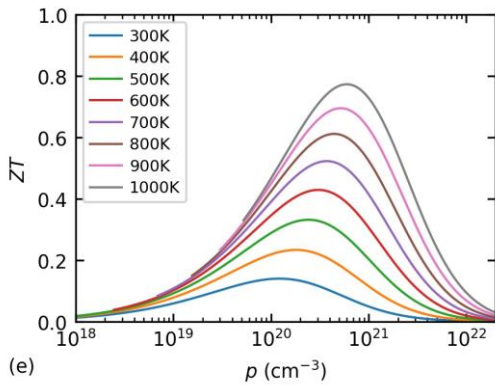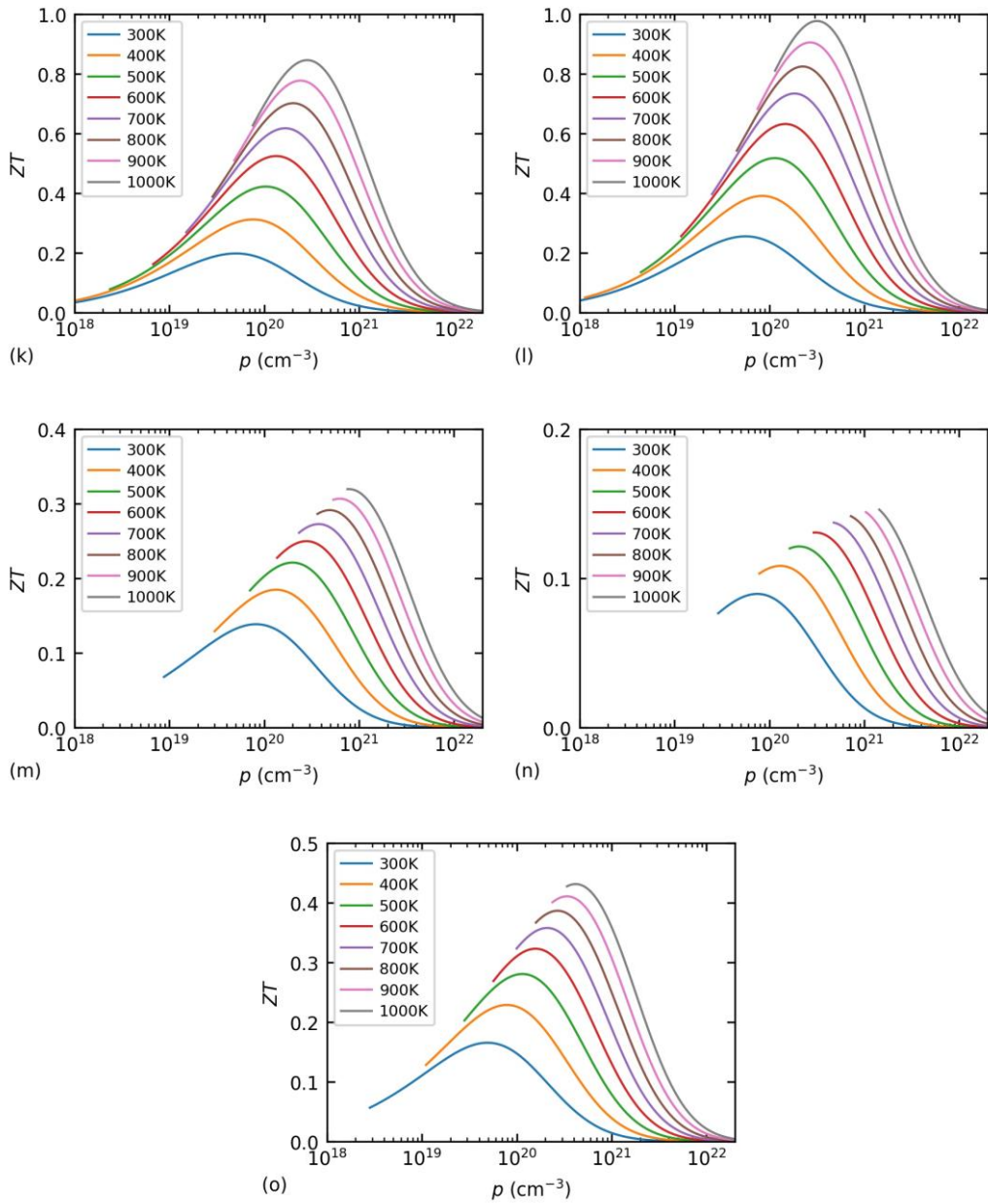
Figure 4.6. Figure of merit at varying temperatures and carrier concentrations for (a) CoAsS, (b) CoAsSe, (c) CoPS, (d) CoPSe, (e) CoSbS, (f) PtSnSe, (g) RhAsSe, (h) RhPSe, (i) IrBiSe, and (j) IrSbTe, (k) RhSbTe, (l) IrBiTe, (m) RhBiSe, (n) RhBiTe, (o) PtGeTe.

4.2. CdSe$_2$

The structure of CdSe$_2$ has a space group *P*a-3 (Fig. 4.7), with the unit cell containing 12 atoms (4 Cd and 8 Se). It is a pyrite-type structure. Cd atoms occupy the corner and face center of the unit cell, each of them forming an octahedron with six Se atoms around. Different octahedrons are connected by one Se atom. Our calculations show that this compound is a promising n-type thermoelectric material. Interestingly, we found an independent preprint also declares that this CdSe$_2$ is a good thermoelectric material [165]. Below, we compare our results with those from the previous study.
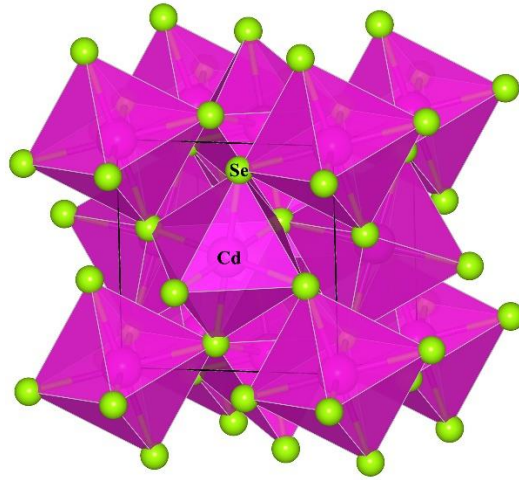
Figure 4.7. Crystal structure of CdSe$_2$.

In the band structure of CdSe$_2$, its VBM is located at the Γ point, whereas the CBM is along the Γ–R path (Fig. 4.8). The orbital projected band structure of CdSe$_2$ shows that both Cd and Se contribute to the formation of the CBM (Fig. 4.9), which is mainly composed of the 5s orbital of Cd and 4p orbital of Se. The CBM is dispersive and has a small conductivity effective mass $m_c^* = 0.41 m_e$ ($0.43 m_e$ in ref. [165]). The band degeneracy N of CBM is 8 and the density of states effective mass $m_d^* = 1.64 m_e$. Therefore, CdSe$_2$ could also have both a high Seebeck coefficient and high electrical conductivity.
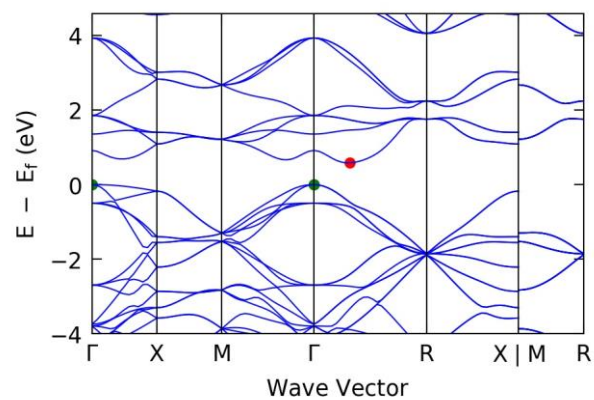
Figure 4.8. Band structure of CdSe$_2$.
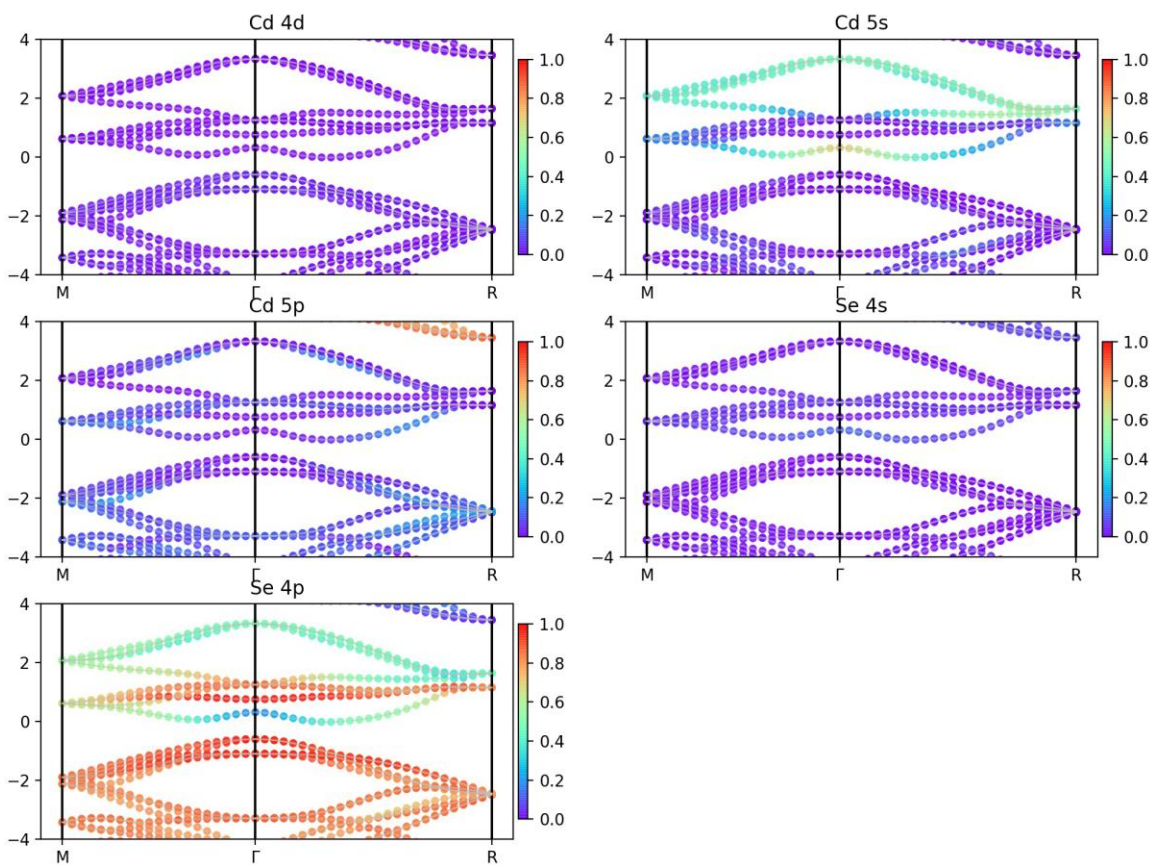
Figure 4.9. Orbital-projected band structure of CdSe$_2$.

Table 4.2. Key parameters for n-type transport

	m_c^* (m_e)	m_d^* (m_e)	$\varXi$ (eV)	N	E_g (eV)	c (GPa)	ε_∞	ε_0
CdSe$_2$	0.41	1.64	10.19	8	0.58	23.96	11.41	19.90

Fig. 4.10 shows the calculated power factor, lattice thermal conductivity, and figure of merit of CdSe$_2$ at different temperatures and carrier concentrations for n-type transport. The power factor is generally high in a wide temperature range (Fig. 4.10a), whereas the lattice thermal conductivity is low, especially at high temperatures (Fig. 4.10b). Therefore, the figure of merit ZT can be larger than 1 at high temperatures (Fig. 4.10c). Our figure of merit is generally in close agreement with the results from ref. [165]. The maximum ZT value at 900 K is 1.22 at a concentration of 1.70×10^{20} cm^{-3} according to our calculations, while it is 1.16 at 1.91×10^{20} cm^{-3} according to ref. [165]. However, the power factor and lattice thermal conductivity values calculated in this work are higher than those in ref. [165]. For example, at 300 K, the maximum power factor is 21.77 µW·cm^{-1}·K^{-2} (9.7 µW·cm^{-1}·K^{-2} in ref. [165]) and lattice thermal conductivity is 2.06 W·m^{-1}·K^{-1} (0.75 W·m^{-1}·K^{-1} in ref. [165]). In the end, both studies independently prove that pyrite CdSe$_2$ has a high ZT and is a promising thermoelectric material.
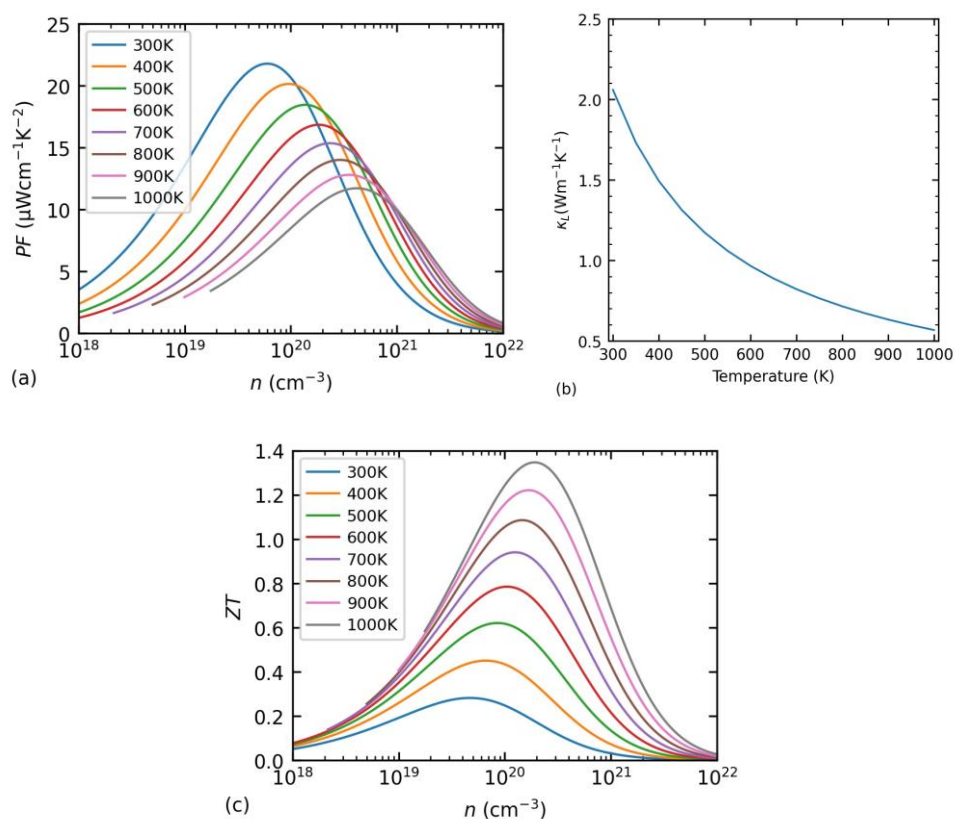
Figure 4.10. Thermoelectric properties of CdSe$_2$ for n-type transport. (a) power factor, (b) lattice thermal conductivity, and (c) figure of merit.

4.3. MAcTe$_2$ (M = I A or III A)

Compounds with this chemical formula, including NaAcTe$_2$, KAcTe$_2$, RbAcTe$_2$, CsAcTe$_2$, GaAcTe$_2$, InAcTe$_2$ and TlAcTe$_2$, could be both good n-type and p-type thermoelectric materials. These compounds have the same structure (space group *Fm-3m*), as shown in Fig. 4.11.
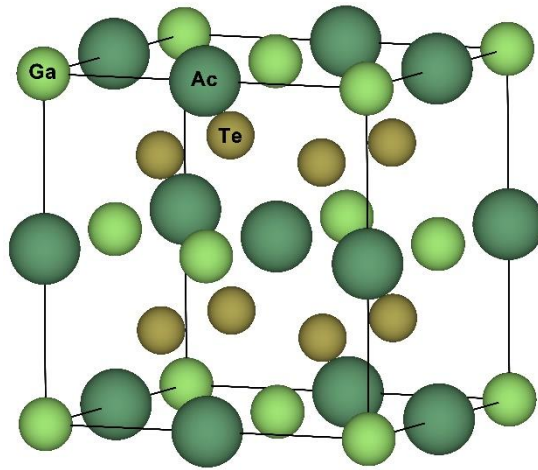
Figure 4.11. Crystal structure of GaAcTe$_2$.

Fig. 4.12 shows the band structures of these compounds. Those in which M belongs to group IIIA are indirect gap semiconductors. Their CBMs are located along the Γ–X path ($N = 6$), whereas their VBMs can be at the high symmetry X or L point (X: $N = 3$, L: $N = 4$). The compounds in which M belongs to group IA are direct gap semiconductors. Their band extrema can be located at either the X or Γ point. These band extrema are dispersive; thus, the carrier mobilities are relatively high. There are multiple extrema near the band gap for either n-type or p-type conductance, and the energy difference among these bands is small (for example, VBMs at X and L for M = IIIA or VBMs at X and Γ for M = IA). Therefore, they all are probably involved in electronic transport at a certain chemical potential.
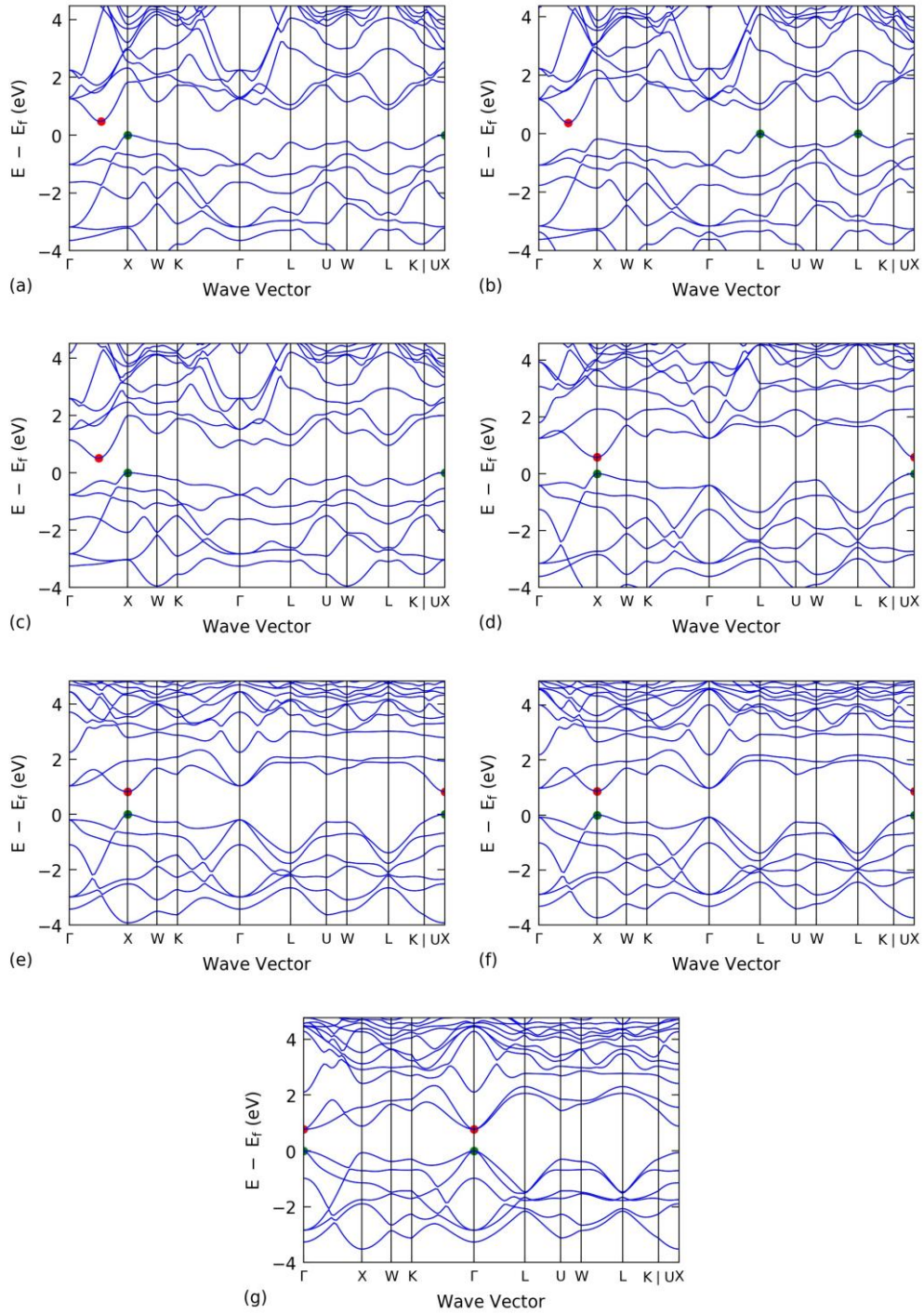
Figure 4.12. Band structures of (a) GaAcTe$_2$, (b) InAcTe$_2$, (c) TlAcTe$_2$, (d) NaAcTe$_2$, (e) KAcTe$_2$, (f) RbAcTe$_2$, and (g) CsAcTe$_2$.

Table 4.3. Key parameters for n-type and p-type transport

		m_c^* (m_e)	m_d^* (m_e)	Ξ (eV)	N	E_g (eV)	c (GPa)	ε_∞	ε_0
GaAcTe$_2$	CBM	0.129	0.457	9.94	6	0.47	20.49	17.52	132.67
	VBM	0.355	1.287	9.97	3				
InAcTe$_2$	CBM	0.128	0.440	10.41	6	0.36	24.72	18.08	95.56
	VBM	0.226	0.591	11.87	4				
	VSB	0.383	1.526	10.28	3	0.55			
TlAcTe$_2$	CBM	0.130	0.469	10.08	6	0.51	27.31	15.69	68.10
	VBM	0.425	2.097	10.13	3				
NaAcTe$_2$	CBM	0.349	0.774	8.58	3	0.58	15.75	9.41	31.53
	VBM	0.341	1.159	9.38	3				
KAcTe$_2$	CBM	0.369	0.789	8.24	3	0.82	25.47	8.67	27.30
	VBM	0.317	0.999	8.88	3				
RbAcTe$_2$	CBM	0.349	0.736	8.18	3	0.87	25.01	8.62	29.31
	VBM	0.310	0.956	8.71	3				
	CSB	1.495	1.495	3.92	1	0.97			
	VSB	2.180	2.180	12.08	1	0.95			
CsAcTe$_2$	CBM	1.515	1.515	6.92	1	0.77	22.03	8.99	36.12
	VBM	1.203	1.203	9.37	1				
	CSB	0.327	0.682	8.48	3	0.89			
	VSB	0.296	0.878	8.74	3	0.83			

Fig. 4.13, 4.14 and 4.15 show the power factor, lattice thermal conductivity, and figure of merit for this group of compounds. Their power factor is generally high, as indicated by their band structures. At the same time, their lattice thermal conductivity is extremely low: for most of them it is already lower than 1 W·m^{-1}·K^{-1} at room temperature. Therefore, these compounds have quite large *ZT* values in a wide range of temperatures and carrier concentrations. However, radioactive element Ac that they contain makes it impractical to manufacture devices based on these compounds.
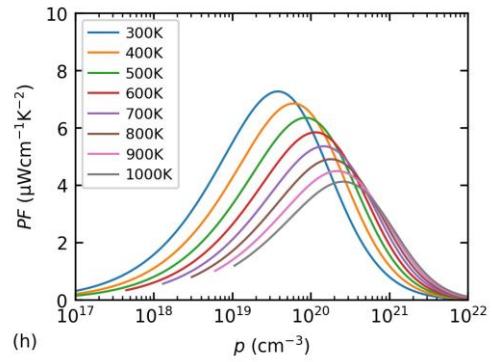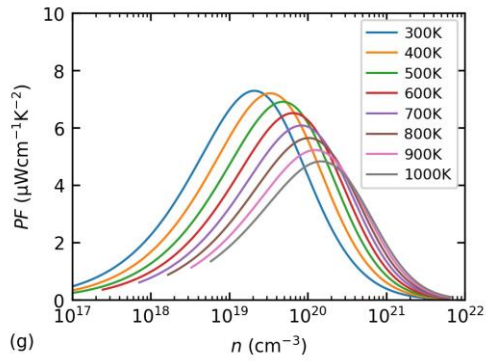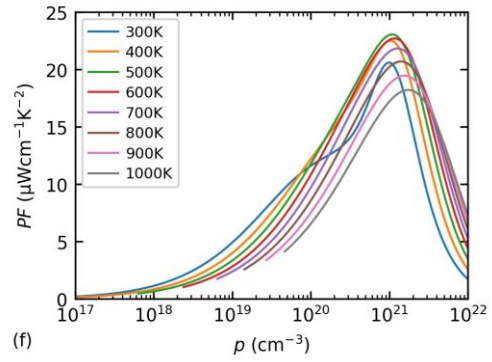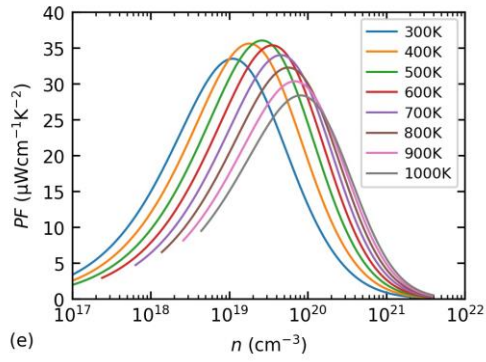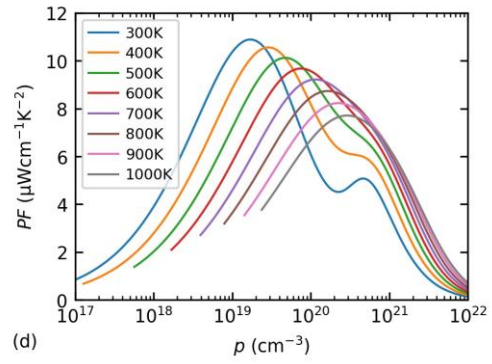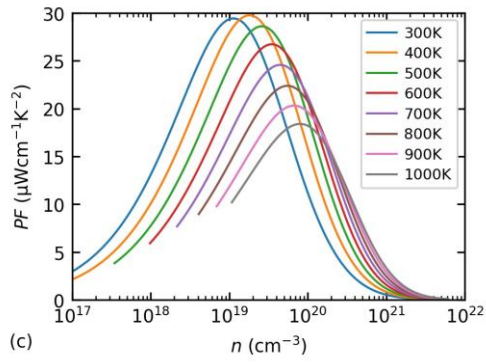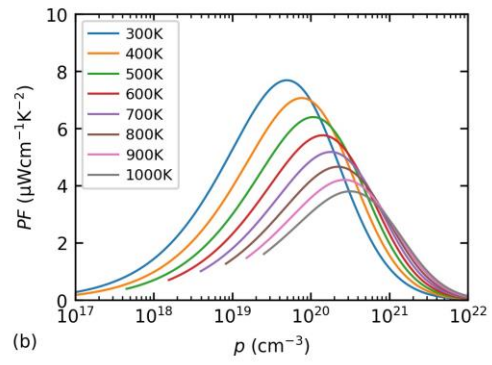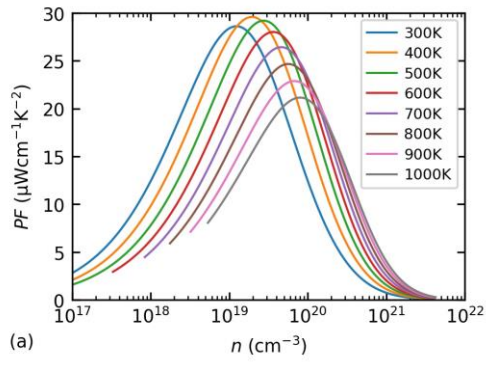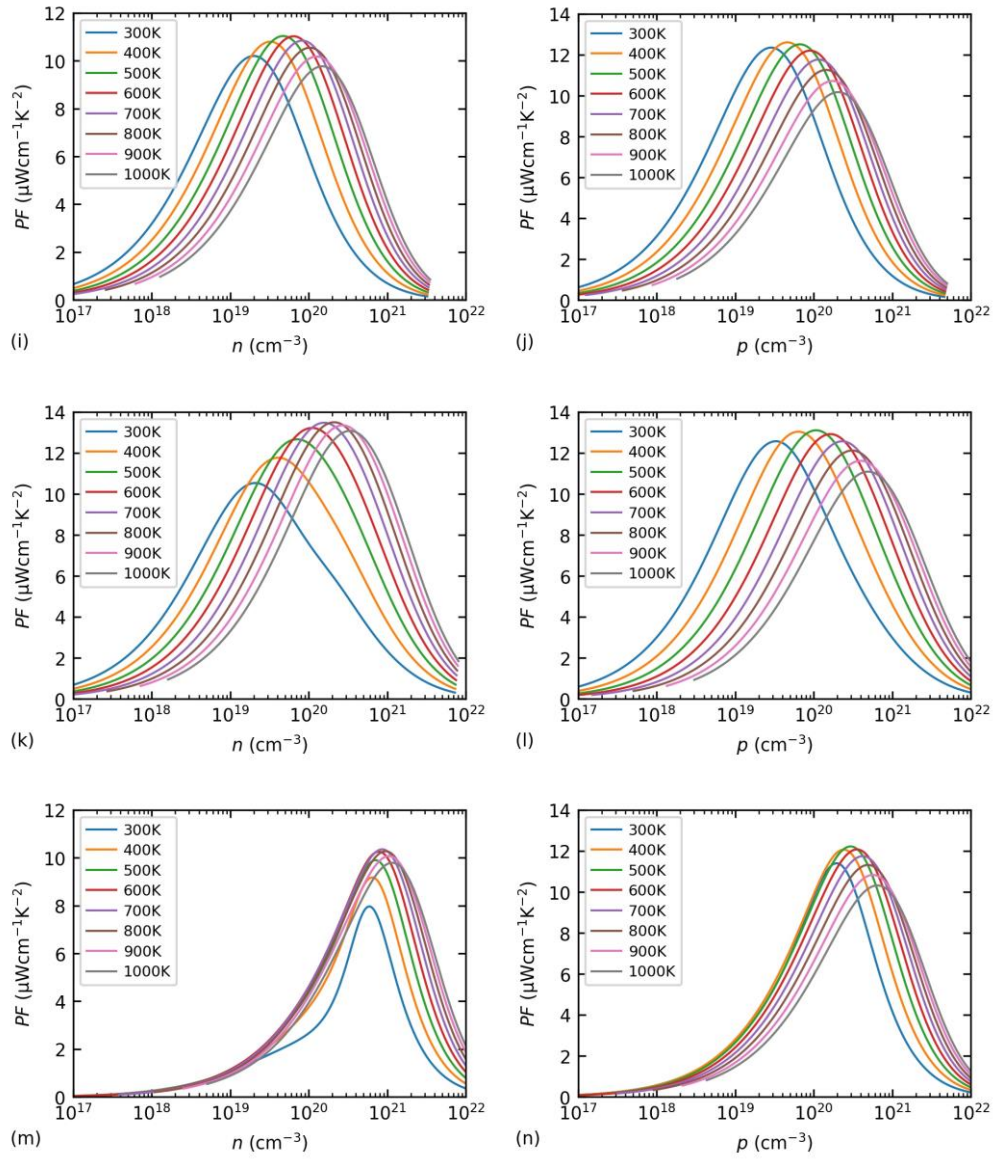
Figure 4.13. Power factor at varying temperatures and carrier concentrations for (a, b) GaAcTe$_2$, (c, d) InAcTe$_2$, (e, f) TlAcTe$_2$, (g, h) NaAcTe$_2$, (i, j) KAcTe$_2$, (k, l) RbAcTe$_2$, and (m, n) CsAcTe$_2$.
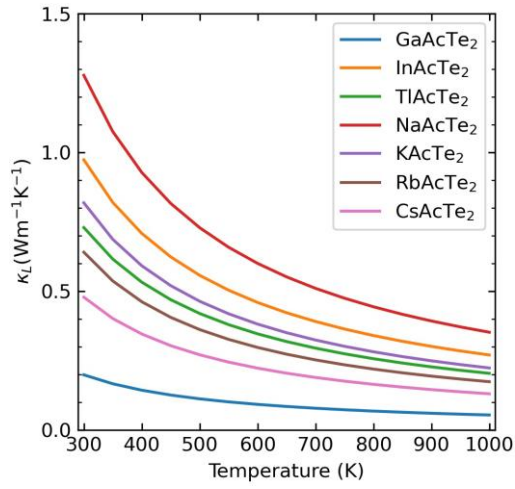
Figure 4.14. Lattice thermal conductivity of MAcTe$_2$ type compounds.

(a)
(b)
(c)
(d)

(e)

(f)

(g)

(h)

(i)

(j)

(k)

(l)

99
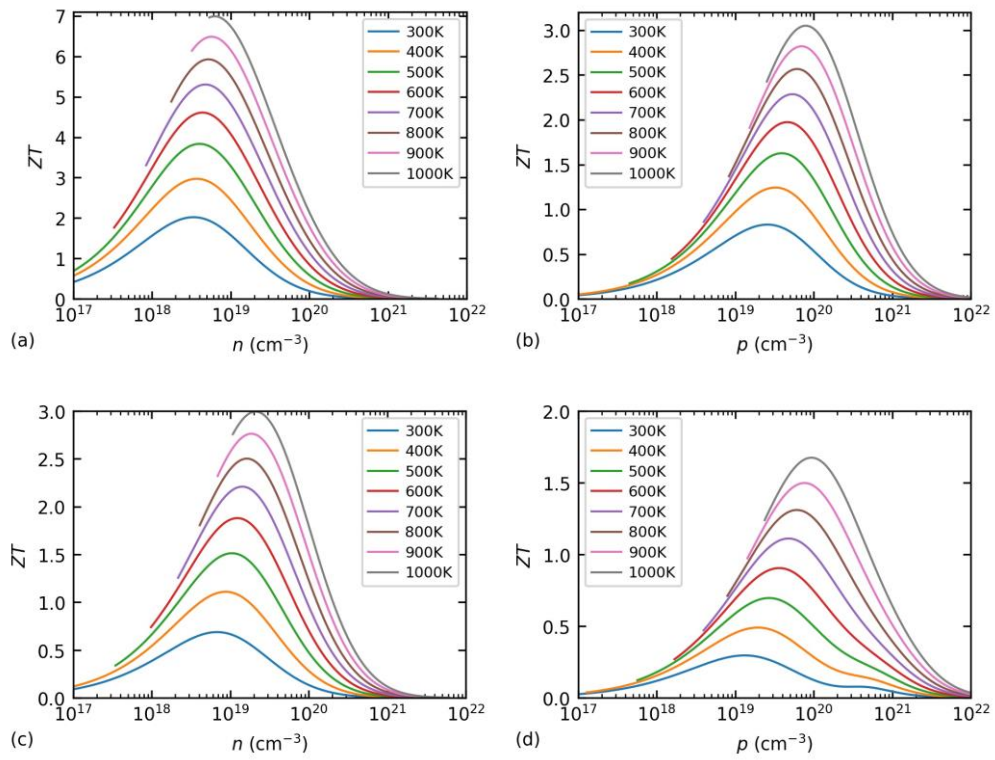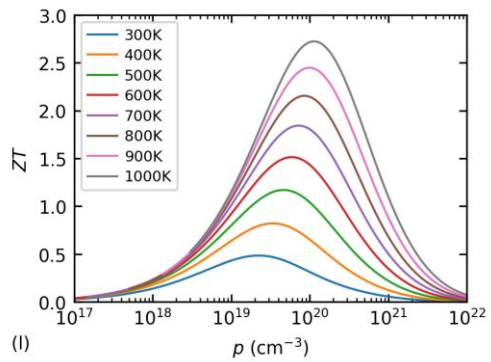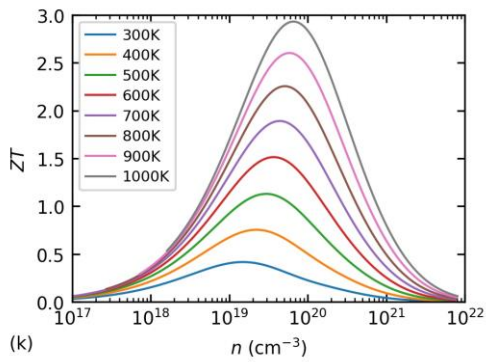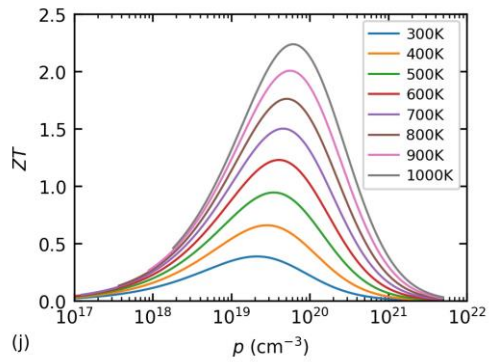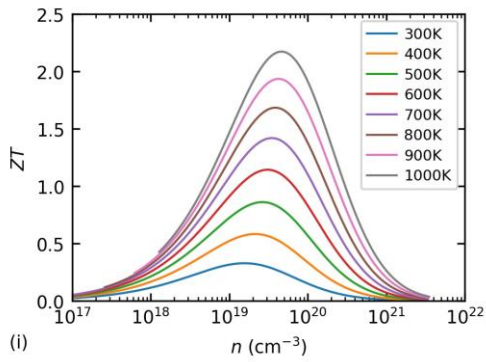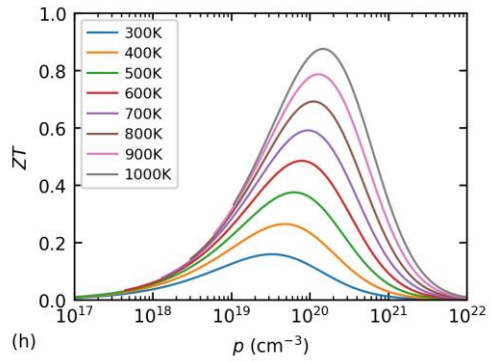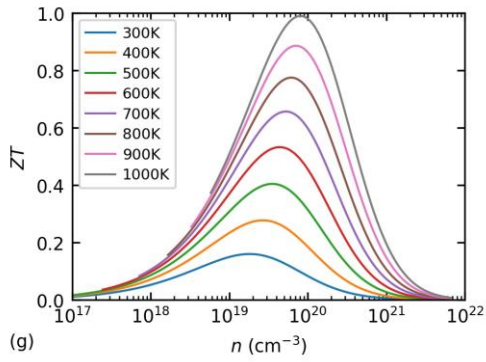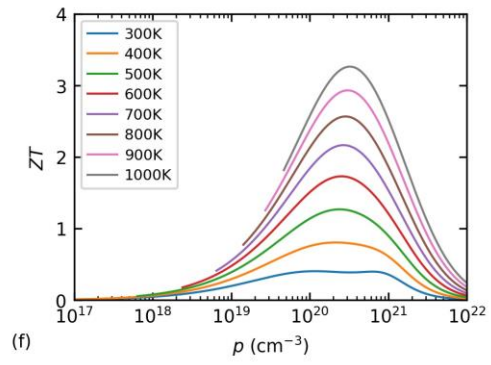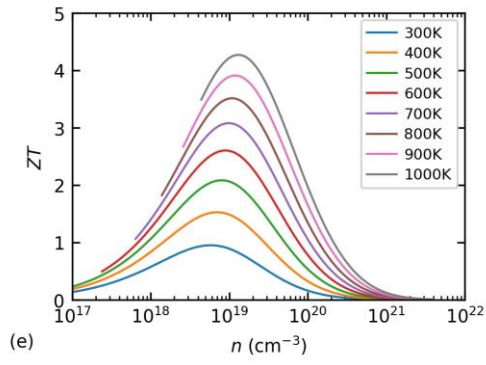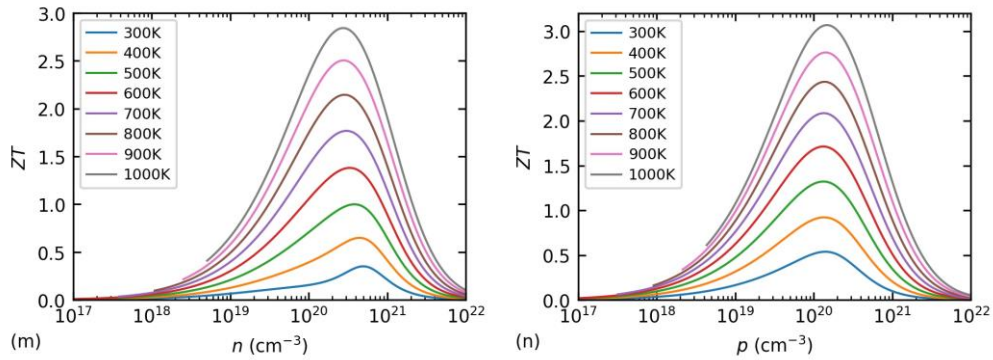
Figure 4.15. Figure of merit at varying temperatures and carrier concentrations for (a, b) GaAcTe$_2$, (c, d) InAcTe$_2$, (e, f) TlAcTe$_2$, (g, h) NaAcTe$_2$, (i, j) KAcTe$_2$, (k, l) RbAcTe$_2$, and (m, n) CsAcTe$_2$.

4.4. X$_2$Y$_4$Z$_8$ (X = II A or II B, Y = III A, Z = VI A)

Compounds with this chemical formula include Hg$_2$Al$_4$Se$_8$, Cd$_2$In$_4$Se$_4$S$_4$, Hg$_2$In$_4$S$_8$, and Mg$_2$In$_4$Se$_8$. They have the same structure, with a space group *Fd*-3*m* (Fig. 4.16). Each atom of group III A forms a distorted octahedron with six atoms of group VI A, whereas each atom of group II A or II B forms a tetrahedron with four atoms of group VI A. The band structures of this group of compounds are shown in Fig. 4.17. The compounds in which X belongs to group II B are indirect gap semiconductors, with the CBMs located at the Γ point, whereas their VBMs are located along the Γ–K path ($N = 12$). Meanwhile, there is a second valence band along the L–U path with the energy very close to the VBM ($N = 24$). Mg$_2$In$_4$Se$_8$ is a direct gap semiconductor with band extrema at the Γ point; it also has a second valence band along the Γ–K path with the energy close to the VBM ($N = 12$). Because the VBMs and second valence bands in these compounds seem quite flat, the mobility of hole is expected to be low. However, high band degeneracy can lead to a large DOS effective mass, therefore, a high value of the Seebeck coefficient is expected.
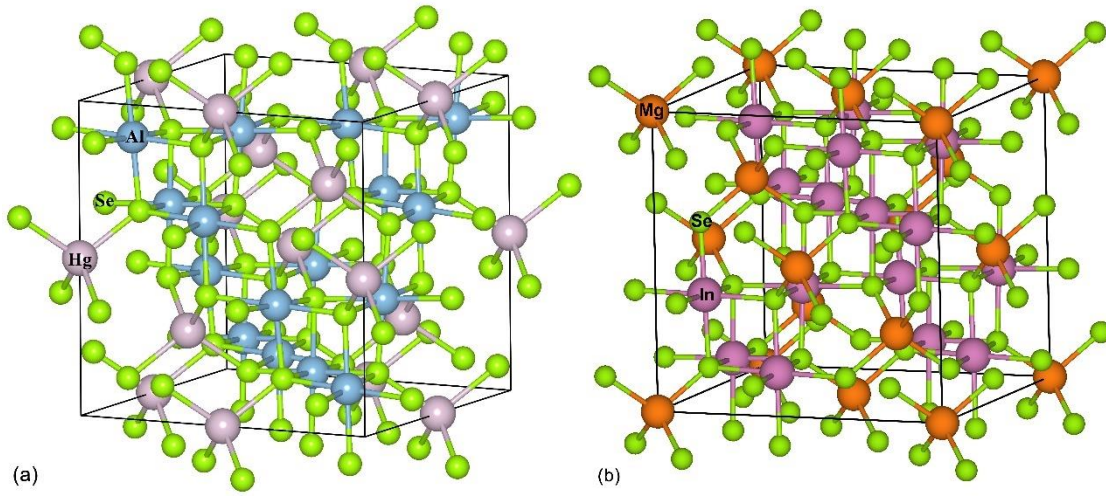
Figure 4.16. Crystal structures of (a) $Hg_2Al_4Se_8$ and (b) $Mg_2In_4Se_8$.
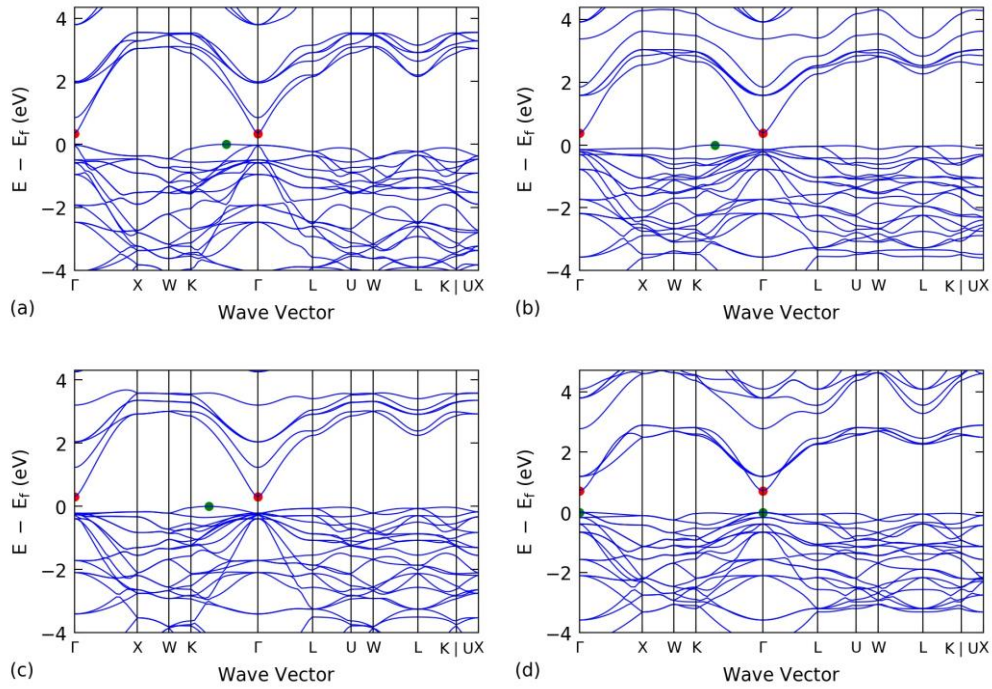
Figure 4.17. Band structures of (a) $Hg_2Al_4Se_8$, (b) $Cd_2In_4Se_4S_4$, (c) $Hg_2In_4S_8$, and (d) $Mg_2In_4Se_8$. The CBM and VBM are shown by red and green dots, respectively.

101

Table 4.4. Key parameters for p-type transport

		m_c^* (m_e)	m_d^* (m_e)	Ξ (eV)	N	E_g (eV)	c (GPa)	ε_∞	ε_0
Hg$_2$Al$_4$Se$_8$	VBM	0.487	4.875	9.48	12	0.34	35.14	14.68	22.89
	VSB	0.581	8.112	9.11	24	0.45			
Cd$_2$In$_4$Se$_4$S$_4$	VBM	1.059	8.512	9.41	12	0.38	27.36	8.98	16.41
	VSB	1.300	11.512	9.34	12	0.40			
Hg$_2$In$_4$S$_8$	VBM	0.882	6.784	10.40	12	0.31	30.29	10.11	21.74
	VSB	0.982	11.979	10.31	24	0.33			
Mg$_2$In$_4$Se$_8$	VBM	5.507	5.507	8.59	1	0.72	26.19	8.02	14.51
	VSB	0.881	8.219	8.65	12	0.74			

Our calculations show that this group of compounds can have high power factor for p-type transport (Fig. 4.18), whereas their lattice thermal conductivity is relatively low (Fig. 4.19). Therefore, the figure of merit can exceed 1 at high temperatures (Fig. 4.20).
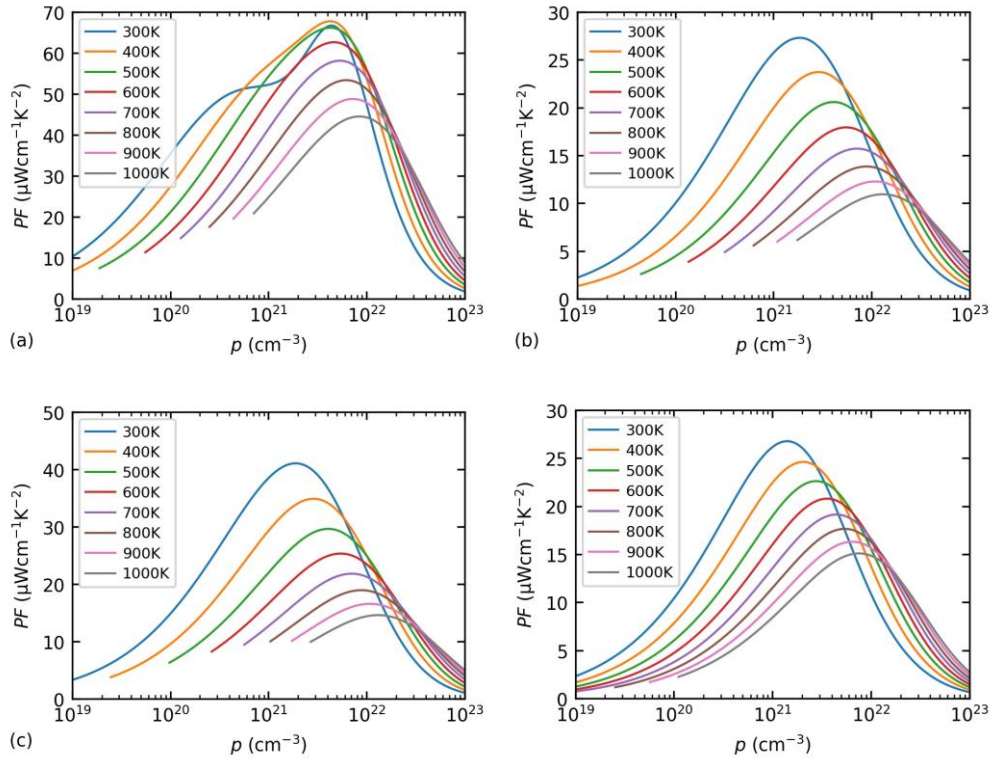
Figure 4.18. Power factor at varying temperatures and carrier concentrations for (a) Hg$_2$Al$_4$Se$_8$, (b) Cd$_2$In$_4$Se$_4$S$_4$, (c) Hg$_2$In$_4$S$_8$, and (d) Mg$_2$In$_4$Se$_8$.
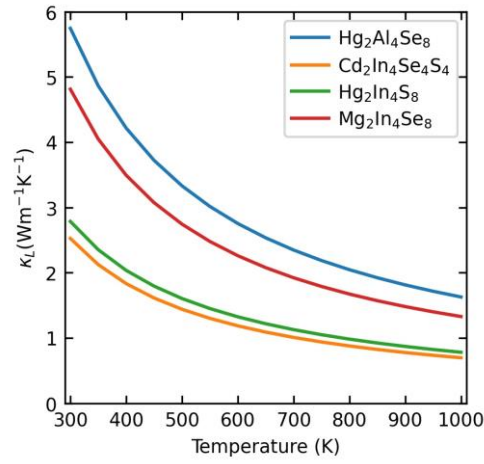
Figure 4.19. Lattice thermal conductivity for this group of compounds.
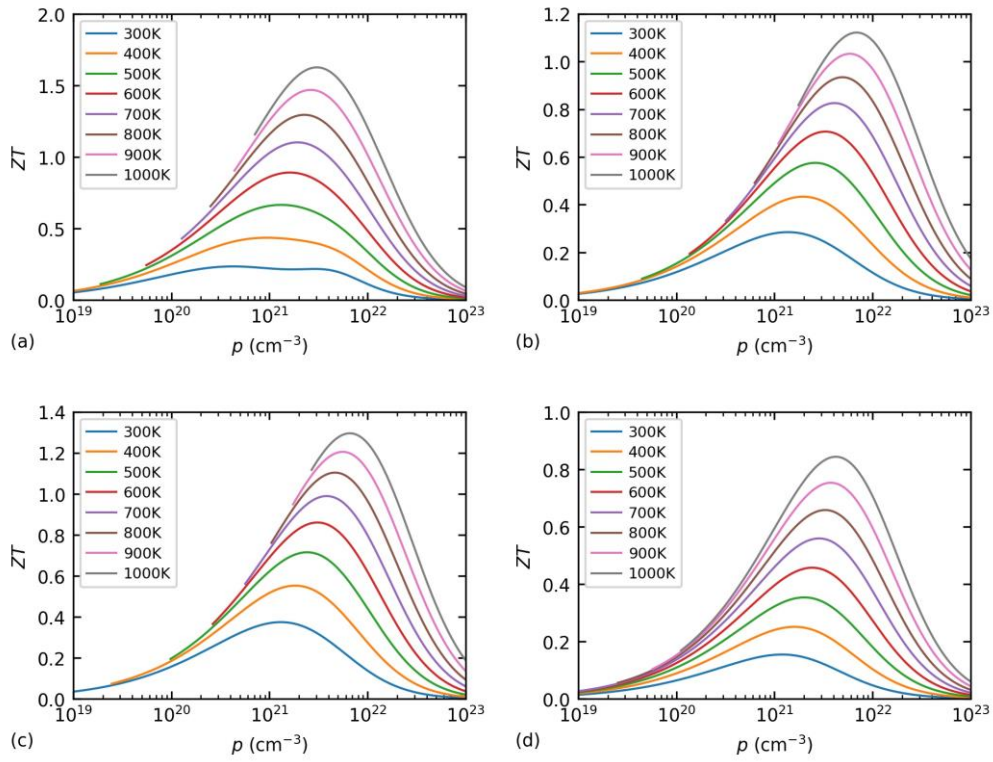
Figure 4.20. Figure of merit at varying temperatures and carrier concentrations for (a) $Hg_2Al_4Se_8$, (b) $Cd_2In_4Se_4S_4$, (c) $Hg_2In_4S_8$, and (d) $Mg_2In_4Se_8$.

4.5. Nb$_6$Sb$_4$Te$_{10}$

This compound has a structure with space group *I*-43*m*, as shown in Fig. 4.21. Each Te atom forms a tetrahedron with three Nb atoms and one Sb atom around it. The band structure (Fig. 4.22) shows that it is an indirect gap semiconductor with the CBM at the P point and the VBM located along the H–N path with high degeneracy $N = 12$. As a results, the DOS effective mass at the VBM is large (Table 4.5).
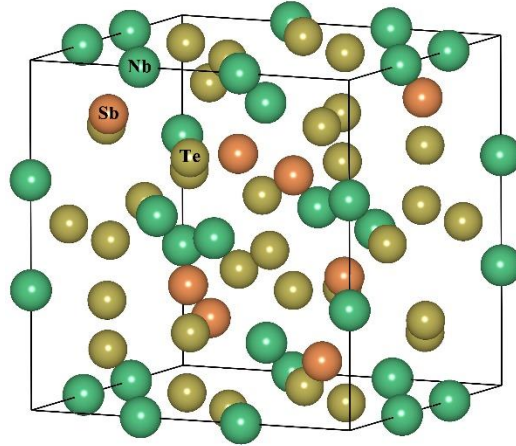
Figure 4.21. Crystal structure of Nb$_6$Sb$_4$Te$_{10}$.
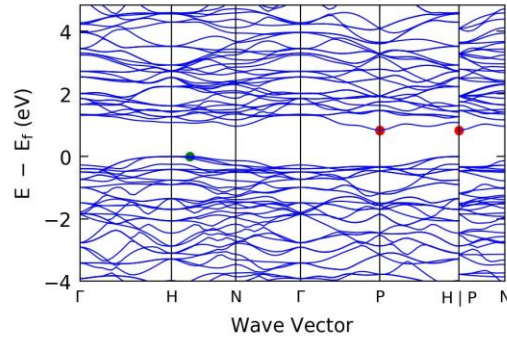
Figure 4.22. Band structure of Nb$_6$Sb$_4$Te$_{10}$.

Table 4.5. Key parameters for p-type transport

	m_c^* (m_e)	m_d^* (m_e)	Ξ (eV)	N	E_g (eV)	c (GPa)	ε_∞	ε_0
Nb$_6$Sb$_4$Te$_{10}$	0.879	5.434	13.60	12	0.84	89.39	23.92	27.24

The calculations show that this compound is a good p-type thermoelectric material. The thermoelectric properties of this compound for p-type transport are shown in Fig. 4.23. Because of its large power factor and relatively low lattice thermal conductivity, the maximum *ZT* value can exceed 1 at high temperature.
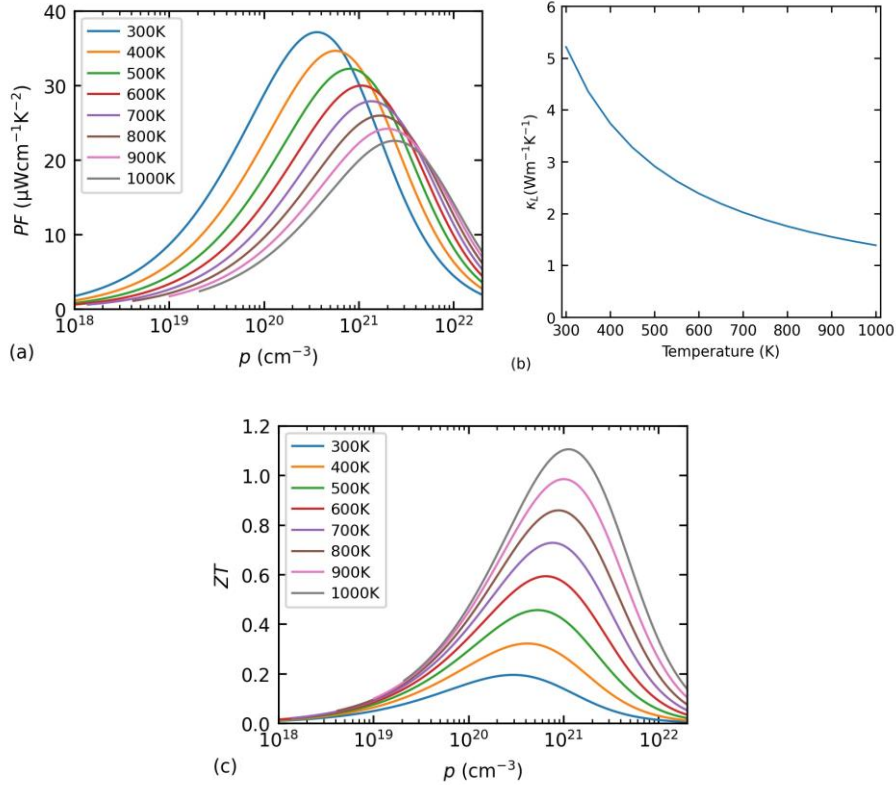
Figure 4.23. Thermoelectric properties of $Nb_6Sb_4Te_{10}$ for p-type transport. (a) power factor, (b) lattice thermal conductivity, and (c) figure of merit.

4.6. MgTe

This compound has a rocksalt structure with space group *Fm-3m*, same as PbTe (Fig. 4.24). Its band structure (Fig. 4.25) shows that it is an indirect gap semiconductor. The CBM, located at X point ($N = 3$), is dispersive, therefore m_c^* is small. The VBM is along Γ–K path ($N = 12$) and is flat, resulting in large m_d^*. Our calculation show that this compound has a high power factor for both n- and p-type transport, especially for p-type (Fig. 4.26). The maximum figure of merit for p-type transport can exceed 1 at high temperatures.
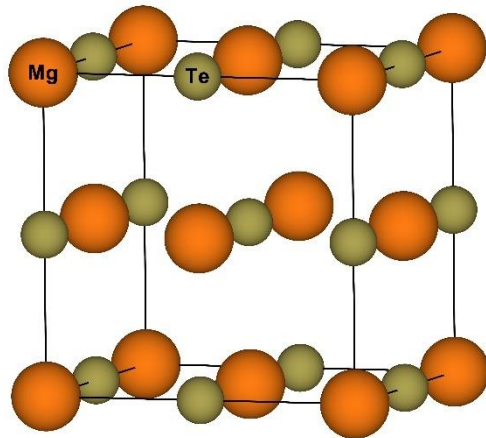
Figure 4.24. Crystal structure of MgTe.
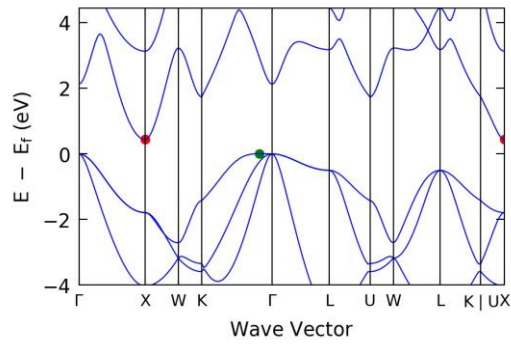
Figure 4.25. Band structure of MgTe.

Table 4.6. Key parameters for n-type and p-type transport

		m_c^* (m_e)	m_d^* (m_e)	Ξ (eV)	N	E_g (eV)	c (GPa)	ε_∞	ε_0
MgTe	CBM	0.210	0.481	10.13	3	0.43	38.58	8.92	25.25
	VBM	0.443	5.220	9.54	12				

106
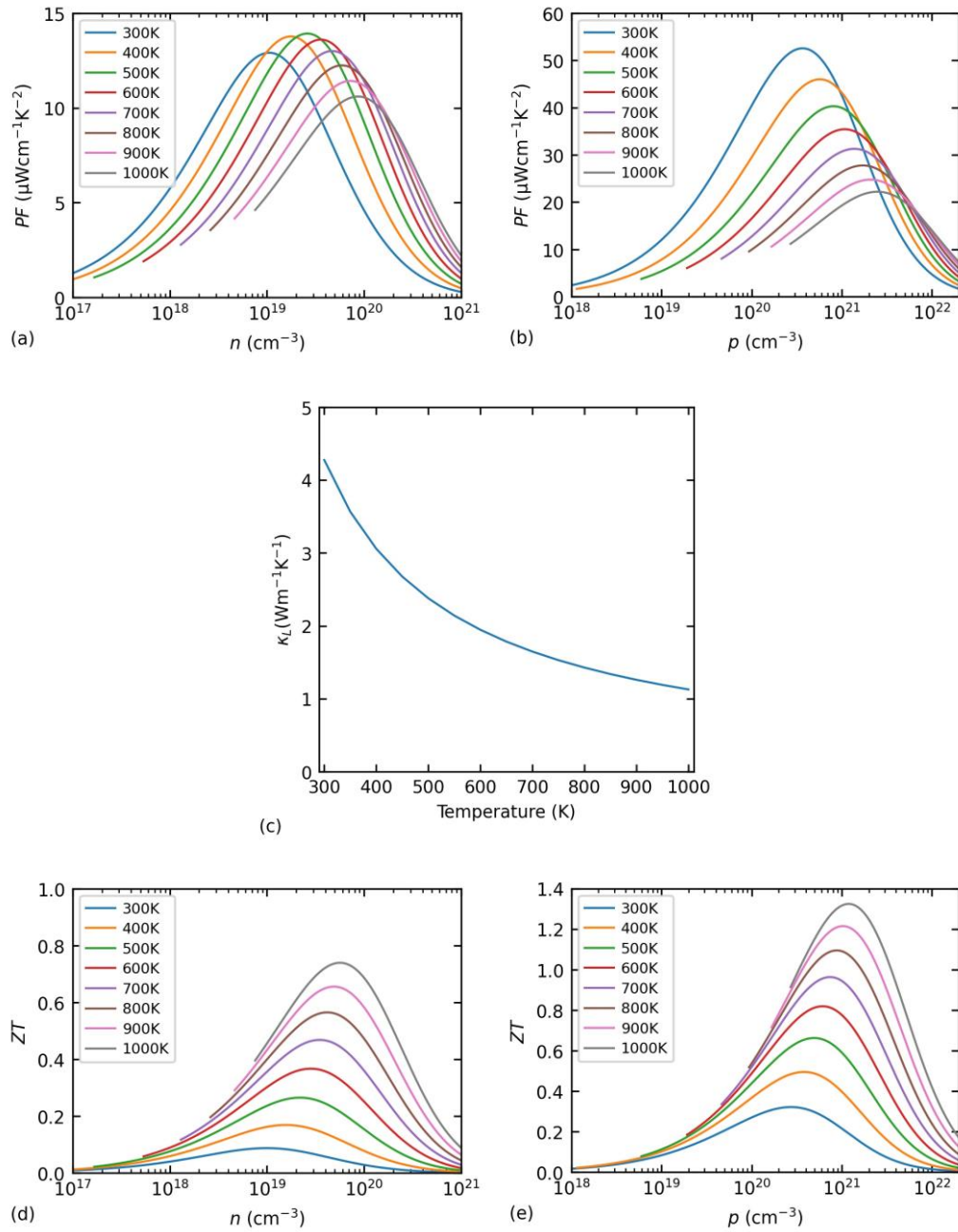
Figure 4.26. Thermoelectric properties of MgTe for n-type and p-type transport. (a, b) power factor, (c) lattice thermal conductivity, and (d, e) figure of merit.

4.7. Dy$_8$P$_8$S$_8$

This compound adopts a layered orthorhombic structure with a space group *Pnma* (Fig. 4.27). There are two-atom-thick DyS slabs (along the *a-b* plane) with strong Dy–S bonding within the plane of the slabs. Each Dy (or S) atom is bonded to five neighboring S (or Dy) atoms in a distorted zig-zag-type structure. The P atoms form zigzag chain along the *a* axis direction within the *a-b* plane. The bond length of P-P atoms is about 2.23 Å, prerequisite of a single P-P bond. Therefore, one of the structural units is the $_1(P^{-1})$ chain anion, and the compound can be rationalized as $Dy^{3+}P^{-1}S^{-2}$. The band structure shows that it is an indirect gap semiconductor with the CBM at the Y point ($N = 1$) and VBM at the T point ($N = 1$). It has a second valence band along the Y–Γ path with the energy very close to the VBM ($N = 2$). our calculations show that this compound is a promising thermoelectric material for both n- and p-type transport. Although its power factor values are not very high, the lattice thermal conductivity is quite low (Fig. 4.29). Therefore, the figure of merit for both n-type and p-type transport could be above 1.
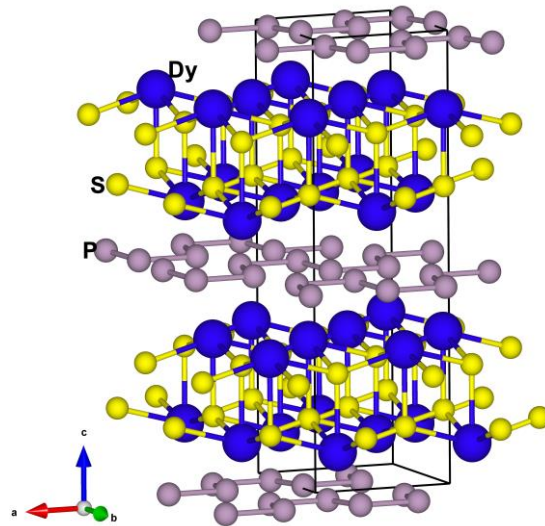
Figure 4.27. Crystal structure of Dy$_8$P$_8$S$_8$.
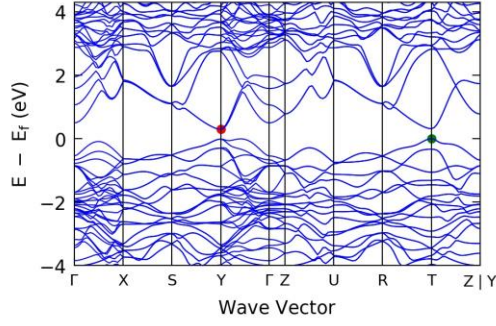
Figure 4.28. Band structure of Dy$_8$P$_8$S$_8$.

Table 4.7. Key parameters for n-type and p-type transport

		m_c^* (m_e)	m_d^* (m_e)	Ξ (eV)	N	E_g (eV)	c (GPa)	ε_∞	ε_0
	CBM	0.471	0.696	4.49	1				
Dy$_8$P$_8$S$_8$	VBM	0.365	0.678	8.43	1	0.30	72.87	13.67	24.00
	VSB	0.738	1.184	6.69	2				

(a)

(b)

(c)

109
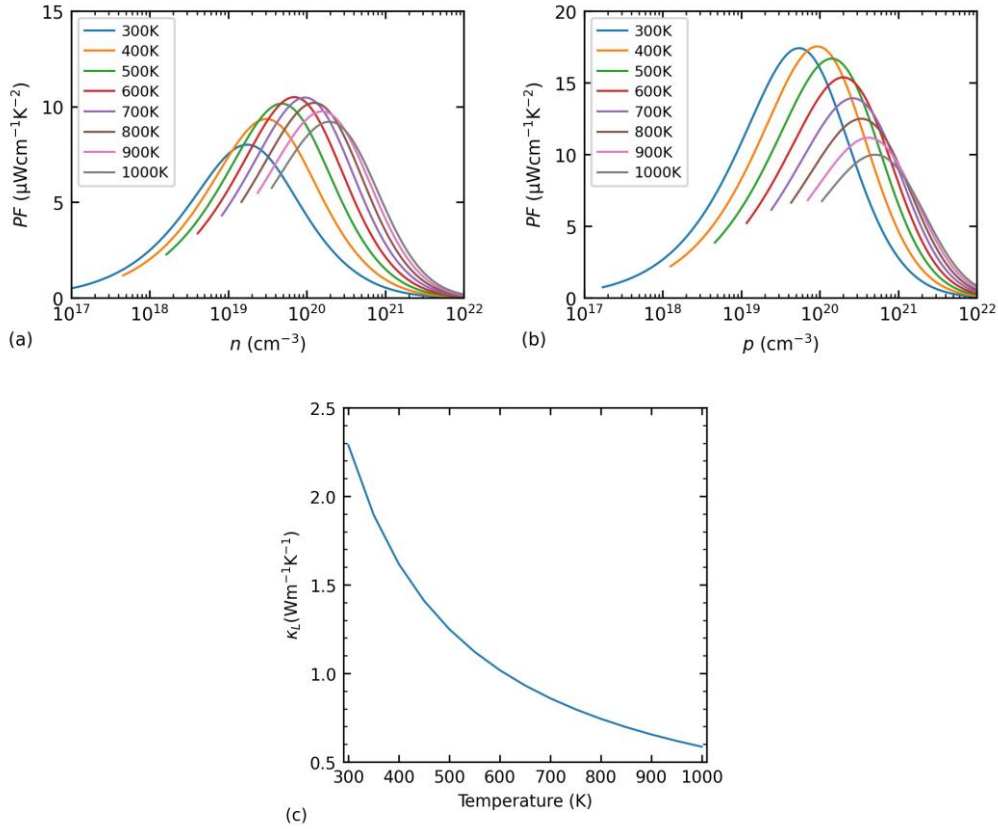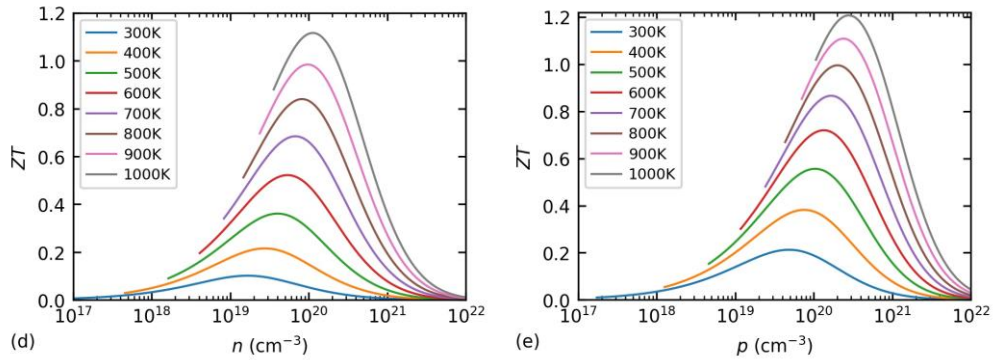
Figure 4.29. Thermoelectric properties of $Dy_8P_8S_8$ for n-type and p-type transport. (a, b) power factor, (c) lattice thermal conductivity, and (d, e) figure of merit.

4.8. SnSe-like compounds

SnSe is a well-known thermoelectric material and has been deeply studied. It is natural to think that compounds composed of nearby elements in the periodic table and having similar crystal structure should also have good thermoelectric performance. Our calculation did find such compounds. Compounds having the similar crystal structure as the low temperature α-phase SnSe (space group Pnma) include $Sn_2Ge_2Se_4$, $Ge_4Se_2S_2$, Ge_4Se_4, $Sn_2Pb_2S_4$, Ge_4Te_4. The structures of these compounds are shown in Fig. 4.30. The unit cell contains eight atoms (four atoms of group IVA and four of group VIA). The atoms of groups IVA and VIA are connected with strong heteropolar bonds to form the crystalline layers. In each layer, an atom of group IVA (or VIA) is bonded to three neighboring atoms of group VIA (or IVA) in a distorted zig-zag structure. The adjacent layers along the c-axis are weakly bonded by a combination of the van der Waals forces and electrostatic attractions. The band structures of these compounds (Fig. 4.31) show multiple band valleys in both the conduction band and valence band near the band gap, suggesting a potential to improve the power factor. Their CBMs can be located along several different high-symmetry paths. However, the degeneracy of the CBM point is always equal to 2. Their VBMs are usually along the Γ–Y line. Our calculations show that these compounds are better to be n-type thermoelectric materials than p-type. However, Ge_4Te_4 is both a good n-type and p-type material. Their figure of merit values can exceed 1 in a wide range of

temperatures and carrier concentrations, as shown in Fig. 4. 34. Although the power factor is not as high as in the cubic materials introduced above (Fig. 4.32), these compounds have extremely low lattice thermal conductivity (Fig. 4.33). Except Ge_4Te_4, the lattice thermal conductivity of these compounds at 300 K is already lower than 0.5 $W \cdot m^{-1} \cdot K^{-1}$, close to the amorphous limit. Such a low lattice thermal conductivity is mainly due to their large Grüneisen coefficients within three acoustic phonon branches (Table 4.9), which indicates strong intrinsic anharmonicity.
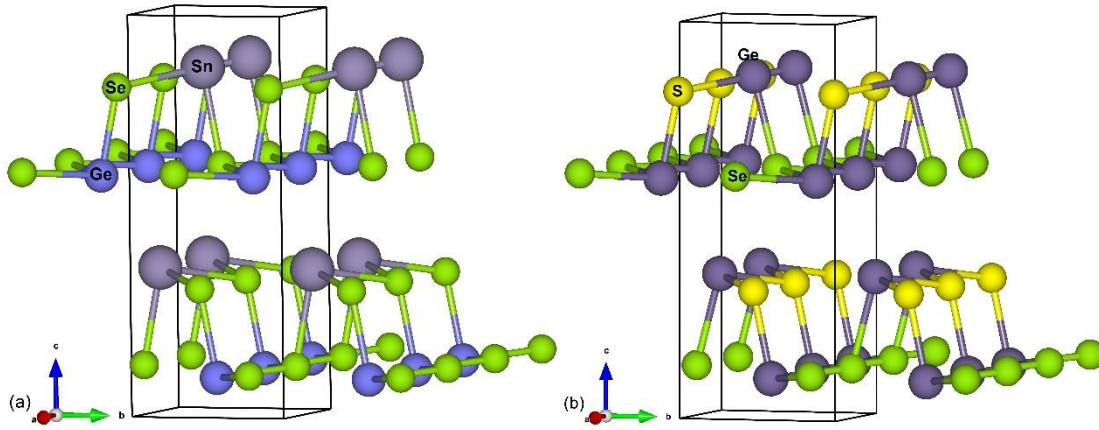
Figure 4.30. Crystal structures of (a) $Sn_2Ge_2Se_4$ and (b) $Ge_4Se_2S_2$.
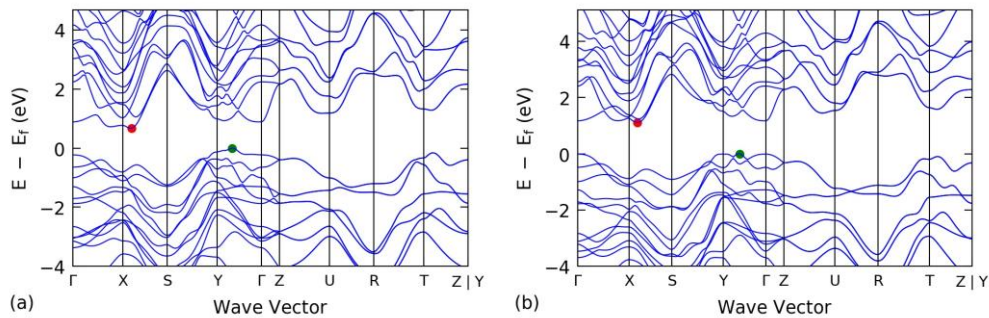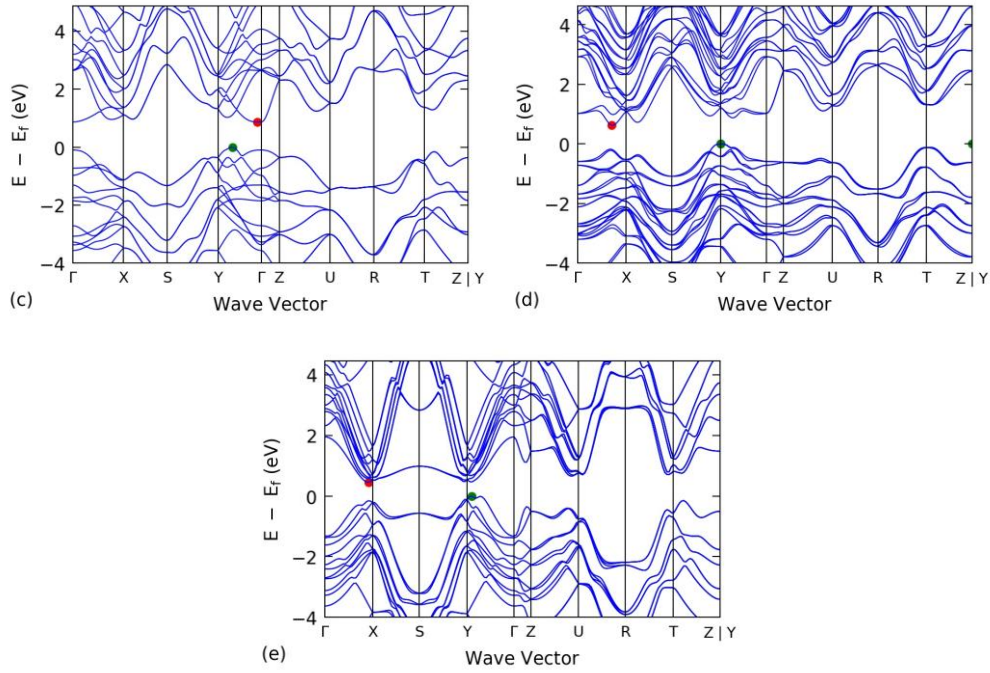
Figure 4.31. Band structures of (a) $Sn_2Ge_2Se_4$, (b) $Ge_4Se_2S_2$, (c) Ge_4Se_4, (d) $Sn_2Pb_2S_4$, and (e) Ge_4Te_4.

Table 4.8. Key parameters for this group of compounds

		m_c^* (m_e)	m_d^* (m_e)	Ξ (eV)	N	E_g (eV)	c (GPa)	ε_∞	ε_0
$Sn_2Ge_2Se_4$	CBM	0.259	0.432	9.05	2	0.67	17.96	16.33	31.44
	CSB	0.379	0.633	8.25	2	0.72			
$Ge_4Se_2S_2$	CBM	0.331	0.575	9.26	2	1.12	19.84	13.09	21.90
	CSB	0.278	0.961	7.40	1	1.17			
Ge_4Se_4	CBM	0.258	1.237	7.18	2	0.87	17.62	14.69	22.67
$Sn_2Pb_2S_4$	CBM	0.200	0.327	8.20	2	0.63	20.82	12.91	36.36
	CSB	0.233	0.396	8.75	2	0.72			
Ge_4Te_4	CBM	0.134	0.229	7.99	2	0.45	31.06	50.20	619.44
	VBM	0.086	0.215	11.64	2				
	CSB	0.168	0.291	7.81	2	0.46			

112
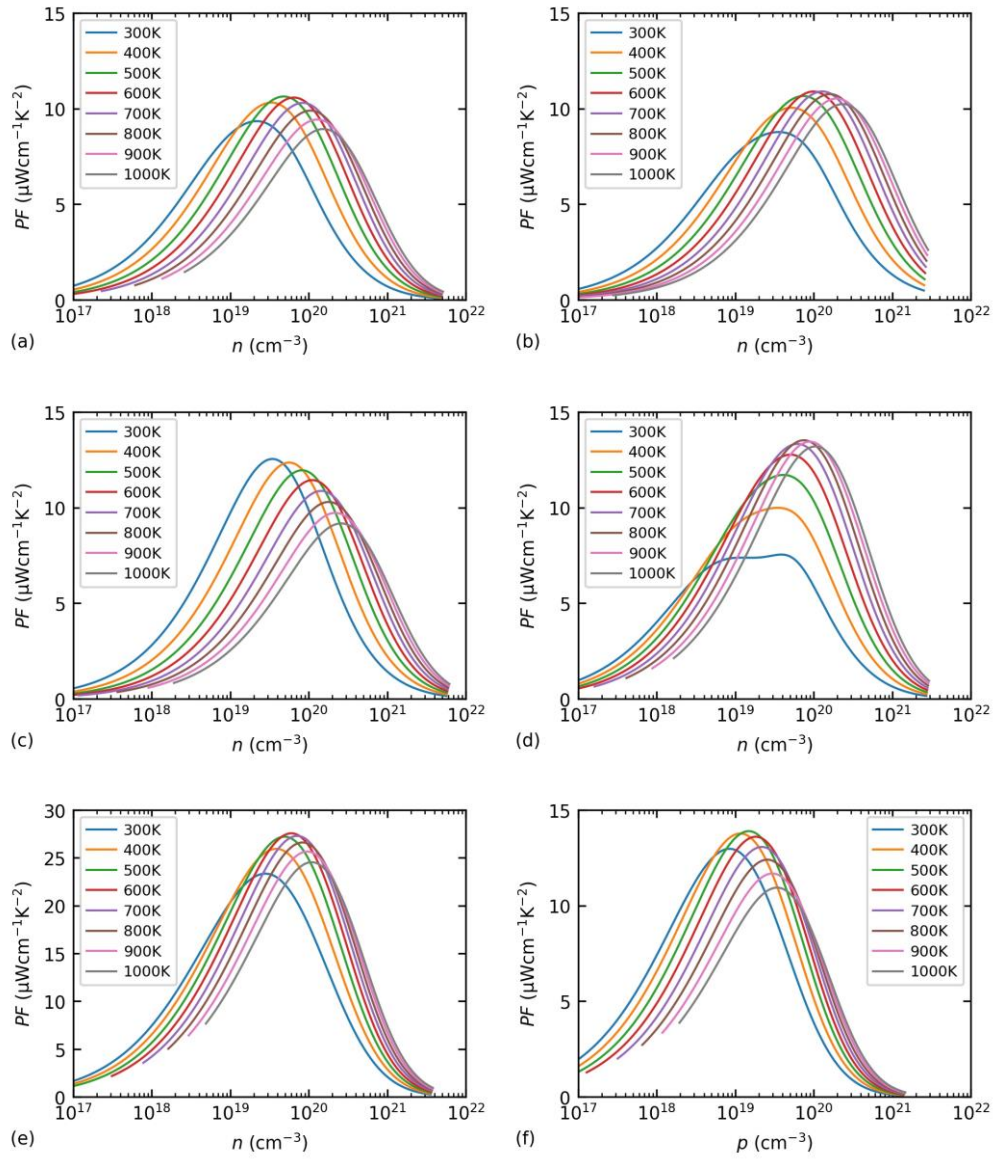
Figure 4.32. Power factor at varying temperatures and carrier concentrations for (a) $Sn_2Ge_2Se_4$, (b) $Ge_4Se_2S_2$, (c) Ge_4Se_4, (d) $Sn_2Pb_2S_4$, and (e, f) Ge_4Te_4.
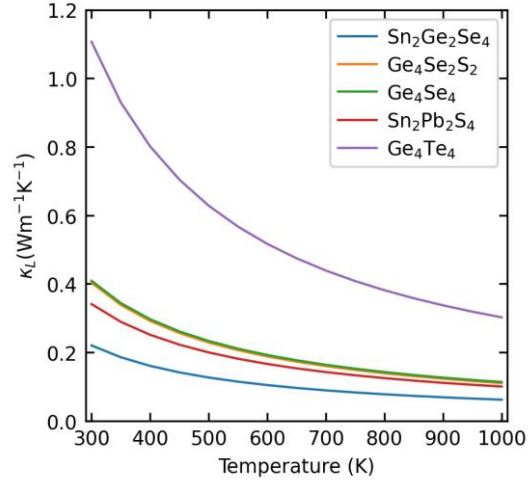
Figure 4.33. Lattice thermal conductivity of this group of compounds.

Table 4.9. Phonon properties of three acoustic branches for this group of compounds. v is the phonon velocity, γ is the Grüneisen parameter

	v_{TA}	$v_{TA'}$	v_{LA}	γ_{TA}	$\gamma_{TA'}$	γ_{LA}
$Sn_2Ge_2Se_4$	1552.21	2333.82	3085.96	5.23	3.97	3.75
$Ge_4Se_2S_2$	2478.90	2024.00	3231.27	5.17	3.39	3.01
Ge_4Se_4	3618.81	1646.25	3019.41	5.08	4.01	2.48
$Sn_2Pb_2S_4$	1453.16	2057.29	2863.01	4.66	2.87	2.76
Ge_4Te_4	1718.25	2694.27	3481.99	3.64	2.78	2.39

(a)

(b)
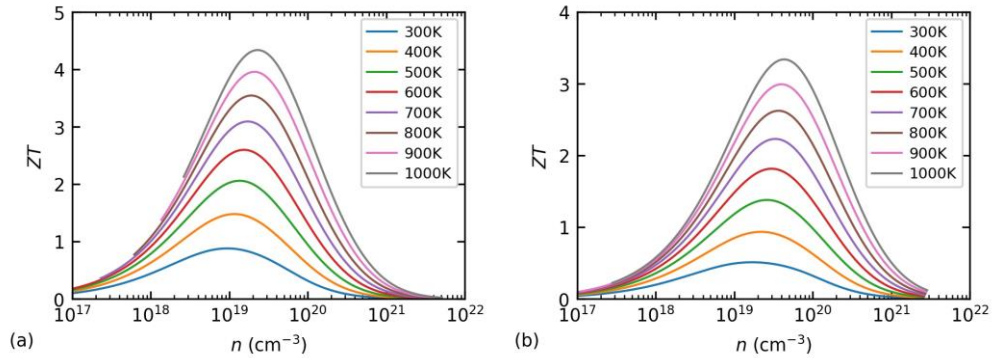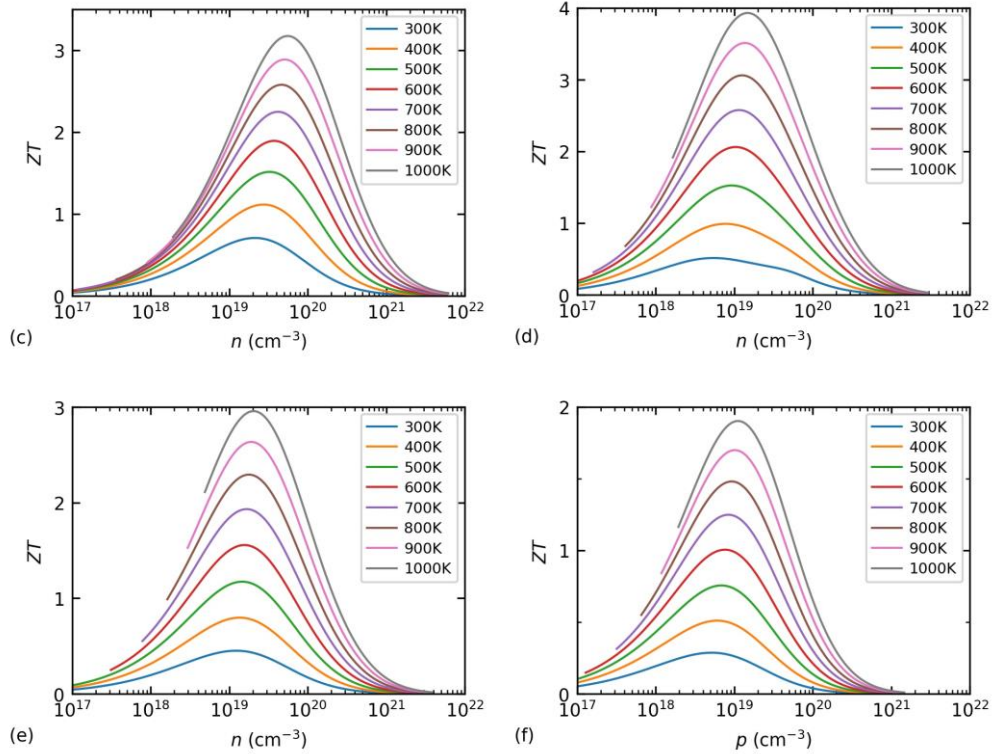
Figure 4.34. Figure of merit at varying temperatures and carrier concentrations for (a) $Sn_2Ge_2Se_4$, (b) $Ge_4Se_2S_2$, (c) Ge_4Se_4, (d) $Sn_2Pb_2S_4$, and (e, f) Ge_4Te_4.

Besides the compounds having the similar structure as α-phase SnSe, we also found compounds having the similar crystal structure as high temperature β-phase SnSe (space group *Cmcm*). These compounds include Pb_4Se_4, Pb_4S_4 and their structures are shown in Fig. 4.35. The unit cell also contains eight atoms (four atoms of group IVA, and four of group VIA) and adopts a double-layered structure. However, different from the α-phase structure, within each layer of the β-phase, one atom of group IVA (or VIA) is instead bonded to five neighboring atoms of group VIA (or IVA) in a less distorted structure. The band structures of these compounds (Fig. 4.36) show that they are direct gap semiconductors with the band extrema along the T–Y path ($N = 2$). Similar to the α-phase structure, there are multiple band valleys in both conduction and valence bands near the band gap. Our calculations show that these compounds are excellent n-type and p-type thermoelectric materials, their figure of merit could be higher than 1 in a wide range of

temperatures and carrier concentrations. This is mainly due to their high power factor and relatively low lattice thermal conductivity.
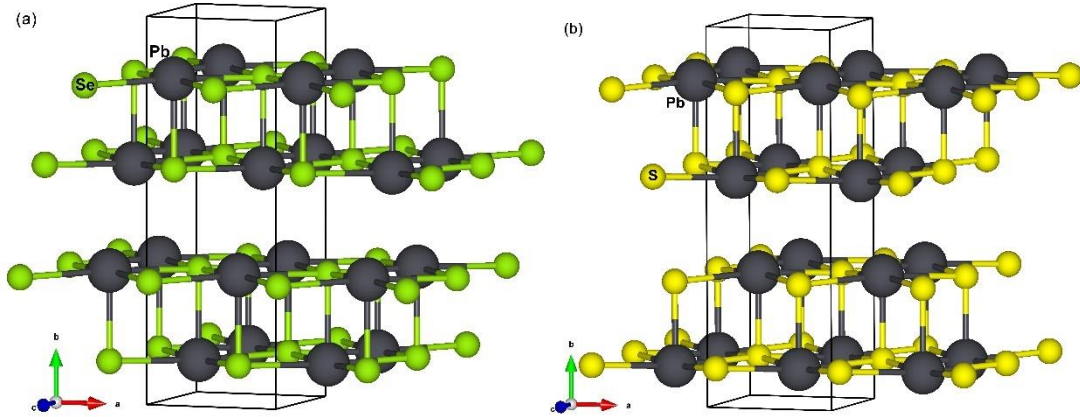
Figure 4.35. Crystal structures of (a) Pb_4Se_4 and (b) Pb_4S_4.
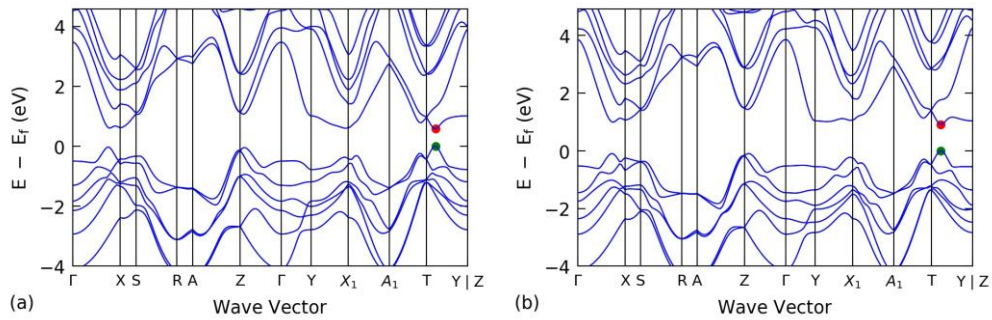
Figure 4.36. Band structures of (a) Pb_4Se_4 and (b) Pb_4S_4.

Table 4.10. Key parameters for n-type and p-type transport

		m_c^* (m_e)	m_d^* (m_e)	Ξ (eV)	N	E_g (eV)	c (GPa)	ε_∞	ε_0
	CBM	0.140	0.245	9.97	2	0.58			
Pb_4Se_4	VBM	0.152	0.399	22.84	2		76.49	16.62	465.99
	CSB	0.232	0.432	6.19	2	0.60			
	VSB	0.161	0.371	9.89	2	0.61			
	CBM	0.186	0.323	8.60	2	0.92			
Pb_4S_4	VBM	0.211	0.535	10.23	2		139.12	12.60	1187.3
	CSB	0.187	0.316	8.52	2	0.99			
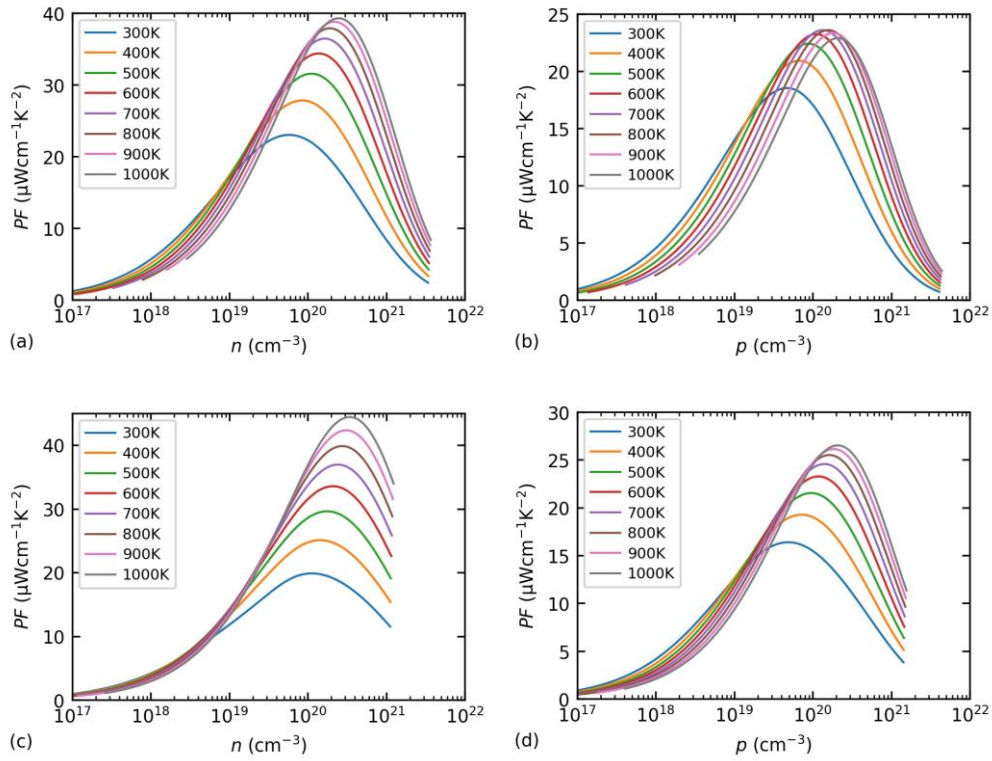
Figure 4.37. Power factor at varying temperatures and carrier concentrations for (a, b) Pb_4Se_4 and (c, d) Pb_4S_4.
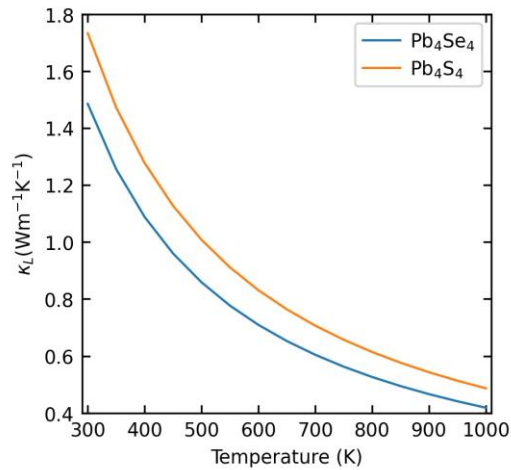
Figure 4.38. Lattice thermal conductivity of this group of compounds.

Table 4.11. Phonon properties of three acoustic branches for this group of compounds

	v_{TA}	$v_{TA'}$	v_{LA}	γ_{TA}	$\gamma_{TA'}$	γ_{LA}
Pb_4Se_4	1045.73	1986.53	2537.70	4.85	2.26	1.34
Pb_4S_4	896.77	1909.94	2736.21	6.89	2.91	1.79
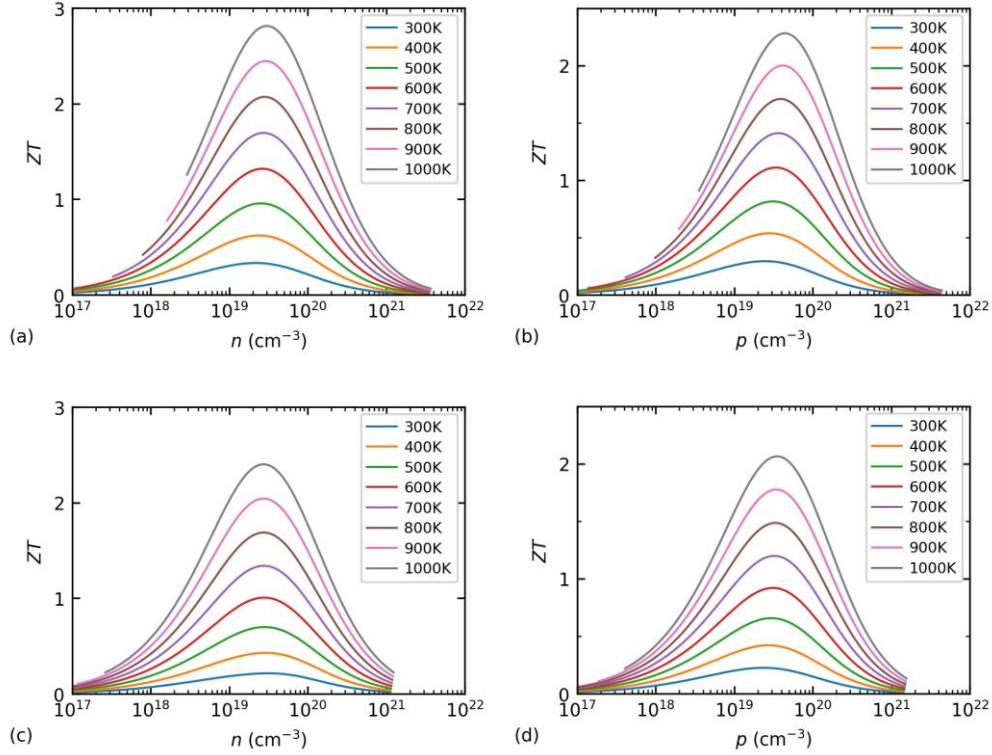
Figure 4.39. Figure of merit at varying temperatures and carrier concentrations for (a, b) Pb_4Se_4 and (c, d) Pb_4S_4.

4.9. $Cu_4Sb_4Se_8$ and $Ba_4Cu_8Te_8$

These two compounds have a similar orthorhombic structure with a space group *Pnma* (Fig. 4.40). In $Cu_4Sb_4Se_8$, the Cu and the Sb atoms connect with each other through the Se atoms. If viewing the structure along the *a* axis, these atoms form distorted rings and the hollow extends along the *a* axis. In $Ba_4Cu_8Te_8$, the Cu atom connects with four nearest neighboring Te atoms in a tetrahedral coordination. Again, if viewing the structure along the *a* axis, the Cu and Te atoms form distorted rings and the hollow extends along the *a* axis. The difference for $Ba_4Cu_8Te_8$ is, the Ba atoms are distributed inside the hollow space.

This structure is beneficial for impeding the transport of phonons, and therefore is expected to have lower lattice thermal conductivity compared with $Cu_4Sb_4Se_8$. The band structures of these compounds are shown in Fig. 4.41. For $Cu_4Sb_4Se_8$, the CBM is located along the R–T path ($N = 2$) and there are multiple valleys in the conduction band. For $Ba_4Cu_8Te_8$, the CBM is located along Γ–Z path ($N = 2$) and there is a second conduction band along the Γ–Y path with almost the same energy as the CBM ($N = 2$). Our calculations show that these two compounds are promising n-type thermoelectric materials. Their power factor values are similar, with the maximum values just above 10 μW·cm^{-1}·K^{-2} (Fig. 4.42). There is a significant difference in the lattice thermal conductivity κ_L, whose value for $Ba_4Cu_8Te_8$ is almost one fifth that of $Cu_4Sb_4Se_8$ (Fig. 4.43). In $Ba_4Cu_8Te_8$, the phonon velocities are lower than those in $Cu_4Sb_4Se_8$, and the Grüneisen parameters of two acoustic branches in $Ba_4Cu_8Te_8$ are two times larger than those in $Cu_4Sb_4Se_8$ (Table 4.13). Therefore, the structure of $Ba_4Cu_8Te_8$ has stronger anharmonicity, indicating Ba atoms as efficient scattering centers. The figure of merit *ZT* of $Ba_4Cu_8Te_8$ is almost three times larger than that of $Cu_4Sb_4Se_8$ (Fig. 4.44), which is mainly due to its much lower lattice thermal conductivity.
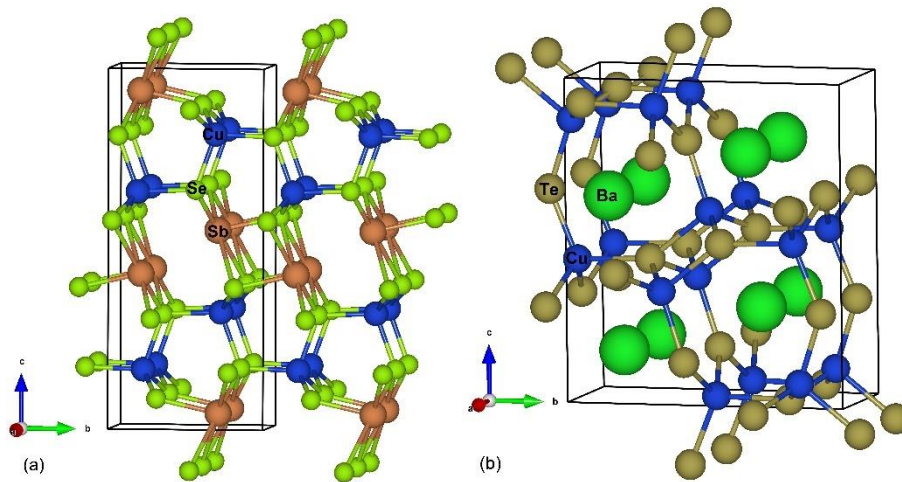
Figure 4.40. Crystal structures of (a) $Cu_4Sb_4Se_8$ and (b) $Ba_4Cu_8Te_8$.
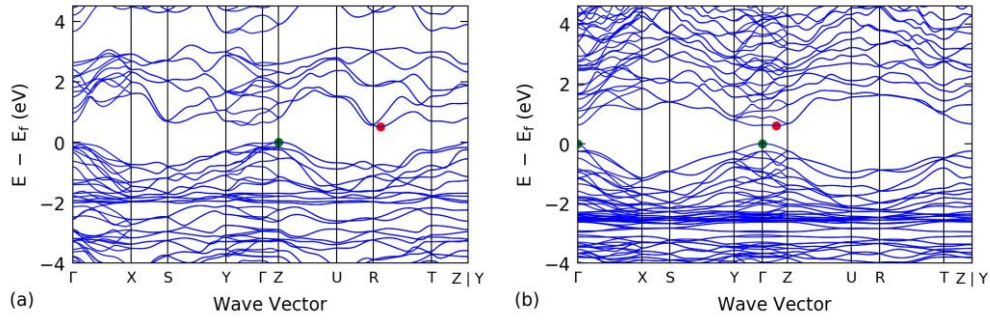
Figure 4.41. Band structures of (a) $Cu_4Sb_4Se_8$ and (b) $Ba_4Cu_8Te_8$.

Table 4.12. Key parameters for n-type transport

		m_c^* (m_e)	m_d^* (m_e)	Ξ (eV)	N	E_g (eV)	c (GPa)	ε_∞	ε_0
$Cu_4Sb_4Se_8$	CBM	0.463	0.749	7.76	2	0.51	32.27	19.60	37.15
	CSB	0.329	0.587	10.43	2	0.55			
$Ba_4Cu_8Te_8$	CBM	0.432	0.930	7.91	2	0.60	19.97	12.47	20.00
	CSB	0.336	0.602	8.30	2	0.60			
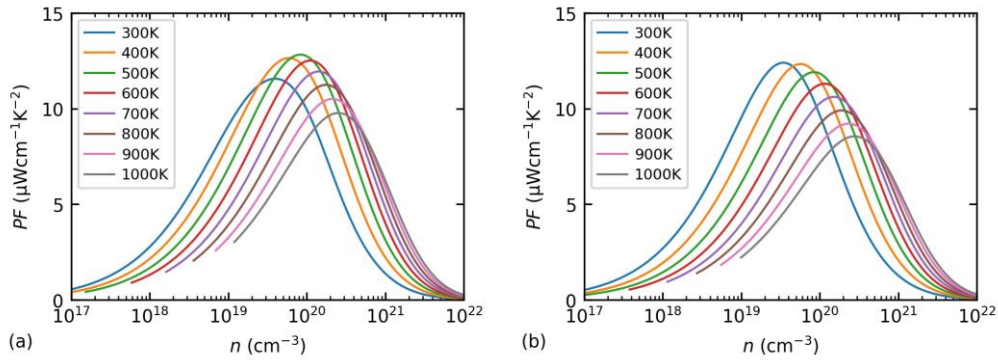
Figure 4.42. Power factor at varying temperatures and carrier concentrations for (a) $Cu_4Sb_4Se_8$ and (b) $Ba_4Cu_8Te_8$.
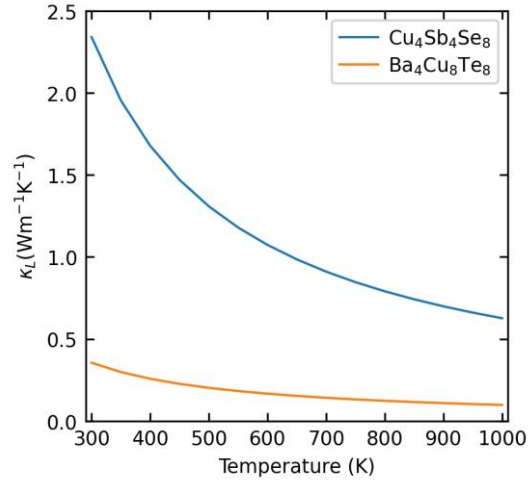
Figure 4.43. Lattice thermal conductivity of this group of compounds.

Table 4.13. Phonon properties of three acoustic branches for this group of compounds

	v_{TA}	$v_{TA'}$	v_{LA}	γ_{TA}	$\gamma_{TA'}$	γ_{LA}
$Cu_4Sb_4Se_8$	1770.43	1986.67	3727.88	10.55	1.22	1.00
$Ba_4Cu_8Te_8$	1666.39	1841.97	3412.00	5.21	2.55	2.77
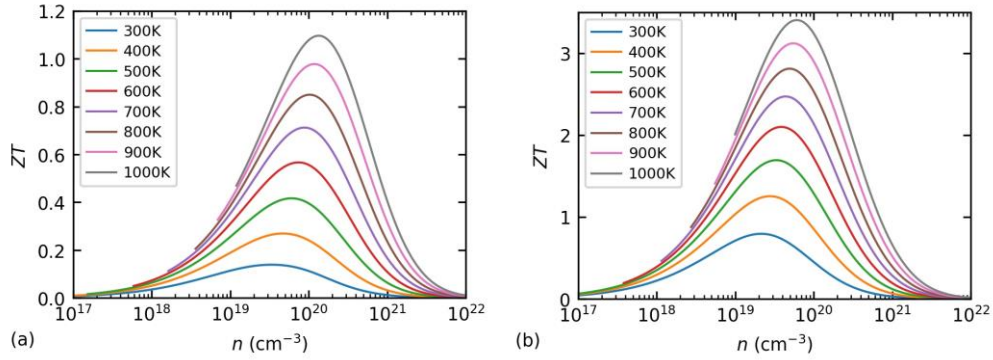
Figure 4.44. Figure of merit at varying temperatures and carrier concentrations for (a) $Cu_4Sb_4Se_8$ and (b) $Ba_4Cu_8Te_8$.

4.10. $Cs_6Cu_4Bi_{10}S_{20}$

This compound has an orthorhombic structure with a space group *Pnnm* (Fig. 4.45) and the unit cell containing 40 atoms. The Bi, S, and Cu atoms are interconnected with each other to form a framework, whereas the Cs atoms are distributed in the voids of this framework. In the band structure of this compound (Fig. 4.46), the CBM is located along the $\Gamma-Y$ path ($N = 2$), while the VBM is along the $\Gamma-Z$ path ($N = 2$). The conduction and valence bands are much more flat along the $\Gamma-Y$ and $\Gamma-Z$ paths than that along the $\Gamma-X$ path. The $\Gamma-X$, $\Gamma-Y$, and $\Gamma-Z$ paths correspond to the *a*, *b* and *c* directions of the lattice, therefore, the transport properties in this material are expected to be highly anisotropic. Our calculation shows that this compound is an outstanding n-type thermoelectric material. Although the power factor is not very high, the lattice thermal conductivity is extremely low, reaching the so-called "amorphous limit" (Fig. 4.47). Such a low lattice thermal conductivity is mainly due to the very strong anharmonicity inside the lattice. This leads to the figure of merit values above 1 in a wide range of temperatures and carrier concentrations.
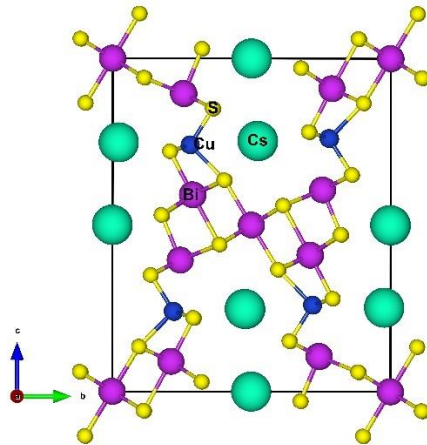
Figure 4.45. Crystal structure of $Cs_6Cu_4Bi_{10}S_{20}$.
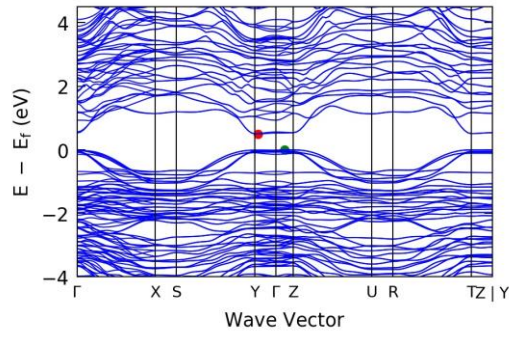
Figure 4.46. Band structure of $Cs_6Cu_4Bi_{10}S_{20}$.

Table 4.14. Key parameters for n-type transport

	m_c^* (m_e)	m_d^* (m_e)	Ξ (eV)	N	E_g (eV)	c (GPa)	ε_∞	ε_0
$Cs_6Cu_4Bi_{10}S_{20}$	0.401	1.564	5.77	2	0.50	18.75	9.01	55.19
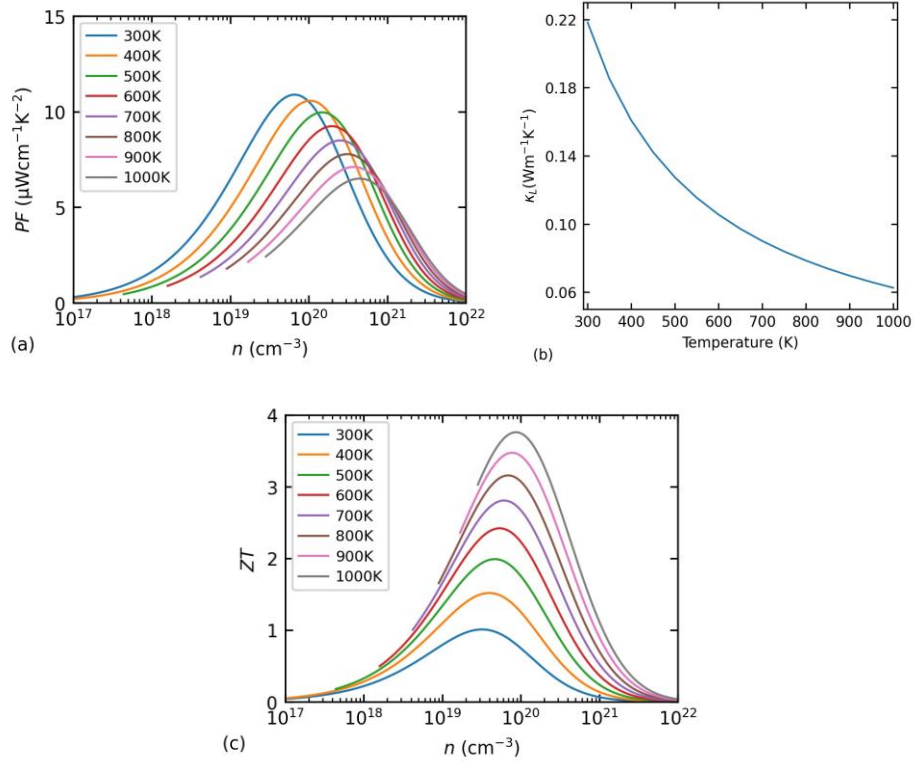
Figure 4.47. Thermoelectric properties of $Cs_6Cu_4Bi_{10}S_{20}$ for n-type transport. (a) power factor, (b) lattice thermal conductivity, and (c) figure of merit.

4.11. $Ca_4Sn_4S_{12}$

This compound has an orthorhombic structure with a space group *Pnma*, (Fig. 4.48). The Sn atom is bonded to six nearest neighboring S atoms to form an octahedron, and the Ca atom is connected with three nearest S atoms to form a tetrahedron. The octahedron shares one S corner with the neighboring tetrahedron. In the band structure (Fig. 4.49), the CBM is located along the Γ–Y path, whereas the VBM is along the Γ–X path, both having a band degeneracy $N = 2$. Multiple valleys are seen near the band gap. Our calculations show that this compound is a good n-type thermoelectric material. It has high power factor and relatively low lattice thermal conductivity. Therefore, its figure of merit can exceed 1 at high temperatures.
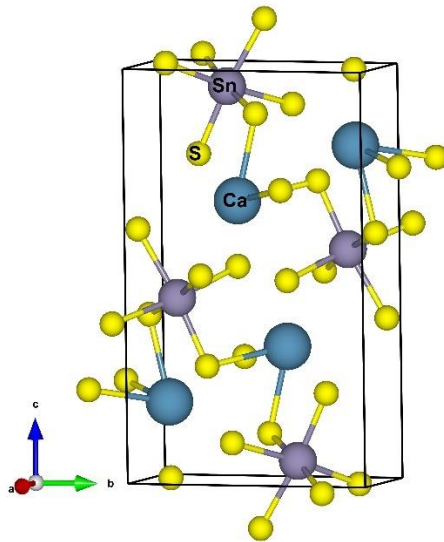
Figure 4.48. Crystal structure of $Ca_4Sn_4S_{12}$.
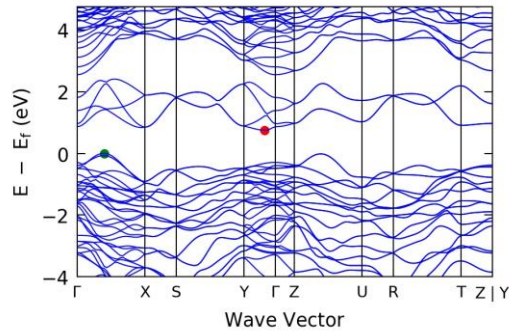
Figure 4.49. Band structure of $Ca_4Sn_4S_{12}$.

Table 4.15. Key parameters for n-type transport

		m_c^* (m_e)	m_d^* (m_e)	Ξ (eV)	N	E_g (eV)	c (GPa)	ε_∞	ε_0
$Ca_4Sn_4S_{12}$	CBM	0.450	0.777	8.99	2	0.75	29.75	9.06	23.57
	CSB	0.446	0.723	8.39	2	0.84			
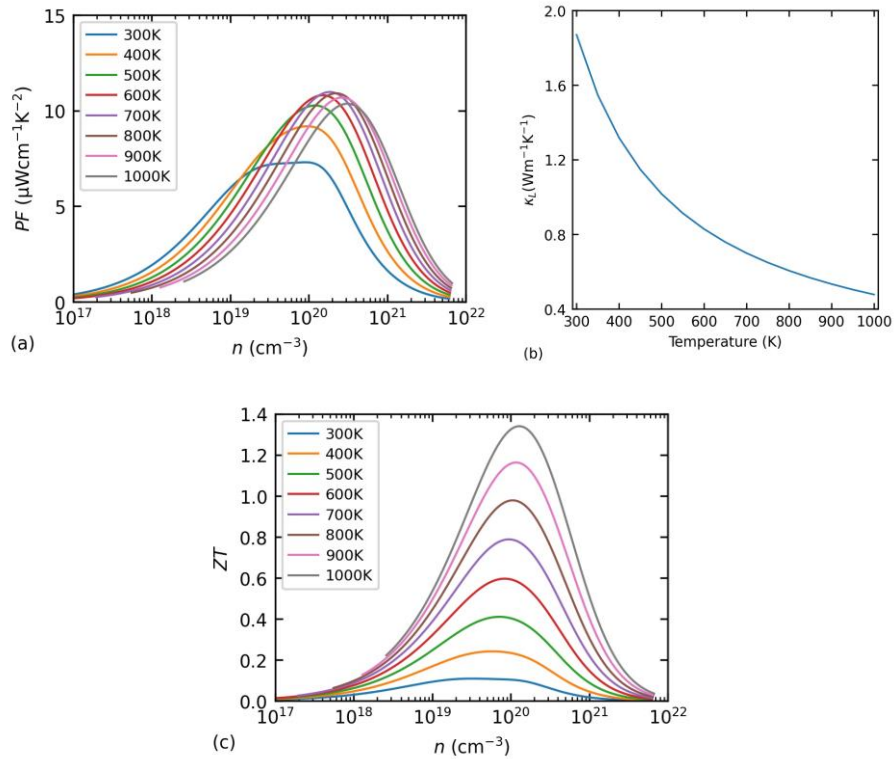
Figure 4.50. Thermoelectric properties of $Ca_4Sn_4S_{12}$ for n-type transport. (a) power factor, (b) lattice thermal conductivity, and (c) figure of merit.

4.12. Ba$_2$ZrS$_4$ and Ba$_2$HfS$_4$

These two compounds have a tetragonal structure with a space group $I4/mmm$ (Fig. 4.51) and the unit cell containing 14 atoms. Each transition metal atom (Zr and Hf) is surrounded by six nearest neighboring S atoms to form an octahedron. In the band structures of these compounds (Fig. 4.52), the CBMs are at the Γ point, while the VBMs are at the X point ($N = 2$). Besides, there are multiple valleys near the band gap in the valence band. Our calculations show that these two compounds are excellent thermoelectric materials for both n-type and p-type transport. Their figure of merit could be higher than 1 in a wide range of temperatures and carrier concentrations, which is mainly due to their high power factor and quite low lattice thermal conductivity.
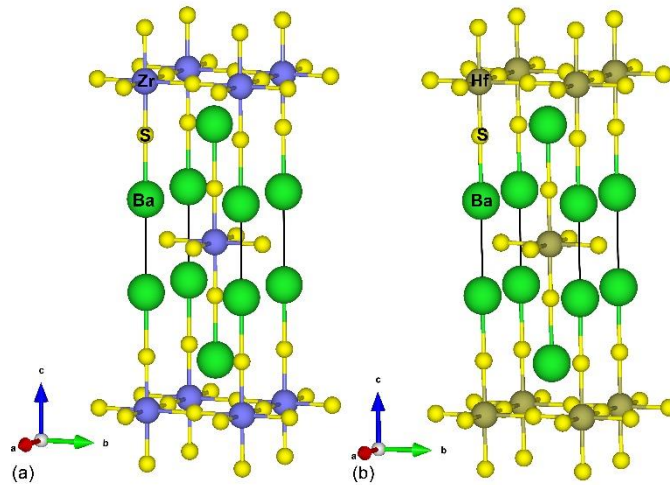
Figure 4.51. Crystal structures of (a) Ba$_2$ZrS$_4$ and (b) Ba$_2$HfS$_4$.
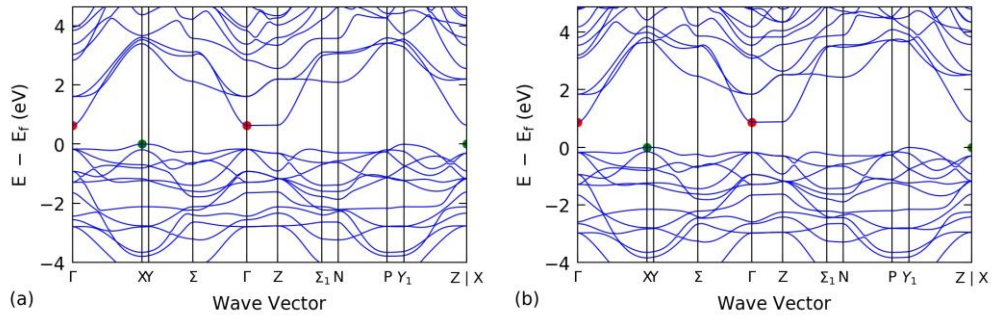
Figure 4.52. Band structures of (a) Ba_2ZrS_4 and (b) Ba_2HfS_4.

Table 4.16. Key parameters for n-type and p-type transport

		m_c^* (m_e)	m_d^* (m_e)	Ξ (eV)	N	E_g (eV)	c (GPa)	ε_∞	ε_0
	CBM	0.264	1.002	5.07	1	0.63			
Ba_2ZrS_4	VBM	0.889	2.153	6.34	2		38.17	7.18	57.87
	VSB	0.887	3.253	6.35	4	0.64			
	CBM	0.264	0.904	4.50	1	0.87			
Ba_2HfS_4	VBM	0.877	2.161	5.89	2		40.65	6.74	38.49
	VSB	0.878	3.271	5.91	4	0.88			

(c) n (cm^{-3})

(d) p (cm^{-3})

Figure 4.53. Power factor at varying temperatures and carrier concentrations for (a, b) Ba$_2$ZrS$_4$ and (c, d) Ba$_2$HfS$_4$.
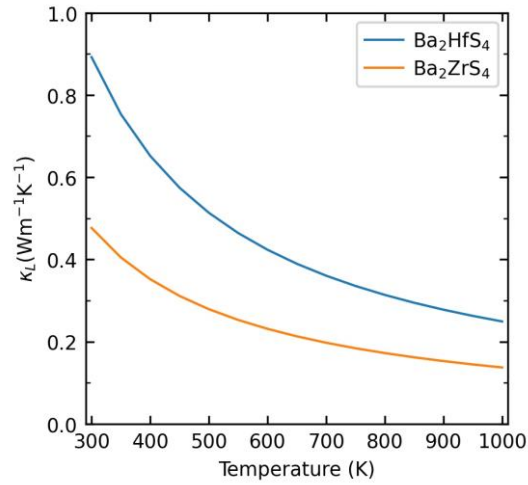
Figure 4.54. Lattice thermal conductivity of this group of compounds.

(a) n (cm^{-3})

(b) p (cm^{-3})
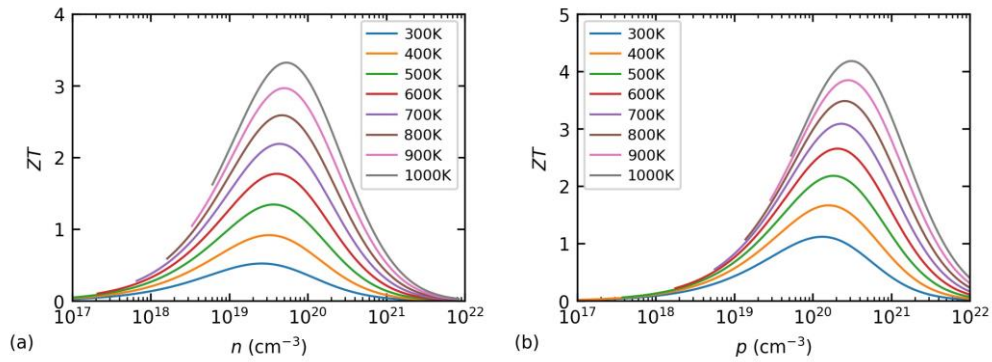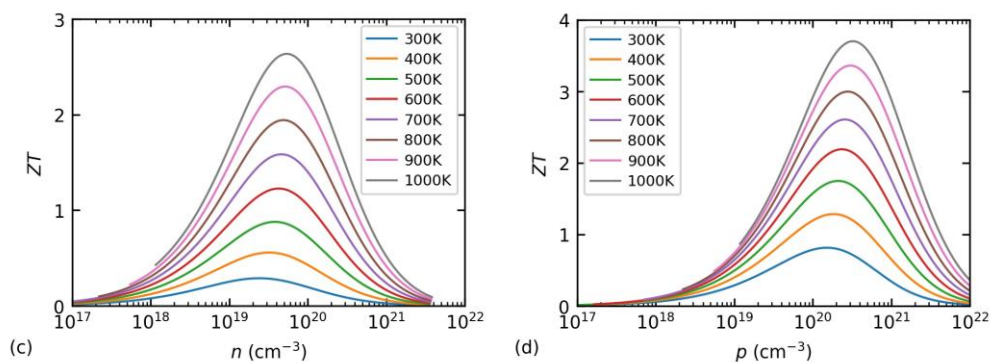
Figure 4.55. Figure of merit at varying temperatures and carrier concentrations for (a, b) Ba_2ZrS_4 and (c, d) Ba_2HfS_4.

4.13. Ga_2Te_5

This compound has a tetragonal structure with a space group $I4/m$ (Fig. 4.56). The Ga atom is bonded to four nearest neighboring Te atoms to form a tetrahedron. In the band structure of this compound (Fig. 4.57), the CBM is located along the X–P path and is dispersive with a band degeneracy $N = 4$. The VBM is located at the X point ($N = 2$). Our calculations show that this compound is an outstanding n-type thermoelectric material having a relatively high power factor and quite low lattice thermal conductivity. The figure of merit can exceed 1 in a wide range of temperatures and carrier concentrations.
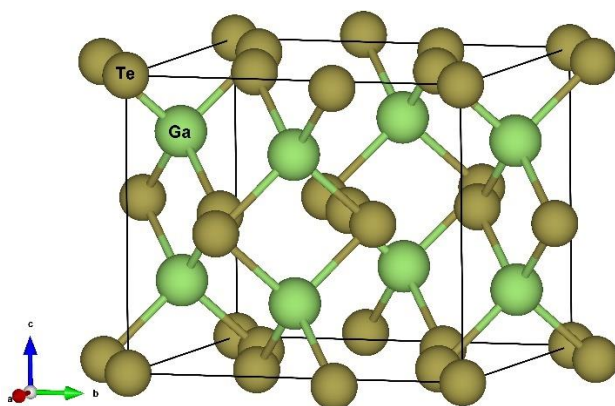
Figure 4.56. Crystal structure of Ga_2Te_5.
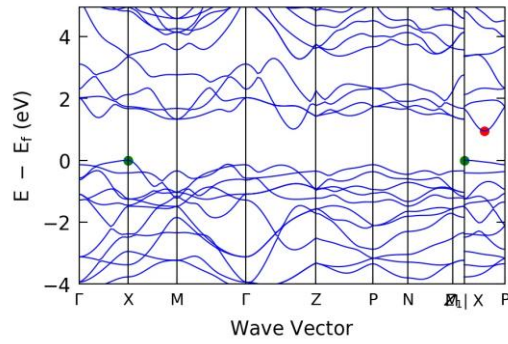
Figure 4.57. Band structure of Ga$_2$Te$_5$.

Table 4.17. Key parameters for n-type transport

		m_c^* (m_e)	m_d^* (m_e)	Ξ (eV)	N	E_g (eV)	c (GPa)	ε_∞	ε_0
Ga$_2$Te$_5$	CBM	0.186	0.482	8.76	4	0.94	17.90	13.93	22.62
	CSB	0.261	0.469	8.14	2	1.00			
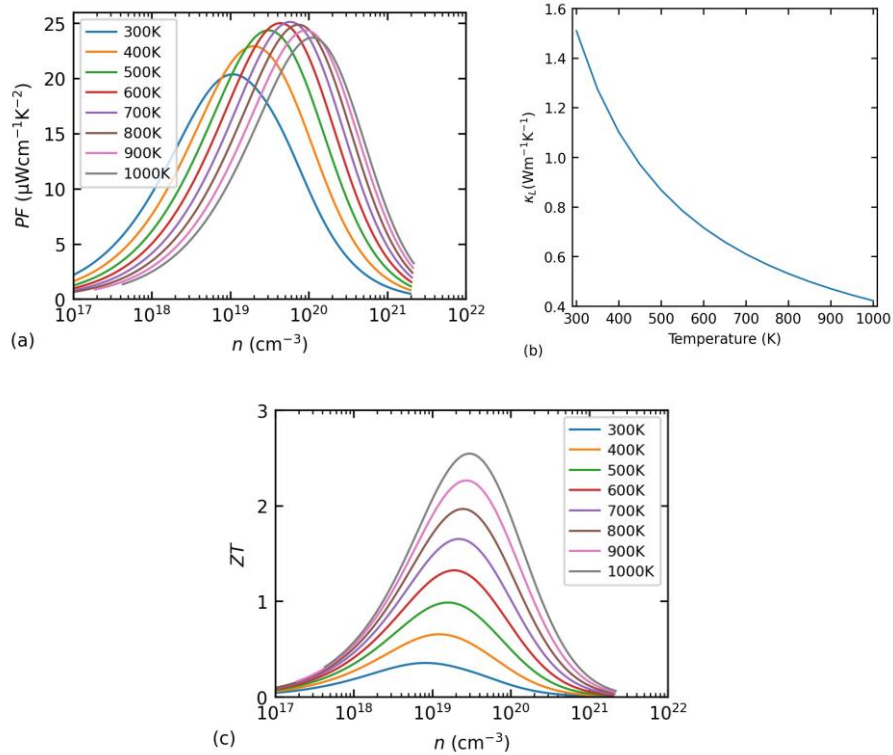
Figure 4.58. Thermoelectric properties of Ga$_2$Te$_5$ for n-type transport. (a) power factor, (b) lattice thermal conductivity, and (c) figure of merit.

4.14. BaCu$_2$Se$_2$

This compound has a tetragonal structure with a space group *I*4/*mmm* and the unit cell containing 10 atoms. Each Cu atom is bonded to four nearest neighboring Se atoms to form a tetrahedron. These tetrahedrons connect with each other by sharing one edge, forming a Cu–Se layer. The layers of Ba and Cu–Se atoms are alternately stacked along the *c*-axis. The band structure of this compound (Fig. 4. 60) shows that it is a direct gap semiconductor with the CBM and VBM located at the Γ point. Meanwhile, it has a second valence band along Y$_1$–Z path ($N = 4$). Our calculations show that this compound is a promising p-type thermoelectric material whose figure of merit can exceed 1 in a wide range of temperatures and carrier concentrations, which is mainly due to its very low lattice thermal conductivity.
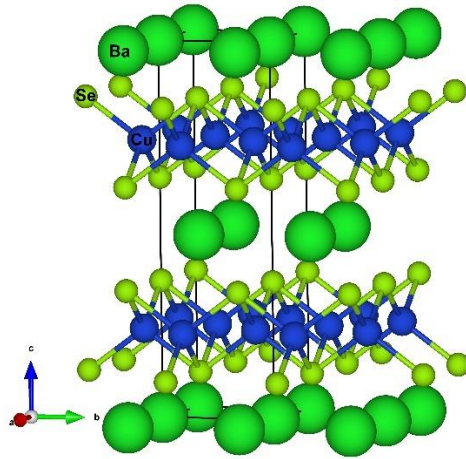
Figure 4.59. Crystal structure of BaCu$_2$Se$_2$.
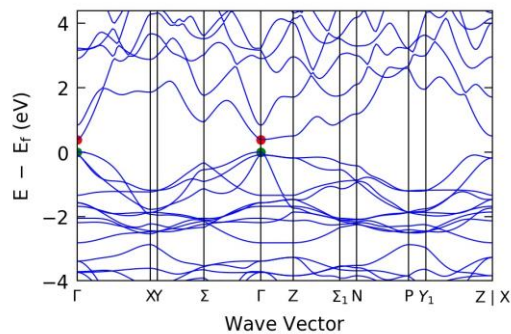
Figure 4.60. Band structure of BaCu$_2$Se$_2$.

131

Table 4.18. Key parameters for p-type transport

		m_c^* (m_e)	m_d^* (m_e)	Ξ (eV)	N	E_g (eV)	c (GPa)	ε_∞	ε_0
BaCu$_2$Se$_2$	VBM	0.284	0.976	7.52	1	0.39	30.95	12.41	30.95
	VSB	1.029	2.744	7.97	4	0.48			
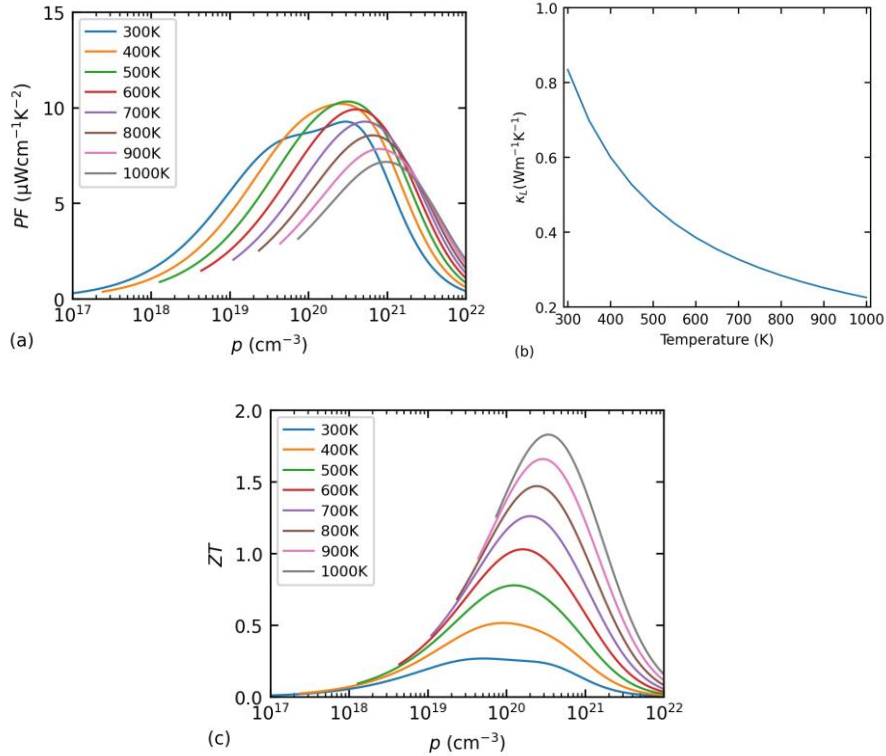
Figure 4.61. Thermoelectric properties of BaCu$_2$Se$_2$ for p-type transport. (a) power factor, (b) lattice thermal conductivity, and (c) figure of merit.

4.15. CaIn$_2$Te$_4$

This compound adopts a tetragonal structure with a space group $I422$ (Fig. 4.62) and the unit cell containing 14 atoms. The In atom is bonded to four nearest neighboring Te atoms to form a tetrahedron. These tetrahedra are connected in chains along the c-axis, while Ca atoms are distributed in the empty space among the tetrahedron chains. The band structure of this compound (Fig. 4.63) shows that it is an indirect gap semiconductor with the CBM at the M point and the VBM at the Γ point. Meanwhile, there is a second valence band

132

locating along the Γ–X path with the energy 0.01 eV lower than the VBM ($N = 4$). Our calculations show that this compound is a promising p-type thermoelectric material (Fig. 4.64) having a relatively low lattice thermal conductivity, whose figure of merit can exceed 1 at high temperatures.
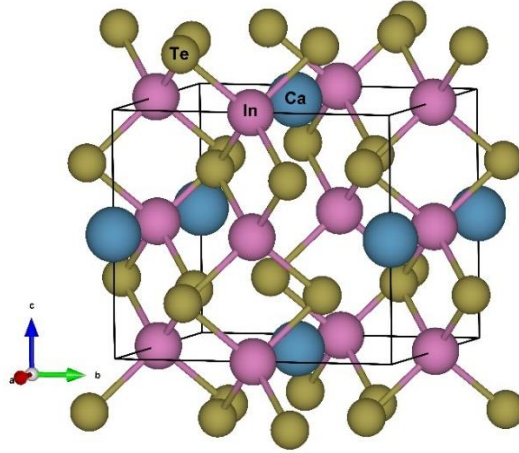
Figure 4.62. Crystal structure of CaIn$_2$Te$_4$.
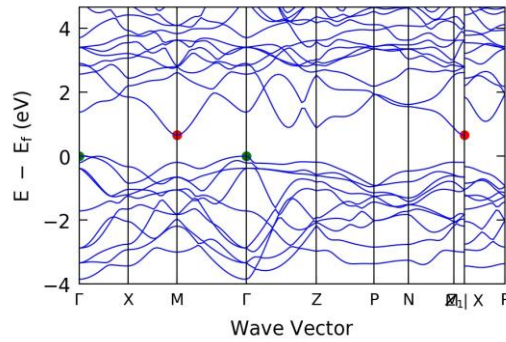
Figure 4.63. Band structure of CaIn$_2$Te$_4$.

Table 4.19. Key parameters for p-type transport

		m_c^* (m_e)	m_d^* (m_e)	Ξ (eV)	N	E_g (eV)	c (GPa)	ε_∞	ε_0
CaIn$_2$Te$_4$	VBM	0.249	0.833	10.25	1	0.65	18.98	10.88	54.80
	VSB	0.469	1.429	10.16	4	0.66			
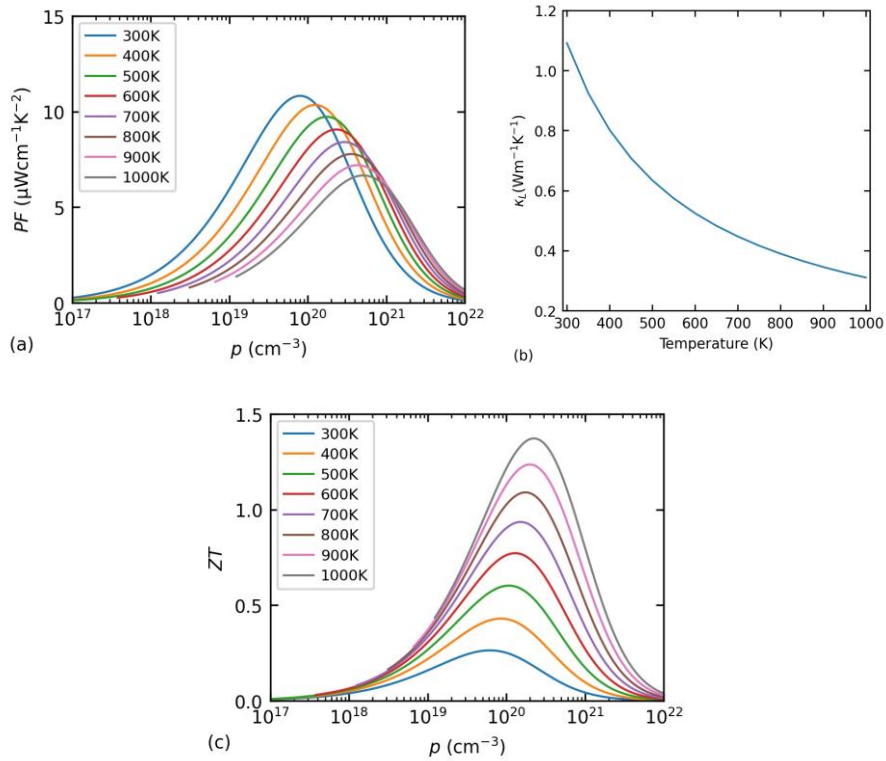
Figure 4.64. Thermoelectric properties of $CaIn_2Te_4$ for p-type transport. (a) power factor, (b) lattice thermal conductivity, and (c) figure of merit.

4.16. Discussion

The above sections introduce part of the promising thermoelectric materials founded in this work. From their data of structure and transport properties, we can get some clues about what makes a good thermoelectric material. For cubic compounds, due to their high symmetry, the conduction band or valence band along specific directions in the Brillouin zone could have high band degeneracy, which means there will be multiple carrier pockets involved in transport process. In this case, the DOS effective mass for conduction band or valence band could be large, while the conductivity effective mass of carriers could keep small. Therefore, both Seebeck coefficient and electrical conductivity of them could be high, leading to a high power factor. Meanwhile, if the cubic compounds contain some heavy elements, such as in $MAcTe_2$-like compounds, the phonons could be efficiently scattered and their lattice thermal conductivity could be greatly reduced. For tetragonal and

134

orthorhombic compounds, the band degeneracy of their conduction or valence bands is not large ($N < 4$) because of their lower symmetry. Thus, the power factor of these compounds is not as high as that of cubic compounds. However, the tetragonal and orthorhombic compounds have much more chance to have low lattice thermal conductivity. According to our calculation, those materials, such as SnSe-like compounds, $Ba_4Cu_8Te_8$, $Cs_6Cu_4Bi_{10}S_{20}$, have their κ_L as low as the amorphous limit. Such a low κ_L originates from their structure: they are anisotropic, contain layers or voids with heavy atoms (such as Ba, Cs) loosely bonded to surrounding atoms. Thus, these compounds have strong anharmonicity intrinsically in their lattice. In order to accurately calculate their κ_L, in principle the high order interaction beyond three-phonon process should be included. However, such a calculation is always time-consuming. In our model, the overall anharmonicity is mainly reflected by the value of phonon velocity and Grüneisen coefficient. It seems our model tend to underestimate κ_L of those compounds with strong anharmonicity (as shown in Fig. 2.6, 4.33, 4.43, 4.47b), mainly because the calculated Grüneisen coefficients are quite large (Table 1 in Ref. [111], Table 4.9, 4.13). More accurate κ_L could be obtained if the accuracy of Grüneisen coefficients can be improved.

Furthermore, for the convenience of experimental verification, 10 compounds introduced in the previous sections, which we think as the most promising thermoelectric materials, are selected and shown in Table 4.20. Experimental investigation on these compounds is strongly encouraged.

Table 4.20. The most promising thermoelectric compounds founded in this work, expecting for experimental verification

Formula	Crystal system	Stability	doping	Including toxic element	Including expensive element	PF_{max} ($\mu W \cdot cm^{-1} \cdot K^{-1}$)	$\kappa_{L,300K}$ ($W \cdot m^{-1} \cdot K^{-1}$)	ZT_{max}
$Co_4P_4S_4$	Cubic	Stable	p	No	No	101.50	32.66	0.79
$Sn_4Pt_4Se_4$	Cubic	Stable	p	No	Yes	63.22	4.38	1.51
Cd_4Se_8	Cubic	Stable	n	Yes	No	21.77	2.06	1.35
$Hg_2In_4S_8$	Cubic	Stable	p	Yes	No	41.04	2.79	1.30

$Nb_6Sb_4Te_{10}$	Cubic	Stable	p	No	Yes	37.13	5.21	1.11
$Dy_8P_8S_8$	Orthor-hombic	Stable	n, p	No	No	10.52 (n) 17.63 (p)	2.29	1.11 (n) 1.21 (p)
Ge_4Se_4	Orthor-hombic	Stable	n	No	No	12.54	0.41	3.17
$Cu_4Sb_4Se_8$	Orthor-hombic	Stable	n	No	No	12.82	2.34	1.09
$Ba_2Hf_1S_4$	Tetragonal	Stable	n, p	No	No	16.68 (n) 34.08 (p)	0.89	2.63 (n) 3.70 (p)
Ga_2Te_5	Tetragonal	Stable	n	No	Yes	25.12	1.51	2.54

Chapter 5. Conclusions

We developed a powerful computer program AICON for calculating the transport properties of bulk semiconductors, including the phonon transport properties and electronic transport properties. The algorithm for the phonon transport properties is based on the Debye–Callaway model. Going beyond the original Callaway model, we also took into account the contribution from optical phonons. Our method factors in the phonon-phonon normal scattering, Umklapp scattering, and isotope scattering processes; all the necessary parameters, including the phonon velocity, Grüneisen parameter, and Debye temperature, can be calculated using first-principles methods. The algorithm for the electronic transport properties is based on the generalized Kane band model and perturbation theory in the framework of the relaxation time approximation. We reoptimized the original formulas to achieve highly efficient numerical calculations. In this method, we take into account three scattering mechanisms for electrons: acoustic phonon scattering, polar optical phonon scattering, and ionized impurity scattering. All key input parameters, such as the deformation potential constants, effective mass, and dielectric constants, can be calculated using first-principles methods. The capabilities of the phonon transport model and electronic transport model were tested on a group of common semiconductors and insulators, respectively. The reviewed cases proved the robustness and accuracy of our method. What's more, we also implemented an automatic workflow tool so that the users only need to provide structural files and some necessary settings for each DFT calculation, then the whole workflow can run and check automatically.

We used AICON to find promising thermoelectric materials among the structures extracted from a database. Totally, we have screened 463 compounds and 361 of them (94 cubic, 267 tetragonal and orthorhombic) finished the complete processes of electronic transport properties calculation. Among them, 94 compounds (47 cubic, 47 tetragonal and orthorhombic) were identified as having high power factor ($PF > 10$ µW·cm^{-1}·K^{-2}) for either n-type or p-type transport, including six already well-known thermoelectric materials. The statistical analysis of the obtained data shows that m_d^*/m_c^* can be a good indicator for the power factor, and $m_d^*/(m_c^* \kappa_L^{300K})$ is a good indicator for the figure of

merit. Thus, we can use these simple parameters for a fast evaluation of the thermoelectric performance of a compound. Among the novel thermoelectric materials with cubic structure, we found CoAsS-like compounds, $Hg_2Al_4Se_8$, $Cd_2In_4Se_4S_4$, $Hg_2In_4S_8$, $Mg_2In_4Se_8$, $Nb_6Sb_4Te_{10}$ and others as promising p-type thermoelectric materials; $CdSe_2$, MgTe and other compounds were found as promising n-type materials. These compounds have very high power factor values comparable with or even exceeding those of the state-of-the-art thermoelectric materials, and normal lattice thermal conductivity. They can have the figure of merit larger than 1 at high temperatures, which can be further improved by reducing the lattice thermal conductivity. For compounds with tetragonal and orthorhombic structure, the representative ones include SnSe-like compounds, $Cu_4Sb_4Se_8$, $Ba_4Cu_8Te_8$, $Cs_6Cu_4Bi_{10}S_{20}$ and others for n-type transport; $BaCu_2Se_2$ and $CaIn_2Te_4$ for p-type transport; Ba_2ZrS_4 and Ba_2HfS_4 for both n-type and p-type transport. These compounds have relatively high power factor and very low lattice thermal conductivity, therefore their figure of merit can exceed 1 in a wide range of temperatures and carrier concentrations. We found that for cubic structures, good thermoelectric performance is usually due to high power factor. Their band extrema (CBM and VBM) are usually located along a high-symmetry path; thus, the bands involved in transport have a large band degeneracy. Because of high band degeneracy, cubic structures can have both high Seebeck coefficient and high electrical conductivity, leading to a high power factor. For tetragonal and orthorhombic structures, good thermoelectric performance is usually due to their low lattice thermal conductivity. These compounds are usually highly anisotropic and have intrinsically large anharmonicity in their structures, reflected by their large Grüneisen parameter. The methods used in this work can also be applied in other fields where the transport properties of semiconductors need to be calculated.

Bibliography

[1] Baxter, J., Bian, Z., Chen, G., Danielson, D., Dresselhaus, M. S., Fedorov, A. G., ... & Wu, Y. (2009). Nanoscale design to enable the revolution in renewable energy. *Energy & Environmental Science*, 2(6), 559–588.

[2] Rowe D. M., Thermoelectrics handbook: macro to nano, CRC press, 2005.

[3] Goldsmid H. J., Introduction to thermoelectricity, Springer Science & Business Media, 2009.

[4] Snyder, J. G., Toberer, E. (2008). Complex thermoelectric materials. *Nature Materials* **7,** 105–114.

[5] Goldsmid H. J., Douglas R. W., (1954). The use of semiconductors in thermoelectric refrigeration. *British Journal of Applied Physics*, 5(11), 386.

[6] Ure Jr, and Roland W. (1962). Thermoelectricity: science and engineering. *American Journal of Physics*, 30(1), 78–78.

[7] Rosi, F. D. (1968). Thermoelectricity and thermoelectric power generation. *Solid-State Electronics*, 11(9), 833–868.

[8] Rosi, F. D., Hockings, E. F., & Lindenblad, N. E. (1961). Semiconducting materials for thermoelectric power generation. *RCA (Radio Corporation of America) Review (US)*, *22*.

[9] Scherrer, H., & Scherrer, S. (2006). Thermoelectric properties of bismuth antimony telluride solid solutions. *Thermoelectrics Handbook: Macro to Nano*, 27-12.

[10] Kutasov, V. A., Lukyanova, L. N., & Vedernikov, M. V. (2006). Shifting the maximum figure-of-merit of $(Bi,Sb)_2(Te,Se)_3$ thermoelectrics to lower temperatures. *Thermoelectrics Handbook: Macro to Nano*, 37-7.

[11] Wood C., (1988). Materials for thermoelectric energy conversion. *Reports on Progress in Physics*, 51(4), 459.

[12] Fritts, R. W. (1960). Thermoelectric materials and devices. *N.-Y.: Reinhold Publ. Co.*, 143–162.

[13] Fleischmann, H., Luy, H., & Rupprecht, J. (1963). Neuere Untersuchungen an halbleitenden IV VI-IV VI2-Mischkristallen. *Zeitschrift für Naturforschung A*, 18(5), 646–649.

[14] Hsu, K. F., Loo, S., Guo, F., Chen, W., Dyck, J. S., Uher, C., ... & Kanatzidis, M. G. (2004). Cubic AgPb$_m$SbTe$_{2+m}$: bulk thermoelectric materials with high figure of merit. *Science*, 303(5659), 818–821.

[15] Skrabek, E. A., & Trimmer, D. S. (1995). Properties of the general TAGS system. *CRC handbook of thermoelectrics*, 267–275.

[16] Vining, C. B., Laskow, W., Hanson, J. O., Van der Beck, R. R., & Gorsuch, P. D. (1991). Thermoelectric properties of pressure-sintered Si$_{0.8}$Ge$_{0.2}$ thermoelectric alloys. *Journal of applied physics*, 69(8), 4333–4340.

[17] Bhandari, C. M., & Rowe, D. M. (1983). Modern thermoelectrics. *Holt, Rinehartand Winston Ltd*.

[18] Hicks, L. D., & Dresselhaus, M. S. (1993). Effect of quantum-well structures on the thermoelectric figure of merit. *Physical Review B*, 47(19), 12727.

[19] Hicks, L. D., & Dresselhaus, M. S. (1993). Thermoelectric figure of merit of a one-dimensional conductor. *Physical review B*, 47(24), 16631.

[20] Venkatasubramanian, R., Siivola, E., Colpitts, T., & O'quinn, B. (2001). Thin-film thermoelectric devices with high room-temperature figures of merit. *Nature*, 413(6856), 597–602.

[21] Harman, T. C., Taylor, P. J., Walsh, M. P., & LaForge, B. E. (2002). Quantum dot superlattice thermoelectric materials and devices. *science*, 297(5590), 2229–2232.

[22] Hochbaum, A. I., Chen, R., Delgado, R. D., Liang, W., Garnett, E. C., Najarian, M., ... & Yang, P. (2008). Enhanced thermoelectric performance of rough silicon nanowires. *Nature*, 451(7175), 163–167.

[23] Boukai, A. I., Bunimovich, Y., Tahir-Kheli, J., Yu, J. K., Goddard Iii, W. A., & Heath, J. R. (2008). Silicon nanowires as efficient thermoelectric materials. *nature*, 451(7175), 168–171.

[24] Poudel, B., Hao, Q., Ma, Y., Lan, Y., Minnich, A., Yu, B., ... & Ren, Z. (2008). High-thermoelectric performance of nanostructured bismuth antimony telluride bulk alloys. *Science*, 320(5876), 634–638.

[25] Ma, Y., Hao, Q., Poudel, B., Lan, Y., Yu, B., Wang, D., ... & Ren, Z. (2008). Enhanced thermoelectric figure-of-merit in p-type nanostructured bismuth antimony tellurium alloys made from elemental chunks. *Nano Letters*, 8(8), 2580–2584.

[26] Wang, X. W., Lee, H., Lan, Y. C., Zhu, G. H., Joshi, G., Wang, D. Z., ... & Ren, Z. F. (2008). Enhanced thermoelectric figure of merit in nanostructured n-type silicon germanium bulk alloy. *Applied Physics Letters*, 93(19), 193121.

[27] Joshi, G., Lee, H., Lan, Y., Wang, X., Zhu, G., Wang, D., ... & Ren, Z. (2008). Enhanced thermoelectric figure-of-merit in nanostructured p-type silicon germanium bulk alloys. *Nano letters*, 8(12), 4670–4674.

[28] Harman, T. C., Walsh, M. P., & Turner, G. W. (2005). Nanostructured thermoelectric materials. *Journal of electronic materials*, 34(5), L19–L22.

[29] Slack, G. A. (1995). New materials and performance limits for thermoelectric cooling. *CRC handbook of thermoelectrics*, 407–440.

[30] Kleinke, H. (2010). New bulk materials for thermoelectric power generation: clathrates and complex antimonides. *Chemistry of materials*, 22(3), 604–611.

[31] Shi, X., Yang, J., Salvador, J. R., Chi, M., Cho, J. Y., Wang, H., ... & Chen, L. (2011). Multiple-filled skutterudites: high thermoelectric figure of merit through separately optimizing electrical and thermal transports. *Journal of the American Chemical Society*, 133(20), 7837–7846.

[32] Rull-Bravo, M., Moure, A., Fernández, J. F., & Martín-González, M. (2015). Skutterudites as thermoelectric materials: revisited. *Rsc Advances*, 5(52), 41653–41667.

[33] Toberer, E. S., May, A. F., & Snyder, G. J. (2010). Zintl chemistry for designing high efficiency thermoelectric materials. *Chemistry of Materials*, 22(3), 624–634.

[34] Biswas, K., He, J., Blum, I. D., Wu, C. I., Hogan, T. P., Seidman, D. N., ... & Kanatzidis, M. G. (2012). High-performance bulk thermoelectrics with all-scale hierarchical architectures. *Nature*, 489(7416), 414–418.

[35] Kurosaki, K., Kosuga, A., Muta, H., Uno, M., & Yamanaka, S. (2005). Ag_9TlTe_5: a high-performance thermoelectric bulk material with extremely low thermal conductivity. *Applied Physics Letters*, 87(6), 061919.

[36] Zhao, L. D., Lo, S. H., Zhang, Y., Sun, H., Tan, G., Uher, C., ... & Kanatzidis, M. G. (2014). Ultralow thermal conductivity and high thermoelectric figure of merit in SnSe crystals. *Nature*, 508(7496), 373–377.

[37] Lee, Y. K., Luo, Z., Cho, S. P., Kanatzidis, M. G., & Chung, I. (2019). Surface oxide removal for polycrystalline SnSe reveals near-single-crystal thermoelectric performance. *Joule*, 3(3), 719–731.

[38] Zhou, C., Lee, Y. K., Yu, Y., Byun, S., Luo, Z. Z., Lee, H., ... & Kanatzidis, M. G. (2021). Polycrystalline SnSe with a thermoelectric figure of merit greater than the single crystal. *Nature Materials*, 20(10), 1378–1384.

[39] He, W., Wang, D., Wu, H., Xiao, Y., Zhang, Y., He, D., ... & Zhao, L. D. (2019). High thermoelectric performance in low-cost $SnS_{0.91}Se_{0.09}$ crystals. *Science*, 365(6460), 1418–1424.

[40] Liu, H., Shi, X., Xu, F., Zhang, L., Zhang, W., Chen, L., ... & Snyder, G. J. (2012). Copper ion liquid-like thermoelectrics. *Nature materials*, 11(5), 422–425.

[41] Liu, W. D., Yang, L., Chen, Z. G., & Zou, J. (2020). Promising and eco-friendly Cu_2X-based thermoelectric materials: progress and applications. *Advanced Materials*, 32(8), 1905703.

[42] Zhang, Z., Zhao, K., Wei, T. R., Qiu, P., Chen, L., & Shi, X. (2020). Cu_2Se-Based liquid-like thermoelectric materials: looking back and stepping forward. *Energy & Environmental Science*, 13(10), 3307–3329.

[43] Nozariasbmarz, A., Agarwal, A., Coutant, Z. A., Hall, M. J., Liu, J., Liu, R., ... & Vashaee, D. (2017). Thermoelectric silicides: a review. *Japanese Journal of Applied Physics*, 56(5S1), 05DA04.

[44] Chen, S., & Ren, Z. (2013). Recent progress of half-Heusler for moderate temperature thermoelectric applications. *Materials today*, 16(10), 387–395.

[45] Huang, L., Zhang, Q., Yuan, B., Lai, X., Yan, X., & Ren, Z. (2016). Recent progress in half-Heusler thermoelectric materials. *Materials Research Bulletin*, 76, 107–112.

[46] Zhang, Q., Sun, Y., Xu, W., & Zhu, D. (2014). Organic thermoelectric materials: emerging green energy materials converting heat to electricity directly and efficiently. *Advanced Materials*, 26(40), 6829–6851.

[47] He, M., Qiu, F., & Lin, Z. (2013). Towards high-performance polymer-based thermoelectric materials. *Energy & Environmental Science*, 6(5), 1352–1361.

[48] Zang, J., Chen, J., Chen, Z., Li, Y., Zhang, J., Song, T., & Sun, B. (2021). Printed flexible thermoelectric materials and devices. *Journal of Materials Chemistry A*, 9, 19439–19464.

[49] G. J. Snyder, E. S. Toberer. (2008) Complex thermoelectric materials. *Nature materials*, 7(2), 105–114.

[50] Sootsman, J. R., Chung, D. Y., & Kanatzidis, M. G. (2009). New and old concepts in thermoelectric materials. *Angewandte Chemie International Edition*, 48(46), 8616–8639.

[51] Pei, Y., Wang, H., & Snyder, G. J. (2012). Band engineering of thermoelectric materials. *Advanced materials*, 24(46), 6125–6135.

[52] Shi, X., Chen, L., & Uher, C. (2016). Recent advances in high-performance bulk thermoelectric materials. *International Materials Reviews*, 61(6), 379–415.

[53] Tan, G., Zhao, L. D., & Kanatzidis, M. G. (2016). Rationally designing high-performance bulk thermoelectric materials. *Chemical reviews*, 116(19), 12123–12149.

[54] Gayner, C., & Kar, K. K. (2016). Recent advances in thermoelectric materials. *Progress in Materials Science*, 83, 330–382.

[55] Zhu, T., Liu, Y., Fu, C., Heremans, J. P., Snyder, J. G., & Zhao, X. (2017). Compromise and synergy in high-efficiency thermoelectric materials. *Advanced materials*, 29(14), 1605884.

[56] Han, C., Sun, Q., Li, Z., & Dou, S. X. (2016). Thermoelectric enhancement of different kinds of metal chalcogenides. *Advanced Energy Materials*, 6(15), 1600498.

[57] Wei, J., Yang, L., Ma, Z., Song, P., Zhang, M., Ma, J., ... & Wang, X. (2020). Review of current high-ZT thermoelectric materials. *Journal of Materials Science*, 55(27), 12642–12704.

[58] Jaziri, N., Boughamoura, A., Müller, J., Mezghani, B., Tounsi, F., & Ismail, M. (2020). A comprehensive review of Thermoelectric Generators: Technologies and common applications. *Energy Reports*, 6, 264–287.

[59] Nozariasbmarz, A., Collins, H., Dsouza, K., Polash, M. H., Hosseini, M., Hyland, M., ... & Vashaee, D. (2020). Review of wearable thermoelectric energy harvesting: From body temperature to electronic systems. *Applied Energy*, 258, 114069.

[60] Anatychuk L. I., & Luste, O. J. (2006). Modern thermodynamic theory of thermoelectricity. *Thermoelectrics Handbook: Macro to Nano*, 2-5.

[61] Madsen, G. K., Carrete, J., & Verstraete, M. J. (2018). BoltzTraP2, a program for interpolating band structures and calculating semi-classical transport coefficients. *Computer Physics Communications*, 231, 140–145.

[62] Pizzi, G., Volja, D., Kozinsky, B., Fornari, M., & Marzari, N. (2014). BoltzWann: A code for the evaluation of thermoelectric and electronic transport properties with a maximally-localized Wannier functions basis. *Computer Physics Communications*, 185(1), 422–429.

[63] Samsonidze, G., & Kozinsky, B. (2018). Accelerated screening of thermoelectric materials by first-principles computations of electron–phonon scattering. *Advanced Energy Materials*, 8(20), 1800246.

[64] Deng, T., Wu, G., Sullivan, M. B., Wong, Z. M., Hippalgaonkar, K., Wang, J. S., & Yang, S. W. (2020). EPIC STAR: a reliable and efficient approach for phonon-and impurity-limited charge transport calculations. *npj Computational Materials*, 6(1), 1–11.

[65] Ganose, A. M., Park, J., Faghaninia, A., Woods-Robinson, R., Persson, K. A., & Jain, A. (2021). Efficient calculation of carrier scattering rates from first principles. *Nature communications*, 12(1), 1–9.

[66] Zhou, J. J., Park, J., Lu, I. T., Maliyov, I., Tong, X., & Bernardi, M. (2021). Perturbo: A software package for ab initio electron–phonon interactions, charge transport and ultrafast dynamics. *Computer Physics Communications*, 264, 107970.

[67] Protik, N. H., Li, C., Pruneda, M., Broido, D., & Ordejón, P. (2022). The elphbolt ab initio solver for the coupled electron-phonon Boltzmann transport equations. *npj Computational Materials*, 8(1), 1–9.

[68] Zhou, J. J., & Bernardi, M. (2016). Ab initio electron mobility and polar phonon scattering in GaAs. *Physical Review B*, 94(20), 201201.

[69] Cao, J., Querales-Flores, J. D., Murphy, A. R., Fahy, S., & Savić, I. (2018). Dominant electron-phonon scattering mechanisms in n-type PbTe from first principles. *Physical Review B*, 98(20), 205202.

[70] Poncé, S., Jena, D., & Giustino, F. (2019). Hole mobility of strained GaN from first principles. *Physical Review B*, 100(8), 085204.

[71] Bardeen, J., & Shockley, W. (1950). Deformation potentials and mobilities in non-polar crystals. *Physical review*, 80(1), 72.

[72] Herring, C., & Vogt, E. (1956). Transport and deformation-potential theory for many-valley semiconductors with anisotropic scattering. *Physical review*, 101(3), 944.

[73] Ravich, Y. I., Efimova, B. A., & Tamarchenko, V. I. (1971). Scattering of current carriers and transport phenomena in lead chalcogenides. *physica status solidi (b)*, 43(1), 11–33.

[74] Ravich, I. I. (2013). *Semiconducting lead chalcogenides* (Vol. 5). Springer Science & Business Media.

[75] Bilc, D. I., Mahanti, S. D., & Kanatzidis, M. G. (2006). Electronic transport properties of PbTe and $AgPb_mSbTe_{2+m}$ systems. *Physical Review B*, 74(12), 125202.

[76] Pei, Y., Shi, X., LaLonde, A., Wang, H., Chen, L., & Snyder, G. J. (2011). Convergence of electronic bands for high performance bulk thermoelectrics. *Nature*, 473(7345), 66–69.

[77] Pei, Y., LaLonde, A. D., Wang, H., & Snyder, G. J. (2012). Low effective mass leading to high thermoelectric performance. *Energy & Environmental Science*, 5(7), 7963–7969.

[78] Witting, I. T., Ricci, F., Chasapis, T. C., Hautier, G., & Snyder, G. J. (2020). The Thermoelectric Properties of n-type Bismuth Telluride: Bismuth Selenide Alloys. *Research*, 2020, 1–15.

[79] Broido, D. A., Malorny, M., Birner, G., Mingo, N., & Stewart, D. A. (2007). Intrinsic lattice thermal conductivity of semiconductors from first principles. *Applied Physics Letters*, 91(23), 231922.

[80] Togo, A., Chaput, L., & Tanaka, I. (2015). Distributions of phonon lifetimes in Brillouin zones. *Physical review B*, 91(9), 094306.

[81] Li, W., Carrete, J., Katcho, N. A., & Mingo, N. (2014). ShengBTE: A solver of the Boltzmann transport equation for phonons. *Computer Physics Communications*, 185(6), 1747–1758.

[82] Tadano, T., Gohda, Y., & Tsuneyuki, S. (2014). Anharmonic force constants extracted from first-principles molecular dynamics: applications to heat transfer simulations. *Journal of Physics: Condensed Matter*, 26(22), 225402.

[83] Schelling, P. K., Phillpot, S. R., & Keblinski, P. (2002). Comparison of atomic-level simulation methods for computing thermal conductivity. *Physical Review B*, 65(14), 144306.

[84] McGaughey, A. J., & Kaviany, M. (2006). Phonon transport in molecular dynamics simulations: formulation and thermal conductivity prediction. *Advances in heat transfer*, 39, 169–255.

[85] Green, M. S. (1954). Markoff random processes and the statistical mechanics of time-dependent phenomena. II. Irreversible processes in fluids. *The Journal of Chemical Physics*, 22(3), 398–413.

[86] Kubo, R. (1957). Statistical-mechanical theory of irreversible processes. I. General theory and simple applications to magnetic and conduction problems. *Journal of the Physical Society of Japan*, 12(6), 570–586.

[87] Toher, C., Plata, J. J., Levy, O., De Jong, M., Asta, M., Nardelli, M. B., & Curtarolo, S. (2014). High-throughput computational screening of thermal conductivity, Debye temperature, and Grüneisen parameter using a quasiharmonic Debye model. *Physical Review B*, 90(17), 174107.

[88] Morelli, D. T., & Slack, G. A. (2006). High lattice thermal conductivity solids. In *High thermal conductivity materials* (pp. 37–68). Springer, New York, NY.

[89] Callaway, J. (1959). Model for lattice thermal conductivity at low temperatures. *Physical Review*, 113(4), 1046.

[90] Asen-Palmer, M., Bartkowski, K., Gmelin, E., Cardona, M., Zhernov, A. P., Inyushkin, A. V., ... & Haller, E. E. (1997). Thermal conductivity of germanium crystals with different isotopic compositions. *Physical review B*, 56(15), 9431.

[91] Morelli, D. T., Heremans, J. P., & Slack, G. A. (2002). Estimation of the isotope effect on the lattice thermal conductivity of group IV and group III-V semiconductors. *Physical Review B*, 66(19), 195304.

[92] Zhang, Y. (2016). First-principles Debye–Callaway approach to lattice thermal conductivity. *Journal of Materiomics*, 2(3), 237–247.

[93] Gorai, P., Stevanović, V., & Toberer, E. S. (2017). Computationally guided discovery of thermoelectric materials. *Nature Reviews Materials*, 2(9), 1–16.

[94] Hao, S., Dravid, V. P., Kanatzidis, M. G., & Wolverton, C. (2019). Computational strategies for design and discovery of nanostructured thermoelectrics. *npj Computational Materials*, 5(1), 1–10.

[95] Moreno, J. J. G., Cao, J., Fronzi, M., & Assadi, M. H. N. (2020). A review of recent progress in thermoelectric materials through computational methods. *Materials for Renewable and Sustainable Energy*, 9(3), 1–22.

[96] Madsen, G. K. (2006). Automated search for new thermoelectric materials: the case of LiZnSb. *Journal of the American Chemical Society*, 128(37), 12140–12146.

[97] Yang, J., Li, H., Wu, T., Zhang, W., Chen, L., & Yang, J. (2008). Evaluation of half-Heusler compounds as thermoelectric materials based on the calculated electrical transport properties. *Advanced Functional Materials*, 18(19), 2880–2888.

[98] Zhu, H., Hautier, G., Aydemir, U., Gibbs, Z. M., Li, G., Bajaj, S., ... & Ceder, G. (2015). Computational and experimental investigation of $TmAgTe_2$ and XYZ_2 compounds, a new group of thermoelectric materials identified by first-principles high-throughput screening. *Journal of Materials Chemistry C*, 3(40), 10554–10565.

[99] Carrete, J., Mingo, N., Wang, S., & Curtarolo, S. (2014). Nanograined Half-Heusler Semiconductors as Advanced Thermoelectrics: An Ab Initio High-Throughput Statistical Study. *Advanced Functional Materials*, 24(47), 7427–7432.

[100] Xi, L., Pan, S., Li, X., Xu, Y., Ni, J., Sun, X., ... & Zhang, W. (2018). Discovery of high-performance thermoelectric chalcogenides through reliable high-throughput material screening. *Journal of the American Chemical Society*, 140(34), 10785–10793.

[101] Yan, J., Gorai, P., Ortiz, B., Miller, S., Barnett, S. A., Mason, T., ... & Toberer, E. S. (2015). Material descriptors for predicting thermoelectric performance. *Energy & Environmental Science*, 8(3), 983–994.

[102] Gorai, P., Parilla, P., Toberer, E. S., & Stevanovic, V. (2015). Computational exploration of the binary A1B1 chemical space for thermoelectric performance. *Chemistry of Materials*, 27(18), 6213–6221.

[103] Gorai, P., Toberer, E. S., & Stevanović, V. (2016). Computational identification of promising thermoelectric materials among known quasi-2D binary compounds. *Journal of Materials Chemistry A*, 4(28), 11110–11116.

[104] Jia, T., Feng, Z., Guo, S., Zhang, X., & Zhang, Y. (2020). Screening promising thermoelectric materials in binary chalcogenides through high-throughput computations. *ACS applied materials & interfaces*, 12(10), 11852–11864.

[105] Klemens, P. G. (1955). The scattering of low-frequency lattice waves by static imperfections. *Proceedings of the Physical Society. Section A*, 68(12), 1113.

[106] Togo, A., Oba, F., & Tanaka, I. (2008). First-principles calculations of the ferroelastic transition between rutile-type and $CaCl_2$-type SiO_2 at high pressures. *Physical Review B*, 78(13), 134106.

[107] Voigt, W. (1910). *Lehrbuch der kristallphysik:(mit ausschluss der kristalloptik)* (Vol. 34). BG Teubner.

[108] Reuss, A. J. Z. A. M. M. (1929). Calculation of the flow limits of mixed crystals on the basis of the plasticity of monocrystals. *Z. Angew. Math. Mech*, 9, 49–58.

[109] Hill, R. (1952). The elastic behavior of a crystalline aggregate. *Proceedings of the Physical Society. Section A*, 65(5), 349.

[110] A. Fonari, C. Sutton, Effective mass calculator, can be found under, https://github .com /afonari/, 2012.

[111] Fan, T., & Oganov, A. R. (2020). AICON: A program for calculating thermal conductivity quickly and accurately. *Computer Physics Communications*, 251, 107074.

[112] Fan, T., & Oganov, A. R. (2021). AICON2: A program for calculating transport properties quickly and accurately. *Computer Physics Communications*, 266, 108027.

[113] McKinney, W. (2011). pandas: a foundational Python library for data analysis and statistics. *Python for high performance and scientific computing*, 14(9), 1–9.

[114] Ong, S. P., Richards, W. D., Jain, A., Hautier, G., Kocher, M., Cholia, S., ... & Ceder, G. (2013). Python Materials Genomics (pymatgen): A robust, open-source python library for materials analysis. *Computational Materials Science*, 68, 314–319.

[115] Mathew, K., Montoya, J. H., Faghaninia, A., Dwarakanath, S., Aykol, M., Tang, H., ... & Jain, A. (2017). Atomate: A high-level interface to generate, execute, and analyze computational materials science workflows. *Computational Materials Science*, 139, 140–152.

[116] Jain, A., Ong, S. P., Chen, W., Medasani, B., Qu, X., Kocher, M., ... & Persson, K. A. (2015). FireWorks: A dynamic workflow system designed for high-throughput applications. *Concurrency and Computation: Practice and Experience*, 27(17), 5037–5059.

[117] Tani, J. I., & Kido, H. (2005). Thermoelectric properties of Bi-doped Mg_2Si semiconductors. *Physica B: Condensed Matter*, 364(1-4), 218–224.

[118] Martin, J. J., & Shanks, H. R. (1974). Thermal conductivity of magnesium plumbide. *Journal of Applied Physics*, 45(6), 2428–2431.

[119] Onn, D., Witek, A., Qiu, Y. Z., Anthony, T. R., & Banholzer, W. F. (1992). Some aspects of the thermal conductivity of isotopically enriched diamond single crystals. *Physical review letters*, 68(18), 2806.

[120] Wei, L., Kuo, P. K., Thomas, R. L., Anthony, T. R., & Banholzer, W. F. (1993). Thermal conductivity of isotopically modified single crystal diamond. *Physical review letters*, 70(24), 3764.

[121] Ward, A., Broido, D. A., Stewart, D. A., & Deinzer, G. (2009). Ab initio theory of the lattice thermal conductivity in diamond. *Physical Review B*, 80(12), 125203.

[122] Kremer, R. K., Graf, K., Cardona, M., Devyatykh, G. G., Gusev, A. V., Gibin, A. M., ... & Pohl, H. J. (2004). Thermal conductivity of isotopically enriched 28Si: revisited. *Solid state communications*, 131(8), 499–503.

[123] Touloukian, Y. S., Powell, R. W., Ho, C. Y., & Klemens, P. G. (1970). *Thermophysical properties of matter-the tprc data series. volume 1. thermal conductivity-metallic elements and alloys*. THERMOPHYSICAL AND ELECTRONIC PROPERTIES INFORMATION ANALYSIS CENTER LAFAYETTE IN.

[124] Tate, J., Ju, H. L., Moon, J. C., Zakutayev, A., Richard, A. P., Russell, J., & McIntyre, D. H. (2009). Origin of p-type conduction in single-crystal CuAlO$_2$. *Physical review B*, 80(16), 165206.

[125] Pödör, B., Balázs, J., & Hársy, M. (1971). Electron concentration and mobility in CdS single crystals. *physica status solidi (a)*, 8(2), 613–624.

[126] Smith, F. T. J. (1970). High temperature electrical properties of CdSe: Evidence for a native donor. *Solid State Communications*, 8(4), 263–266.

[127] Btirmeister Jr, R. A., & Stevenson, D. A. (1967). Electrical Properties of n-Type CdSe. *physica status solidi (b)*, 24(2), 683–694.

[128] Segall, B., Lorenz, M. R., & Halsted, R. E. (1963). Electrical properties of n-type CdTe. *Physical Review*, 129(6), 2471.

[129] Smith, F. T. J. (1970). Electrically active point defects in cadmium telluride. *Metallurgical and Materials Transactions B*, 1(3), 617–621.

[130] Rode, D. L., & Knight, S. (1971). Electron transport in GaAs. *Physical Review B*, 3(8), 2534.

[131] Amith, A., Kudman, I., & Steigmeier, E. F. (1965). Electron and phonon scattering in GaAs at high temperatures. *Physical Review*, 138(4A), A1270.

[132] Steigerwald, D., Rudaz, S., Liu, H., Kern, R. S., Götz, W., & Fletcher, R. (1997). III–V nitride semiconductors for high-performance blue and green light-emitting devices. *Jom*, 49(9), 18–23.

[133] Taylor, R. C., Woods, J. F., & Lorenz, M. R. (1968). Electrical and Optical Properties of Vapor-Grown GaP. *Journal of Applied Physics*, 39(12), 5404–5411.

[134] Galavanov, V. V., & Siukaev, N. V. (1970). On mechanism of electron scattering in InP. *physica status solidi (b)*, 38(2), 523–530.

[135] Petritz, R. L., & Scanlon, W. W. (1955). Mobility of electrons and holes in the polar crystal, PbS. *Physical Review*, 97(6), 1620.

[136] Pei, Y., LaLonde, A., Iwanaga, S., & Snyder, G. J. (2011). High thermoelectric figure of merit in heavy hole dominated PbTe. *Energy & Environmental Science*, 4(6), 2085–2089.

[137] Shinohara, M., Yamanaka, M., Daimon, H., Sakuma, E., Okumura, H., Misawa, S., ... & Yoshida, S. (1988). Growth of high-mobility 3C-SiC epilayers by chemical vapor deposition. *Japanese journal of applied physics*, 27(3A), L434.

[138] Fonstad, C. G., & Rediker, R. H. (1971). Electrical properties of high-quality stannic oxide crystals. *Journal of applied physics*, 42(7), 2911–2918.

[139] Hutson, A. R. (1957). Hall effect studies of doped zinc oxide single crystals. *Physical review*, 108(2), 222.

[140] Kröger, F. A. (1956). Some optical and electrical measurements on blue fluorescent ZnS-Cl single crystals. *Physica*, 22(6-12), 637–643.

[141] Aven, M. (1971). High Electron Mobility in Zinc Selenide Through Low-Temperature Annealing. *Journal of Applied Physics*, 42(3), 1204–1208.

[142] Witting, I. T., Chasapis, T. C., Ricci, F., Peters, M., Heinz, N. A., Hautier, G., & Snyder, G. J. (2019). The thermoelectric properties of bismuth telluride. *Advanced Electronic Materials*, 5(6), 1800904.

[143] Jeon, H. W., Ha, H. P., Hyun, D. B., & Shim, J. D. (1991). Electrical and thermoelectrical properties of undoped Bi_2Te_3-Sb_2Te_3 and Bi_2Te_3-Sb_2Te_3-Sb_2Se_3 single crystals. *Journal of Physics and Chemistry of Solids*, 52(4), 579–585.

[144] Morikawa, K. (1965). Seebeck effect in cadmium sulfide. *Journal of the Physical Society of Japan*, 20(5), 786–794.

[145] Sutadhar, S. K., & Chattopadhyay, D. (1979). Thermoelectric power of n-GaAs. *Journal of Physics C: Solid State Physics*, 12(9), 1693.

[146] Sułkowski, C., Chuchmała, A., Zaleski, A. J., Matusiak, M., Mucha, J., Głuchowski, P., & Stręk, W. (2010). Transport properties, specific heat and thermal conductivity of GaN nanocrystalline ceramic. *Journal of Solid State Chemistry*, 183(10), 2501–2505.

[147] Kudman, I., & Steigmeier, E. F. (1964). Thermal conductivity and Seebeck coefficient of InP. *Physical Review*, 133(6A), A1665.

[148] Wang, H., Schechtel, E., Pei, Y., & Snyder, G. J. (2013). High Thermoelectric Efficiency of n-type PbS. *Advanced Energy Materials*, 3(4), 488–495.

[149] Morgan, D. F., & Wright, D. A. (1966). Electrical properties of single crystals of antimony-doped stannic oxide. *British Journal of Applied Physics*, 17(3), 337.

[150] Tsubota, T., Ohtaki, M., Eguchi, K., & Arai, H. (1997). Thermoelectric properties of Al-doped ZnO as a promising oxidematerial for high-temperature thermoelectric conversion. *Journal of Materials Chemistry*, 7(1), 85–90.

[151] Jain, A., Ong, S. P., Hautier, G., Chen, W., Richards, W. D., Dacek, S., ... & Persson, K. A. (2013). Commentary: The Materials Project: A materials genome approach to accelerating materials innovation. *APL materials*, 1(1), 011002.

[152] Kresse, G., & Furthmüller, J. (1996). Efficient iterative schemes for ab initio total-energy calculations using a plane-wave basis set. *Physical review B*, 54(16), 11169.

[153] Kresse, G., & Furthmüller, J. (1996). Efficiency of ab-initio total energy calculations for metals and semiconductors using a plane-wave basis set. *Computational materials science*, 6(1), 15–50.

[154] Perdew, J. P., Burke, K., & Ernzerhof, M. (1996). Generalized gradient approximation made simple. *Physical review letters*, 77(18), 3865.

[155] Gonze, X., & Lee, C. (1997). Dynamical matrices, Born effective charges, dielectric permittivity tensors, and interatomic force constants from density-functional perturbation theory. *Physical Review B*, 55(16), 10355.

[156] Togo, A., & Tanaka, I. (2015). First principles phonon calculations in materials science. *Scripta Materialia*, 108, 1–5.

[157] Tran, F., & Blaha, P. (2009). Accurate band gaps of semiconductors and insulators with a semilocal exchange-correlation potential. *Physical review letters*, 102(22), 226401.

[158] Borlido, P., Aull, T., Huran, A. W., Tran, F., Marques, M. A., & Botti, S. (2019). Large-scale benchmark of exchange–correlation functionals for the determination of electronic band gaps of solids. *Journal of chemical theory and computation*, 15(9), 5069–5079.

[159] Gan, Y., Wang, G., Zhou, J., & Sun, Z. (2021). Prediction of thermoelectric performance for layered IV-V-VI semiconductors by high-throughput ab initio calculations and machine learning. *npj Computational Materials*, 7(1), 1–10.

[160] Wang, X., Zeng, S., Wang, Z., & Ni, J. (2020). Identification of crystalline materials with ultra-low thermal conductivity based on machine learning study. *The Journal of Physical Chemistry C*, 124(16), 8488–8495.

[161] Butler, K. T., Davies, D. W., Cartwright, H., Isayev, O., & Walsh, A. (2018). Machine learning for molecular and materials science. *Nature*, 559(7715), 547–555.

[162] Maintz, S., Deringer, V. L., Tchougréeff, A. L., & Dronskowski, R. (2013). Analytic projection from plane-wave and PAW wavefunctions and application to chemical-bonding analysis in solids. *Journal of computational chemistry*, 34(29), 2557–2567.

[163] Maintz, S., Deringer, V. L., Tchougréeff, A. L., & Dronskowski, R. (2016). LOBSTER: A tool to extract chemical bonding from plane-wave based DFT.

[164] Nelson, R., Ertural, C., George, J., Deringer, V. L., Hautier, G., & Dronskowski, R. (2020). LOBSTER: Local orbital projections, atomic charges, and chemical-bonding analysis from projector-augmented-wave-based density-functional theory. *Journal of Computational Chemistry*, 41(21), 1931–1940.

[165] Jia, T., Carrete, J., Zhang, Y., & Madsen, G. K. (2020). Low thermal conductivities and excellent thermoelectric performances of the pyrite-type IIB-VIA$_2$ dichalcogenides: ZnS$_2$, CdS$_2$ and CdSe$_2$. *arXiv preprint arXiv:2005.05916*.

Appendices

A1. X_4Y_8 (X = VIII B, Y = VI A)

Compounds with this chemical formula include Fe_4S_8, Ru_4S_8, Ru_4Se_8, $Ru_4Se_4S_4$. These compounds have the same structure with a space group *Pa*-3 (Fig. A1). Each atom of group VIIIB forms an octahedron with six atoms of group VIA. Their band structures are shown in Fig. A2. Our calculations show that this group of compounds can have high power factor for p-type transport. However, their lattice thermal conductivity can also be high, therefore the figure of merit is not large.
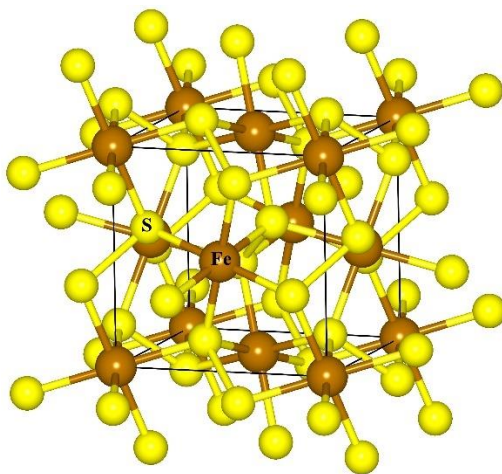
Figure A1. Crystal structure of pyrite Fe_4S_8.
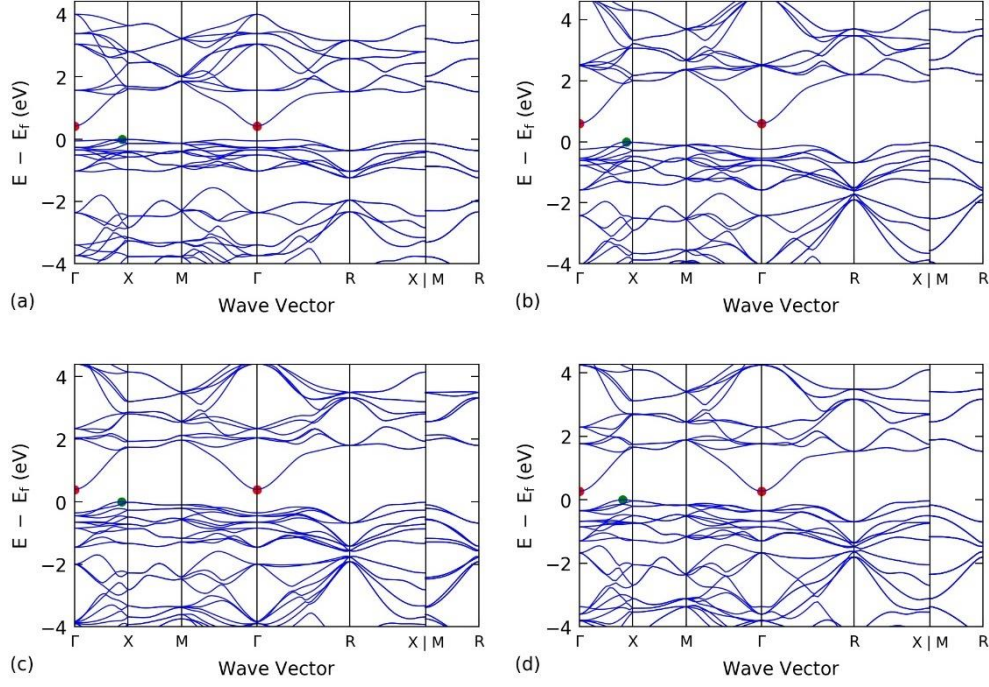
Figure A2. Band structures of (a) Fe_4S_8, (b) Ru_4S_8, (c) $Ru_4Se_4S_4$, and (d) Ru_4Se_8. The CBM and VBM are shown by red and green dots, respectively.

Table A1. Key parameters for p-type transport

	m_c^* (m_e)	m_d^* (m_e)	Ξ (eV)	N	E_g (eV)	c (GPa)	ε_∞	ε_0
Fe_4S_8	1.830	6.922	13.56	6	0.42	176.45	21.21	28.34
Ru_4S_8	0.969	3.822	13.87	6	0.60	162.54	16.65	20.70
$Ru_4Se_4S_4$	1.127	4.039	13.11	6	0.39	140.84	18.25	23.48
Ru_4Se_8	1.087	3.792	12.20	6	0.27	125.45	19.56	25.71
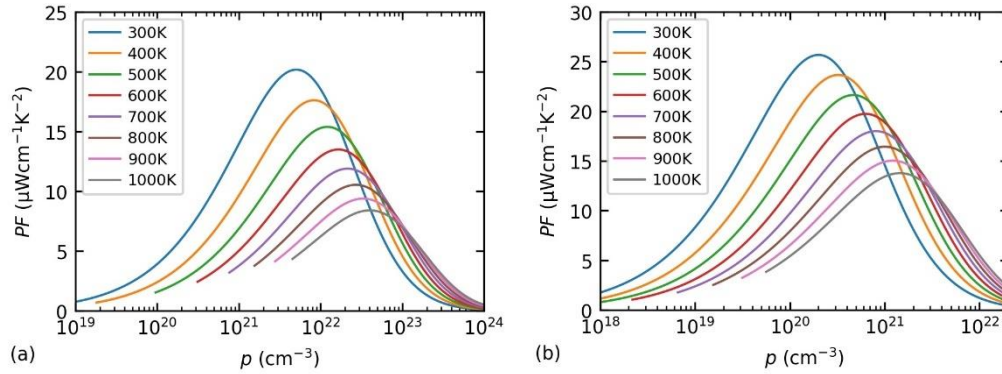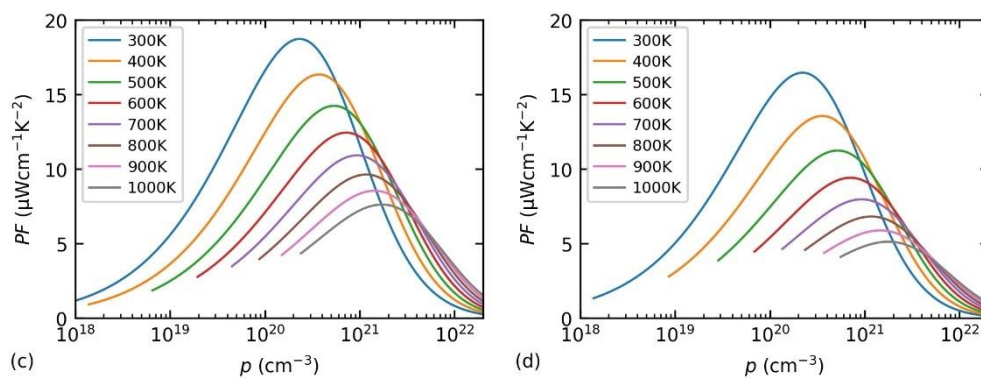
Figure A3. Power factor at varying temperatures and carrier concentrations for (a) Fe_4S_8, (b) Ru_4S_8, (c) $Ru_4Se_4S_4$, and (d) Ru_4Se_8.
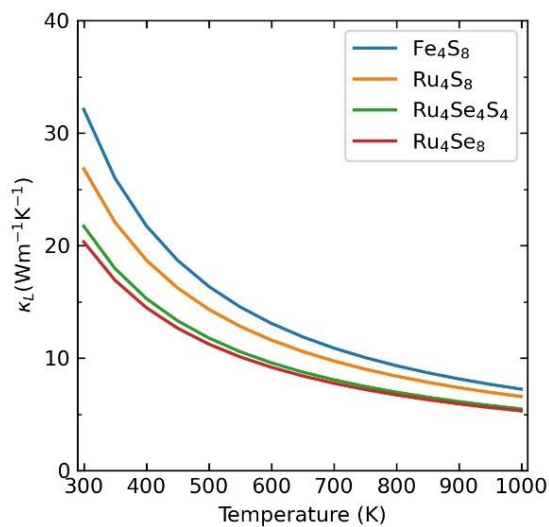
Figure A4. Lattice thermal conductivity of this group of compounds.
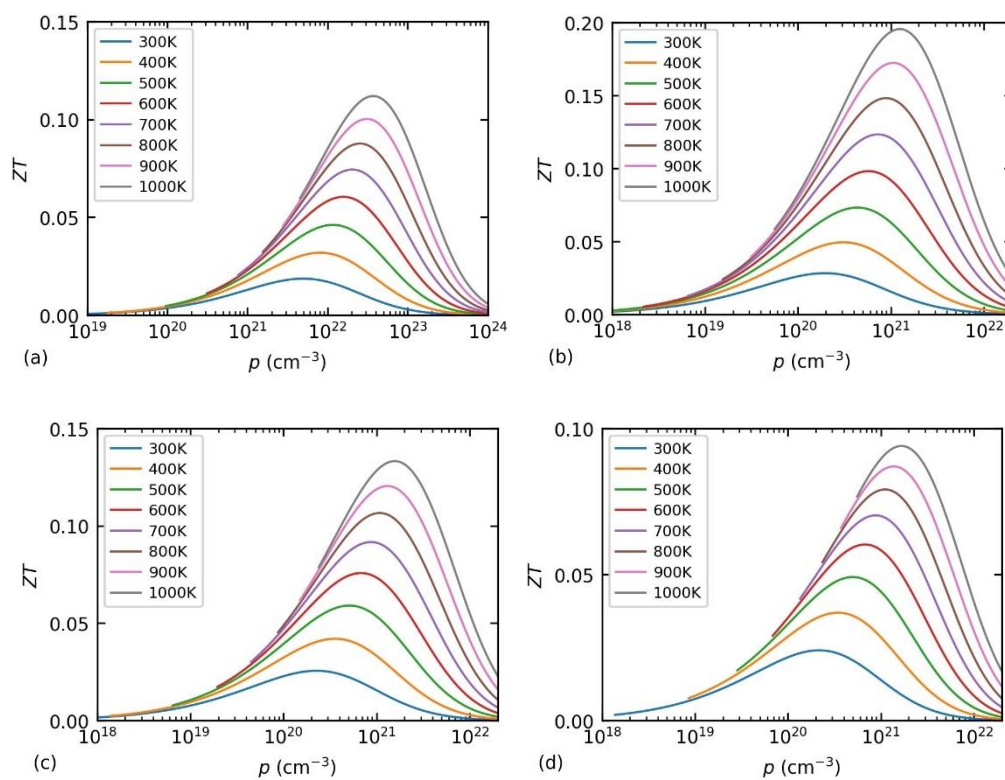
Figure A5. Figure of merit at varying temperatures and carrier concentrations for (a) Fe_4S_8, (b) Ru_4S_8, (c) $Ru_4Se_4S_4$, and (d) Ru_4Se_8.

A2. ScCoTe, TiFeTe and ZrFeTe

These three compounds have the same crystal structure with a space group $F\text{-}43m$, (Fig. A6). Their band structures are shown in Fig. A7. Our calculations show that they are promising n-type thermoelectric materials.
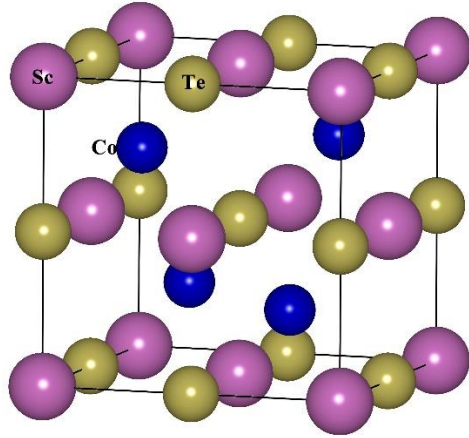
Figure A6. Crystal structure of ScCoTe.
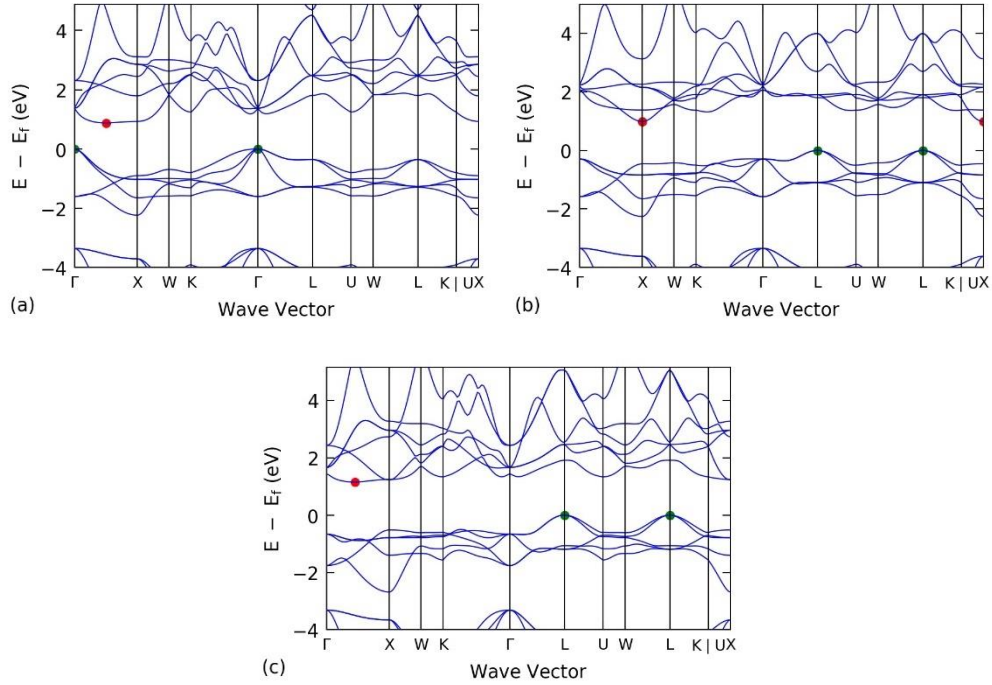
Figure A7. Band structures of (a) ScCoTe, (b) TiFeTe, and (c) ZrFeTe. The CBM and VBM are shown by red and green dots, respectively.

Table A2. Key parameters for n-type transport

	m_c^* (m_e)	m_d^* (m_e)	Ξ (eV)	N	E_g (eV)	c (GPa)	ε_∞	ε_0
ScCoTe	0.613	3.242	11.79	6	0.88	89.75	18.09	25.94
TiFeTe	0.691	1.457	12.57	3	0.98	102.56	21.34	38.27
ZrFeTe	0.630	3.224	14.54	6	1.16	100.59	20.26	38.23
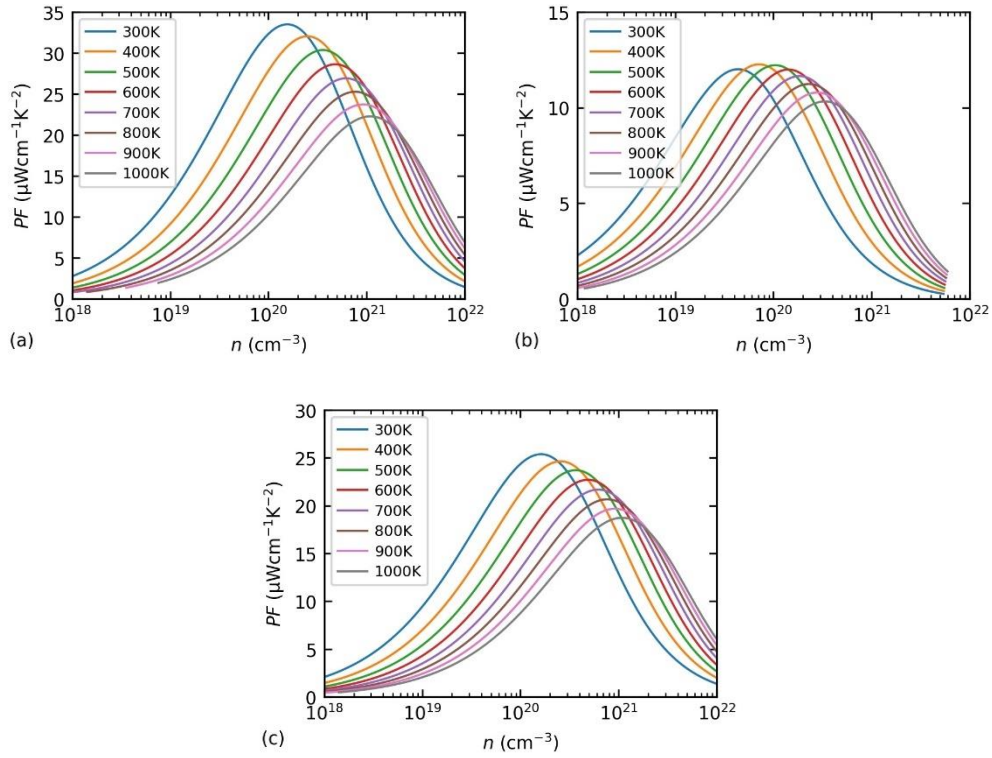
Figure A8. Power factors at varying temperatures and carrier concentrations for (a) ScCoTe, (b) TiFeTe, and (c) ZrFeTe.
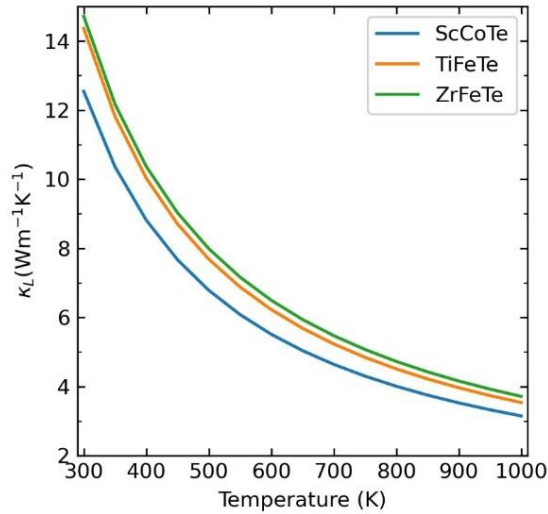
Figure A9. Lattice thermal conductivity of this group of compounds.
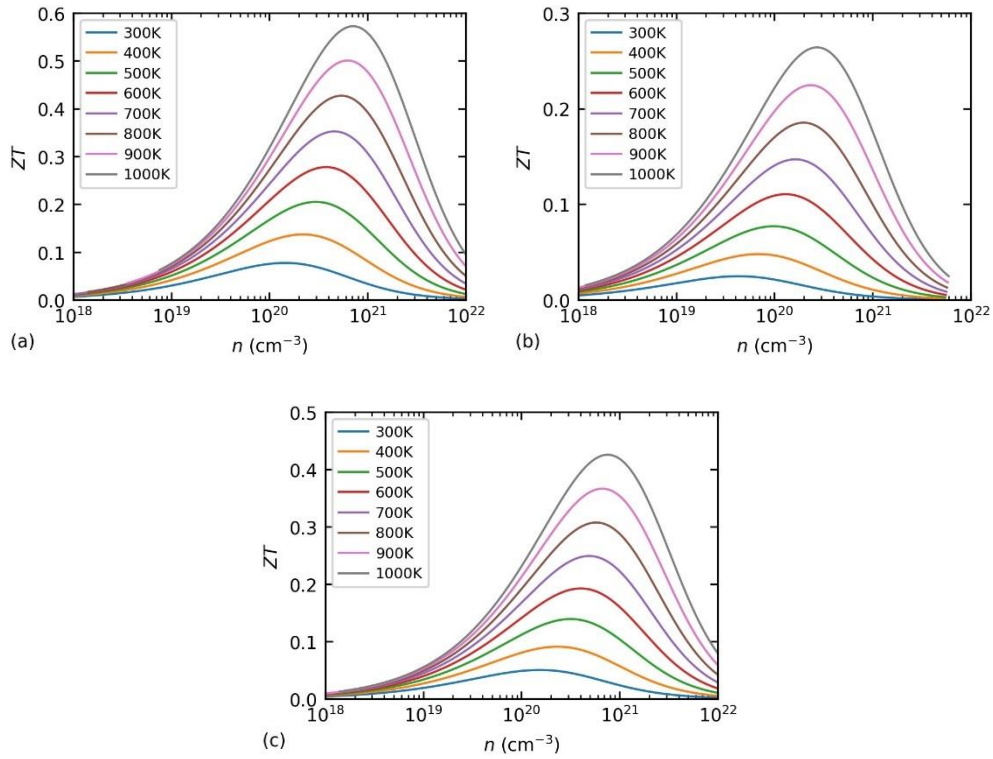
Figure A10. Figure of merit at varying temperatures and carrier concentrations for (a) ScCoTe, (b) TiFeTe, and (c) ZrFeTe.

A3. $Mg_2Co_4S_8$ and $Zn_2Co_4S_8$

These two compounds have the same crystal structure with a space group *Fd-3m* (Fig. A11). Their band structures are shown in Fig. A12. Our calculations show that these compounds have a high power factor for both n- and p-type transport. However, their lattice thermal conductivity is also high, therefore the figure of merit is low.
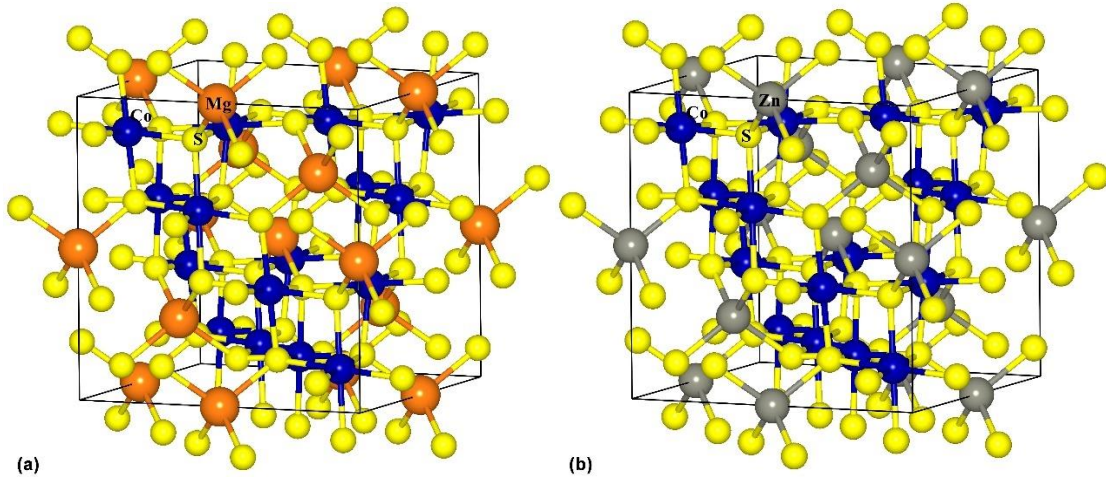
Figure A11. Crystal structure of (a) $Mg_2Co_4S_8$ and (b) $Zn_2Co_4S_8$.
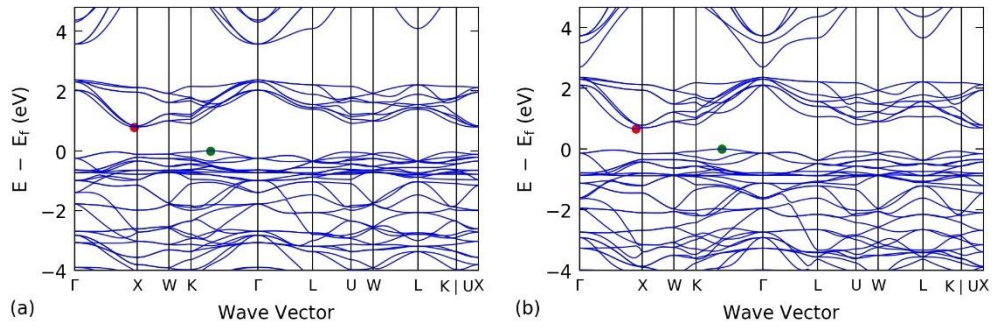
Figure A12. Band structures of (a) $Mg_2Co_4S_8$ and (b) $Zn_2Co_4S_8$. The CBM and VBM are shown by red and green dots, respectively.

Table A3. Key parameters for n-type and p-type transport

		m_c^* (m_e)	m_d^* (m_e)	Ξ (eV)	N	E_g (eV)	c (GPa)	ε_∞	ε_0
$Mg_2Co_4S_8$	CBM	0.583	1.984	11.90	6	0.79	57.42	15.49	16.66
	VBM	1.718	11.472	10.96	12				
$Zn_2Co_4S_8$	CBM	0.561	1.868	12.98	6	0.67	74.87	17.39	18.19
	VBM	1.795	12.060	12.09	12				
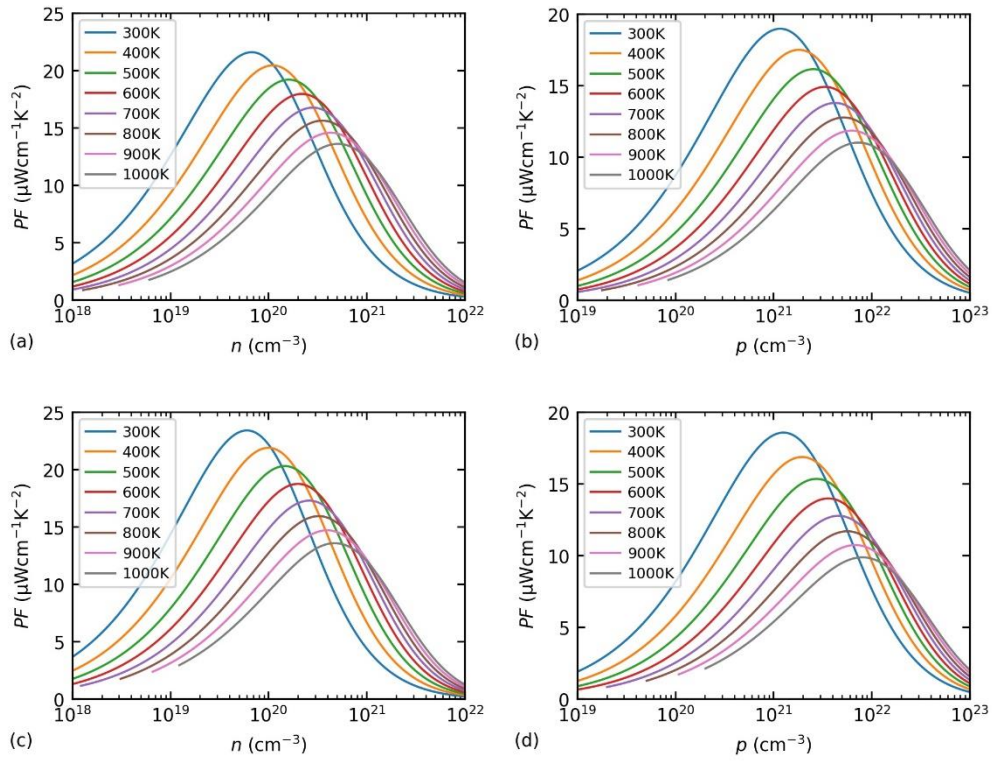
Figure A13. Power factor at varying temperatures and carrier concentrations for (a, b) $Mg_2Co_4S_8$ and (c, d) $Zn_2Co_4S_8$.
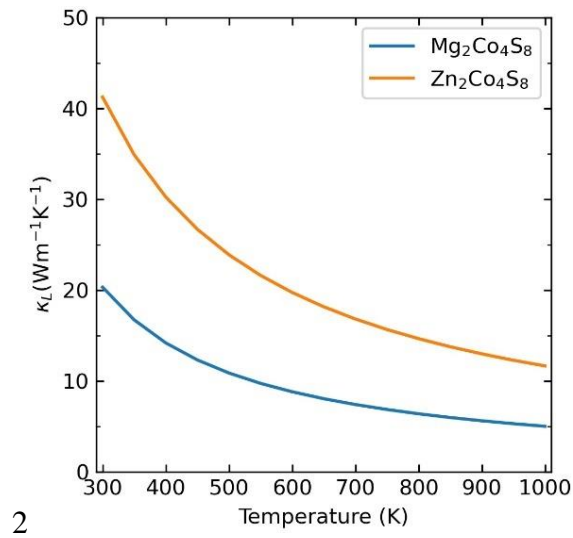
Figure A14. Lattice thermal conductivity of this group of compounds.
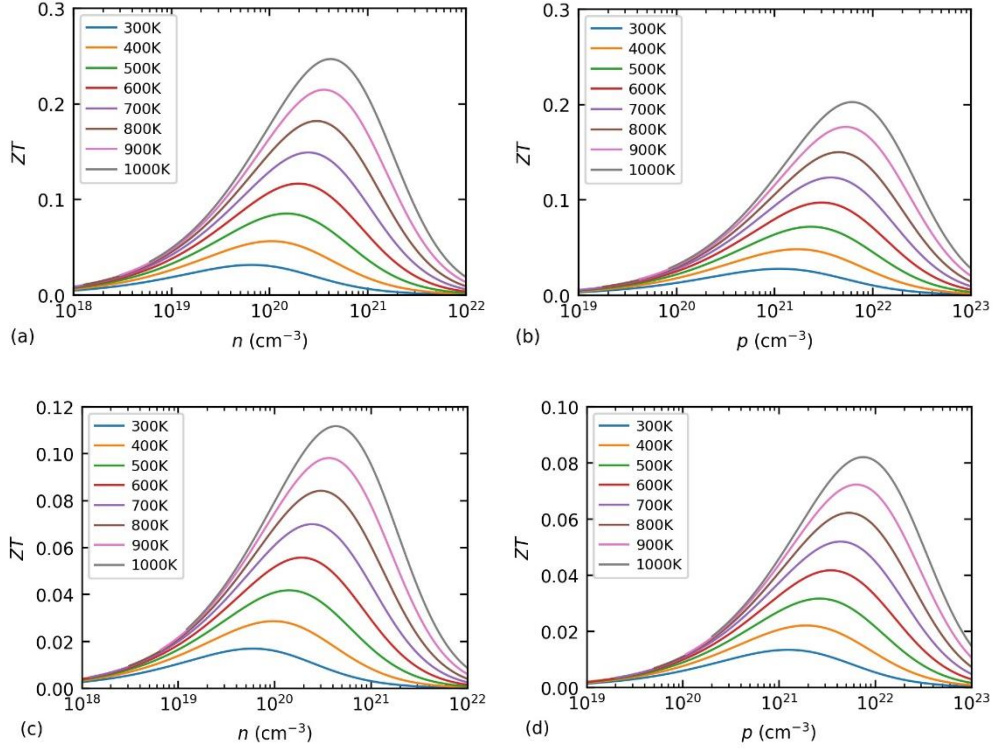
Figure A15. Figure of merit at varying temperatures and carrier concentrations for (a, b) $Mg_2Co_4S_8$ and (c, d) $Zn_2Co_4S_8$.

A4. Al₅CuSe₈

This compound has a structure with a space group *F*-43*m* (Fig. A16). Our calculations show that it is a promising thermoelectric material for p-type transport.

Table A4. Key parameters for p-type transport

	m_c^* (m_e)	m_d^* (m_e)	Ξ (eV)	N	E_g (eV)	c (GPa)	ε_∞	ε_0
Al₅CuSe₈	0.761	5.404	9.88	12	0.50	45.58	8.84	13.88
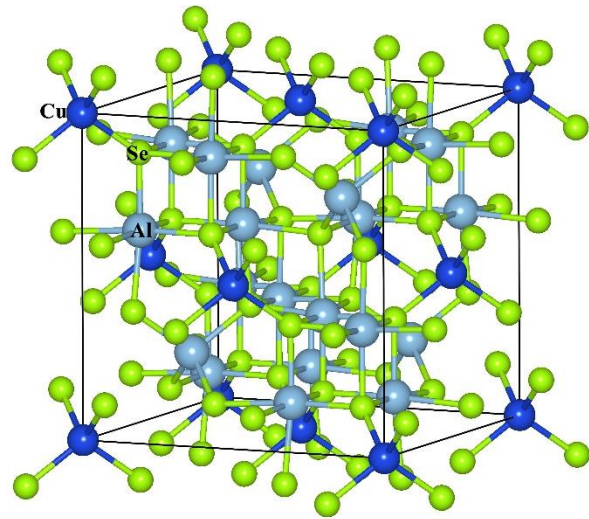
Figure A16. Crystal structure of Al$_5$CuSe$_8$.
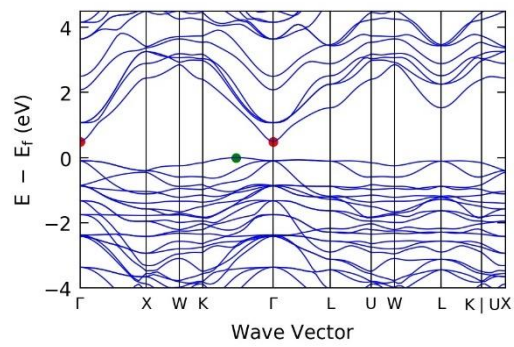
Figure A17. Band structure of Al$_5$CuSe$_8$.

(c)
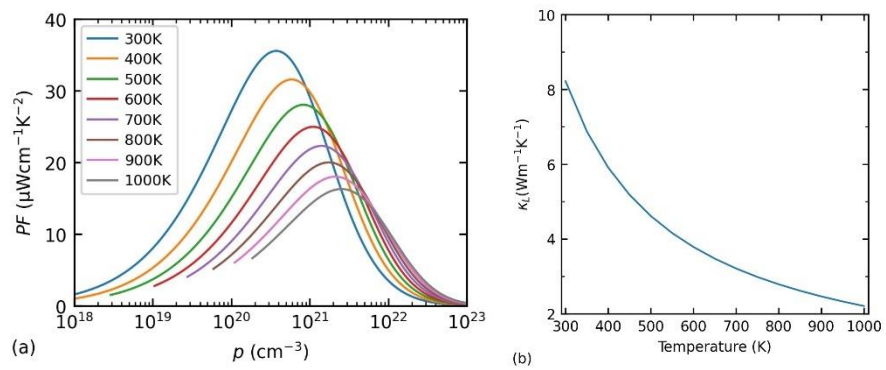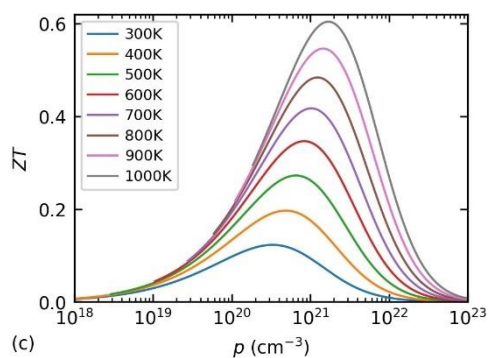
Figure A18. Thermoelectric properties of Al$_5$CuSe$_8$ for p-type transport. (a) power factor, (b) lattice thermal conductivity, and (c) figure of merit.

A5. CeSe$_2$

This compound has a structure with a space group *Fd*-3*m* (Fig. A.19). Our calculations show that it is a promising thermoelectric material for p-type transport.
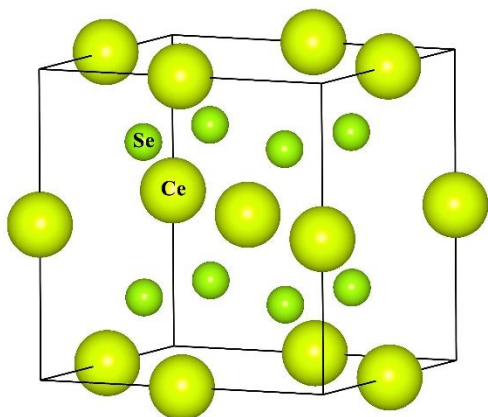
Figure A19. Crystal structure of CeSe$_2$.
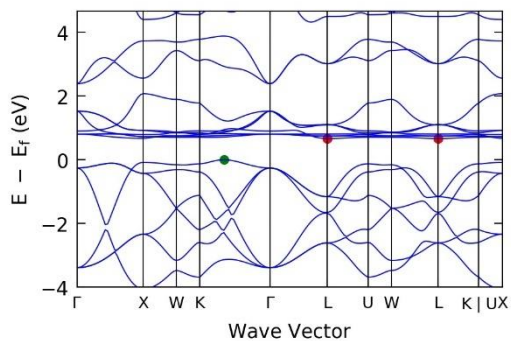
Figure A20. Band structure of CeSe$_2$.

165

Table A5. Key parameters for p-type transport

	m_c^* (m_e)	m_d^* (m_e)	Ξ (eV)	N	E_g (eV)	c (GPa)	ε_∞	ε_0
Ce$_4$Se$_8$	0.812	5.966	9.55	12	0.67	21.10	19.46	32.84

(a)

(b)

(c)
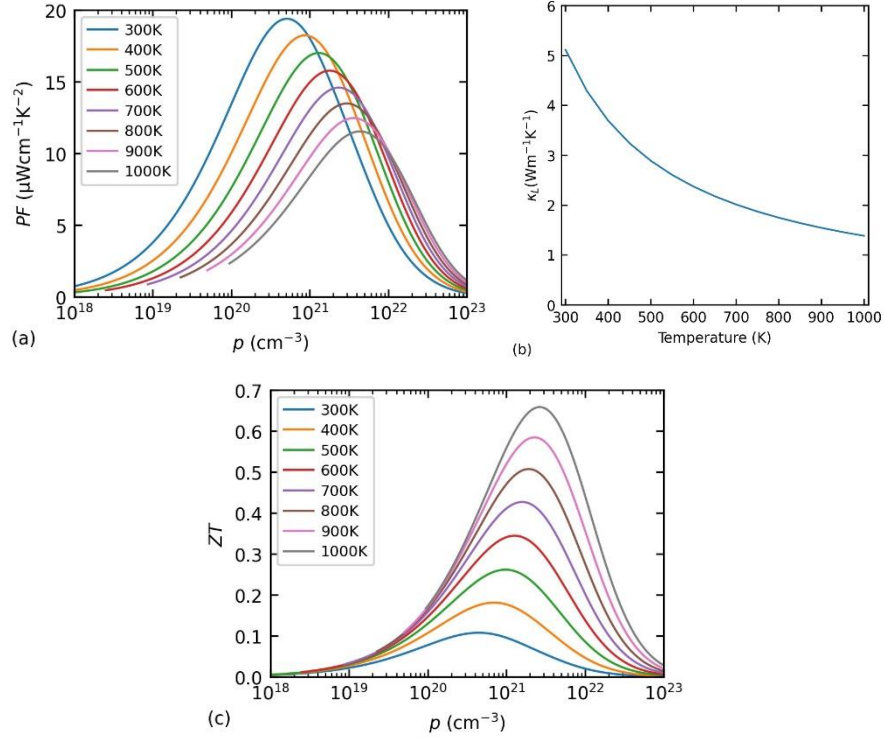
Figure A21. Thermoelectric properties of CeSe$_2$ for p-type transport. (a) power factor, (b) lattice thermal conductivity, and (c) figure of merit.

A6. Y$_4$Pt$_4$S$_{14}$

This compound has a structure with a space group *Fd-3m* (Fig. A22). Our calculations show that it is a promising thermoelectric material for p-type transport.

166
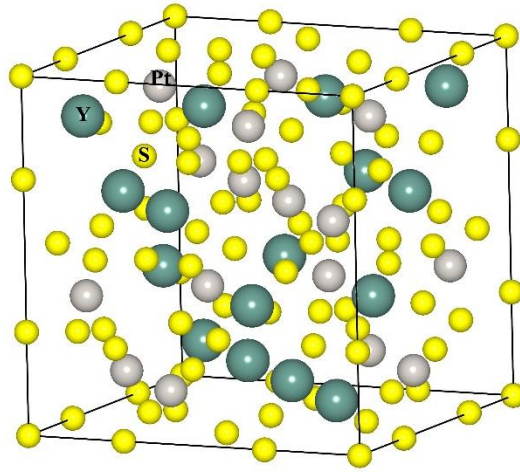
Figure A22. Crystal structure of $Y_4Pt_4S_{14}$.
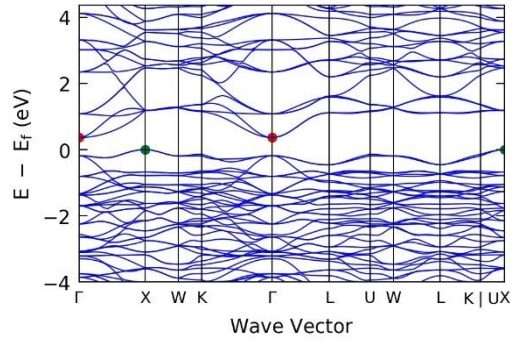
Figure A23. Band structure of $Y_4Pt_4S_{14}$.

Table A6. Key parameters for p-type transport

		m_c^* (m_e)	m_d^* (m_e)	Ξ (eV)	N	E_g (eV)	c (GPa)	ε_∞	ε_0
$Y_4Pt_4S_{14}$	VBM	0.611	1.282	10.64	3	0.36	63.19	14.95	22.69
	VSB	1.365	9.033	10.47	12	0.50			
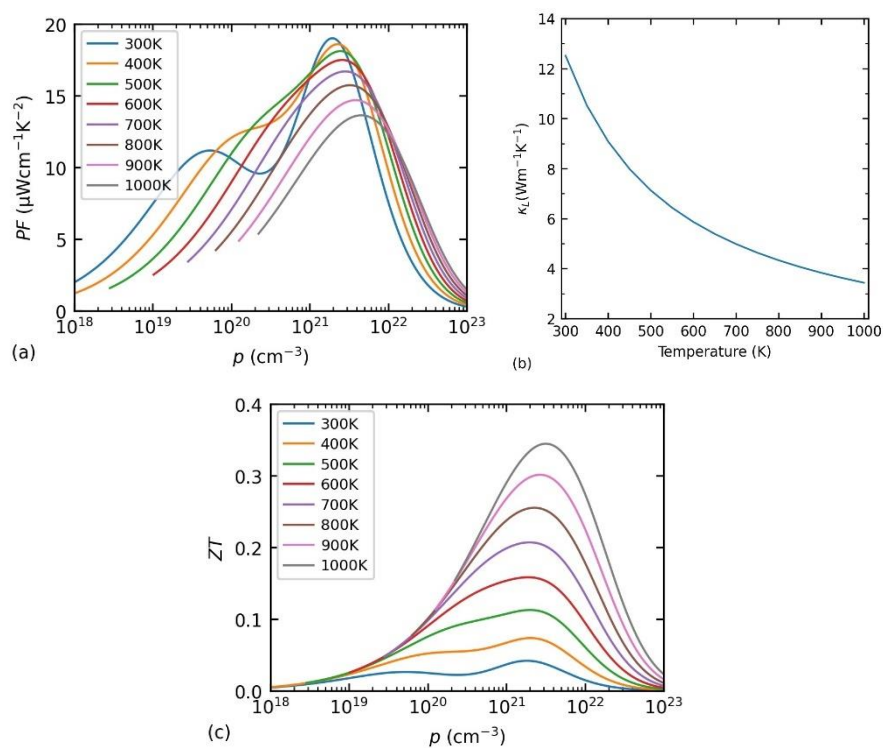
Figure A24. Thermoelectric properties of $Y_4Pt_4S_{14}$ for p-type transport. (a) power factor, (b) lattice thermal conductivity, and (c) figure of merit.

A.7. $Li_4Co_4S_8$

This compound has a structure with a space group *Fd*-3*m* (Fig. A25). Our calculations show that it is a promising thermoelectric material for p-type transport.
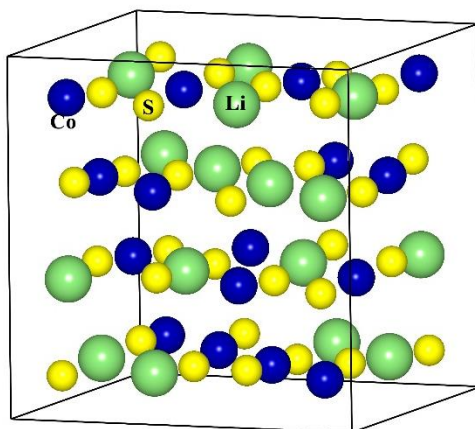
Figure A25. Crystal structure of $Li_4Co_4S_8$.
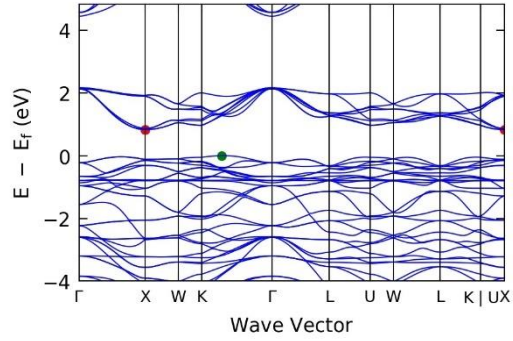
Figure A26. Band structure of Li$_4$Co$_4$S$_8$.

Table A7. Key parameters for p-type transport

	m_c^* (m_e)	m_d^* (m_e)	Ξ (eV)	N	E_g (eV)	c (GPa)	ε_∞	ε_0
Li$_4$Co$_4$S$_8$	1.993	12.395	10.95	12	0.83	61.97	17.42	28.24
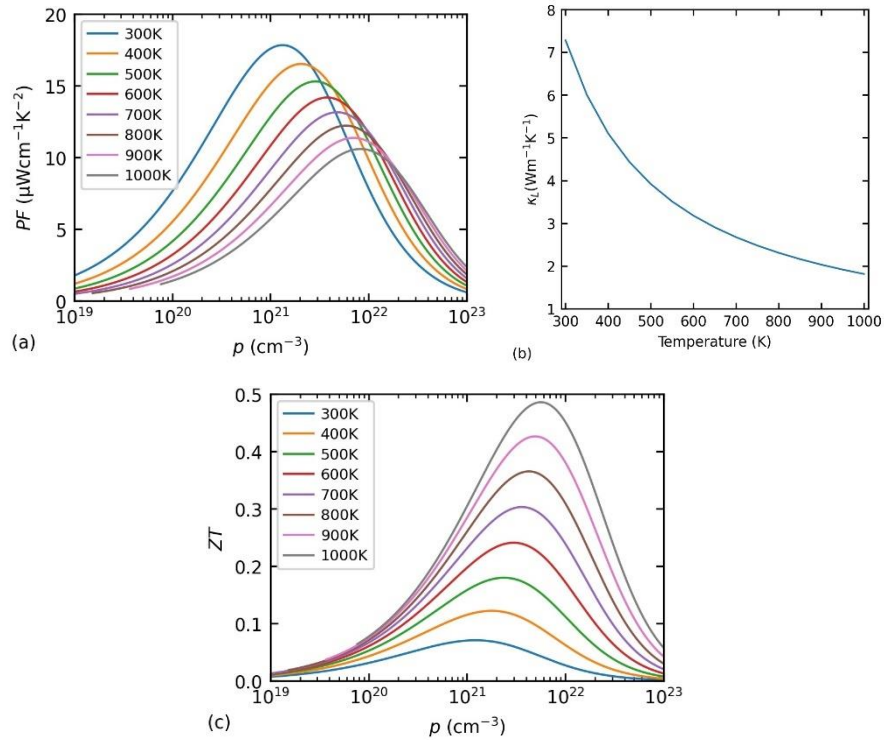
Figure A27. Thermoelectric properties of Li$_4$Co$_4$S$_8$ for p-type transport. (a) power factor, (b) lattice thermal conductivity, and (c) figure of merit.

A8. Ba$_2$Te$_4$
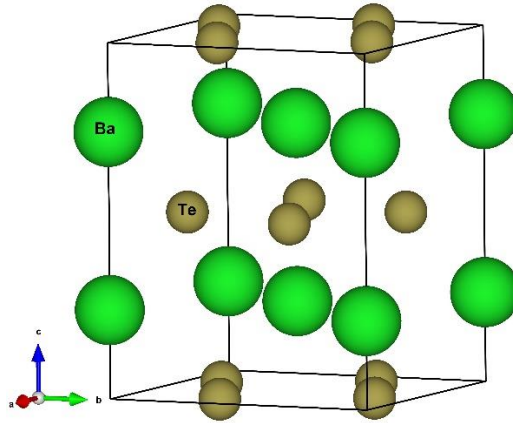
Figure A28. Crystal structure of Ba_2Te_4.
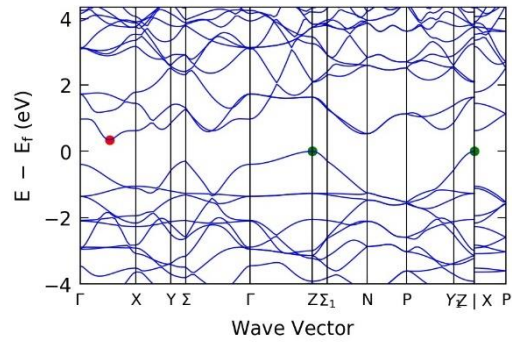
Figure A29. Band structure of Ba_2Te_4.

Table A8. Key parameters for n-type transport

	m_c^* (m_e)	m_d^* (m_e)	Ξ (eV)	N	E_g (eV)	c (GPa)	ε_∞	ε_0
Ba_2Te_4	0.345	1.275	7.31	4	0.34	20.79	8.83	13.34
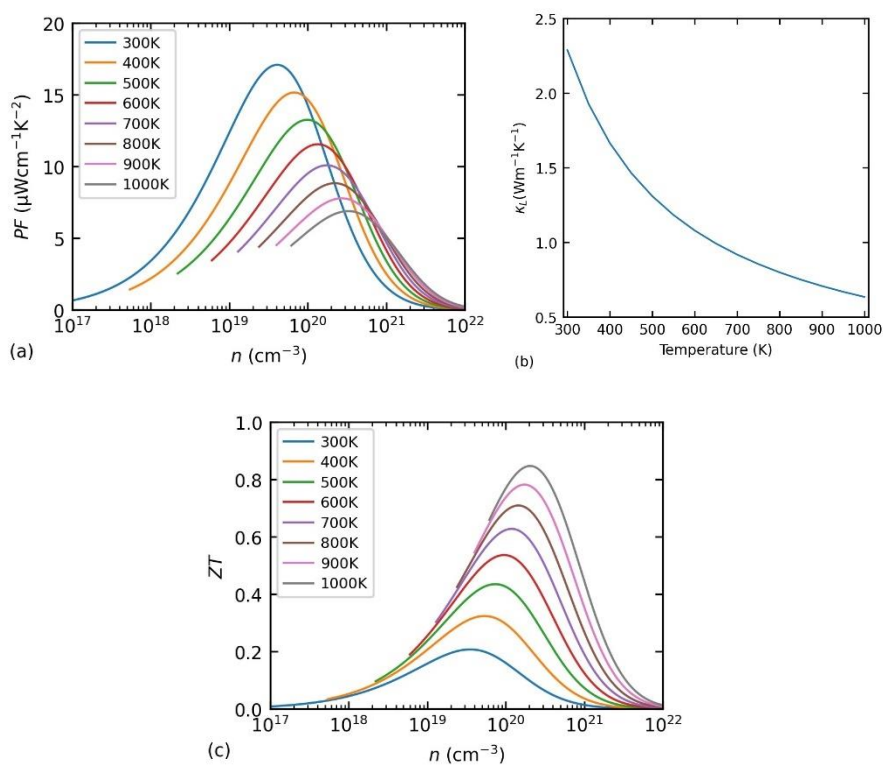
Figure A.30. Thermoelectric properties of Ba_2Te_4 for n-type transport. (a) power factor, (b) lattice thermal conductivity, and (c) figure of merit.

A9. Er₄As₄Se₄
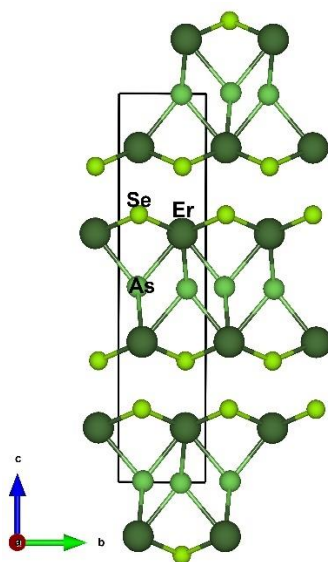
Figure A31. Crystal structure of Er₄As₄Se₄.
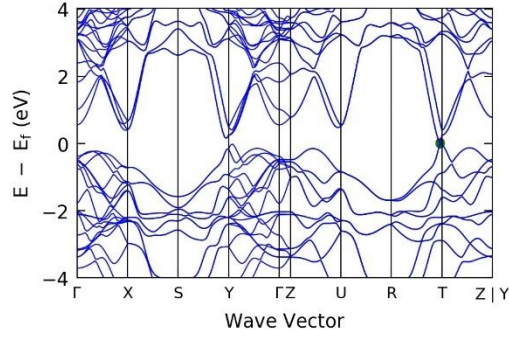
Figure A32. Band structure of Er₄As₄Se₄.

Table A9. Key parameters for n-type and p-type transport

		$m_c^*\,(m_e)$	$m_d^*\,(m_e)$	$\Xi\,(\mathrm{eV})$	N	$E_g\,(\mathrm{eV})$	$c\,(\mathrm{GPa})$	ε_∞	ε_0
Er₄As₄Se₄	CBM	0.023	0.048	7.20	2	0.02	68.07	41.13	47.16
	VBM	0.025	0.048	9.11	2				

(a)

(b)

(c)
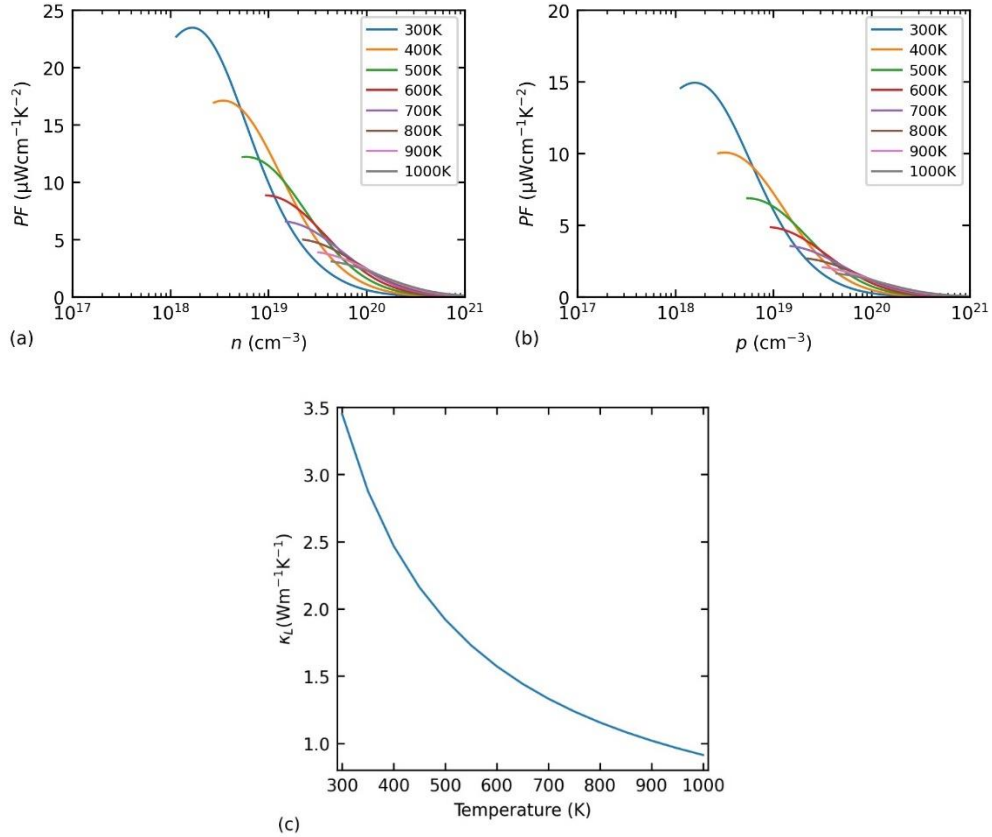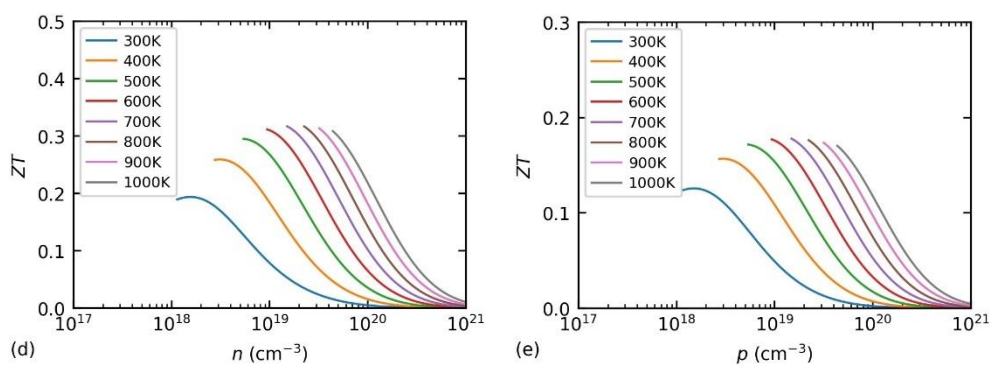
Figure A33. Thermoelectric properties of $Er_4As_4Se_4$ for n-type and p-type transport. (a, b) power factor, (c) lattice thermal conductivity, and (d, e) figure of merit.

A10. Dy₄As₄Se₄
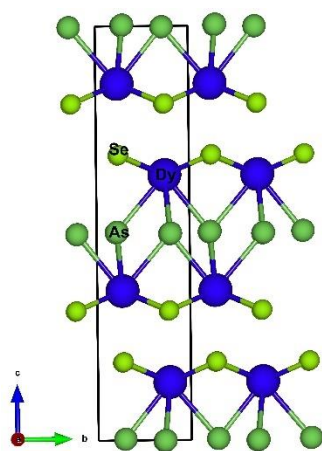
Figure A34. Crystal structure of Dy₄As₄Se₄.
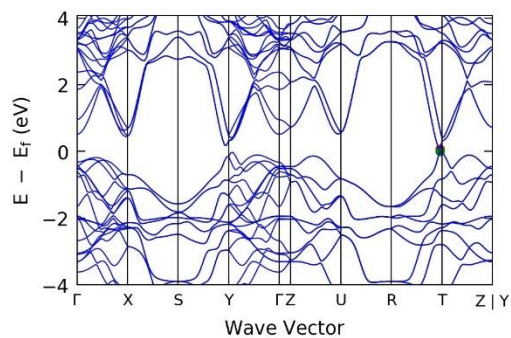
Figure A35. Band structure of Dy₄As₄Se₄.

Table A10. Key parameters for n-type and p-type transport

		m_c^* (m_e)	m_d^* (m_e)	Ξ (eV)	N	E_g (eV)	c (GPa)	ε_∞	ε_0
Dy$_4$As$_4$Se$_4$	CBM	0.031	0.073	4.83	2	0.07	66.56	28.40	33.67
	VBM	0.036	0.072	9.24	2				

(a)

(b)

(c)

(d)

(e)
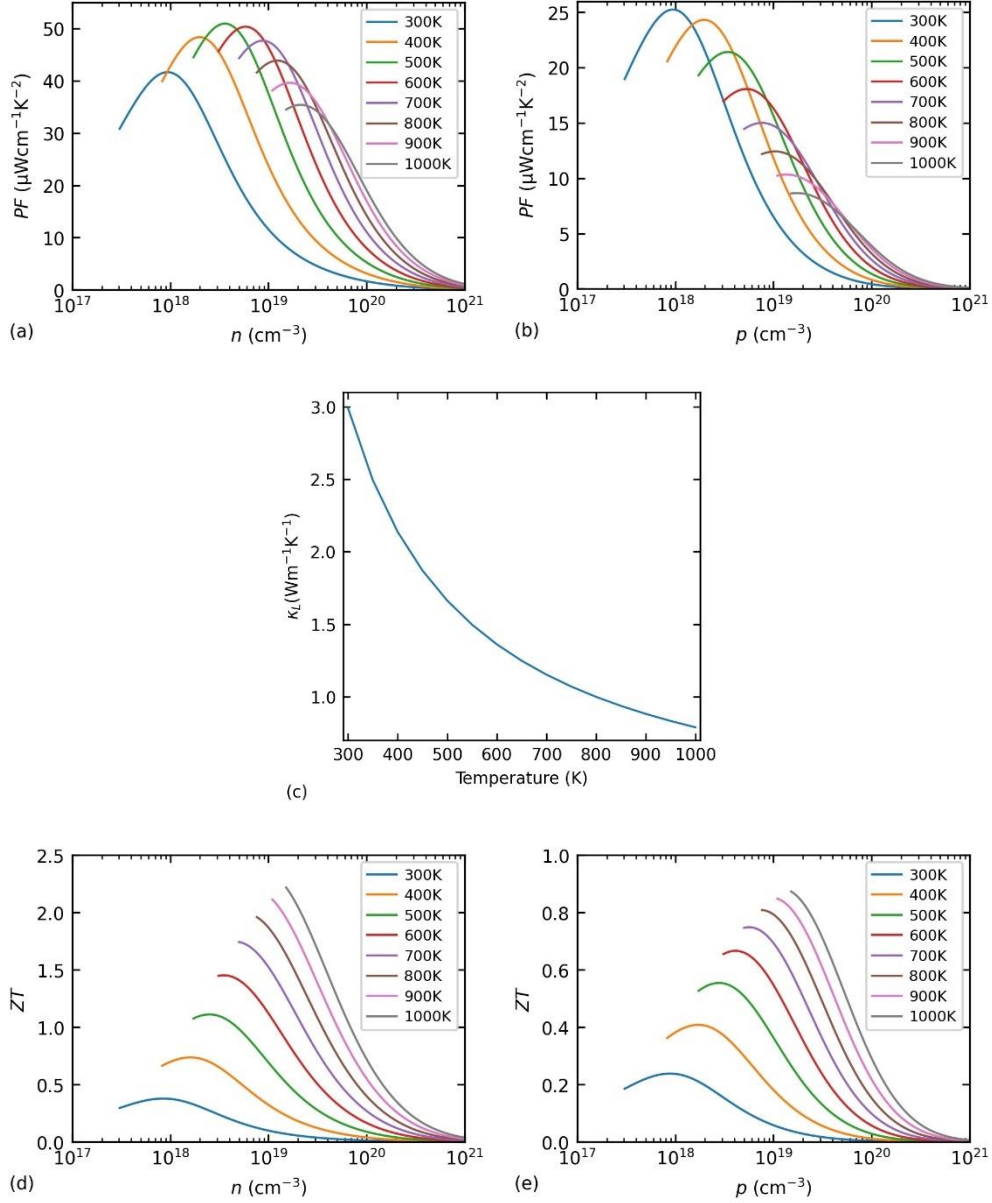
Figure A36. Thermoelectric properties of $Dy_4As_4Se_4$ for n-type and p-type transport. (a, b) power factor, (c) lattice thermal conductivity, and (d, e) figure of merit.

A11. Er_2Se_3
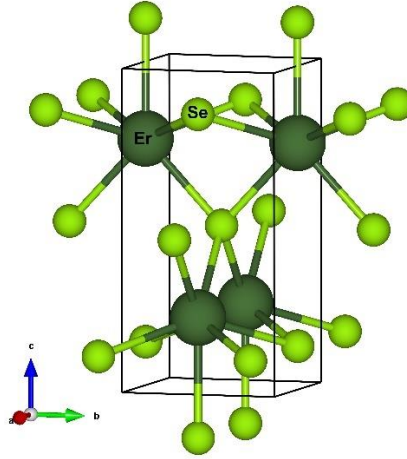
Figure A37. Crystal structure of Er_2Se_3.
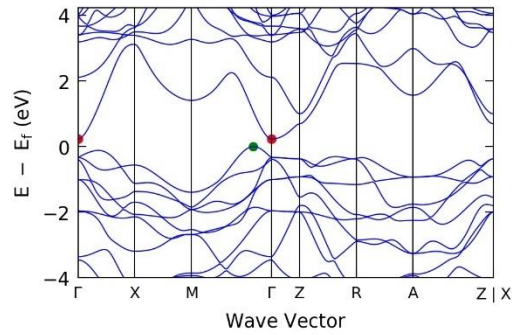
Figure A38. Band structure of Er_2Se_3.

Table A11. Key parameters for p-type transport

	m_c^* (m_e)	m_d^* (m_e)	Ξ (eV)	N	E_g (eV)	c (GPa)	ε_∞	ε_0
Er_2Se_3	0.517	1.317	7.78	4	0.23	53.67	9.27	17.08
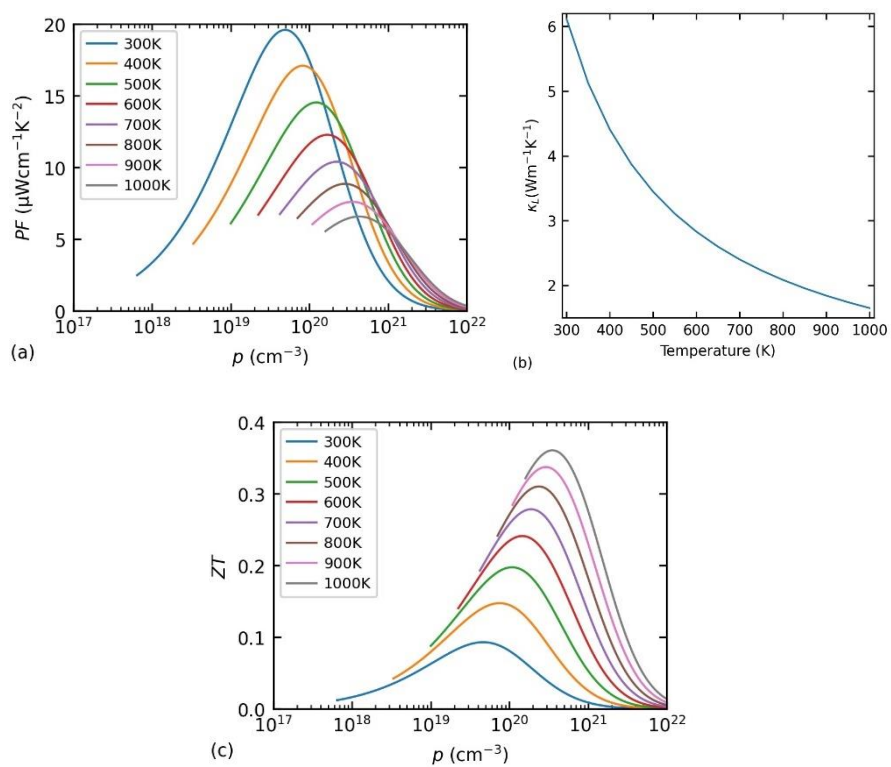
Figure A39. Thermoelectric properties of Er$_2$Se$_3$ for p-type transport. (a) power factor, (b) lattice thermal conductivity, and (c) figure of merit.

A12. Co$_4$As$_4$S$_4$
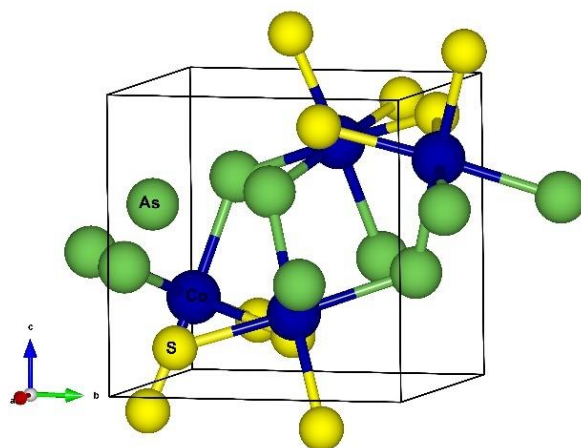
Figure A40. Crystal structure of Co$_4$As$_4$S$_4$.
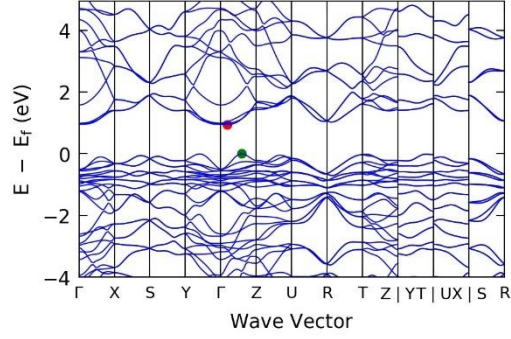
Figure A41. Band structure of Co₄As₄S₄.

Table A12. Key parameters for p-type transport

		m_c^* (m_e)	m_d^* (m_e)	Ξ (eV)	N	E_g (eV)	c (GPa)	ε_∞	ε_0
Co₄As₄S₄	VBM	0.721	1.436	13.78	2	0.94	139.37	24.40	31.37
	VSB	0.907	1.788	13.56	2	0.95			
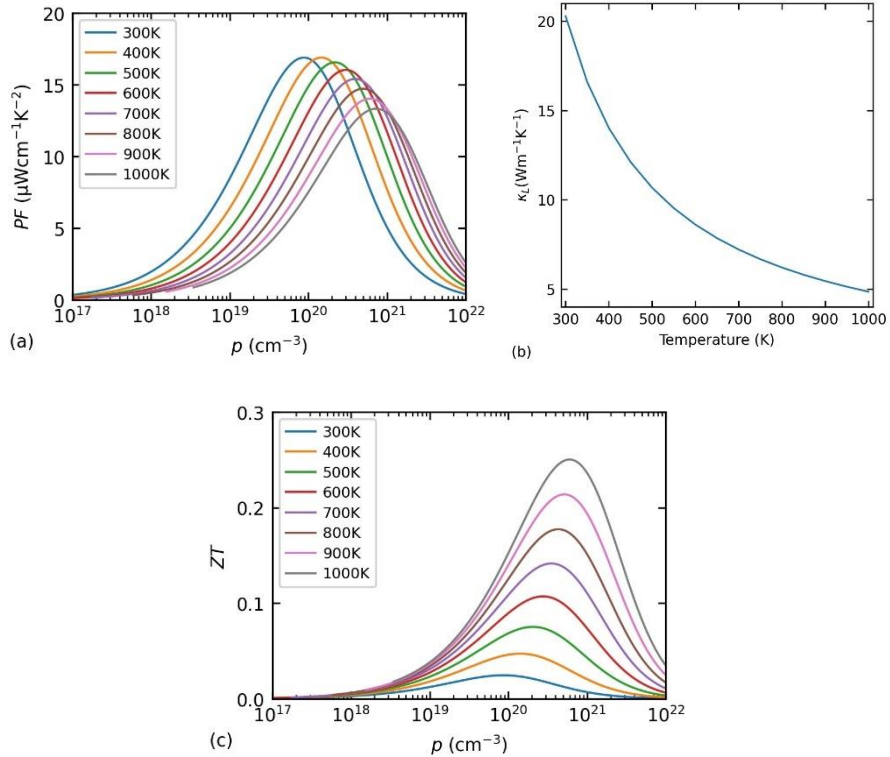
Figure A42. Thermoelectric properties of Co₄As₄S₄ for p-type transport. (a) power factor, (b) lattice thermal conductivity, and (c) figure of merit.

A13. Er₄Te₄As₄
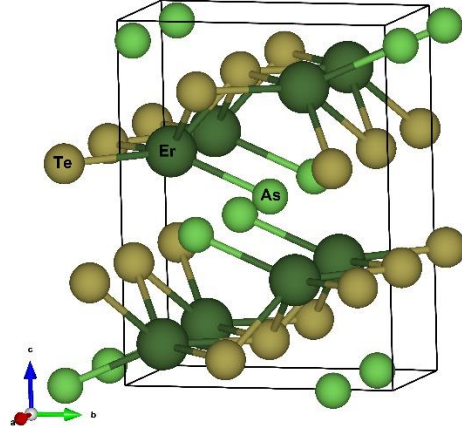
Figure A43. Crystal structure of Er₄Te₄As₄.
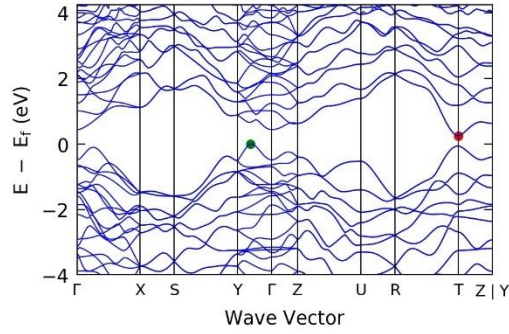
Figure A44. Band structure of Er₄Te₄As₄.

Table A13. Key parameters for p-type transport

		m_c^* (m_e)	m_d^* (m_e)	Ξ (eV)	N	E_g (eV)	c (GPa)	ε_∞	ε_0
Er₄Te₄As₄	VBM	0.306	2.926	10.47	2	0.25	61.01	25.97	33.56
	VSB	0.173	0.182	9.98	1	0.31			
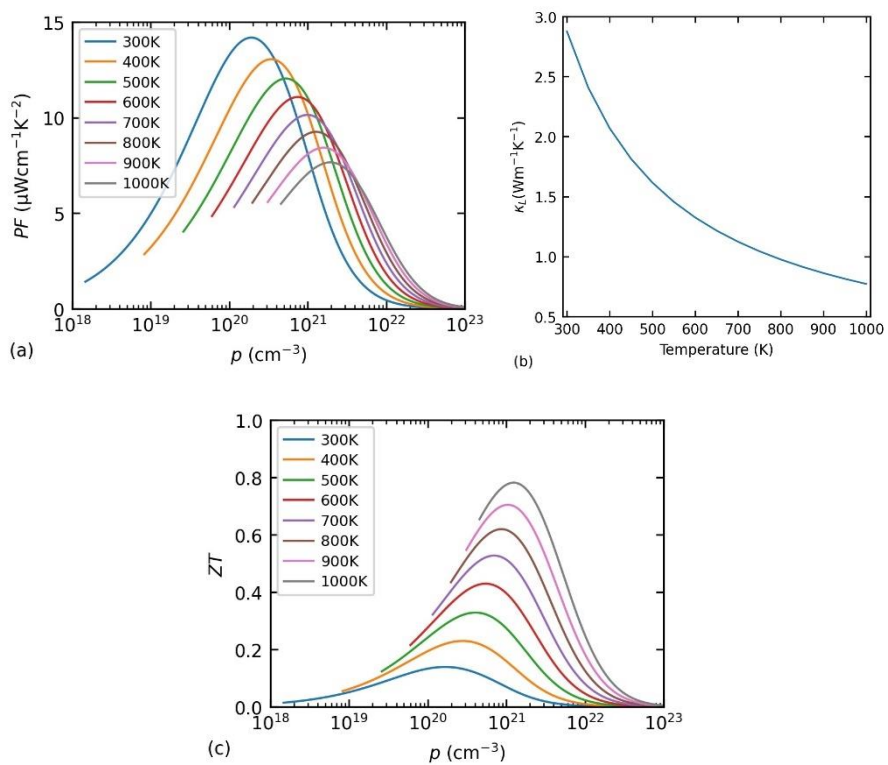
Figure A45. Thermoelectric properties of Er$_4$Te$_4$As$_4$ for p-type transport. (a) power factor, (b) lattice thermal conductivity, and (c) figure of merit.

A14. Dy$_4$Te$_4$As$_4$
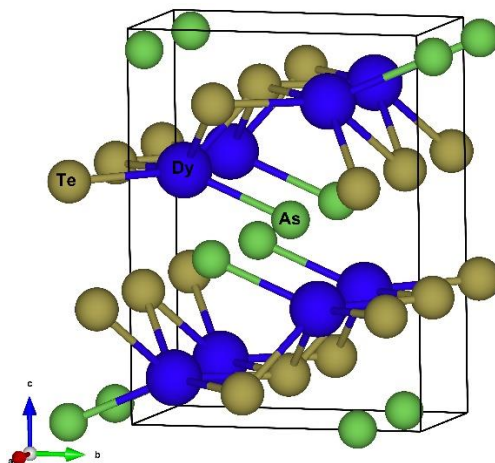
Figure A46. Crystal structure of Dy$_4$Te$_4$As$_4$.
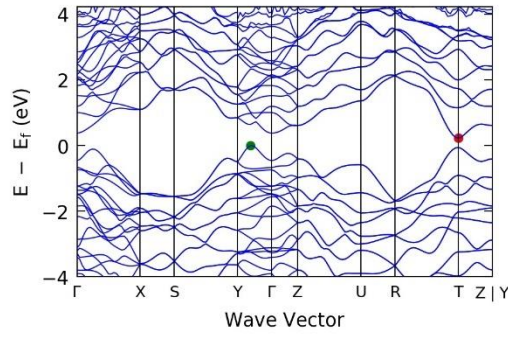
Figure A47. Band structure of Dy$_4$Te$_4$As$_4$.

Table A14. Key parameters for p-type transport

		m_c^* (m_e)	m_d^* (m_e)	Ξ (eV)	N	E_g (eV)	c (GPa)	ε_∞	ε_0
Dy$_4$Te$_4$As$_4$	VBM	0.316	3.197	10.43	2	0.22	60.23	27.24	34.91
	VSB	0.163	0.169	9.94	1	0.28			

(a)

(b)

(c)
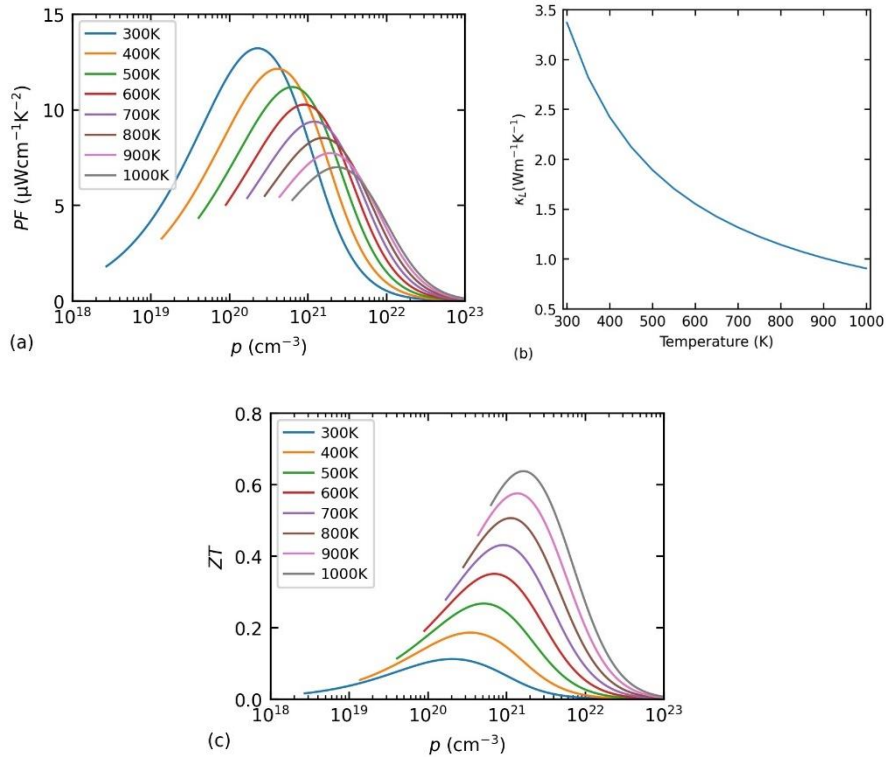
Figure A48. Thermoelectric properties of Dy$_4$Te$_4$As$_4$ for p-type transport. (a) power factor, (b) lattice thermal conductivity, and (c) figure of merit.

A15. Ga₂HgTe₄
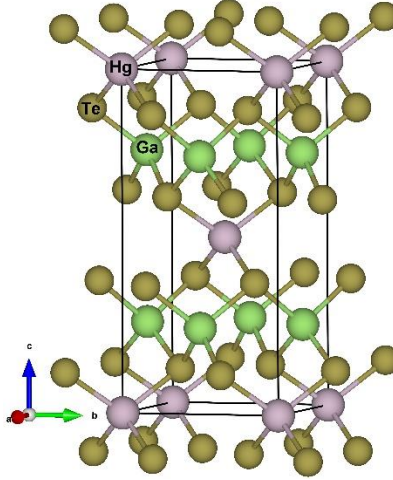
Figure A49. Crystal structure of Ga$_2$HgTe$_4$.
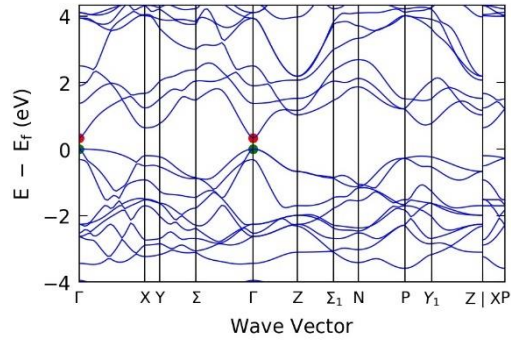
Figure A50. Band structure of Ga$_2$HgTe$_4$.

Table A15. Key parameters for p-type transport

		m_c^* (m_e)	m_d^* (m_e)	Ξ (eV)	N	E_g (eV)	c (GPa)	ε_∞	ε_0
Ga₂HgTe₄	VBM	0.549	0.549	10.48	1	0.33	52.12	16.38	21.58
	VSB	0.334	2.027	9.43	2	0.52			
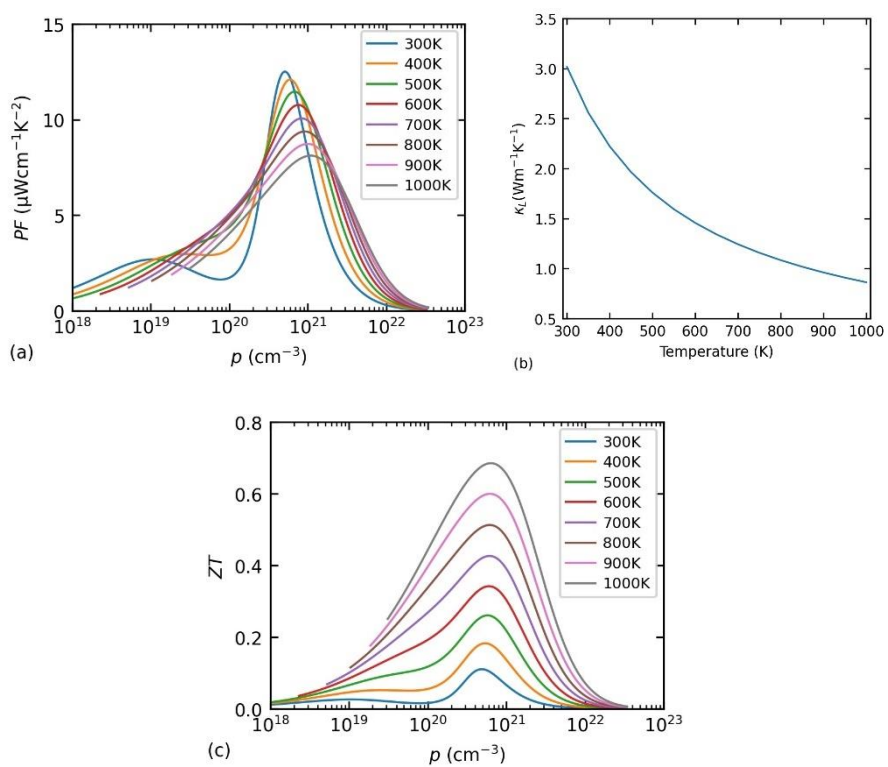
Figure A51. Thermoelectric properties of Ga$_2$HgTe$_4$ for p-type transport. (a) power factor, (b) lattice thermal conductivity, and (c) figure of merit.

A16. Cd$_4$TeSe$_3$
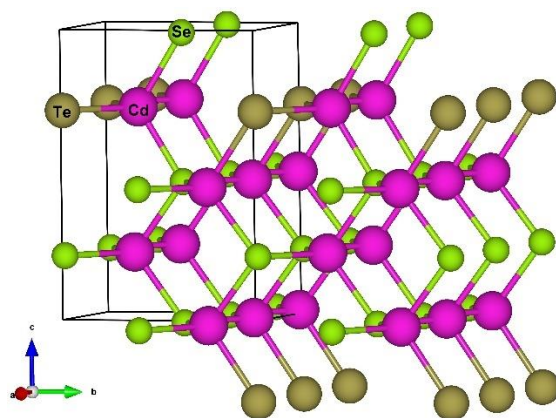
Figure A52. Crystal structure of Cd$_4$TeSe$_3$.
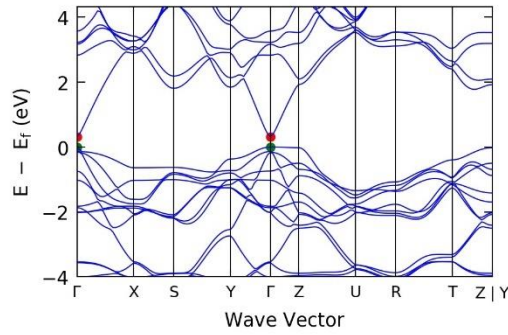
Figure A53. Band structure of Cd_4TeSe_3.

Table A16. Key parameters for p-type transport

	m_c^* (m_e)	m_d^* (m_e)	Ξ (eV)	N	E_g (eV)	c (GPa)	ε_∞	ε_0
Cd_4TeSe_3	0.121	0.762	7.66	1	0.32	21.59	10.72	14.74
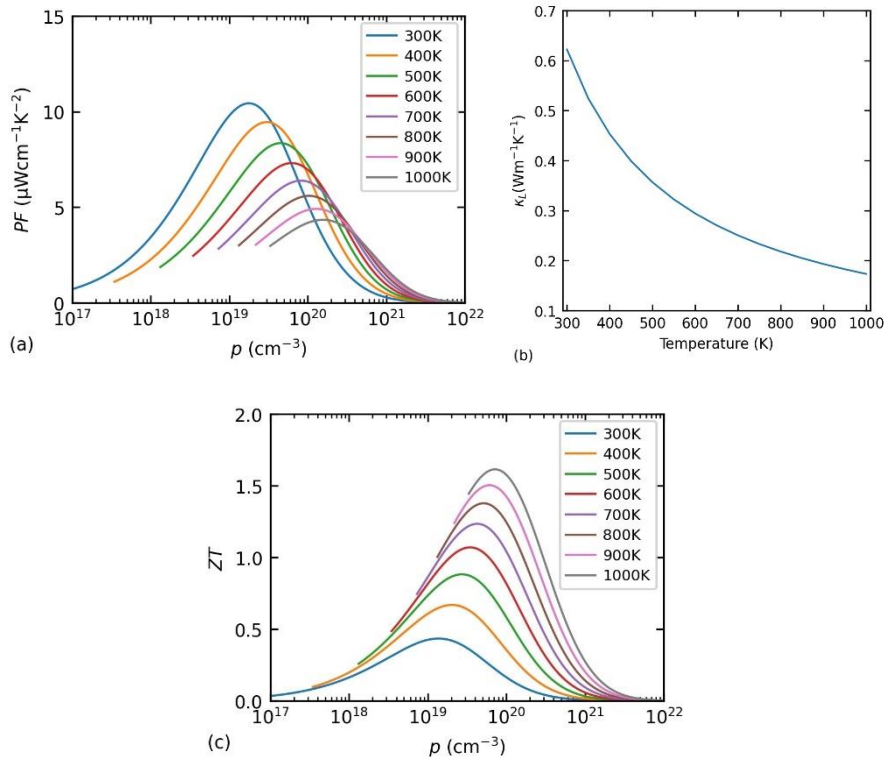
Figure A54. Thermoelectric properties of Cd_4TeSe_3 for p-type transport. (a) power factor, (b) lattice thermal conductivity, and (c) figure of merit.